CRANFIELD UNIVERSITY

Yading Wang

Protection of magnesium alloys from corrosion using magnesium rich surfaces.

SATM
PhD in Manufacturing

Academic Year: June 2021

Supervisors: Dr S A Impey, Dr A J Pidcock

CRANFIELD UNIVERSITY

Yading Wang

Protection of magnesium alloys from corrosion using magnesium rich surfaces.

SATM
PhD in Manufacturing

Academic Year: June 2021

Supervisors: Dr S A Impey, Dr A Pidcock

This thesis is submitted in partial fulfilment of the requirements for the degree of PhD

ABSTRACT

Mg alloys have great potential in engineering applications for saving energy consumption due to the high strength to weight ratio. Mg alloys are also biocompatible and biodegradable with biomedical applications such as orthopaedic and vascular implants. Controlling the corrosion of Mg alloy components is necessary to sustain their performance over the design lifespan. A low corrosion rate is also preferred for implants to mitigate negative effects such as hydrogen evolution during corrosion.

Surface films can be used to control the corrosion of an Mg alloy effectively. In this work, $Mg(OH)_2$ coatings were deposited on Mg alloy substrates (AZ31 and ZM21) by hydrothermal (H.T.) steam treatment as a benchmark and subsequently by novel processing using electrochemical (E.C.) and additive treatment with an Mg^{2+} rich solution. The microstructures and compositions of the alloys are characterised both with and without coatings.

Corrosion tests were conducted in various test solutions, including 3.5% NaCl, 0.9% NaCl and Hank's solutions. Electrochemical techniques and mass change measurement are used for the corrosion testing of initial exposure and longer-term immersion, respectively.

The processing parameters of the electrochemical and additive methods were optimised based on the corrosion behaviour of the coated samples.

This research shows that the $Mg(OH)_2$ based coating can enhance the corrosion protection of the Mg alloy substrates, with at least a 3 fold reduction in corrosion rates compared to uncoated substrates. Comparing hydrothermal coatings, the electrochemical and additive (EC+Additive) coatings not only show similar corrosion performance but also greater manufacturing flexibility and repairability with potential for further enhancement.

Key words (magnesium, corrosion, E.I.S., hydrothermal, electrochemical, additive).

ACKNOWLEDGEMENTS

Four years later news arrived in Athens city.

From the other side of mountains and valleys.

I wasn't lost but jogging with the breeze.

Triumph is triumph, now we should celebrate it.

Thank you, Sue, thank you Andy for your supervision, Thank you for your inspiration and encouragement. What I learned from you will benefit me for life.

Thank you, Christine C, Christine T, Tracy, Xianwei, and Steve for your help and support. I cannot go that far without you.

Thank you Nofrizal, Mohammad, Luis, Fabian, Sarah and Victoria I miss the time in the lab and office with you.

Thank you, Mama, Papa. You gave life to me and provided everything that make me better. I love you!!

Thank you my wife Claire. I will always listen to you,

Although I am the navigator travelling for holiday and know the geography, my sweetheart you are always right on a bigger map♥.

TABLE OF CONTENTS

LIST OF FIGURES

LIST OF TABLES

LIST OF EQUATIONS

LIST OF ABBREVIATIONS

A	Area
AC	Alternating current
ASTM	American Society for Testing and Materials
B	Stern-Geary constant
b_a	Anodic Tafel slope
b_c	Cathodic Tafel slope
C_{dl}	Double layer capacitance
CE	Counter electrode
C_{pf}	Surface layer capacitance
DC	Direct current
DI	De-ionised
E_{anode}	Anode electrode potential
$E_{cathode}$	Cathode electrode potential
E_{corr}	Corrosion potential
E_{OCP}	Open circuit potential
EC	Electrochemical
EDX	Energy dispersive X-ray spectroscopy
EIS	Electrochemical impedance spectroscopy
F	Faraday's constant
FIB	Focused ion beam
GF	'Goodfellow'
HBSS	Hanks’ balanced salt solution
HCP	Hexagonal close packed
HE	Hydrogen Evolution
HT	Hydrothermal (treatment)
i_0	Standard exchange current density
i_A	Anodic half reaction current density
i_c	Cathodic half reaction current density
i_{corr}	Corrosion current density
IPA	Isopropyl alcohol
LPR	Linear polarisation resistance
LDH	Layered double hydroxide
M	1. Metal; 2. Molar mass
m	Mass
ME	Magnesium Elektron
NS	Normal Saline

OCP	Open circuit potential (test)
PBS	phosphate-buffered saline
R	Gas constant
R_{ct}	Charge transfer resistance
RE	Reference electrode
R_p	Polarisation resistance
R_{pf}	Surface layer resistance
R_0	Electrolyte/solution resistance
RT	Room temperature
SBF	Simulated body fluid.
SCE	Saturated calomel electrode
SEM	Scanning electron microscope
SHE	Standard hydrogen electrode
T	Temperature
t	Time
WE	Working electrode
XRD	X-ray diffraction
Z	Valency
Zω	frequency-dependant impedance
α_A	Anodic transfer coefficients
α_C	Cathodic transfer coefficients
φ	Electrostatic potential
η	Overpotential
ω	Frequency
ρ	Density

1 INTRODUCTION

1.1 Background

Magnesium based alloys exhibit favourable properties of high strength to weight ratio, good castability, machinability, and have high potential in the automotive and aerospace industries. Magnesium alloys are also biocompatible, biodegradable and promising in a range of medical applications. However, there are concerns about the Mg alloy for its high chemical activity of magnesium, leading to corrosion problems and limiting further development and application.

Corrosion protection over time in different environments is important to consider. For example, in automotive applications, longevity and surface appearance are critical. For biomedical applications, careful control of the dissolution of implants is more appropriate. Understanding the protection mechanism and controlling substrate or implant lifetime in different environments is desirable.

Mg alloys used in implants are mainly divided into orthopaedic and vascular implants. The main drawback of the use of magnesium in implants is its high corrosion rate in the physiological environment. Magnesium hydroxide $Mg(OH)_2$ is a natural aqueous corrosion product of Mg which can act as a barrier to reduce any further corrosion of the substrate. Thus, a $Mg(OH)_2$ surface layer potentially could enhance the corrosion protection of Mg alloy substrates, slowing down the degradation of Mg implants. Hydrogen release is associated with Mg degradation, and it is paramount to control the degradation rate of Mg implants to limit the rate and volume of hydrogen evolution.

Applying coatings to magnesium alloys is the most effective way to minimise corrosion. In addition to a barrier between the metal and the environment, a coating keeps magnesium parts from contacting other metal parts, providing an opportunity to address any dissimilar metal (galvanic) corrosion. Several surface modification strategies are available such as conversion coatings, anodising, plating, gas-phase deposition, laser surface alloying and polymer coatings [Gray, 2002; Abela,2011].

The research drive is to identify a suitable coating technique and coating that is environmentally friendly, energy efficient to apply while minimising any demand for additional chemicals. Additional elements can add expense, may be undesirable considering human health and the environment. If the coating is damaged, the electrochemical potential difference between coating and substrate is small, minimising detrimental galvanic interaction.

A naturally formed corrosion product layer of $Mg(OH)_2$ exhibits limited thickness and porous morphology, and is susceptible to detrimental elements in aqueous medium (e.g. Cl^-) and impurities in the alloys (e.g. Fe). Thick, dense $Mg(OH)_2$ coatings can be developed which exhibit greater protection than that naturally formed. Hence a hydrothermal treatment (HT) for magnesium alloys has been reported where alloy surfaces react with steam, water or non-toxic solutions to form dense $Mg(OH)_2$ films [Ishizaki, 2013; Zhu, 2011&2012 et al.]. Higher corrosion resistance by this coating was reported. Such coating strategy shows great potential due to the processing low cost, reduced impact on the environment and biocompatibility and is worth further investigation. In literature, most results report corrosion rates of the films as a one-off static values, and there is a considerable variation between papers. Further quantification of the corrosion resistance and rate of film breakdown is also needed.

A novel electrochemical approach for depositing $Mg(OH)_2$ films on Mg alloys was first investigated in previous research at Cranfield [Wang, 2015; Pidcock, 2014]. This type of film showed some corrosion protection with a more flexible coating procedure than the hydrothermal method for a range of components.

This PhD project aims to investigate and demonstrate the corrosion protectiveness of process $Mg(OH)_2$ based coatings on Mg alloys. The work started with replicating and characterising hydrothermal coatings using literature sources, and testing corrosion performance. The formed hydrothermal coatings are considered a benchmark for subsequent investigations using two routes (a) a novel electrochemical route and (b) additive (layer by layer) coating that apply $Mg(OH)_2$ salts on Mg alloy layer by layer, details see chapter 3. The $Mg(OH)_2$ film formation, and the corrosion performance with time of exposure in saline aqueous

environments for all methods were examined. Longevity and durability for corrosion protection are considered for film processing parameters such as temperature and processing time. The $Mg(OH)_2$ coating composition, microstructure, and corrosion performance with time in the corrosion environment are examined in detail.

1.2 Aim and objectives.

This research aims to demonstrate the corrosion protection of magnesium alloys by manufacturing $Mg(OH)_2$ based films on Mg alloy and quantify the corrosion resistance performance. Objectives to achieve the aim are to:

O1. Develop $Mg(OH)_2$ films formed with a hydrothermal (HT) method (for benchmarking).
O2. Form $Mg(OH)_2$ films on Mg alloy surfaces with a novel electrochemical (EC) method and optimise parameters and conditions using an additive approach.
O3. Quantify the corrosion performance of $Mg(OH)_2$ coatings.
O4. Evaluate $Mg(OH)_2$ film for biocompatibility to control Mg alloy degradation.
O5. Compare $Mg(OH)_2$ film development and performance and make recommendations. compare and reflect on $Mg(OH)_2$ film development and performance.
O6. Evaluate $Mg(OH)_2$ film for biocompatibility to control Mg alloy degradation.

1.3 Thesis structure

The thesis comprises nine chapters. Chapter 2 firstly reviews the background of magnesium, alloys, and their applications (Chapter 2.2). The next section focuses on the corrosion behaviour of Mg alloys (Chapter 2.3). The end of chapter 2 reviews recent literature on the corrosion protection of Mg alloys from coatings with emphasis on the coating systems of $Mg(OH)_2$.

Chapter 3 provides methodological approaches and strategies for overall research (Chapter 3.1). Experimental methods used to gather results are introduced along with the sample pre-treatment, experimental procedures and parameters, and equipment used for experiment and analysis (Chapter 3.2).

Chapters 4 and 5 cover the characterisation and analysis results of the Mg alloys and the Mg alloys with $Mg(OH)_2$ films by the hydrothermal as a benchmark, and the novel electrochemical and additive methods were firstly studied in this work. Chapter 6 focuses on the quantitative corrosion measurements and post-degradation analysis of the Mg alloy substrates and the substrates with $Mg(OH)_2$ films. Chapter 7 provides a corrosion assessment of substrate in solutions with the salts as a body fluid for biocompatible.

Chapter 8 is general discussion. It summarises and compares the corrosion behaviour of the coatings, discussing the possible mechanism involved. The performance of $Mg(OH)_2$ coatings with other methods in literature is compared. Finally, the applicability of these coating methods in real application and production is considered.

Chapter 9 summarises the main findings, intellectual contribution, and further work.

2 Literature review

2.1 Background of Mg and its alloy

Magnesium is the eighth-most abundant element in the earth's crust [Russell, 2005; Housecroft 2008; Kainer, 2003] and the third most abundant element in seawater with a concentration of 0.013% [Floor, 2006] with magnesium the lightest engineering alloy. As an alloy, it has great potential for energy saving due to its high specific strength (14060 mx10$^{3)}$, a sixth higher than Al alloys (12081 mx10$^{3)}$, and three times that of steel (4539 mx10$^{3)}$ [Kulekci, 2008].

Magnesium based alloys were first developed in the early 20th century due to the large consumption of materials during WWII. Lightweight, high strength magnesium alloys were widely used as vehicle and aircraft components.

The development of magnesium slowed down because of the low corrosion resistance, poor creep resistance, poor formability for cold wrought, and higher production cost. It is reported that less than 1 weight per cent of magnesium alloy has been used for vehicles since 2004 [Blawert, 2004].

In recent years, much research on magnesium alloys has been carried out in automotive applications due to the potential increases in fuel-saving and reductions in environmental impact. Potentially 20%-70% weight loss of a vehicle can be achieved using magnesium alloy components rather than other alloys such as steel and aluminium [Kulekci,2008].

Nowadays, magnesium alloys are mainly used for some interior vehicles parts, such as instrument panels and door inners. Magnesium alloy parts used in an interior are less likely to undergo severe aqueous corrosion than exterior parts. Power train systems at a lower temperature (<175°C) also use magnesium alloys [Blawert, 2004]. To extend the use of magnesium alloys on exterior parts of a vehicle, a more advanced corrosion protection solution is required for the future.

Since the later 1990s, Investigations have been carried out for bio-degradable implants preventing the need for a second operation from removing implants after

tissue healing [Song, 2011]. Mg alloys have become an important candidate in such applications, especially in cardiovascular and orthopaedic operations.

2.2 Mg Alloys

Mg is in the 3rd period, 2nd group on the periodic table with an atomic mass of 24.305. Mg has a density of 1.738g/cm^2 at room temperature (RT), with a melting point of 650°C. Mg exhibits a hexagonal closed packed structure with an a/c ratio of 1.624 at RT [Polmear, 2006].

Mg can be alloyed with various elements to have desired properties or for ease of processing. One of the most conventional code systems of Mg Alloys is designed by the American Society for Testing and Materials (ASTM) [ASTM B951-10,(2010)]. This ASTM code comprises two letters that represent two principal elements in the orders of the quantities, followed by two numbers that represent the proportion of the two elements in wt%. Table 2.2.1 lists the common alloying elements for magnesium and their code [ASTM B951-10, 2010; Polmear, 2006; Avedesian,1999]. For example, AZ31 represents a Mg alloy that contains approximately 3^{wt}% Al and 1^{wt}% Zn. The code is also followed with letters and numbers to represent heat treatment post fabrication [Polmear, 2006; M. Avedesian,1999]. Alloying systems based on the major alloying elements: manganese, aluminium, zinc, zirconium, and rare earth elements are currently commercially produced [Avedesian,1999].

Table 2.2.1. Letters Representing Alloying elements [ASTM B951-10,2010]

A	Aluminium	Q	Silver
C	Copper	S	Silicon
E	Rare Earth	T	Tin
H	Thorium	V	Gadolinium
J	Strontium	W	Yttrium
K	Zirconium	Z	Zinc
M	Manganese		

The general effects of the elements in Mg alloy are studied in various publications and a summary given by Polmear [Polmear, 2006] is listed in Table 2.2.2.

Table 2.2.2. General effects of some Mg alloying elements [Polmear, 2006, adapted by Pidcock 2014].

Alloying element	Melting and casting behaviour	Mechanical and technological properties	Corrosion behaviour
Ag	-	Improves elevated temperature tensile and creep properties in the presence of rare earths	Detrimental influence on corrosion behaviour
Al	Improves castability, tendency to micro-porosity	Solid solution hardener, precipitation hardening at low temperatures (<120°C)	Minor influence
Be	Significantly reduces oxidation of melt surface at very low concentrations (<30 ppm), leads to coarse grains	-	-
Ca	Effective grain refining effect, slight suppression of oxidation of the molten metal	Improves creep properties	Detrimental influence on corrosion behaviour
Cu	System with easily forming metallic glasses, improves castability	-	Detrimental influence on corrosion behaviour, limitation necessary
Fe	Magnesium hardly reacts with mild steel crucibles	-	Detrimental influence on corrosion behaviour, limitation necessary
Li	Increases evaporation and burning behaviour, melting only in protected and sealed furnaces	Solid solution hardener at ambient temperatures, reduces density, enhances ductility	Decreases corrosion properties strongly, coating to protect from humidity is necessary
Mn	Control of Fe content by precipitating Fe-Mn compound, refinement of precipitates	Increases creep resistance	Improves corrosion behaviour due to iron control effect
Ni	System with easily forming metallic glasses	-	Detrimental influence on corrosion behaviour, limitation necessary
Rare earths	Improves castability, reduces micro-porosity	Solid solution and precipitation hardening at ambient temperatures, improve elevated temperature tensile and creep properties	Improve corrosion behaviour
Si	Decreases castability, forms stable silicide compounds with many other alloying elements, compatible with Al, Zn, and Ag, weak grain refiner	Improves creep properties	Detrimental influence
Th	Supresses micro-porosity	Improves elevated temperature tensile and creep properties, improves ductility, most efficient alloying element	-
Y	Grain refining effect	Improves elevated temperature tensile and creep properties	Improves corrosion behaviour
Zn	Increases fluidity of the melt, weak grain refiner, tendency to micro-porosity	Precipitation hardening, improves strength at ambient temperatures, tendency to brittleness and hot shortness unless Zr refined	Minor influence, sufficient Zn content compensates for the detrimental effect of Cu
Zr	Most effective grain refiner, incompatible with Si, Al, and Mn, removes Fe, Al, and Si from the melt	Improves ambient temperature tensile properties slightly	-

2.2.1 Mg-Al-Zn alloys (AZ series)

Mg-Al-Zn, from the AZ series, is one of the most common alloy systems. It typically contains 3 wt% to 1wt% Al and 1 wt% to 3wt% to improve its specific strength [Polmear, 2006]. A small amount of Mn (<0.5wt%) is also added to limit the corrosion rates and mechanical properties [Pidcock, 2014].

The proportions of Al and Zn in Mg-Al-Zn alloys exceed the maximum solid solubility limit at approximately 1 wt% for Al and 0. 3wt% for Zn at RT, respectively [Friedrich,2006; Avedesian, 1999; Nayeb-Hashemi, 1988]. Second phase precipitates are likely to form, which can improve the strength of the alloy by precipitate hardening [Liang, 2017].

According to the binary phase diagrams between Mg to Al, γ-$Mg_{17}Al_{12}$ is one primary precipitate as seen in Figure 2.2.1 [Friedrich 2006].

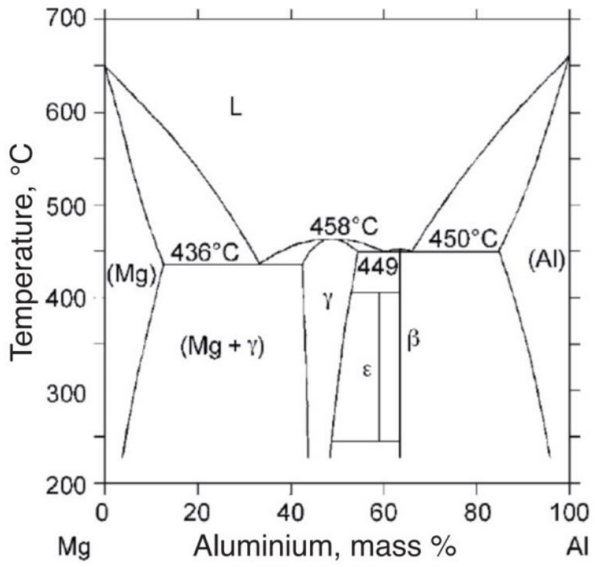

Figure 2.2.1 Mg-Al Binary Phase diagram with Mass% scale [Friedrich, 2006]

Apart from the binary γ phase, tertiary Mg-Al-Zn phases may also exist. A review by Krebs identified the tertiary phase in Mg alloys as τ-$Mg_{32}(Al\ Zn)_{49}$ and φ-$Mg_6(Al, Zn)_5$ in AZ series alloys [Krebs, 2017]. However, whether the precipitates exist strongly depends on the alloy composition, processing, and heat treatment. $Mg_{17}Al_{12}$ phase is seldom recognised with extruded AZ31 alloy, having the lowest Al proportion amongst the AZ series [Stanford 2013].

The absence of $Mg_{17}Al_{12}$ in wrought AZ31 alloy is possible because Al contributes to forming another intermetallic phase of Al_xMn_y, with the remaining Al in solid solution.

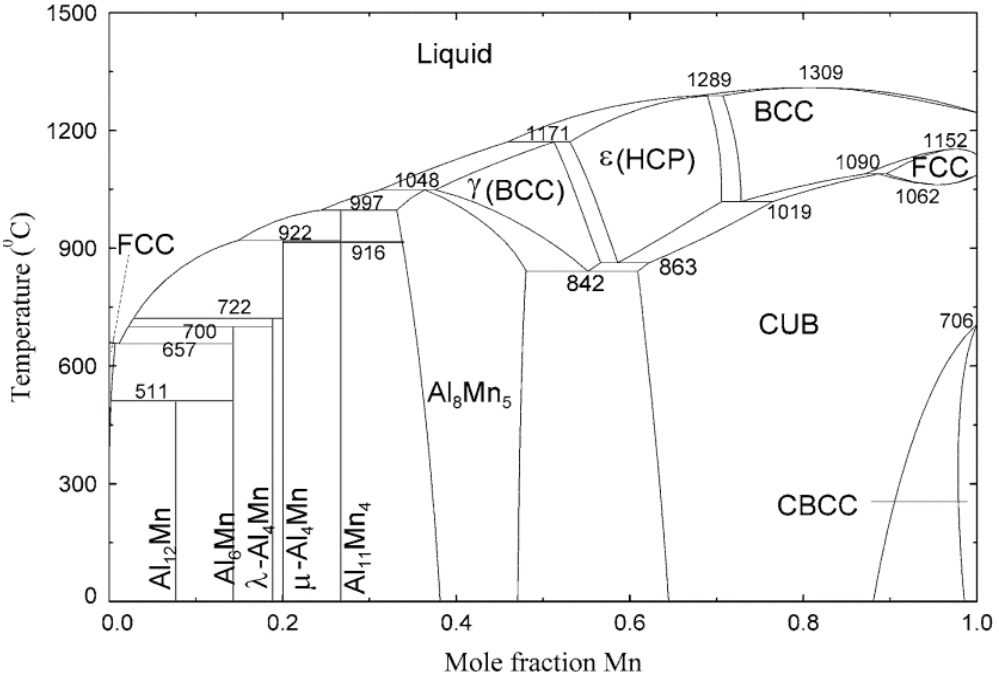

Figure 2.2.2 Al-Mn binary phase diagram [Friedrich 2006].

Table 2.2.3 A list of AlMn phases with corresponding Al: Mn mass ratios based on the Al-Mn binary phase diagram.

	Al: Mn ratio (lower margin)	Al: Mn ratio (higher margin)
Al_8Mn_5	1.1	1.7
$Al_{11}Mn_4$	1.7	2.7
Al_4Mn (μ)	2.7	4.4
Al_4Mn (λ)	4.4	6
Al_6Mn	6	12
$Al_{12}Mn$	12	>12

Various studies have identified Al_xMn_y intermetallics in AZ31. Al_xMn_y intermetallics formed include Al_8Mn_5, Al_6Mn_5, $Al_{11}Mn_4$, Al_4Mn (μ and λ), Al_6Mn and

$Al_{12}Mn$, according to the Al-Mn binary phase diagram in Figure 2.2.2, [Friedrich 2006]. A list of AlMn phases with corresponding Al: Mn mass ratios based on the Al-Mn binary phase diagram is given in Table 2.2.3. Mn has a good affinity with Fe to form AlMnFe intermetallics including $Al_6Mn(Fe)$, $Al_6(MnFe)$, $Al_8Mn_5(Fe)$ and $Al_3Fe(Mn)$ [Song, 2003].

2.2.2 Mg-Zn alloy

Accumulation of Al has been suggested to be associated with various neurological disorders [El-Rahman, 2003]. L. Nan has reviewed alloy systems suitable for biomedical use where Mg-Zn based alloys are commonly used, including Mg-Zn, Mg-Zn-Mn, Mg-Zn-Ca, Mg-Zn-Zr, and Mg-Zn-Y systems [Nan, 2013]. Zn is also a trace element with an intake upper limit of Zn 40mg [Institute of Medicine, 2001]. The addition of Zn to Mg to produce a Mg–Zn scaffold improves both the biodegradability and mechanical properties of Mg alloys [Seyedraoufi, 2018]. For binary Mg-Zn MgZn and Mg_2Zn_3, are likely to form [Polmear, 2006]. The Mg-Zn binary phase diagram is shown in Figure 2.2.3 [Gale, 2004].

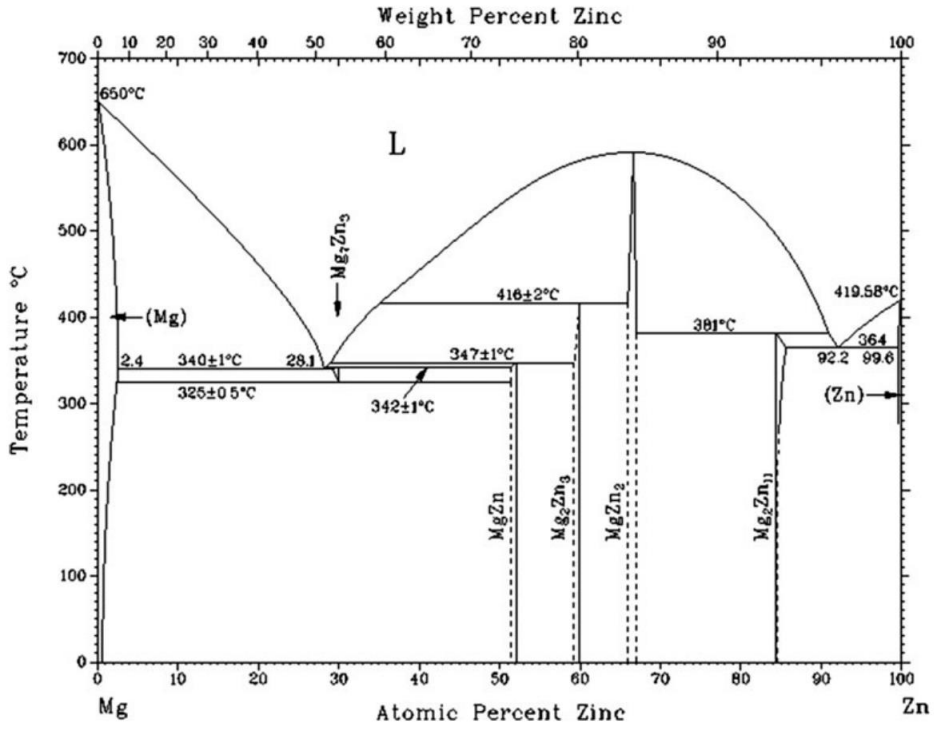

Figure 2.2.3 Mg-Zn binary phase diagram [Gale, 2004].

The influence of alloy elements on the corrosion behaviour of Mg alloy is further studied, and the relevant literature is reviewed in the next section 2.3.

2.3 Corrosion behaviour of magnesium and its alloys

Although magnesium alloys have better corrosion performance in dry atmospheres than some iron or aluminium based engineering alloys [Kanier, 2003], Mg alloys are much more vulnerable in aqueous environments such as seawater, and industrial acids or humid air and being splashed by aqueous solutions.

It is important to understand the corrosion mechanism of magnesium alloy before further exploring its corrosion protection. The following review is mostly based on studying magnesium corrosion in a static aqueous environment.

This section reviews the background electrochemistry of aqueous corrosion for general metals and Mg. Conventional corrosion tests and analytical tools for Mg are then introduced. The literature is relevant to several aspects including electrochemistry of Mg corrosion, the compositional and microstructural influence of the alloying elements on Mg alloys, and conventional methods of corrosion tests and analyses.

2.3.1 Electrochemistry

2.3.1.1 Corrosion reactions

The natural conversion of magnesium to a more stable form such as its oxide or hydroxide in an aqueous environment in a process known as corrosion is presented in literature [Scully, 1990; Fontana, 1987]. Generally, an electrochemical cell is generated, as in Figure 2.3.1 [Pidcock, 2014]. It consists of electrodes (an anode and a cathode), an aqueous solution and electrical connections between the electrodes.

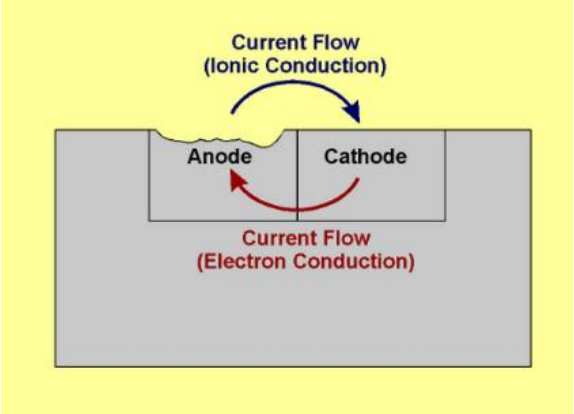

Figure 2.3.1 Schematic illustration of the corrosion mechanism of metals [Pidcock, 2014].

A redox (reduction-oxidation) reaction occurs in the corrosion cell. Driven by the potential difference between a more positive cathode and a more negative anode. Reactions occur spontaneously when these two electrodes are connected externally [Bard, 2011]. An oxidation half-reaction occurs in the anode and a reduction half-reaction in the cathode.

At the anodic site, the metal atoms form positive ions, dissolved into the solution. The main process for metal to lose its mass, and hence corrosion occurs.

It is expressed by equation 2.1:

$$\text{Anodic partial reaction } M \rightarrow M^{Z+} + Ze \qquad \textbf{(2-1)}$$

M is the metal, z is the valency of the metal, and e^- is the electron.

At the cathodic site, there are two types of cathodic reactions in an aqueous environment [Scully, 1990]:

Reduction of the dissolved oxygen, shown in Equation 2.2:

$$O_{2\,(solution)} + 4e^- + 2H_2O \rightarrow 4\,OH^- \qquad \textbf{(2-2)}$$

Reduction of hydrogen ions and evolution of hydrogen gas, Equation 2.3:

$$2H^+_{(in\ solution)} + 2e^- \rightarrow H_{2\,(evolves\ from\ metal\ surface)} \qquad \textbf{(2-3)}$$

Oxidation and dissolution of every atom of the anode metal mean a loss of electrons depending on the valency of the metal type. Therefore, the current

density from the movement of electrons is an important value related to the corrosion rate.

In the case of magnesium substrates, Mg reacts with water molecules to form magnesium hydroxide and hydrogen evolution (HE) occurs (Equation 2-4). The reaction can be divided into an oxidation half-reaction and a reduction half-reaction at anodic sites and cathodic sites respectively. Mg oxidises to Mg^{2+} ions at the anodic site and dissolved into solution, releasing two electrons (Equation 2-5). At the cathodic site, water molecules are reduced and split into hydroxide ions and hydrogen ions and the hydrogen ions are reduced to hydrogen gas H_2, (Equation 2-6).

The cation Mg^{2+} and anion OH^- form the corrosion product of $Mg(OH)_2$. A schematic illustration is shown in Figure 2.3.2

Overall reaction: $$Mg + 2H_2O \rightarrow Mg(OH)_2 + H_2 \quad \textbf{(2-4)}$$

Anodic reaction: $$Mg \rightarrow Mg^{2+} + 2e^- \quad \textbf{(2-5)}$$

Cathodic reaction: $$2e + 2H_2O \rightarrow H_2(g) + 2OH^- \quad \textbf{(2-6)}$$

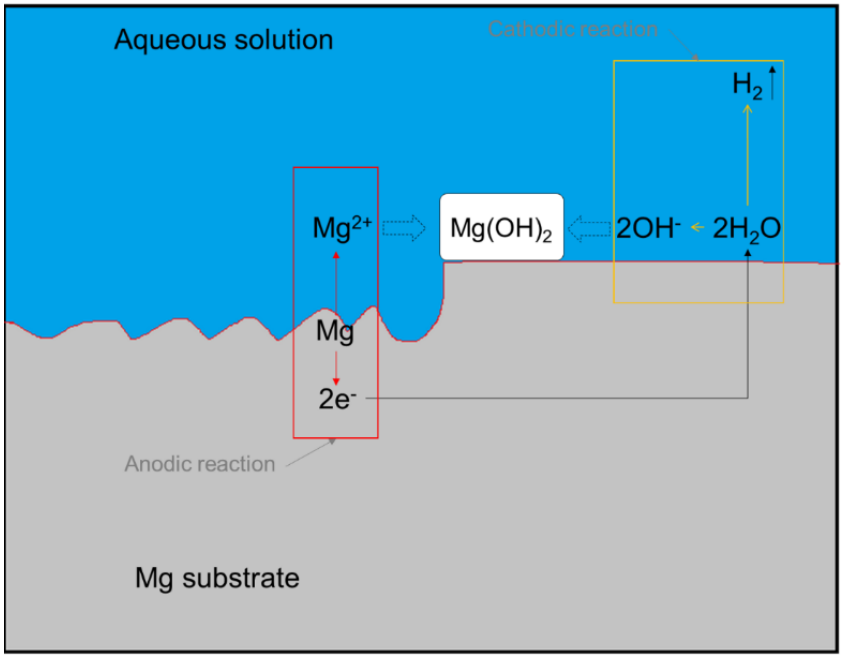

Figure 2.3.2 Schematic illustration of the self-corrosion of Mg substrate.

2.3.1.2 Corrosion potential

To examine and quantify the corrosion rate of the sample with electrochemical methods, the potential E and current density i during corrosion are required.

When a metal is immersed in a solution, there is a potential, E_{cell} (V) the potential across the metal-solution interface (Equation 2-7) [Fernandez-Solis, 2016].

$$E_{cell} = \phi^{metal} - \phi^{solution} \quad \textbf{(2-7)}$$

Where ϕ^{metal} and $\phi^{solution}$ are the electrostatic potentials of the metal and solution respectively with Mg (the electrode) immersed in the solution (electrolyte).

The potential is a thermodynamic value that indicates the driving force of the corrosion reaction. The relation between the standard potential and the free energy ΔG (KJ/mol) of the reaction can be expressed by Nernst equation (Equation 2-8).

$$\Delta G = -zFE^{0}{}_{cell} \quad \textbf{(2-8)}$$

z is the number of electrons transferred in the cell reaction or half-reaction (valence number), F is the Faraday constant (96485C/mol). When E_{cell} is positive, the free energy becomes negative thus the reaction occurs spontaneously. In general terms [Scully, 1990]:

$$E_{cell} = E^{0}{}_{cell} + \frac{RT}{zF} ln \frac{a_{ox}}{a_{red}} \quad \textbf{(2-9)}$$

E^{0}_{cell} is the standard potential of the cell (at RT, 1 atm pressure with the ion concentration of 1mol/dm^3). Where R is the ideal gas constant(8.3145 J/Mol K), T is the temperature in Kelvin (K), a_{ox} and a_{red} are the activities of the oxidised and reduced species respectively, and they can be approximated as the concentration in diluted solution [Fernandez-Solis, 2016].

The potential of the metallic sample is measured experimentally with an open circuit test (OCP). In the OCP test, a reference electrode is added with the working electrode (the sample). The resting potential of the working electrode (the sample) compared to the reference electrode can be measured and is called

the open circuit potential E_{OCP} (V). In the case of self-corrosion such as Mg, when the sample is at equilibrium, the potential of the cell is equal to the open circuit potential and it is also the potential where corrosion occurs, E_{corr} (V).

$$E_{cell} = E_{ocp} = E_{corr} \quad \textbf{(2-10)}$$

Pourbaix Diagram

A Pourbaix Diagram or E-pH diagram generally summarises the thermodynamic stability of Mg in an aqueous solution.

The main uses of the Pourbaix diagrams are [Fontana 1987]:

1. Predicting the spontaneous direction of the reaction.
2. Estimating the composition of corrosion products.
3. Predicting environmental changes to prevent or reduce corrosive attacks.

Figure 2.3.3(a) shows a simplified Pourbaix diagram of magnesium on the left [Pourbaix, 1974] and (b) gives detailed information on the possible stable substances in the Pourbaix diagram [Song, 2011].

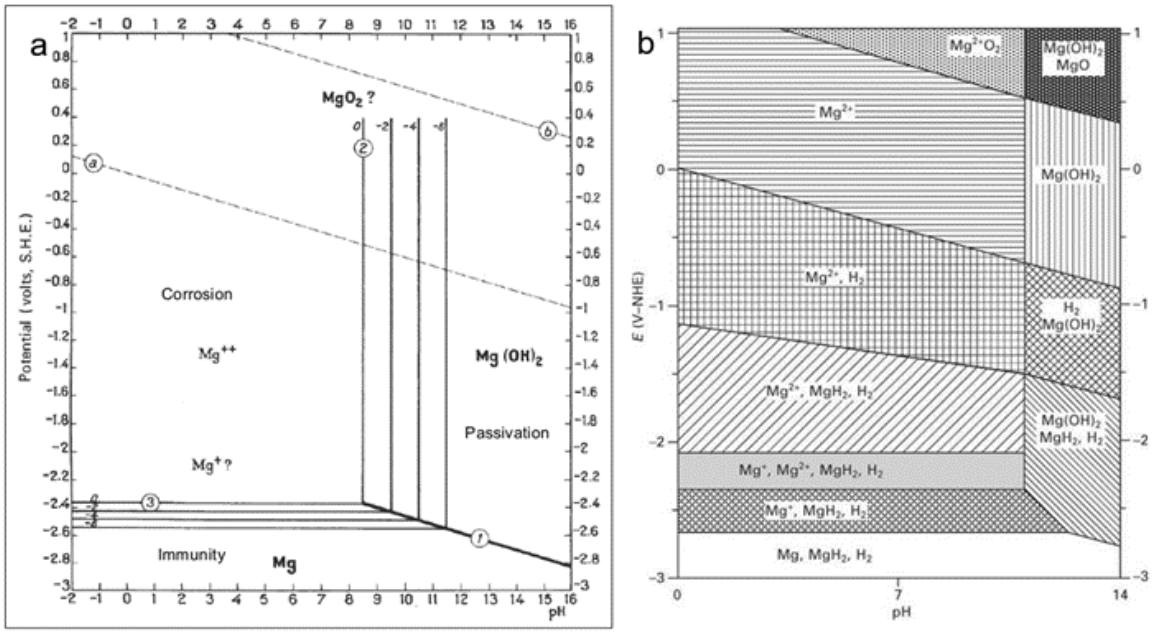

Figure 2.3.3. (a) A Pourbaix diagram of magnesium, (b) E-pH diagram with possible stable substances in the Mg-H_2O electrochemical system (right) [Pourbaix, 1974; Song, 2011].

In Figure 2.3.3 a there are three regions, 'immunity', 'corrosion' and 'passivation'.

In the 'immunity' region, the applied potential is below -2.4 and -2.6 volts standard hydrogen electrode (SHE), which is lower than the intrinsic potential state of magnesium. Therefore, magnesium acts as the cathode and thermodynamically, corrosion does not happen.

With no exterior potential or a positive potential higher than the potential state of magnesium, magnesium acts as the anode and its surface forms hydroxides. Then either 'passivation' or 'corrosion' occurs depending on the pH value.

At the 'passivation' region, where the solution has a sufficiently high pH value, the hydroxide tends to be stable and becomes a barrier preventing further oxidation of the metal.

In the 'corrosion' region, the pH value of the solution is low, the hydroxide layer on the magnesium surface cannot be sustained and tends to decompose, leading to further corrosion. The pH value from passivation to corrosion for magnesium is usually between 8.5 and 10.5, depending on the concentration of Mg^{2+} ions in the solution. It means that in neutral solutions, magnesium tends to corrode.

However, it can be noted that the Pourbaix diagram does not include kinetic information [Scully, 1990; Song, 2011]. If the rate is negligible, even though the reaction is likely to occur according to the Pourbaix diagram, the metal will still be inert [Fontana, 1987].

Two types of magnesium hydroxide, 'labile' and 'stable', can be formed during corrosion [Pourbaix, 1974]. They have different structures, and the 'stable' form dissolves much more slowly than the 'labile' one [Gjaldbaek 1925].

Another limitation of the Pourbaix diagram is that only basic/simple ions in solution are considered. In a real environment, other ionic species also affect corrosion. With a certain amount of chlorine ions in the solution, corrosion can occur at a pH value that is in a passivation region [Song, 2011]. Other species give an opposite effect to passivation. Song et al. list such ions, which include

dichromate, molybdate, nitrate, phosphates, metal-phosphate, vanadate, tartrate and oxalate [Song, 2011].

2.3.1.3 Corrosion kinetics

To study the kinetics of the corrosion, requires the corrosion current density i_{corr}. The current is proportional to the amount of the material oxidised in the corrosion reaction (dissolved metal), expressed with Faraday's Law:

$$I = \frac{dq}{dt} = \frac{nzF}{t} \quad \textbf{(2-11)}$$

The current density i is the current per unit area (A/m^2), and it is proportional to the corrosion rate of the sample. n is the total amount of transformed substance, F is the Faraday constant (96485C/mol), t is time in seconds (s).

When a homogeneous metal with a uniform surface undergoes self-corrosion, The cell is usually at equilibrium. This is because corrosion reactions happen locally and the anodic and cathodic sites are uniformly distributed on the sample surface. The anodic and cathodic sites quickly move or switch during corrosion if the surface profile changes. The current flow from different locations on the surface are balanced with each other. In general terms, the cell is at equilibrium:

At every site where corrosion reactions happen：

$$i_A = -i_C \neq 0 \quad \textbf{(2-12)}$$

For the whole sample at equilibrium:

$$i_0 = \sum i_A = -\sum i_c \approx 0 \quad \textbf{(2-13)}$$

i_A and i_C are the current density (A/cm^2) of the anodic and cathodic half-reactions respectively. i_0 is the standard exchange current density of the sample.

Therefore, in this case, there is zero net current flow through the sample and it cannot be directly measured with an ammeter to the cell.

Instead, the cell shifts from the equilibrium state to gather the data to evaluate the corrosion current density i_{corr}. In an electrochemical corrosion measurement, a reference electrode and a counter electrode are applied with the working

electrode (the sample) in the electrolyte to build a test cell. The cell is polarised by applying an overpotential, η, (V) to the sample where:

$$E = \eta + E^{equilibrium} = \eta + E_{ocp} \quad \textbf{(2-14)}$$

With an overpotential, the partial current density i_A and i_C are not in balance. A net current density i is generated. The relation between potential and current density is described by the Butler-Volmer equation:

$$\mathrm{i} = \mathrm{i}_0[\exp\left(\frac{\alpha_A z F \eta}{RT}\right) - \exp\left(\frac{\alpha_C z F \eta}{RT}\right)] \quad \textbf{(2-15)}$$

As mentioned, i_0 is the exchange current density, $i_0 = 0$ at $\eta = 0$, α_A and α_C are transfer coefficients for anodic and cathodic reactions respectively. Each of them has a value between 0 and 1 [Fernadez, 2016].

When the over-potential is large, the Butler-Volmer equation can be expressed as:

Anodic: $$\mathrm{i}_A = \mathrm{i}_0 \exp\left(\frac{\alpha_A z F \eta}{RT}\right) \quad \textbf{(2-16)}$$

Cathodic: $$\mathrm{i}_C = \mathrm{i}_0 \exp\left(\frac{\alpha_C z F \eta}{RT}\right) \quad \textbf{(2-17)}$$

Then transferred to:

Anodic: $$\eta_a = 2.3 \frac{RT}{\alpha_A z F} (log\ i - log\ i_0) \quad \textbf{(2-18)}$$

Cathodic: $$\eta_c = 2.3 \frac{RT}{\alpha_C z F} (log\ i - log\ i_0) \quad \textbf{(2-19)}$$

Simplified to

Anodic: $$\eta_a = a_a + b_a\ log\ i \quad \textbf{(2-20)}$$

Cathodic: $$\eta_c = a_c + b_c\ log\ i \quad \textbf{(2-21)}$$

This represents a linear relationship between the overpotential and the logarithm of the current density. ‘a’ and ‘b’ values for anodic and cathodic are the intercept gradient of the line respectively and:

$$a = -b\ log\ i_0 \quad \textbf{(2-22)}$$

$$b = -2.3\ \frac{RT}{\alpha zF} \quad \textbf{(2-23)}$$

'b' values are important for converting resistance to corrosion current density in Linear Polarisation Resistance (LPR) and Electrochemical Impedance Spectroscopy (EIS) tests. These are introduced in section 2.3.2.2.

When the over-potential is small, the Butler-Volmer equation can be simplified as:

$$\mathrm{i} = \mathrm{i}_0(\frac{zF\eta}{RT}) \quad \textbf{(2-24)}$$

Here the current density is linearly proportional to the overpotential.

Negative difference effect (NDE) or Anomalous hydrogen evolution (HE)

The hydrogen evolution (HE) reaction is the primary cathodic reaction in Mg corrosion. It takes place spontaneously on Mg under open circuit (unpolarized) conditions [Esmaily, 2017]. In theory, according to Butler-Volmer equation (Equation 2-15), the anodic reaction rate (metal dissolution) increases and the cathodic reaction rate (HE) ought to reduce when Mg is anodically polarised. However, in the real case, increased rates of HE are observed when Mg is anodically polarised. This phenomenon is named as Negative difference Effect (NDE) by Atrens [Atrens, 2007] or Anomalous HE [Esmaily, 2017]. As a consequence of the existence of anomalous HE, Mg and its alloys do not follow Faraday's law and it is not possible to estimate the amount of Mg dissolved under anodic polarization using just electrochemical methods [Esmaily, 2017]

The univalent Mg^+ theory is promoted by Song and Atrens to explain NDE or Anomalous HE, which is based on a hypothetical existence of Mg^+ as an intermediate in the anodic dissolution of Mg [Atrens, 2015]. In this theory, Mg^+ reacts with water to form Mg^{2+} and H_2 [Atrens, 2015]. More Mg^+ is produced as the rate of Mg dissolution increases thus increasing the HE [Atrens, 2015]. However, this theory remains unsolved and has raised criticism because there is

no direct evidence of the existence of aqueous Mg^{+} and this species has never been detected by any experimental technique. [Esmaily, 2017].

Apart from the univalent Mg theory, research was conducted comprehensively to explain NDE or anomalous HE with other mechanisms [Bokris, 2000; William 2008, 2013, 2015; Frankel 2013, 2014, 2015; Fajardo, 2015, 2016, 2017; Birbilis, 2014; Cain 2015; Lysne 2015; Hoche, 2016, Lamaka, 2016; Samaniego, 2015]. These works studied the influence of the corrosion film, surface enrichment with impurities and the increased catalytic activities of the NDE or anomalous HE phenomenon of Mg. Evidence has shown these influencing factors can play a role in HE but further investigation is necessary [Esmaily, 2017].

2.3.2 Corrosion test methods

Various methods and techniques can be applied to quantify the aqueous corrosion of Mg and its alloy. These are reviewed by various authors including Esmaily et al. [Esmaily, 2017]. The tests can be divided into general and localised electrochemical methods and non-electrochemical methods as in Figure 2.3.4.

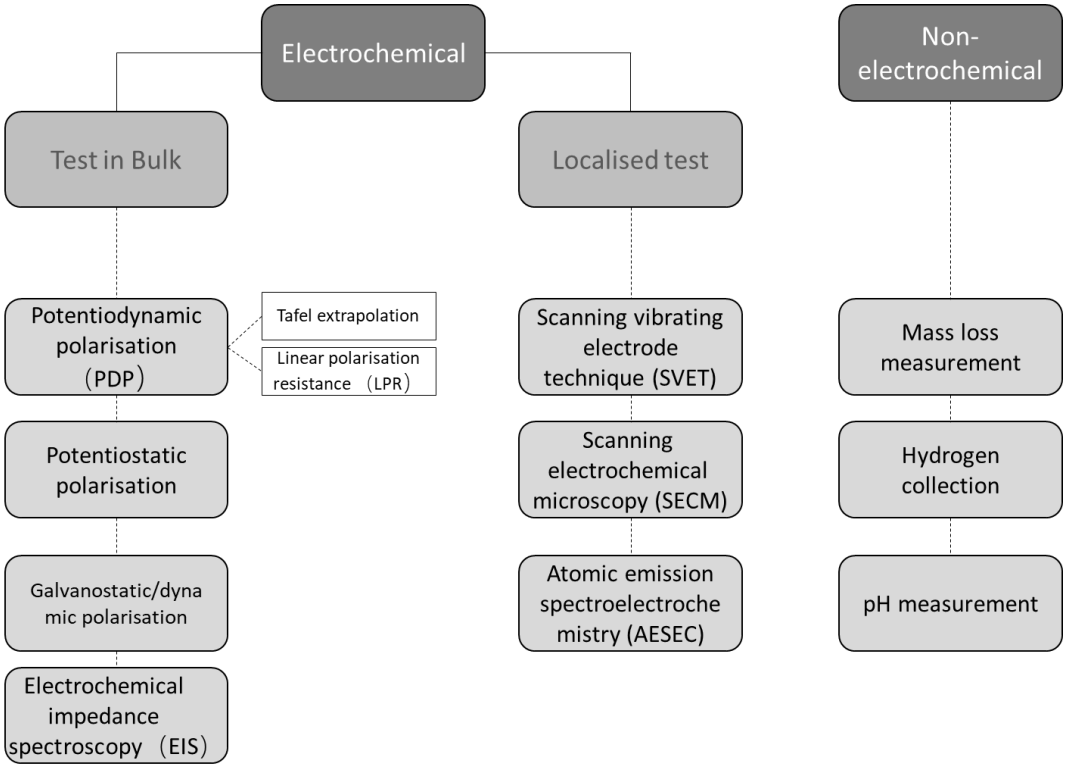

Figure 2.3.4. Corrosion test methods for Mg in aqueous conditions, adapted from the review by Esmaily [Esmaily 2017].

Mg and its alloys do not follow Faraday's law and it is not possible to estimate the amount of Mg dissolved under anodic polarization using just electrochemical methods because of the existence of anomalous HE [Esmaily, 2017].

2.3.2.1 Potential dynamic polarisation (PDP)

Potential dynamic polarisation (PDP employs a potentiostat, reference electrode, and counter electrode to scan the potential of an electrode over a fixed interval at a fixed rate [Frankel, 2014].

There is linear behaviour between the overpotential and logarithm of the current density. A method called Tafel extrapolation fits the experimental polarised E vs Log i curve to the Butler-Volmer equation.

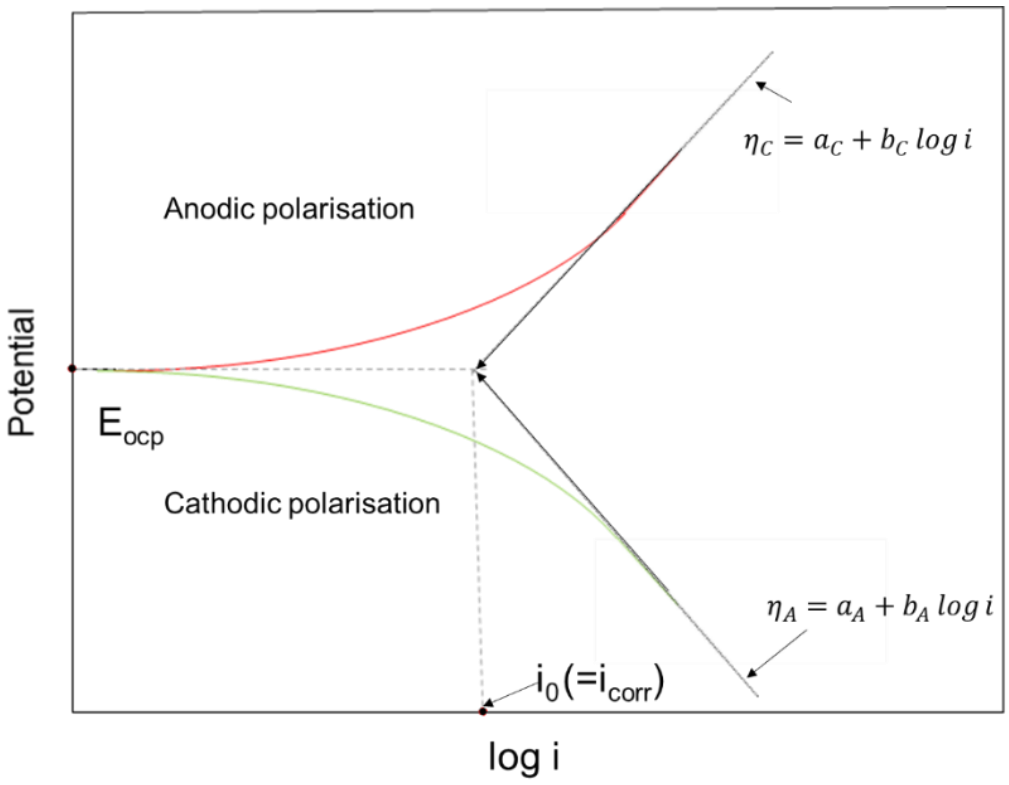

Figure 2.3.5. Ideal Potentiodynamic polarisation curves that fit on the Tafel region and E_{OCP} and i_0 are indicated.

An illustration of an ideal polarised plot with Tafel extrapolation is shown in Figure 2.3.5. Where the red and green curves are the experimental polarisation curves with anodic and cathodic polarisation respectively. Linear fitting lines, which can be expressed as Equations 2-20 and 2-21, are drawn and extrapolated to an

equilibrium state ($\eta = 0, E = E_{ocp}$) to obtain the exchange current density i_0 that is equal to the self-corrosion current of the sample.

As an alternative to Tafel extrapolation, a linear polarisation resistance **(**LPR) scan can be applied in the PDP test. It involves voltage sweep(s) with a smaller overpotential η=±10mV at a rate of 10mV/min. There is a linear relationship between the over-potential and the given current density where Ohm's law applies. The polarised resistance R_p (Ω) can thus be calculated by dividing the change of potential by the change of the current density (Equation 2-25). R_p indicates the corrosion resistance for a sample and its relation to i_{corr} and corrosion rates in mm/year is shown in section 2.3.2.2.

$$R_p = \frac{\Delta E}{\Delta I} \quad \textbf{(2-25)}$$

Even though PDP using Tafel extrapolation and LPR are most popular methods to quantify the corrosion rate for Mg, there are several limitations. Accurate analysis by these methods requires both half-reactions be controlled by activation polarization [Esmaily, 2017]. A large amount of hydrogen bubbles during polarisation increase the resistance for the current flow resulting in progressively larger ohmic potential drops that are difficult to assess accurately [Fajardo, 2015]. The distortions in the shape of the polarization curve make accurate determination of the Tafel slope difficult [Fajardo, 2015]. The Tafel extrapolation on Mg is usually a destructive one-off test. The potentials are significantly shifted (e.g. η=±500mV). Anodic polarisation increases the anodic reaction and leads to physical changes and even damage to the sample. It includes forming a corrosion product layer that affects the exposed area and the reaction rate is coverage dependant [Winzer, 2005]. The accuracy of using Tafel is in question. Shi et al found the relative deviation in the evaluation of the corrosion rate from Tafel extrapolation ranged from 48% to 96% [Shi, 2010].

The i_{corr} values inferred from potentiodynamic polarization curves for pure Mg/Mg alloys may not reflect the actual rate of corrosion of the metal, since other parasitic chemical/electrochemical reactions may simultaneously occur at the Mg surface [Esmaily, 2017]. Nevertheless, the polarization curves are useful for

assessing approximate corrosion rates and the influence of various parameters such as alloying content. [Esmaily, 2017].

Other methods and techniques such as EIS (electrochemical, are suggested to complement the research that uses PDP methods [Shi, 2010; Esmaily, 2017].

2.3.2.2 Electrochemical Impedance Spectroscopy (EIS)

With EIS tests, more influence of components such as the bulk solution, pre-existed coating and diffusion process can be separately identified in this technique.

The EIS test involves applying a time-varying voltage and measurement of the current response, and the voltage-current ratio gives the frequency-dependant impedance $Z_{(\omega)}$ [Frankel, 2014].

Impedance is a measure of the ability of a circuit to resist the flow of electrical current. It is similar to the resistance at DC Voltage/Current but more complex when there is an AC voltage/current with a frequency.

During an EIS test, a spectrum of voltage sweeps is made to the system [Pidcock 2014]. The frequency is usually between 10^6 and 10^{-4} Hz [Bard, 2001].

When a metal is immersed in the electrolyte, an electric double layer is at the metal/electrolyte interface consisting of a fixed inner layer and a movable diffuse layer. An example is shown in Figure 2.3.6a. Due to the excessive electrons produced by the metal dissolution reaction, the metal surface is negatively charged. The negatively charged sample surface attracts positive ions to form the fixed inner layer. The mobile diffuse layer formed from the attraction of the inner layer but keeps a distance because of the repulsion of the charged sample surface [Pidcock 2014]. With an AC voltage, the double layer behaves more like a capacitor C_{dl}. With a DC voltage, the double layer is likely to behave as a resistor R_{ct}.

This system can be approximately described by combining capacitors and resistors called the Randles circuit, shown in Figure 2.3.6b. R_0 is the resistance of the bulk solution.

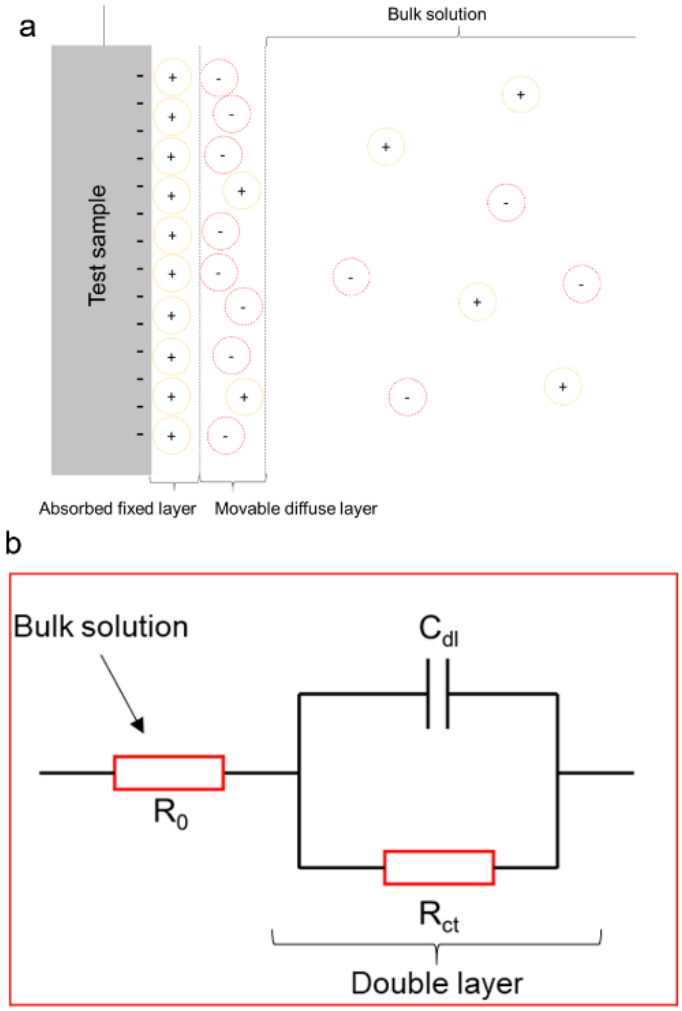

Figure 2.3.6. Schematic illustration of a) electric double layer and b) the equivalent circuit of an electric system in the EIS test.

Due to the different responses of the resistor and capacitor to the frequency of the applied voltage. The frequency dependant impedance Z(ω) for the system composed of both resistor and capacitor can be mathematically expressed as the following equation in terms of magnitude, |Z| (Ω), and a phase shift, Φ.

$$Z(\omega) = \frac{E_t}{I_t} = \frac{|E| \sin(\omega t)}{|I| \sin(\omega t + \emptyset)} = |Z| \frac{\sin(\omega t)}{\sin(\omega t + \emptyset)} \quad \textbf{(2-26)}$$

ω is the frequency (Hz), and |E| and |I| are the magnitude or modulus of the applied Potential and response current.

$Z_{(\omega)}$ can also be expressed as a complex number as shown in Equation 2-27

$$Z(\omega) = \frac{E}{I} = |Z| \exp(j\emptyset) = |Z|(\cos\emptyset + jsin\ \emptyset) \quad \textbf{(2-27)}$$

$|Z|$ is the magnitude or modulus of the impedance, j is the imaginary number and.

As a complex number, the measured impedance $Z_{(\omega)}$ in the EIS test is plotted in a Nyquist plot. In the plot, the x-axis represents the real part of impedance, Z'; the y-axis represents the imaginary part of impedance, Z''. An example of a Nyquist plot with a Randle circuit is shown in Figure 2.3.7. It has the equivalent circuit of Figure 2.3.6b. The EIS measurements start from high frequency to low frequency and produced data points from left to right in the plot. The distribution of the data points has a semicirclular shape.

When the frequency is very high, the current only passes through C_{dl} and bypasses R_{ct}. At this point (the left corner of the semicircle), the total impedance of the system is equal to the resistance of the bulk solution R_0. When the frequency is very low, the impedance of C_{dl} is too high that the current bypass C_{dl} and only passes through R_{ct}. At this point (right corner of the semicircle), the total impedance of the system is equal to R_0+ R_{ct}. the charge transfer resistance R_{ct} can be obtained in the Nyquist plot by deducting the low-frequency point by the high-frequency point.

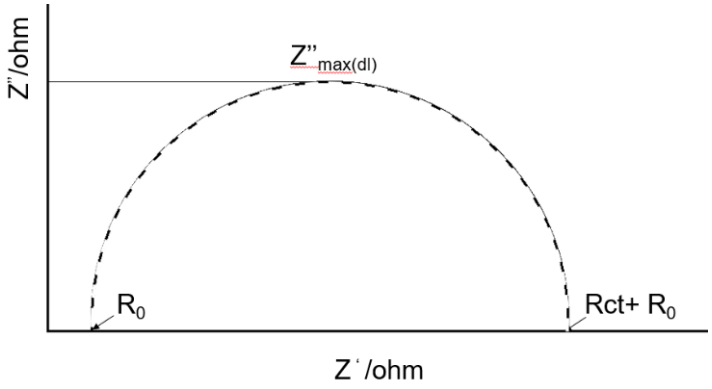

Figure 2.3.7. Example of the Nyquist plot for the EIS test on metal in the electrolyte, corresponding to the Randle circuit.

For a sample with a permeable coating, the electrolyte penetrates the film via pores and defects and contacts the metallic substrate. Both film-electrolyte interphase and substrate-electrolyte interface exist in the system, the equivalent

circuit of the system in this situation/model is shown in Figure 2.3.8. It introduces additional impedance elements C_{pf} and R_{pf} to simulate the capacitor and resistor behaviours of the film. The corresponding example of a Nyquist plot is shown in Figure 2.3.9. It is usually composed of two semicircles, the left one represents the data from the film, and the right one represents the metallic substrate. The size of semicircles can be either larger or smaller than the others, which depends on the coating and substrate itself.

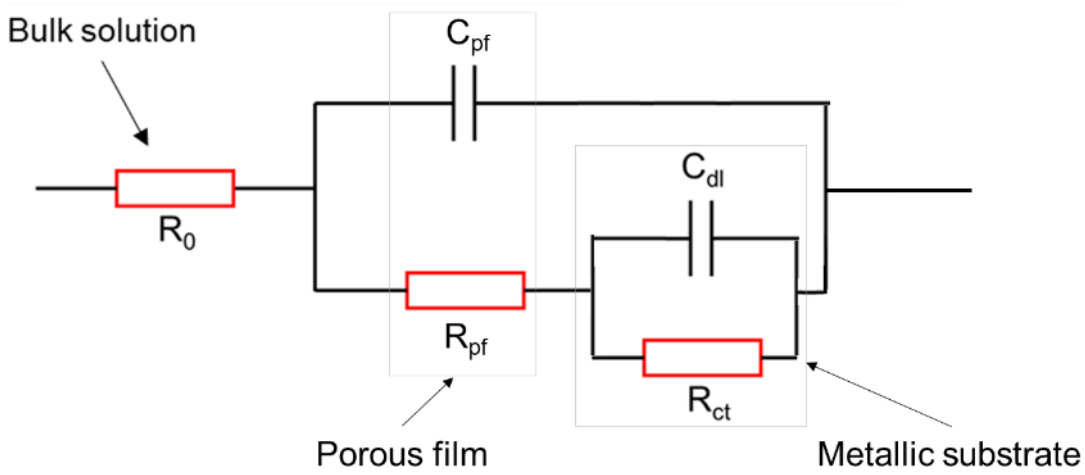

Figure 2.3.8. Equivalent circuit model of the EIS test for a sample with a permeable coating

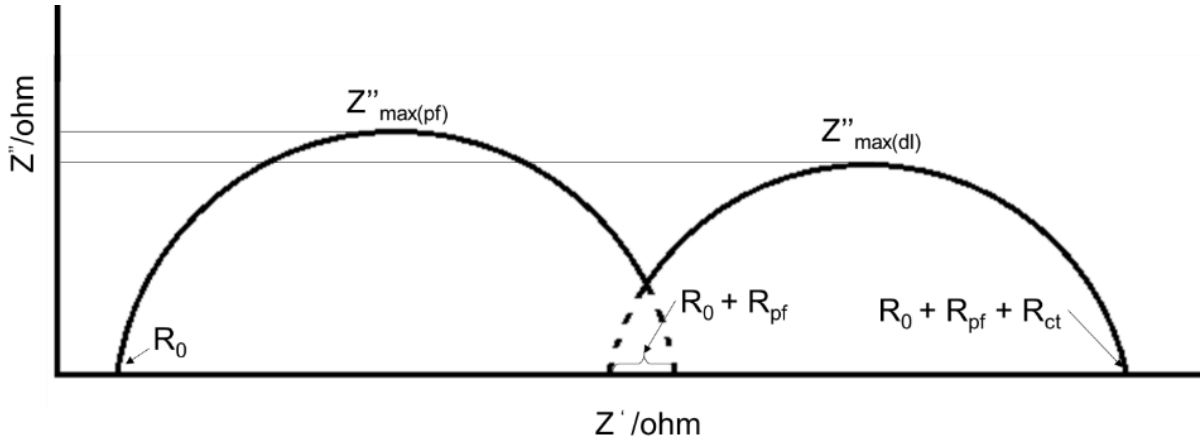

Figure 2.3.9. Example of the Nyquist plot of the EIS test for a sample with permeable coating.

Both charge transfer resistance R_{ct} in EIS and polarised resistance R_p in LPR give the resistance to the corrosion reaction. R_p and R_{ct} also imply the current flow,

hence the presence of an electron transfer reaction [Fernandez, 2016]. With the Stern-Geary equation R_{ct} and R_p can be converted directly to current density:

$$i_{corr} = \frac{B}{R_{ct} \text{ or } R_p} \quad \textbf{(2-28)}$$

'B' is Stern-Geary constant (mV) and:

$$B = \frac{b_A b_C}{2.3(b_A + b_C)} \quad \textbf{(2-29)}$$

b_A *and* b_C can be approximated by fitting the Tafel region of the polarisation plots in the potential-dynamic polarisation tests (Equations 2.20 and 2.21).

Corrosion current, $I_{corr,}$ is related to metal loss hence the corrosion rate. For Mg, the relationship between corrosion rate and corrosion current can be determined by Faraday's Law.

$$m = \frac{I_{corr}}{F}\frac{M}{z} \quad \textbf{(2-30)}$$

m is the mass loss of the metal (g), F is Faraday's constant, which equals 96485C/mole. n is the valence number for the metal, which is 2 for Mg. M is the atomic weight of the sample (g/mole).

Once the mass loss of the metal is obtained, the corrosion penetration rate can be then calculated using the following expression:

$$\textit{Corrosion rate (mm/y)} = 3.1536\, x\, 10^8\ \frac{m}{\rho\, At} = 3.1536\, x\, 10^8\ \frac{I_{corr}\, M}{F\, z\, \rho\, At} \quad \textbf{(2-31)}$$

ρ is the density (g/cm^3), A is the surface area (cm^2), and t is the time of exposure.

For magnesium the corrosion rate to corrosion current density at 1x10^{-6}A/cm^2 ≡ 0.023 mm/y [Pidcock, 2014].

The electrochemical corrosion measurement in this work focuses on EIS measurements as it is non-destructive and suitable for testing one sample repeatedly to record the corrosion behaviour of the sample during immersion in the solution. The $Mg(OH)_2$ film contains cracks and pores, suitable for the EIS with a permeable coating model. Polarisation with the Tafel extrapolation is also

carried out in some samples. It can help to estimate the corrosion current density from the charge transfer resistance.

King, 2014 et al. have indicated that such corrosion rate evaluations for Mg using the polarization resistance from EIS data having an inductive loop, should evaluate the polarization resistance as the frequency (f) approaches zero with an extrapolation of the EIS data, designated herein as R_p [King, 2014 quoted by Atrens, 2015]

2.3.2.3 Non-electrochemical techniques

A. mass loss

Mass Loss measurement is the most common method for the study of metal corrosion, and is the benchmark standard [Esmaily, 2017]. In weight loss testing, the specimen mass and specimen geometry are measured before and after exposure to a corrosive environment for a period.

The corrosion rate from weight loss, corrosion rate $P_{mass\ loss}$ in mm per year is determined from Equation 2-32[Atrens 2015]:

$$P_{mass\ loss} = 2.1\frac{\Delta m_{loss}}{At} \quad \textbf{(2-32)}$$

where m is the specimen metallic weight loss in mg, A is the exposed surface area of the specimen in cm^2, and t is the immersion duration per day.

A cleaning process is considered critical as insufficient or excessive cleaning after immersion can lead to inaccuracies [Esmaily 2017]. This includes overestimation or underestimation of the corrosion rate. It is recommended to use a dilute chromic acid solution that may contain silver and barium nitrate [ASTM G1-03,2011; Prasad, 2012; Shi, 2011]. Some research [Shi, 2011] measured the weight associated with the corrosion products, m_{cp} in mg/cm^2, corrosion products were left on the sample and its weight measured after drying and the weight before immersion test deducted as shown in Equation 2-33.

$$m_{cp} = m_{acp} - m_b \quad \textbf{(2-33)}$$

Where m_{acp} is the weight of the specimen per unit area after immersion test and containing corrosion products, m_b is the weight before immersion,

Even though weight loss measurements are simple and well established, they only provide an average corrosion rate over the exposure period and this rate will often change with time [Esmaily, 2017]. A combination with other methods is suggested.

B. H2 collection

The primary cathodic reaction accompanying the dissolution of Mg and its alloys in aqueous electrolytes is water reduction which results in the evolution of hydrogen gas.

In the absence of an external perturbation, charge neutrality requires that the rate of the anodic reaction equals the rate of the cathodic reaction ($i_a = |i_c|$) [Esmaily, 2017]. Consequently, under open-circuit conditions, it is possible to determine the instantaneous corrosion rate from the rate at which HE occurs on the electrode surface [Fajardo, 2015].

The volumetric method of H_2 collection is the most widely used. The corroding sample is covered with a funnel inserted into an inverted burette [Song, 2011].

Hydrogen gas produced as the result of the corrosion reaction accumulates as bubbles that eventually detach from the surface and are collected at the top of the burette by displacing the solution contained within [Esmaily, 2017]. The HE rate V_H in ml/cm^2/day can be obtained and it can be interpreted as the metallic weight loss Δm_{loss} in mg/cm^2/day and corrosion penetration rate, P, in mm/year as shown in Equations 2-34 and 2-35 respectively [Shi, 2011] :

$$\Delta m_{loss} = 1.085 V_H \quad \textbf{(2-34)}$$

$$P = 2.279 V_H \quad \textbf{(2-35)}$$

Because sufficient H_2 is needed to determine the corrosion rate, the volumetric method is not suitable for short term tests [Esmaily, 2017]. A gravimetric method

for real-time HE collection is based on the measurement of the buoyancy force resulting from the accumulation of hydrogen in a submerged container [Curioni, 2014; Fajardo, 2015]. Schematic illustrations of the volumetric and gravimetric H_2 collection experiment setups are shown in Figure 2.3.10 [Esmaily, 2017]

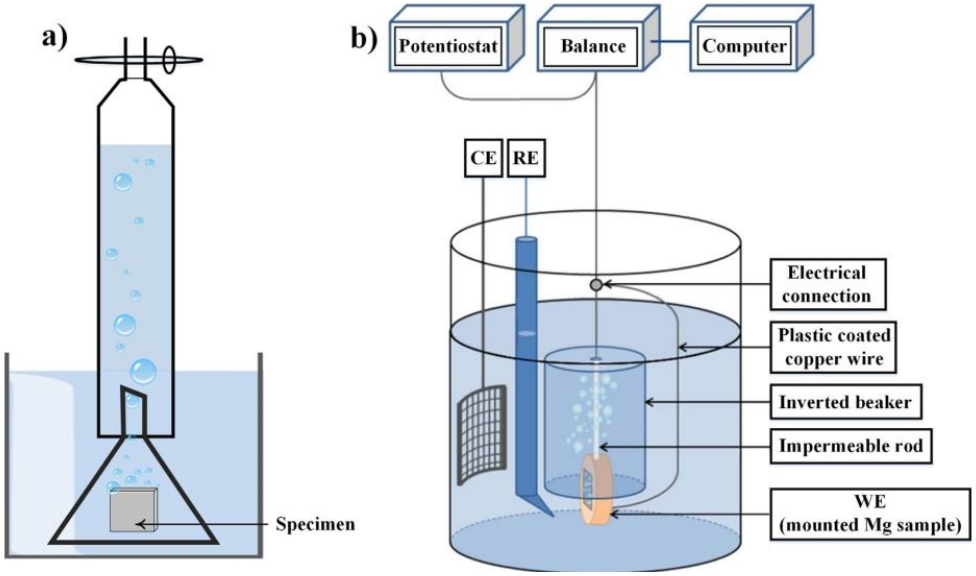

Figure 2.3.10. Schematic illustration of the volumetric and gravimetric hydrogen gas collection experiment setup [Esmaily, 2017].

Apart from immersion tests for corrosion rates, characterisation and analytical techniques such as Scanning/Transmission Electron Microscopy (SEM/TEM), Energy Dispersive X-ray (EDX), X-ray Diffraction (XRD), Focused Ion Beam (FIB), are used to study the corrosion features, the interface of corrosion product layer or protective coating and the compositions of Mg and its alloys. Esmaily et al. reviewed and compared these methods by their application, detection limit/resolution (Figure 2.3.11b) and suitability for qualitative or quantitative assessment as in Figure 2.3.11c [Esmaily, 2017]. An overview of applications (structure/chemistry) and capabilities depth/position) of analytical techniques that can be applied to Mg corrosion research is given in Figure 2.3.11a.

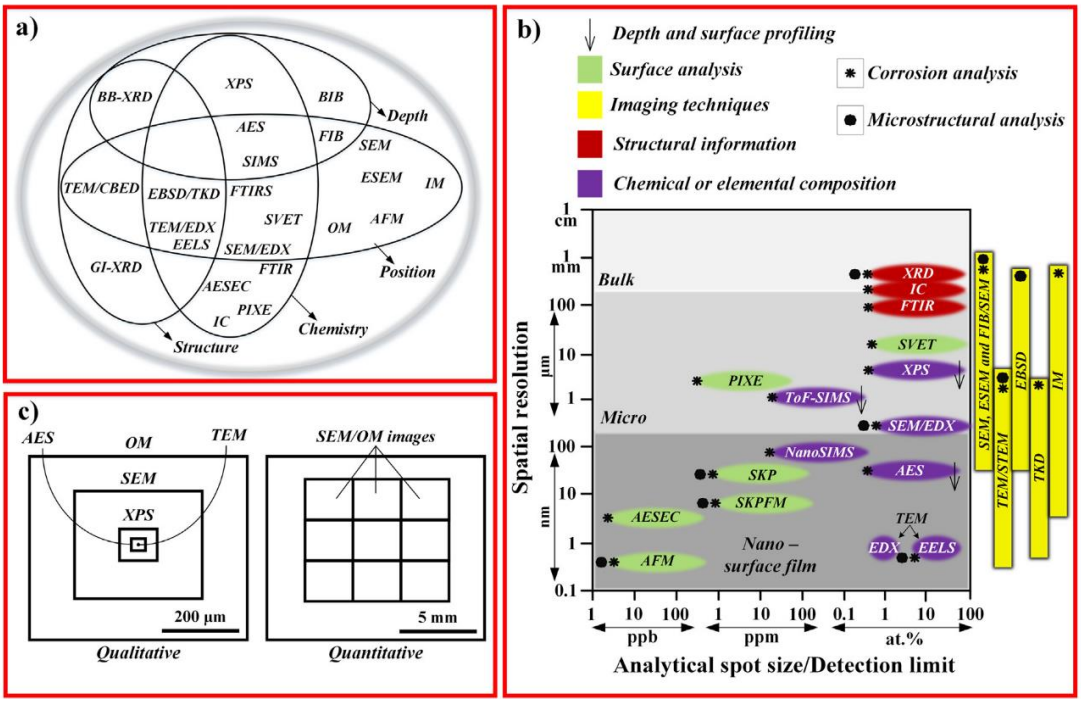

Figure 2.3.11. A comparison of analytical tools in Mg corrosion. a) An overview of applications (structure/chemistry) and capabilities depth/position) b) detection limit versus spatial (lateral) resolution of the described methods, and c) qualitative versus quantitative assessments of microstructure-corrosion relationships in Mg alloys [Esmaily, 2017].

2.3.3 Influence of alloying elements and impurities

The alloying elements and/or impurities have a profound influence on the corrosion behaviour of Mg and its alloy. Study of impurity affecting Mg alloy corrosion was firstly conducted by Boyer [Boyer, 1927] and extended in the 1940s by Hanawalt and Mcnulty [Hanawalt, 1942]. Three critical impurity elements, Fe, Ni and Cu, were identified which significantly increase the corrosion rate of Mg if they exceed a particular tolerance limit (0.0017^{wt}% for Fe, 0.0005 ^{wt}% for Ni and 0.1^{wt}% for Cu [Hanawalt, 1942]. Zn and Mn were found to increase the tolerance limit for Ni [Hanawalt, 1942]. Reichek et al. found interactions occur between alloy elements in Mg and stated the tolerance limit for Fe could be defined as 0.032 ratio with Mn [Reichek, 1985]. It also found the presence of Mg leads to preferential formation of Fe-Al-Mn precipitates to Fe-Al, and mitigates the influence on the bulk alloy for local galvanic corrosion [Lunder, 1987].

The effect of Al on Mg corrosion is complicated. Al and its intermetallic precipitates exhibit more noble potential negativity that leads to local galvanic

corrosion for the bulk alloy. However, previous research by Pardo et al. has found Mg alloys with higher Al content (AZ91D and AM80) than AZ31 with lower Al. A higher Al content can lead to networks of fine dispersed β phase Mg-Al intermetallic that prevent further corrosion of the bulk alloy in 3.5^{wt}% NaCl solution [Pardo, 2008]. Li, Zr and rare earth elements are considered to have positive effects in reducing the corrosion rate of Mg.

Due to the limitations of toxicity and biocompatibility of alloying elements, not all Mg alloys are suitable for biodegradable medical applications [Atrens 2015]. Song proposed that Zn and Mn were two of the most appropriate alloying elements, and through Zn and Mn alloying, purification and anodization, chemically active Mg could be developed into a biodegradable biocompatible implant material with acceptable biodegradation, and a tolerable hydrogen evolution rate. [Song, 2007].

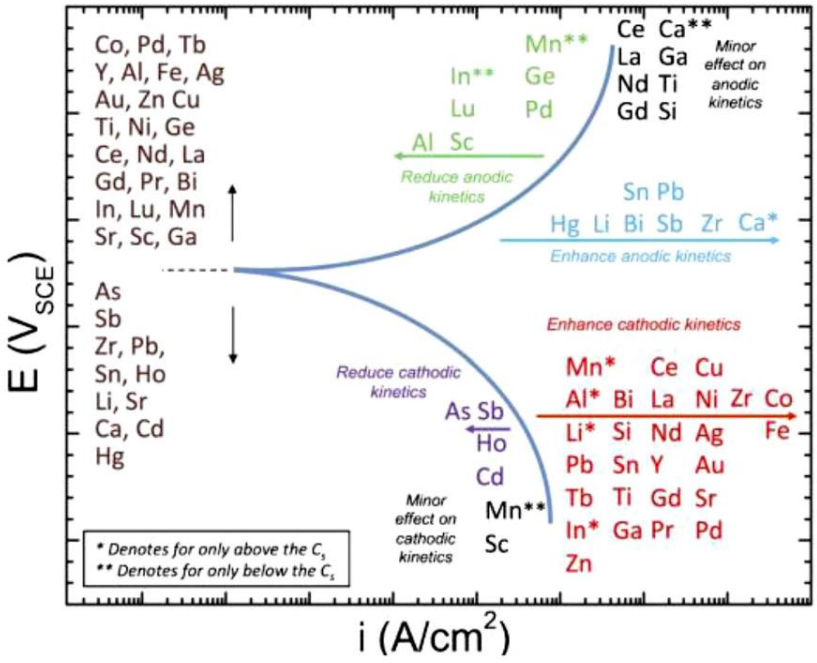

Figure 2.3.12. Schematic representation of the electrochemical impact of alloying elements studied [Gusieva, 2015; reproduced by Li, 2016].

The effect of alloying elements and purities on Mg corrosion were comprehensively studied and reviewed [Atrens, 2015; Li, 2016; Esmaily 2017].

An overview of the electrochemical impact of alloying elements on Mg is shown in Figure 2.3.12.

A review by Cao et al. consider the possibility of passivation of Mg alloys by increasing the purity of Mg and adding alloying with noble elements. They suggested a benchmark corrosion rate of 0.25mm/y in 3.5%NaCl where a passivated Mg alloy results in a corrosion rate about 10 times lower than the benchmark [Cao, 2016].

2.3.4 Processing and grain size effect

Grain refinement may either improve or reduce the corrosion resistance of Mg alloys [Liao, 2012]. Research suggests grain boundaries can act as corrosion barriers. Therefore, grain refinement increases the number of grain boundaries hence decreasing the corrosion of Mg alloy. Aung et al found corrosion resistance of an untwinned microstructure can be reduced by increasing the grain size. The corresponding corrosion rate was found to be increased by 30% with an increase in the average grain size from 65 to 250 lm [Ambat 2000; Aung, 2012]. T. Zhang et al. found the corrosion rate reduced by 30% after grain refinement by decreasing the solid-state extrusion ratio from 44.4 to 11 [Zhang, 2011]. Kim et al. found that grain refinement by high-ratio differential speed rolling improves the corrosion resistance of AZ31 in phosphate-buffered saline solution.

Fine-grain size contributes to the stabilisation of the corrosion product $Mg(OH)_2$ layer deposited on top of the MgO layer. Research by Liao et al. found fine-grained AZ31B alloys have a higher corrosion resistance than the commonly hot-extruded AZ31B alloy with coarser grains in both immersion and cyclic neutral-salt spray tests and passivation to some extent was observed in 0.1 M NaCl solution for fine-grain alloys [Liao, 2012]. However, research also revealed that the grain boundaries do not always hamper corrosion propagation [Song, 2012].

2.3.5 Mg alloy and its corrosion in biomedical application

Mg is naturally available as a trace element in the body and is non-toxic and biocompatible [Gawlik, 2018]. The use of oral magnesium supplements is

generally safe, and the no-observed-adverse-effect level considered to be 250 mg for supplementary magnesium [Vormann, 2003]. Mg ions positively affect various cells and their functions [Park, 2018].

Mg alloys have similar elastic modulus, compressive yield strength and fracture toughness to human skeletons, favourable for orthopaedic operation [Wang, 2012]. A comparison of physical and mechanical properties between Mg and human bone is shown in Table 2.1.1 [Wang 2012]. Mg alloy can reduce the negative effect of stress shielding and improve osseointegration and bond-implant interface strength [Denkena 2007; Gawlik, 2018].

Table 2.3.1. Comparison of both physical and mechanical properties between magnesium and natural bone; adapted by [Wang, 2012].

Properties	Human Cortical Bone	Magnesium
Density (g/cm^3)	1.8-2.1	1.74-1.84
Elastic modulus (GPa)	3-20	41-45
Compressive yield strength (MPa)	120-180	65-345
Fracture toughness (MPa m1/2)	3–6	15-40

Such applications of Mg alloys may be limited due to their fast degradation in the human environment [Wang, 2012]. Studies found that most Mg implants suffer severe degradation prior to recovering the injured tissues [Song, 2017]. Additionally, degradation of Mg in the body evolves hydrogen gas. although relatively strong hydrogen evolution is crucial for cell adherence and implant-bone integration [Gawlik, 2018], excessive gas evolution can also modify the bone remodelling process and impair the consolidation of bones [Iglesias, 2015]. Gas pockets build up around implants, lowering tissue recovery or even blocking the blood system if implants are within the blood veins [Song, 2007].

According to Ghali et al. [E, Ghali 2004], two different corrosion modes are possible, uniform, and localized. Mg alloys with a slow and constant degradation rate (lower than 0.5mm/year [Chen, 2015] are required to provide sufficient time

for bone healing. Song proposed a maximum amount of hydrogen evolving of 0.01 ml/cm^2/day [Song, 2007]. For orthopaedic applications, bone healing support for 6 to 12 months are required and vascular applications require a 3-to-6-month life span [Yang, 2020].

The review by Gawlik et al. suggests the roughness of the implants is important to achieve usable degradation behaviour for Mg implants: implant surfaces with roughness values above S_a or R_a = 0.2 µm are unsuitable for initial cell adherence and cell viability [Gawlik, 2018].

2.3.6 Summary of corrosion rates in literature

Studies regarding the corrosion rates of Mg alloy are reported. Table 2.3.1 lists the corrosion results reported in literature considering alloys AZ31 and ZM21 (which are relevant substrates used in this research). Results from tests by various techniques with a range of solutions and temperatures are listed.

2.4 Corrosion protection of Mg and its alloys

The corrosion of Mg alloys can be controlled by reducing impurity elements, and optimising microstructure to achieve passivation. Nevertheless, surface modification and coating application is considered most effective and flexible.

Gray and Luan 2002 reviewed conventional surface treatments used for the corrosion protection of Mg and its alloys and divided the surface treatment into six categories: electro/electrochemical deposition, conversion coatings, anodising, gas-phase deposition processes, laser surface alloying and cladding, and organic/polymer coatings [Gray, 2002].

Wang et al. reviewed surface modification techniques for Mg alloys in biomedical implantation applications [Wang, 2012]. These techniques are categorised into two: chemical and physical methods as shown in Figure 2.4.1.

Table 2.4.1 Summary of corrosion measurements on Mg alloy AZ31 and ZM21 reported in literature.

Substrate	solution	T (°C)	I_{coor} A/cm^2	Weight loss (mg/cm2/day)	Weight loss (μg/mm^2)	R_p R_{ct} (Ω/cm^2)	Literature
AZ31	3.5% NaCl	RT				100-160 <4 weeks)	A. Pardo, 2008,A
AZ31	3.5% NaCl	RT				200-400 (<7days)	A. Pardo, 2008, B
ZM21 (Ca & CE)	Hanks	37	1.6-2.7×10^{-5}			1000-2000(72h)	D.Song, 2017
AZ31B	3.5% NaCl	RT	1.6×10^{-5}(24h)				Q.Jin 2019
ZM21	Earles solution	37			75		W. Agnieszka 2016 A
	Hanks				20		
	Earles solution +10% FBS				15		
ZM21	Cell culture medium+ 10%FBS	37			53 (4 weeks)	6000 (< 2days)	W. Agnieszka 2016 B
AZ31	Hanks	37		~0.21			Q. Zhao, 2016
AZ31	5% NaCl	RT					T. Ishizaki 2013
AZ31	3.5% NaCl	RT		0.35-0.13 (1 - 30days)			Y.Y. Zhu 2011
AZ31	3.5% NaCl	RT	6.7x10^{-4}				Y.Y. Zhu 2012
AZ31	0.5%	RT	6.6x10^{-6}				H. Jeong
ZM21 (as received, T4 and T5)	Ringer's solution	37	7.25, 0.81 and 7.53 (in μA)			~1600, 3700 & 1100	D.Y. Jiang 2017
Mg as fabricated	DI-water	37		0.14 (<50days)			Liu, 2011
Mg after 24h cell culture	DI-water	37		0.28 (<50days)			Liu, 2011
Mg	RT	37					Zhao, 2014
AZ31	0.9 wt.% NaCl	RT	3.64x10^{-6}			934	Mhaede, 2014
AZ31	5 wt.% NaCl	RT		1.11(24h) 54.23 (1.5h)	1.11 mg/dcm2		Song, 2010
AZ31	PBS (phosphate buffered saline)	37	3.66 ± 3.2x10^{-5}				Pompa, 2015
AZ31	Hanks solution	RT		13-35 (<31days)			Liao, 2012

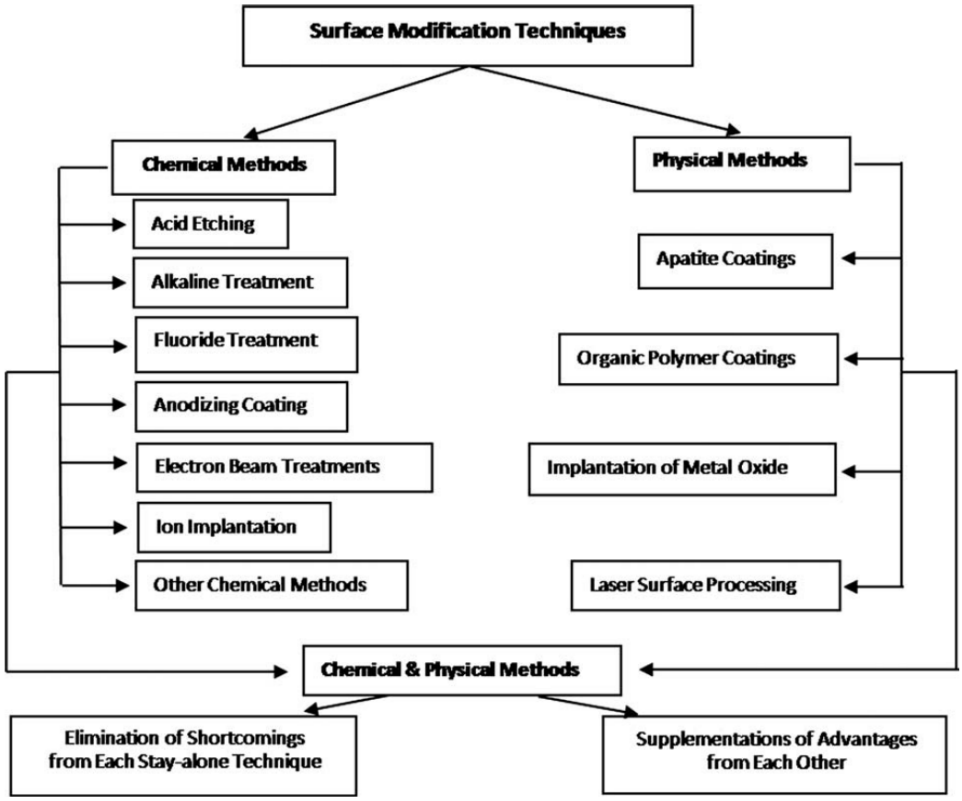

Figure 2.4.1 Main strategies of surface modification techniques for magnesium and its alloys as orthopaedic implants [Wang, 2012]

Many of these techniques produce a surface layer based on the composition of the oxides, hydroxides, phosphates, carbonates, hydro-carbonates and fluorides of Mg and its alloying elements such as Al, Zn and Ca [Wang, 2012, Gawlik, 2018; Song, 2019; Chen, 2011&2014].

2.4.1 $Mg(OH)_2$ surface layer.

Research on $Mg(OH)_2$ based coatings for corrosion protection has increased over the last decade.

$Mg(OH)_2$ can naturally form as a corrosion product but also can be formed artificially. $Mg(OH)_2$ exhibits a higher specific volume and can provide greater coverage to the alloy than MgO with a low Pilling-Bedworth ratio (0.81). It also shows greater bio-compatibility and is more environmentally friendly than many elements. Pilarska et al. reviewed the range of conventional methods for fabricating $Mg(OH)_2$ and applications for $Mg(OH)_2$ are summarised below [Pilarska, 2017]:

Table 2.4.2 Conventional processing methods and applications for $Mg(OH)_2$ [Pilarska, 2017]:

Processing method	Applications
Sol-gel	Sensors
Microwaves	Flame retardants
Gas phase synthesis	Antibacterial agents
Electrochemical method	Membrane Components
Microemulsions	Pollutant neutralisers

The effect of $Mg(OH)_2$ on the corrosion of Mg has been studied and reviewed by several researchers [Feliu, 2013 & 2015; Song, 2003, Zhu 2011 & 2012; Ishizaki, 2013 & 2015; Wang, 2010; Jeong, 2015; Song, 2017].

$Mg(OH)_2$ is reported with various morphologies including flowers, platelet, rods, flakes and tubes depending on the processing methods and processing parameters [Das, 2013; Li, 2000; Henrist, 2003; Yu, 2004].

Taheri investigated the morphology of natural corrosion products of Mg by ageing pure Mg in pure water. An example is shown in Figure 2.4.2a of a bi-layer structure with a porous thin inner MgO (50-90nm) and a less-porous outer $Mg(OH)_2$ layer with interlocked crystal platelets [Taheri, 2012]. He also investigates the corrosion product form in a low NaCl solution (0.01M) and observed a more porous outer layer due to the presence of Cl^-, as Figure 2.4.2b.

In the presence of NaCl, Mg alloys can form local corrosion products with different features from second phase particles. Disciform and filiform (black filaments) corrosion products are typical features formed on AZ31. Investigations by Williams observed that at a fixed Fe concentration, radial disc-like propagation is exhibited in highly concentrated NaCl solutions whereas lower concentrated NaCl environments lead to a filiform-like attack [Wiiliams, 2015]. HE is also at or near the filiform corrosion products [William, 2008]. Cano et al. investigated the corrosion product found when Al-Mn particles act as the cathodic sites to form filiform corrosion products and proposed that Zn-enriched Mg solid solution layers

also act as alternative cathodic sites causing cathodic activation of the corrosion filaments [Cano, 2015].

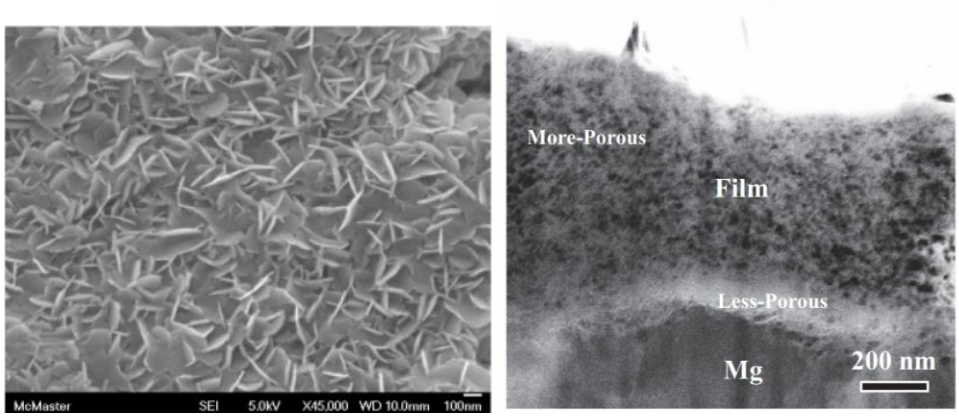

Figure 2.4.2 a), SEM image showing the plate-like morphology of the film on Mg sample after ageing in pure H_2O at RT for 48h [Taheri, 2012]; b) STEM dark-field (DF) image of Mg/film interface formed on Mg in 0.01 M NaCl after conditioning at Ecorr for 24 h showing a more porous region residing on top of a less-porous region [Taheri, 2014].

Feliu et al. and Wang et al. studied the $Mg(OH)_2$ layer formed from the self-corrosion of Mg alloys reporting a protective effect on magnesium. They noted the presence of a carbonate group (CO_3^{2-}) and or a hydro-carbonate group (HCO_3^-) on the $Mg(OH)_2$ film can further enhance its protectiveness [Feliu, 2013 & 2015; Wang 2010].

Ishizaki explored corrosion protection forming $Mg(OH)_2$ films with hydrothermal methods [Ishizaki, 2013 & 2015]. Magnesium alloys were heat-treated with steam from de-ionised water in an autoclave at various temperatures and times. Thick $Mg(OH)_2$ films are produced but with lateral cracks, as seen in Figure 2.4.3. Platelet-like features are observed when the sample underwent corrosion tests in 5% NaCl solution as shown in Figure 2.4.4. In the research by Jeong, Mg alloy samples were immersed in solution followed by heat treatment [Jeong, 2015]. Zhu studied $Mg(OH)_2$ film formation by both de-ionised water and NaOH solution [Zhu 2011&2012]. It is not clear whether samples were immersed in the water/solution by boiling or placed above the water level by steaming.

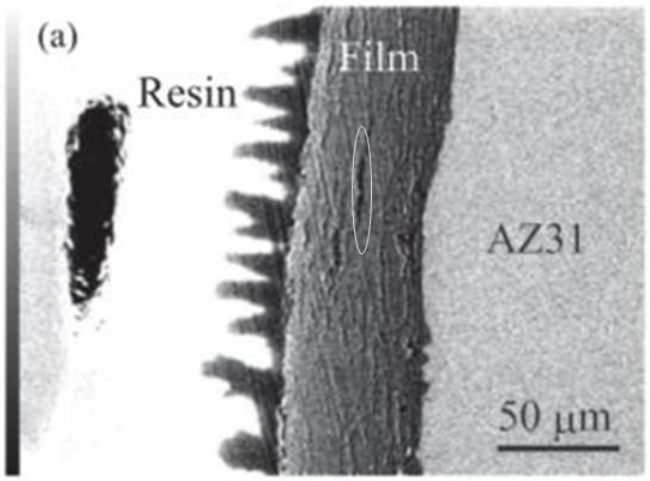

Figure 2.4.3. SEM image of the cross-section of a $Mg(OH)_2$ coated AZ31 alloy formed in steam, cracks are seen in the film parallel to the interface [Ishizaki, 2013 & 2015].

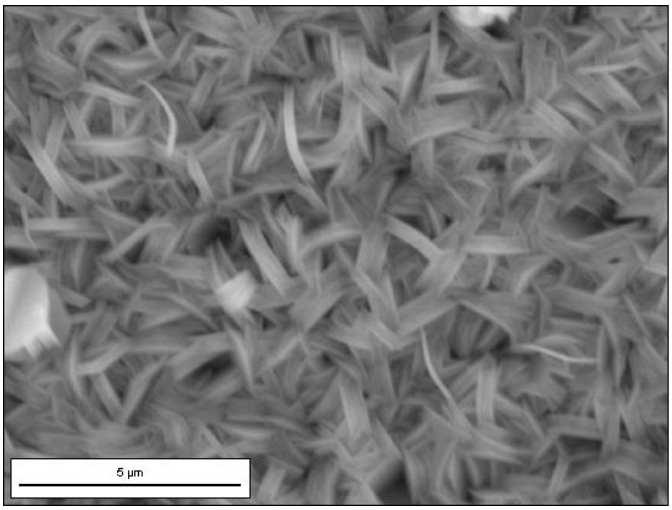

Figure 2.4.4, SEM image of $Mg(OH)_2$ film formed on Mg alloy AZ91D with electrochemical method [Pidcock, 2016].

Song manufactured hydrothermal $Mg(OH)_2$ films on ZM21 (Mg–2Zn–Mn–Ca–Ce) alloy substrate alloy subsequently testing corrosion in Hanks solution at body temperature. They reported that coated sample exhibits higher resistance, $R_{p,}$ than uncoated substrates. The R_p decrease with immersion time, and micro-galvanic corrosion is reduced when the substrate contains fewer second phase particles [Song, 2017].

$Mg(OH)_2$ based composite layers were also studied for biomedical application of Mg alloy. Zhao synthesised dittmarite/$Mg(OH)_2$ composite, where dittmarite is magnesium ammonium phosphate monohydrate, using the hydrothermal method

in a mixed solution of phosphoric acid and diammonium hydrogen phosphate. A dense film with good corrosion resistance is developed which meets cytotoxicity standards of biomaterials [Zhao, 2016].

$Mg(OH)_2$ films on AZ91D alloy were created by Wu using electrochemical deposition in a Mg^{2+} rich solution of $Mg(NO_3)_2$ [Wu, 2015]. Graphene oxide layers were also fabricated to reinforce $Mg(OH)_2$ for improving corrosion resistance and mechanical properties for biomedical applications.

$Mg(OH)_2$ was successfully produced with a range of methods The kinetics of crystalline $Mg(OH)_2$ in saturated solution was studied by Yuan [Yuan, 2014]. Deng synthesised $Mg(OH)_2$ to study the current efficiency of $Mg(OH)_2$ electrode deposition using MgCl solution [Deng, 2015]. Films thickening is observed with increasing time and temperatures of heat treatment. Corrosion rates from Mg alloys with $Mg(OH)_2$ films are given in Table 2.4. This Table also notes the corrosion current densities as reported in the literature.

Table 2.4.3 Corrosion currents of Mg alloy samples with hydrothermally formed $Mg(OH)_2$ taken from literature.

Substrate	Surface treatment	Current density ($\mu A/cm^2$)	Equivalent corrosion rate mm/year	Reference
AZ31B	Steam treatment	$10 \sim 4.8x10^{-5}$	$0.23\sim1.104x10^{-6}$	T. Ishizaki 2013
AMCa602	Steam treatment	1.85×10^{-4}	$4.255x10^{-6}$	T. Ishizaki 2015
AZ31	Hydrothermal treatment	5.4	0.1242	Zhu 2012
AZ31	Hydrothermal Treatment with NaOH solution	$1.5 x10^{-2}$	0.0345	H. Jeong 2015
AZ31	Hydrothermal treatment with fetal bovine serum	563.5 (mg/cm^2 /day)	1183	Song 2010

The research by Ishizaki reports that corrosion current density significantly decreases with hydrothermal coatings compared to uncoated AZ31B substrate The corrosion current density can be as low as $4.8x10^{-11}$ A/cm^2 with coatings steam treated at 160ºC for 4 hours [Ishizaki 2013].

Previous work at Cranfield by the author has investigated $Mg(OH)_2$ [Wang, 2015]. In this work, $Mg(OH)_2$ layers were created on a magnesium alloy AZ61A substrate by coupling Mg alloy with pure Mg or applying an equivalent cathodic current to the substrates shown in Figure 2.4.5 [Wang, 2015].

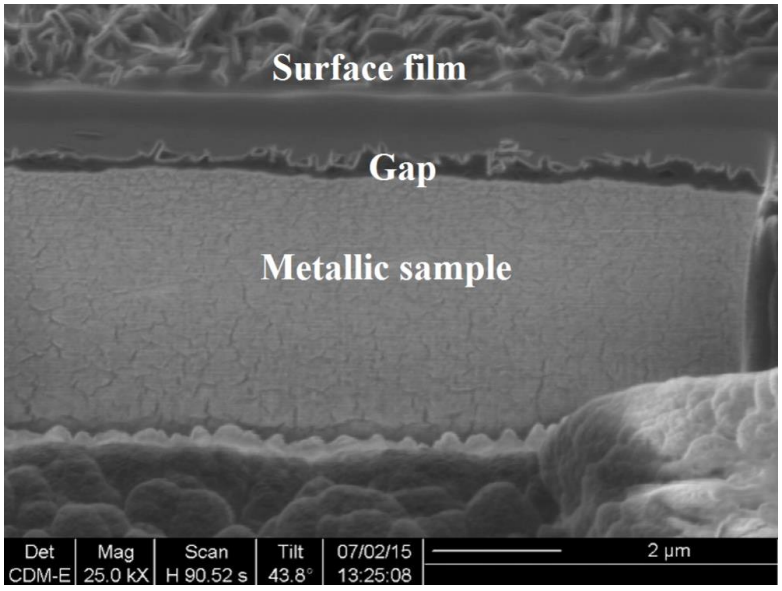

Figure 2.4.5. FIB image of $Mg(OH)_2$ film cross-section formed on Mg alloy AZ61A with electrochemical method [Wang 2015].

The hypothesis for this research to be undertaken is that a magnesium film formed on an Mg alloy surface will enhance the corrosion protection of a Mg alloy. Literature reports that $Mg(OH)_2$ surface films can be produced in several ways, giving a range of morphologies and that some corrosion protection or corrosion resistance has been observed [Ishizaki 2013; Zhu, 2013]. This supports the author's previous findings [Wang 2015]. However correlating performance in a reliable and repeatable way from the manufacturing route, understanding the influence of Mg alloys on the surface film and quantifying the corrosion resistance over time are not readily available. Thus, the research that follows sets out to provide some of this information.

3 Methodology and Experimental procedures

3.1 General methodology

The aim of this research is to demonstrate the corrosion protection of magnesium alloys using magnesium-rich films on Mg alloy surfaces and quantify the corrosion resistance performance.

The approach to this project is shown in a flow chart in Figure 3.1.2. Three stages of work were in the research:

1. $Mg(OH)_2$ Film development,
2. Film Characterisation & analysis and
3. Corrosion assessment and processing optimisation.

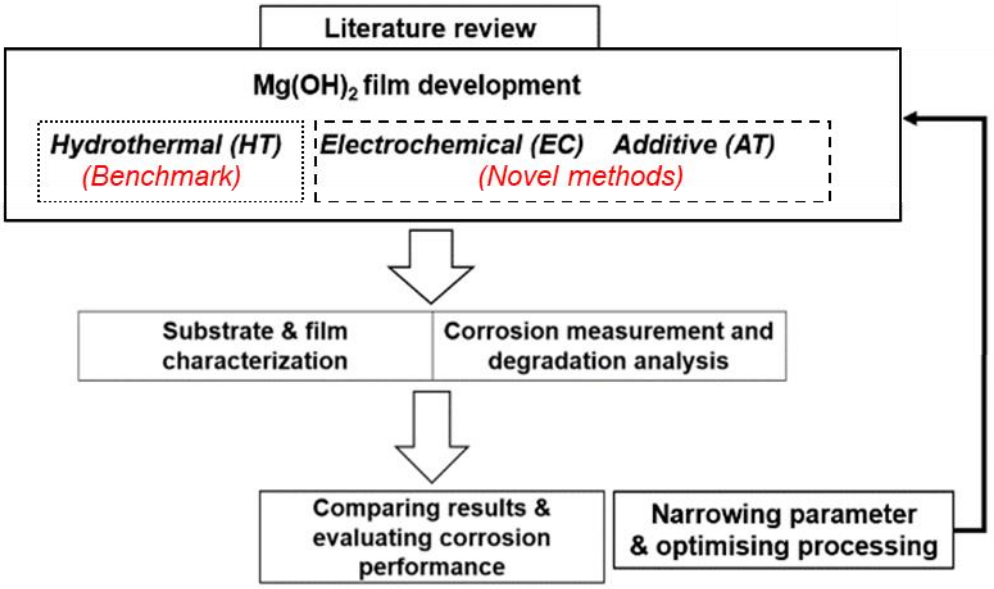

Figure 3-1-1 Flow chart of the methodology.

At the beginning of the research, magnesium-based/ $Mg(OH)_2$ films with different manufacturing approaches are deposited on Mg alloy substrates. These approaches are a) Hydrothermal (HT), b) Electrochemical (EC) and c) Additive applications. The processing parameters adopted initially rely on literature firstly for the HT. The details for the processing approaches are in section 3.3.2.

Once the filmed samples are processed, samples were measured using various corrosion tests and characterised with/without corrosion tests. The details are in

section 3.3.3 and 3.3.4 The results produced in this stage is then compared with each other and the literature.

As the results have been evaluated, there are revisions and feedback to the film developments that lead to the adjusting and optimising of processing procedures and parameters for another round of film development.

3.2 Experimental

3.2.1 Materials and substrate preparation

3.2.1.1 Mg alloy substrate

Samples investigated in this work are from ASTM standard AZ31B alloys with two sources: Goodfellow (AZ31-GF) and Luxfer MEL Technologies (AZ31-ME). In addition ZM21 alloy from Luxfer MEL Technologies (ZM21-ME). The chemical composition of AZ31 and ZM21 are given in table 3.2.1 based on standard [ASTM B951 – 11, 2018].

Table 3.2.1 ASTM standard for Mg alloy chemical composition in wt%

	Al	Si	Ca	Mn	Zn
AZ31	2.5-3.5^{wt}%	0.1	0.04	0.2-1	0.6-1.4
ZM21	-	-	-	>0.5	2

AZ31-GF is a 25mm diameter extruded bar shown in Figure 3.2.2a. Specimens were made by slicing the bar into 2 mm thick round discs with a precision saw

The AZ31-ME and ZM21-ME are discs, 75±1mm in diameter from extruded bar 20±1mm in height. Specimens are taken by slicing the disc vertically into a rectangle plate 2±0.5mm in thick, 20±1mm in width and 25-30mm in length. An example of the specimen is shown in Figure 3.2.1b and 3.2.2c.

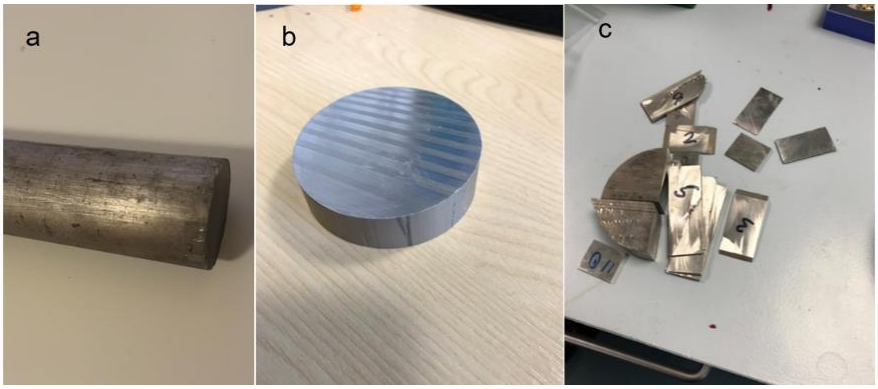

Figure 3.2.1 a) extruded ZM21-GF, b) extruded AZ31 ME disc c) Extruded ZM21-ME disc sliced to samples.

Specimen surfaces were then finished with abrasive silica paper to P4000 using Isopropyl alcohol (IPA) as lubricant. The dimensions of each specimen are measured and recorded with a Vernier Calliper before coating processing or for the tests and characterisations.

3.2.2 $Mg(OH)_2$ film processing

3.2.2.1 Hydrothermal processing

Hydrothermal samples in this work are processed to build for characterisation and corrosion test as a benchmark. Its procedure is based on the previous work by Ishizaki et al. where Mg alloy substrates were steamed in the autoclave above DI water level [Ishizaki, 2013]. AZ31-GF samples were placed into a 45ml PTFE lined autoclave bomb for steam exposure with 10ml de-ionised water. Samples were kept above the water level with a stand made of nickel/chromium wire. A schematic illustration and photo of the experimental set-up are shown in Figure 3.2.2.

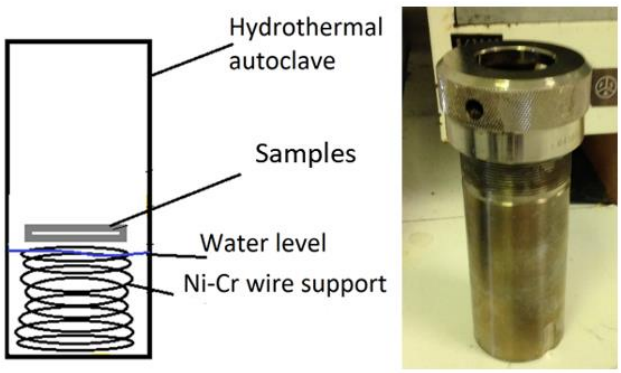

Figure 3.2.2. Experiment set-up for HT processing.

The samples were heated in an oven from RT to 120°C or 160°C. 160°C is the optimal temperature in Ishizaki's work where the sample achieved the lowest current density (tested with the PDP method) [Ishizaki 2013]. Then held from 0.25 to 4 hours. Samples in the autoclave were cooled by air (air-cool) or cooled in the oven after switching the oven off (furnace-cool).

Table 3.2.2 summarises the processing parameters of the hydrothermal samples. It includes processing temperature, heating rates, holding time, cooling methods, and lists analysis methods for this work, applied to the samples.

Table 3.2.2 List of processing parameters for the hydrothermal samples with the following characterisation and analysis referencing Ishizaki [Ishizaki, 2013].

<table>
<tr><th>Substrate</th><th>Processing temperature (C°)</th><th>Time to temperature (min)</th><th>Holding time at temperature (h)</th><th>Cooling method</th><th>Range of characterisation and analysis tools</th></tr>
<tr><td rowspan="9">AZ31-GF</td><td rowspan="2">120</td><td rowspan="2">39</td><td>2</td><td rowspan="2">Air cool</td><td rowspan="2">SEM (cross-sectional)</td></tr>
<tr><td>4</td></tr>
<tr><td rowspan="7">160</td><td rowspan="7">48</td><td>1/6</td><td rowspan="5">Air cool</td><td rowspan="7">SEM (on surface)
SEM (cross-sectional)
EDX (point analysis)
XRD
EIS tests in 3.5wt% NaCl solution
OCP tests in 3.5wt% NaCl solution</td></tr>
<tr><td>1/2</td></tr>
<tr><td>1</td></tr>
<tr><td>2</td></tr>
<tr><td>3</td></tr>
<tr><td>4</td><td>Air cool</td></tr>
<tr><td>6</td><td>Furnace cool</td></tr>
</table>

3.2.2.2 Electrochemical method

The electrochemical (EC) method for depositing $Mg(OH)_2$ coatings were based on the previous work of this author [Wang, 2015] which applied cathodic current to sample in Mg^{2+} rich solution to form $Mg(OH)_2$ surface layer.

EC processing was applied to AZ31-GF and AZ31-ME samples. After samples were prepared, the electrochemical cell was set up for depositing $Mg(OH)_2$ film, as illustrated in Figure 3.2.3. The area-controlled sample, platinum counter electrode and Ag/AgCl/KCl reference electrode were immersed into 900ml Mg^{2+} rich solution in a beaker. The Mg^{2+} rich solution in this work is prepared by the electrolysis of commercial-grade pure magnesium in de-ionised water. 1000 $\mu A/cm^2$ cathodic current is used in the electrolysis for 24h at RT. The solution is saturated in $Mg(OH)_2$ (~0.0064g/L) as it becomes suspension with white $Mg(OH)_2$ particulates. It also has a pH value between 10.5 and 11.5 at RT. This solution contains no Cl^- compared to the solution used in the previous work [Wang, 2012].

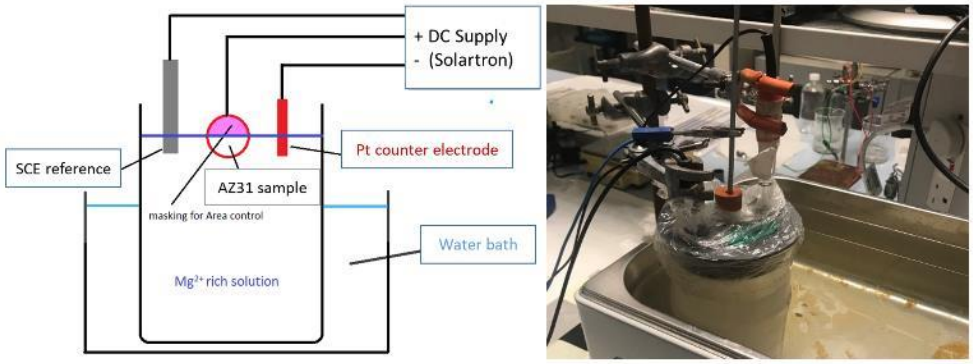

Figure 3.2.3. Experiment set-up for EC processing.

Direct current was applied to the sample with Solartron. The beaker with Mg^{2+} rich solution is placed into a water bath or a hot plate to control the processing temperature. Samples are immersed into the Mg^{2+} solution after the electric supply is switched on, once the solution has reached the targeted temperature. Lid and cling-film cover and refilling system were also employed to mitigate solution level changes due to evaporation. The samples post-EC treatment were clean by IPA and then stored in desiccating chamber for at least 24h before any further tests of characterisation.

The processing parameters were based on the previous work of this author [Wang, 2015], (~42 μA/cm^2 at RT for ~24h). Higher current densities and temperature were explored in the EC processing. Higher current densities and temperature were considered to lead to higher deposition rates and larger crystal growth of $Mg(OH)_2$ hence leading to the chances of film thickening and densification due. The current applied is between 42 to 800 μA/cm^2. The temperature of RT to 60°C, and the EC treatment upto 24 hours, details are shown in Table 3.2.3.

Table 3.2.3 List of processing parameters for the EC samples with the following characterisation and analysis.

Substrate	Processing temperature (C°)	Processing time(h)	Applied current density (μA/cm^2)	Range of characterisation & analysis tests
AZ31-GF AZ31-ME ZM21-ME	RT 60	6 12 24	42 60 90 120 250 420 800	SEM (cross-section) FiB cross-section SEM (on surface) SEM (cross-sectional) EDX (point analysis) XRD EIS tests in 3.5^{wt}% NaCl solution

3.2.2.3 Additive method

This method is a novel method with no previous work. The processing is to heat the sample to the required processing temperature, then aqueous Mg^{2+} rich solution(~0.0064g/L), drop-wise onto the hot sample surface. A layer of $Mg(OH)_2$ salt is formed on the surface after the water evaporates. By repeating the above process, a Layer-by-layer $Mg(OH)_2$ based coating is produced. Schematic illustration and photos of the experiment set up for the additive method are shown in Figure 3.2.4.

The Mg^{2+} rich solution is also prepared by the electrolysis of the pure magnesium in DI-water, same for EC processing.

A hot plate is placed underneath the sample as the heat source. A Mg alloy sheet underlay was placed between the sample and hot plate to avoid contamination. A K-type thermal couple is connected to the underlay to monitor the temperature of the system.

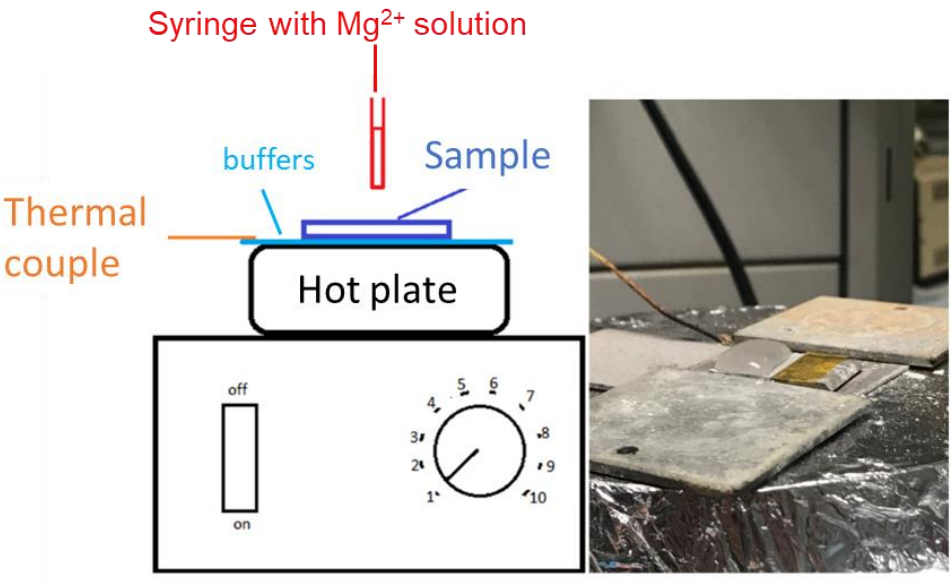

Figure 3.2.4. Experiment set-up for Additive processing.

A syringe is used to control the drop of Mg^{2+} rich solution to the alloy surface. The solution is deposited as droplets until fully covers the top side of the sample surface. The coating process is completed on one side, and then the sample is flipped to coat the other side. The second layer of drops is deposited after the solution from the first layer has dried. This process is repeated several times to achieve a surface layer. 2ml Mg^{2+} rich solution was applied for each layer.

Additive processing was also explored by being applied to the sample after EC treatment (EC+Additive samples), to improve the interface between substrates and coatings. Masking tapes were applied to the metallic region of the EC pre-treated sample to protect a connection made to the alloy with crocodile clips. The masking tapes have the maximum tolerated temperature of 260°C.

Various processing temperatures from 60±5°C to 240±5°C were explored in this work. 60°C, 100°C and 160°C were firstly applied as 60°C and 160°C are the processing temperatures applied to the EC and HT treatment, and 100°C is the boiling point of water at the standard atmospheric pressure. Higher processing temperatures were considered with denser coating hence higher Temperatures up to 240°C were further explored. Details of the parameters are shown in Table 3.2.4.

Table 3.2.4 List of processing parameters for the additive samples with the following characterisation and analysis.

Substrate	With EC Pre-treatment or not	EC pre-treatment temperature (°C)	EC pre-treatment current density (μA/cm^2)	EC processing time (°C)	**Additive Processing temperature (°C)**	Range of characterisation & analysis tests
AZ31-GF	No EC	N/a	N/a	N/a	**60, 100, 160**	Image Analyser (film thickness) SEM (on surface and cross-section) EDX (point analysis and elemental mapping) XRD PDP in 3.5^{wt}% NaCl solution EIS tests in 3.5^{wt}% NaCl, Saline solution and Hanks solution Mass change measurement
	With EC	RT, 60	420	12, 24	**160, 200, 240**	
AZ31-ME	With EC	60		24	**240**	
ZM21-ME	With EC	60		24	**240**	

3.2.3 Corrosion testing

3.2.3.1 Electrochemical testing

The electrochemical testing for the corrosion includes the EIS, OCP and Tafel extrapolation. 3.5^{wt}%, 0.9^{wt}% NaCl (Normal Saline solution) and Hanks balance solution as the electrolytes. 3.5^{wt}% NaCl solution has a similar Cl^- level to the seawater. 0.9^{wt}% NaCl solution has a similar Cl^- level to the body fluid. Hanks balanced solution contains other salts and/or elements, such as calcium, phosphorus and potassium, that simulate the composition of the body fluid. The composition of the Hanks solution is shown in Table 3.2.5 [Hou, 2018]. With the combination of the EIS and Tafel results, the equivalent corrosion current thus the equivalent corrosion rate mm/year can be evaluated.

Table 3.2.5 composition of Hanks balance solution[Hou, 2018]

Ingredient	KCl	KH_2PO_4	$NaHCO_3$	NaCl	Na_2HPO_4	Dextrose
mg/L	400	60	350	8000	48	1000
mM	5.33	0.441	4.17	137.93	0.338	5.56

For the EIS test, Samples were immersed in the test solutions for 24 and 48 hours. EIS measurements were taken at the interval of the immersion. E_{ocp} was also measured before and after EIS measurement. This test equipment was a Solartron 1280 Electrochemical Measurement Unit connected to a Solartron 1281 Multiplexer, and Scribner Associates, including CorrWare, CorrView, ZPlot and ZView V2.8d.

With the Tafel extrapolation, ±500mV cathodic and anodic over-potential were applied to the sample in solution. An Evan's Diagram of potential with current density was produced. An ACM Instruments GillAC and Sequencer with V5 software are used in this testing.

3.2.3.2 Mass change measurement

The mass change measurement records and monitors the corrosion loss and the build-up of the corrosion product when alloy (coated or uncoated) is in solution.

Samples were weighed in an analytical balance with 0.00001g precision. The volume of the alloy was evaluated by measuring edge lengths with a Vernier calliper. The alloys were immersed in either 3.5^{wt}% NaCl solution, 0.9% saline solution or Hank's solution for 2 to 3 weeks at RT. Samples were taken out of the solution every 3 days, dried, and the weight and dimensions were taken. After measurements, the samples are placed back in the solution for further immersion.

3.2.4 Characterisation and analysis

Various techniques were applied to characterise the:

- uncoated alloy substrate as references,
- alloy with $Mg(OH)_2$ films,
- alloy substrate post corrosion tests for qualitatively assessing the corrosion performance.

The characterisation includes optical microscopy, scanning electron microscopy SEM and compositional analysis with EDX and XRD.

Optical images are acquired by a Hirox 3D digital microscope and Nikon compound optical microscope with Leica digital camera and software.

An FEI XL30 scanning electron microscope with a field emission gun (SFEG) and Oxford Instruments XMax 20mm^2. Energy Dispersive (EDS) detector with AztecEnergy V2.2 and AztecHKL V2.2 software was used to examine the hydrothermal coatings on alloys.

A TESCAN Vega 3 scanning electron microscope equipped with the EDS system above was used to examine the EC and additive coatings on alloy samples.

X-ray diffraction (XRD) results are obtained by Bruker D5005 X-ray diffractometer with θ/2θ configuration.

Coated sample cross-sections were frequently characterised by SEM and optical microscopy. The cross-sections were prepared by cold mounting in a resin epoxy, with samples vertically placed in the mould so the sample cross-section to be viewed is parallel to the side of the mounted piece to be ground and polished. Mounted samples were then ground to P4000 SiC paper with oil lubricant followed by polishing on multi-cloths with 6µm and 1µm diamond respectively in oil. FIB cross-sectioning was also used to section coated alloys samples with thin surface films upto 2µm thick.

The following sections 4, 5 and 6 describe the alloy characterisation, $Mg(OH)_2$ films and corrosion performance.

4 Substrate characterisation on Mg alloy AZ31

4.1 Introduction

Mg alloys substrates AZ31-GF, AZ31-ME and ZM21-ME are characterised by optical microscopy, scanning electron microscopy (SEM), Energy Dispersive X-Ray Analysis (EDX), and X-ray diffraction analysis (XRD).

The microstructures of etched and unetched Mg alloys are characterised, and chemical composition and second phase particles are analysed in this chapter. Figure 4.1.1 is a schematic illustration of alloys AZ31-GF, AZ31-ME and ZM21-ME showing the dimensions, viewing planes and processing direction. These two alloys are the substrates for coating deposition discussed in Chapter 5.

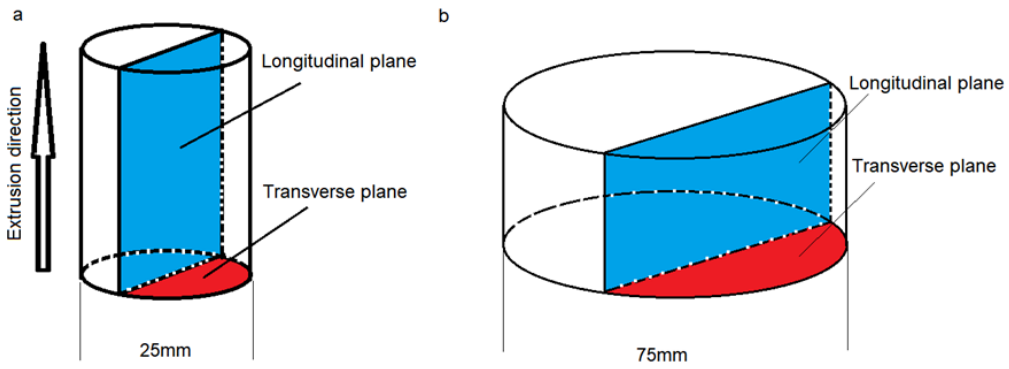

Figure 4.1.1. Schematic illustration of the a) AZ31-GF and b) AZ31-ME and ZM21-ME.

4.2 Characterisation of AZ31-GF

The microstructures of AZ31-GF for both planes parallel and perpendicular to the extrusion directions are shown by the bright-field optical images in Figure 4.2.1. The features are the matrix, particles and scratches before etching, shown in Figure 4.2.1a and 4.2.1b.

The sample surfaces etched by 5% Nital solution for 120s are shown in Figure 4-2-1c and 4.2.1d respectively, for the longitudinal and transverse planes. Grain boundaries were revealed on both planes. The etching was not uniform in the longitudinal plane and grain boundaries are partially revealed. Grains are separated by band-marks that are likely to be extrusion textures. In the transverse

plane, the grains are more equ-axial. Some grain boundaries etch differently, some over etched in some regions and under-etched in others. However second-phase particles are revealed near grain boundaries. The profile of the grain structure on both planes is illustrated in yellow.

Grain size measurements were undertaken [ASTM E112–12, 2010]. The average grains on the longitudinal plane is 15±2μm with a standard deviation of 3.99. and the average grain size on the transverse plane is 11±0.1μm with a standard deviation of 0.6.

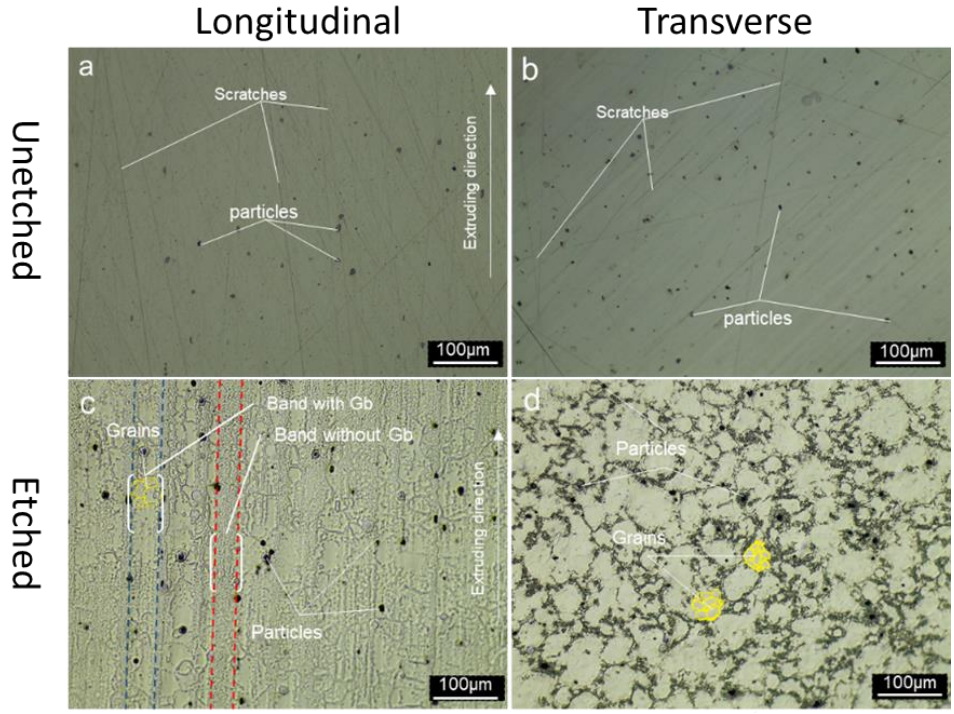

Figure 4.2.1. Optical metallography of AZ31-GF, a) longitudinal plane polished with 1μm diamond in oil, b) transverse plane polished with 1μm diamond in oil, c) longitudinal plane etched with 5% nital d) transverse plane etched with 5% nital.

The particles are distributed at the grain boundaries. They were analysed from the optical images at magnifications 20X and 50X using imaging processing software 'Image J'. The numbers, average sizes and proportions of the particles were measured and evaluated on both viewing planes of AZ31-GF. Filtering and thresholds were applied to reduce the influence of the scratches in the images. Particles with a size less than 1μm^2 or a circularity less than 0.1 were neglected. The statistical results are shown in Table 4.2.1. There is a smaller particle number but a larger average particle size on the longitudinal plane than on the transverse

plane. The particles on the longitudinal plane are more likely to orientate along the extrusion direction. On the transverse plane, the particles are more round-shape or elongated shapes but randomly orientated. The characterisation of $Mg(OH)_2$ films on AZ31-GF, in Chapter 5, focus on the transverse plane.

Compared with different magnifications in both planes, the 50X images are easier to see a higher area percentile (0.3-0.35%) of the particles than 20X time (~0.2%). The possible reason is that finer particles or scratches are more prominent in the higher mag images.

Table 4.2.1 Statistics of second phase particles in AZ31-GF extruded bar at 20X and 50X magnification from the optical microscope on the longitudinal and transverse planes (not taken from Figure 4.2.1)

Sample	AZ31-GF longitudinal		AZ31-GF transverse	
Image magnification	50X	20X	50X	20X
Image area (μm^2)	52683	329510	52621	330340
Number of precipitates	16	63	18	77
Total particle area(μm^2)	183.8	727	157.8	616
Average particle size (μm^2)	11.5	11.55	8.8	8.00
Total particle area percentage (%)	0.35	0.22	0.30	0.19

Figure 4.2.2 shows secondary electron SEM images of AZ31-GF after etching. It shows the same features as in the optical micrograph of Figure 4.2.1b, including the particles and partially revealed grain boundaries. The profile of the grain structure is enhanced with a yellow outline.

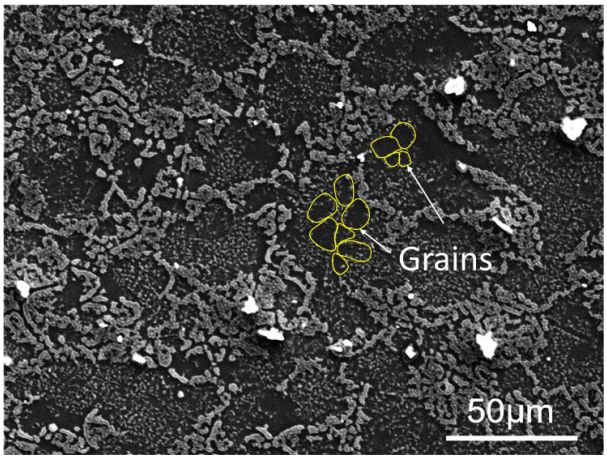

Figure 4.2.2. SEM micrograph of transverse AZ31-GF, 5% Nital etched 120s

Figure 4.2.3 indicates the distribution of the compositional elements corresponding to Figure 4.2.2. The particles are rich in Al and Mn, Fe, and Si are also detected in a few precipitates. Mg is depleted compared to the matrix. Zn is evenly distributed. An enrichment of O is found at the grain boundaries and precipitates. These sites are more likely due to corrosion by etching.

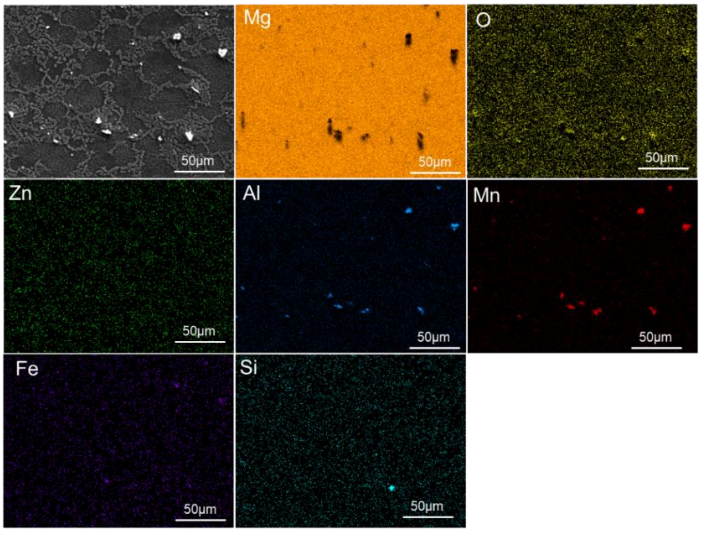

Figure 4.2.3. EDX elemental mapping of AZ31-GF from Figure 4.2.2.

In comparison, compositional point analysis with EDX is applied to the unetched AZ31-GF substrate. The SEM micrograph with spectrum locations and compositions are shown in Figure 4.2.4 and Table 4.2.2 respectively.

For the overall composition, spectrum 3, there are Al, Zn and Mn follow the standard 3.0. 0,6 and 0.26 wt% respectively [ASTM B951-10, 2010]. However, impurities such as Si, Ca, and Fe are over the standard [ASTM B951-10, 2010]. O is also detected which is likely attributed to the surface oxides.

Most second phase particles/precipitates are rich in Al and Mn, with around 17 to 37 wt% for Al and 22 wt% for Mn. Some of these particles contain a high level of Fe, around 0.6 wt%, shown in spectrum 4. Some particles are Ca and O rich but depleted in Al and Mn.

Figure 4.2.4. Backscattered electron images of AZ31-GF transversely with the EDX point analysis location on the image.

Table 4.2.2. Compositional EDX point analysis results of AZ31-GF on the transverse plane.

AZ31-GF wt%	O	Mg	Al	Si	Ca	Mn	Fe	Zn
Overall Spectrum 3	1.48	94.19	3.06	0.14	0.14	0.26	0.1	0.64
Matrix Spectrum 2	0.76	94.79	3.63	0	0	0.19	0.06	0.57
Particle1 Spectrum 4	0.93	41.44	34.2	0.05	0	22.73	0.61	0.04
particle 2 Spectrum 5	20.32	65.26	2.22	0.29	11.5	0.11	0.04	0.27
Particle 3 Spectrum 6	0.55	58.2	17.84	0.24	0.04	22.7	0.06	0.37

4.3 Characterisation of AZ31-ME

Figure 4.3.1 shows the optical microstructures of the AZ3-ME for both orientations before and after etched with 5^{wt}% Nital solution for 150s.

On the longitudinal plane, band-marks are also observed perpendicular to the extruding direction. The band marks and grains are highlighted in Figure 4.3.1c and 4.3.1d. Equ-axial grain structures were revealed on both planes uniformly through the surface after etching. The longitudinal grain sizes are 6.1±0.2µm with a standard deviation of 0.88 and transverse 6.0±0.27µm with a standard deviation of 0.47. The grain size is half the size and less scattered than the AZ31-GF alloy.

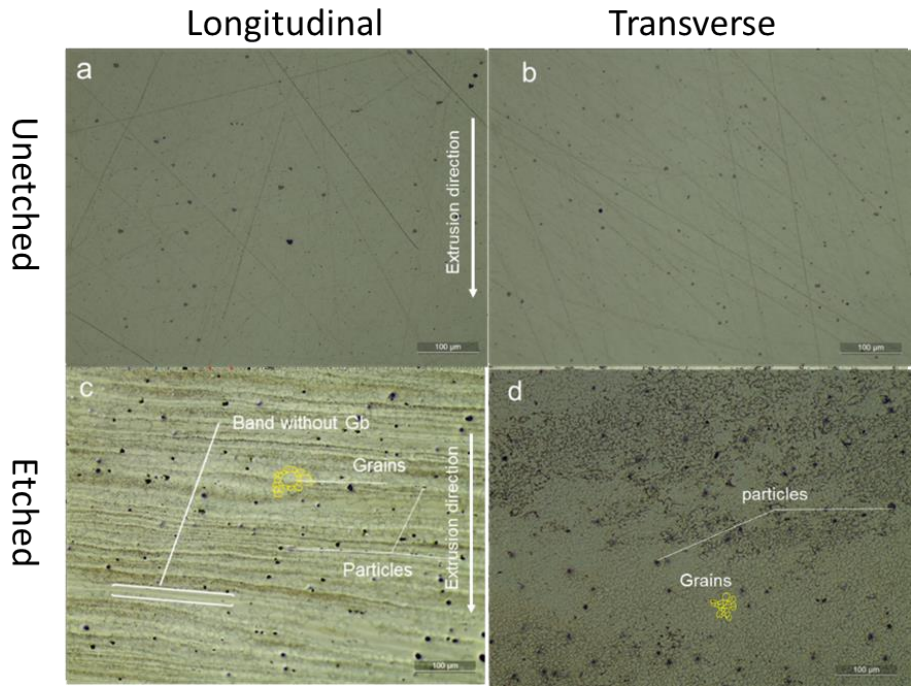

Figure 4.3.1. Optical metallography of AZ31-ME, a) longitudinal, polished 1µm diamond in oil, b) longitudinal etched, c) transverse polished with 1µm diamond in oil and d) transverse etched

Particles were measured with image software from the optical microscopy images. The results are shown in Table 4.3.1. for both magnifications, the number of particles number in the longitudinal direction is around two-thirds of the number in the transverse direction. The average size and total percentage area of the particles are greater in the longitudinal direction.

Table 4.3.1. Statistics of second phase particles in AZ31-ME with optical micrographs 20X and 50X on the longitudinal and transverse planes (not taken from Figure 4.31)

Sample	AZ31-ME longitudinal		AZ31-ME transverse	
Image magnification	50X	20X	50X	20X
Image area (µm^2)	52673	330663	52644	330802
Number of precipitates	10	54	16	75
Total particle area (µm^2)	145	560	108	534
Average particle size (µm^2)	14.5	10.4	6.8	7.1
Total particle area percentage (%)	0.28	0.17	0.21	0.16

For AZ31-ME, the following study is following on the surface on the longitudinal plane. A SEM image of the AZ31-ME is shown in Figure 4.3.2. Elemental mapping is shown in Figure 4.3.3. The grain boundaries are rich in O, and the

particles rich in Al, Mn, and Fe. The other alloying elements Si, Ca and Zn are more uniformly distributed but can be localised distributed near the grain boundaries.

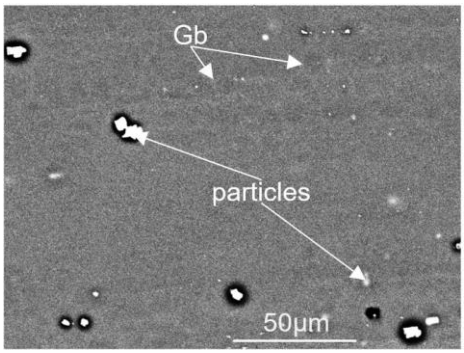

Figure 4.3.2. SEM images of AZ31-ME disc on the longitudinally.

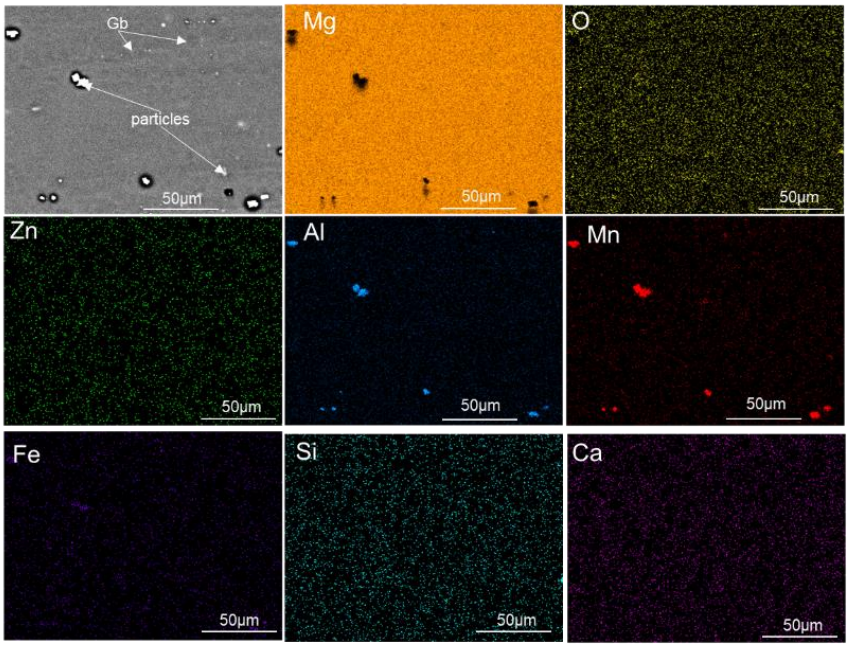

Figure 4.3.3. EDX elemental mapping of AZ31 -ME on the longitudinally.

Compositional point analysis with EDX is applied to the unetched AZ31-ME substrate. A SEM image with the compositional analysis from marked points is shown in Figure 4.3.4 and Table 4.3.2. The overall composition, spectrum 7, AZ31-ME contains 2.88 ^{wt}% Al, 0.63 ^{wt}% and 0.2 ^{wt}% Mn. Other alloying elements such as Si and Ca are within the standards [ASTM B951-10, 2010]. The Fe impurity is about 0.02^{wt}% which is higher than the standard but much lower than the AZ31-GF. The matrix, spectrum 8, has more Mg and Fe and less Al, Mn, Zn and Si than the overall spectrum. Most particles such as spectrum 9-13 and

spectrum 15, are rich in Al and Mn. These precipitates vary from 4.66 to 18.62 wt% in Al and 0.85 to 19.14 wt% for Mn. A higher proportion of Fe is detected in some of the angular particles in spectrums 8 and 12. The grey area, shown in spectrum 14, contains a lower level of Al and Mn but a higher level of Zn than average. It may contain fine intermetallics Mg_2Zn_3 as the elemental mapping of Zn in Figure 4.3.3 also shows a possible localised Zn trace.

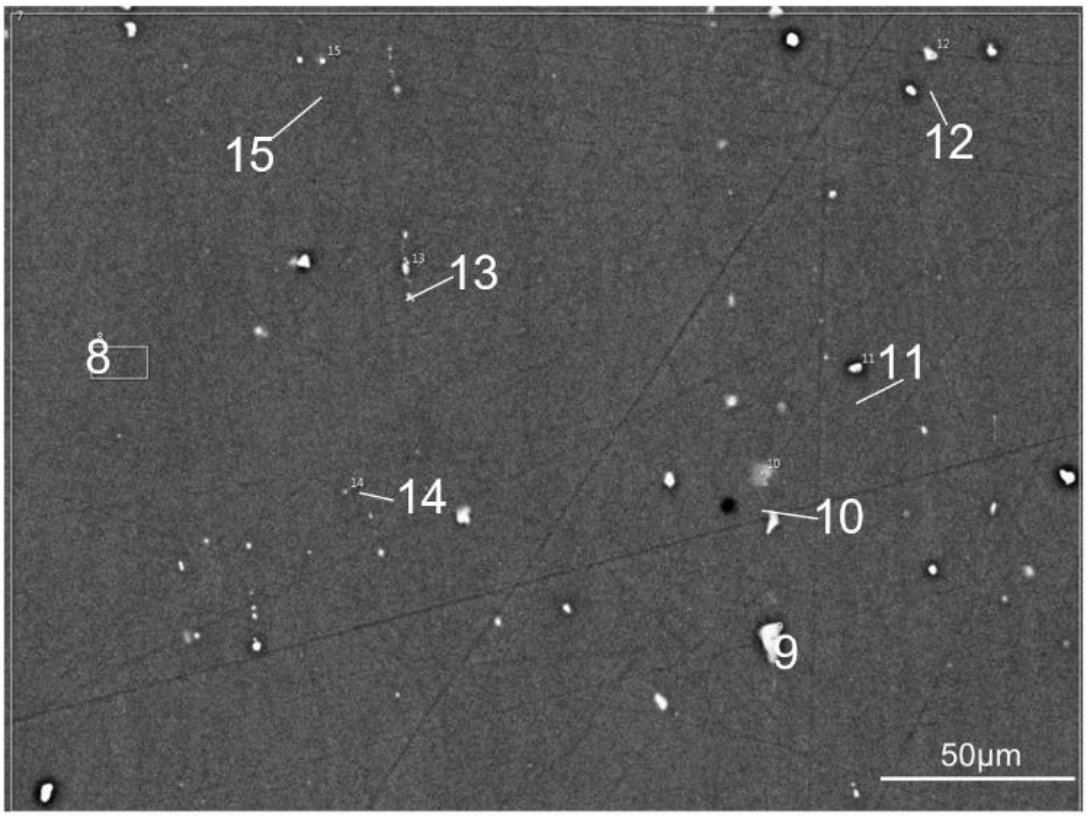

Figure 4.3.4 BSE images of AZ31-ME on the longitudinal plane with the EDX point analysis location on the image.

Table 4.3.2. Compositional EDX point analysis results of AZ31-ME longitudinally. Spectra numbers in brackets

Overall (7)	1.71	94.5	2.88	0.06	0	0.2	0.02	0.63
Matrix (8)	1.61	94.9	2.78	0	0	0.1	0.04	0.57
Coarse angular particle (9)	1.83	75.02	17.04	0.29	0.03	5.3	0.08	0.41
Round particle (10)	0.69	74.1	9.75	0.24	0	14.74	0.02	0.46
Angular particle 2 (11)	4.64	69.69	18.62	0.12	0	6.44	0.03	0.46
Angular particle 3 (12)	1.03	64.37	14.87	0.12	0	19.14	0.3	0.18
Angular particle in a chain (13)	1.84	91.92	4.71	0.06	0.03	0.85	0	0.6
Grey particles (14)	3.61	92.91	2.56	0.02	0	0.16	0.02	0.72
Round particle (15)	0.88	87.2	4.66	0.02	0.05	6.73	0	0.45

4.4 Characterisation of ZM21-ME

The microstructures of ZM21-ME for both longitudinal and transverse planes are shown by the bright-field optical images in Figure 4.4.1, etched with 5^{wt}% Nital solution for 70s. Brandmarks are observed in the longitudinal plane, perpendicular to the extrusion direction. At longitudinal directions, shown in Figure 4.4.1a, the alloy substrate exhibits A structure with an average grain size of 64µm with a standard deviation of 10. Figure 4.4.1b shows the etched ZM21-ME on the transverse direction. The average grain size is 68µm with a standard deviation of 15. The difference in average grain sizes in two directions is small hence likely to be equiaxed grains.

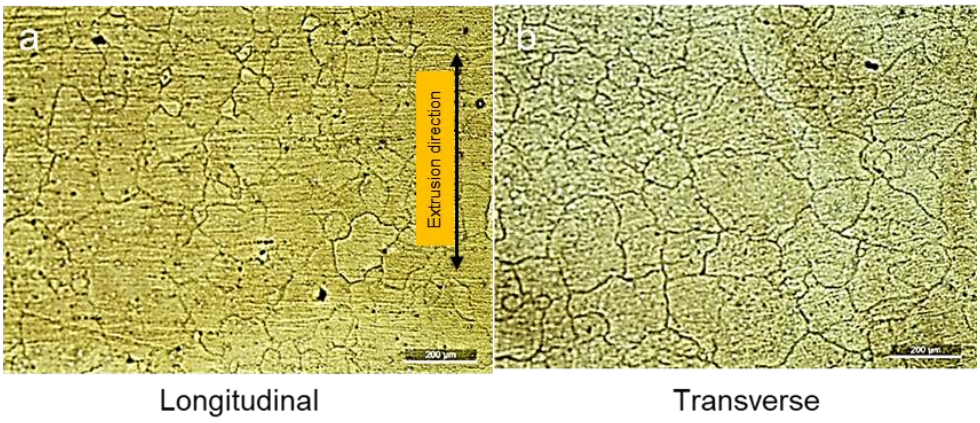

Figure 4.4.1. Optical metallography of ZM21-ME etched with 5% nital for 70 seconds on the a) longitudinal and b) transverse directions.

Sub-granular-like features are also observed within the grains after etched 100s with increasing the picture sharpness, shown in Figure 4.4.2.

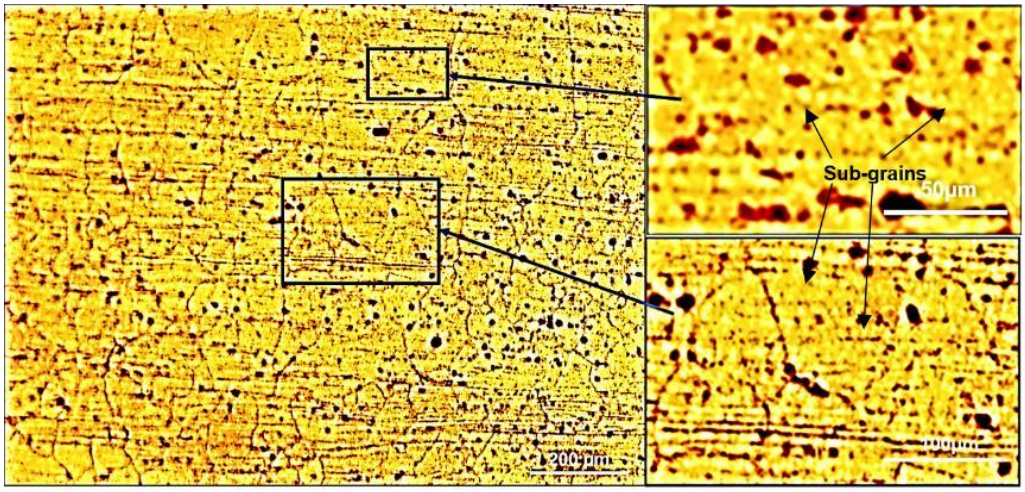

Figure 4.4.2. Optical micrograph of etched ZM21-ME longitudinally.

The optical micrographs of unetched ZM21-ME substrates are shown in Figure 4.4.3. Based on these images, particles of this alloy were measured with image software (results). The results are shown in Table 4.4.1.

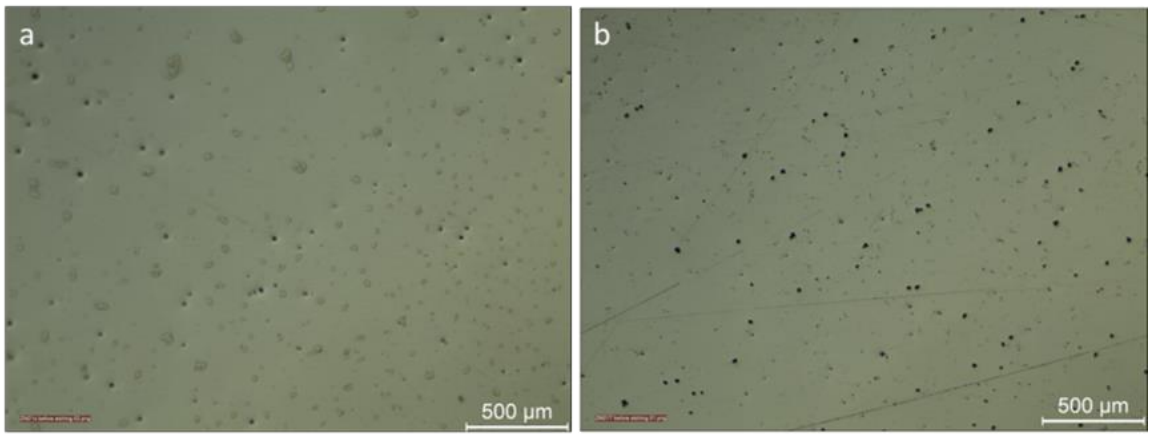

Figure 4.4.3. Optical metallography of ZM21-ME unetched.

Table 4.4.1. Statistic of particles of the ZM21-ME from the optical microscopy images with 10X magnifications longitudinally and transversely.

Statistic\Sample	ZM21-ME longitudinal	ZM21-ME transverse
Image magnification	10X	10X
Area of the image(μm^2)	5084898	5353228
Number of precipitates	170	301
Total particle area(μm^2)	16964	21990
Average particle size(μm^2)	99.4	73.1
Total particle area percentile (%)	0.322	0.421

The ZM21-ME substrate is further characterised with SEM, and the particle composition is analysed with EDX, shown in Figure 4.4.4 and Table 4.4.2.

The etched samples surface generally contains the matrix in black, large white particles, and small grey particles. The overall composition (spectrum 17) is close to the expected standard composition. The matrix has a similar composition except with lower Mn and slightly raised Zn. This is due to the different solubility of Zn and Mn. The fine particles (spectrum 21) have higher O and lower Mg likely to be corrosion products during the etching process. These particles are likely at the boundaries of the fine-grain structure as shown in Figure 4.4.2. The large particles (spectrum 18) are precipitates that contain a much larger amount of O, Si, Mn and Zn. The presence of Fe is also identified.

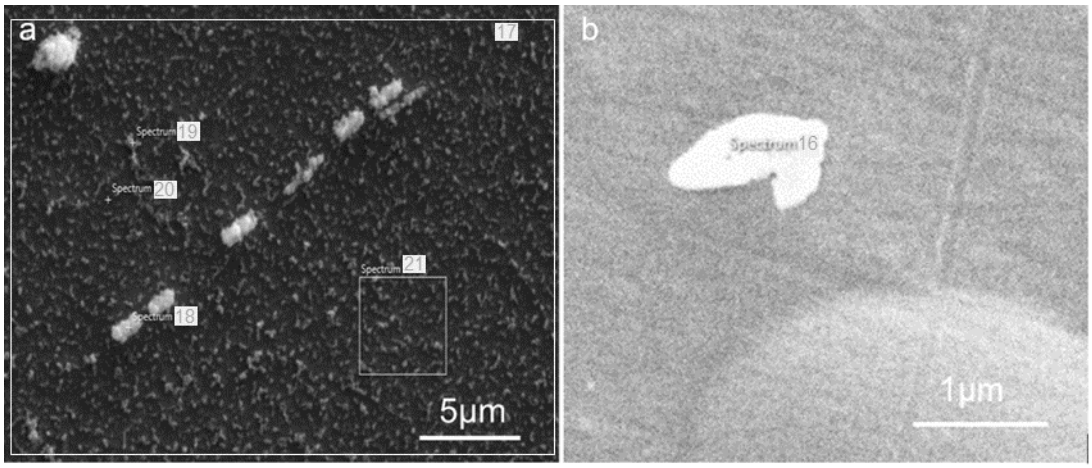

Figure 4.4.4. SEM image of etched ZM21-ME with EDX measurements.

Table 4.4.2 Compositional EDX point analysis results of ZM21-ME.

wt%(atm%)	O	Mg	Si	Ca	Mn	Fe	Zn
Spectrum 17 Overall	4.39 (6.62)	92.95 (92.34)	0	0	0.80 (0.35)	0	1.86 (0.69)
Spectrum 18 Coarse particles	17.53 (26.97)	60.68 (61.41)	4.86 (4.26)	0	12.46 (5.58)	1.55 (0.69)	2.92 (1.09)
Spectrum 19 Fine particle	7.01 (10.45)	90.38 (88.54)	0	0	0.77 (0.32)	0	1.84 (0.68)
Spectrum 20 Matrix	3.99 (6.05)	93.32 (92.90)	0	0	0.75 (0.34)	0	1.94 (0.71)
Spectrum 21 Matrix + fine particles	3.91 (5.92)	93.46 (93.06)	0	0	0.58 (0.25)	0	2.04 (0.76)
Spectrum 16 Coarse particle	9.83 (14.70)	80.77 (79.46)	0	6.53 (3.89)	0.86 (0.37)	0	2.01 (0.74)

4.5 Comments on substrate alloys

Textures by the wrought process are observed in the form of band-marks. All three alloys are extruded samples, but the texture of AZ31-ME and ZM21-ME is perpendicular to the extruding direction. A post-processing treatment may have been applied to AZ31-ME and ZM21-ME post extrusion.

For AZ31-GF alloy, the grain size on the longitudinal direction 15µm is larger than on the transverse direction. The extrusion processing influences the microstructure. Band-marks are observed along the extrusion direction likely due to elongation of the pre-existing grains. With post-processing heat treatment, smaller grain structures are observed with recrystallisation. Extrusion marks respond to the etchant due to different chemical activity and/or the air-formed oxides. This may be responsible for grains partially revealed in the longitudinal plane.

For both AZ31-GF and AZ31-ME alloy, around 0.2% and 0.3% of the areas are second phase particles. Most particles are rich in Al and Mn. It indicates the possible presence of Al_xMn_y intermetallics apart with the primary second phase Mg_xAl_y.

Figure 2.2.2 and Table 2.2.3 provide the Al to Mn ratios for different Al_xMn_y phases [Friedrich, 2006]. From this, possible Al_xMn_y phases previously shown in Figure 4.2.4 and Figure 4.3.4 are estimated in Table 4.5.1. Al_8Mn_5 and µ-Al_4Mn are found in AZ31-GF. Al_8Mn_5 $Al_{11}Mn_4$ and λ-Al_4Mn are seen in AZ31-ME.

Table 4.5.1 List of AlMn rich particles analysed in EDX in Figure 4.2.4 and Figure 4.3.4 with their corresponding Al: Mn and likely phase.

	Al	Mn	Al: Mn ratio	Possible phase
Spectrum 4 (AZ31-GF)	74.97	25.03	3.00	µ-Al_4Mn
Spectrum 6 (AZ31-GF)	61.12	38.88	1.57	Al_8Mn_5
Spectrum 9(AZ31-ME)	86.51	13.49	1.32	Al_8Mn_5
Spectrum 10 (AZ31-ME)	56.95	43.05	5.78	λ-Al_4Mn
Spectrum 11 (AZ31-ME)	85.24	14.76	1.55	Al_8Mn_5
Spectrum 12 (AZ31-ME)	60.84	39.16	1.38	Al_8Mn_5

Spectrum 15 (AZ31-ME)	58.07	41.93	2.03	$Al_{11}Mn_4$

For some of the Al and Mn-rich precipitates higher level of Fe is also detected. It is because of the good affinity between Fe and Mn [Song, 2003]. Zn has a proportion lower than average in the matrix and the AlMn phases but with higher content in grey areas. The grey area and particles are likely to be coherent/semi-coherent β' (Mg_2Zn_3) phase. Other particles may also contain a high level of Ca, which is observed in alloy AZ31-GF.

The composition of the major alloy elements (Mg, Al Zn and Mn) For AZ31-GF and AZ31-ME are similar and both are within the standard composition. However, there are significant differences in the minor element or impurities. Alloy AZ31-GF has a significantly larger proportion of Si, Ca and Fe over standard. One possible reason is that the AZ31-GF is a small diameter extruded bar. The second phase particles containing these elements may have an inhomogeneous distribution. The EDX targets surface area rich in these elements.

When quantifying particles with the imaging software, the particle size could not be deduced due to the filter and thresholding, and some very fine particles less than 1µm are assumed to be part of a scratch and neglected. Nevertheless, this error would be consistent with all measurements.

ZM21-ME exhibits a larger grain size than both batches of AZ31. A possible sub-granular structure is observed within the grains, possibly due to the heat treatment post extrusion. If the fine-grain features exist, they are likely due to recrystallisation. This is also observed in the literature [Thirumurugan, 2011]. It is still difficult to confirm whether these features are sub-grains because there are no figures with higher resolution. Therefore, the observation could be due to the surface roughness or the error of the adjusted figures.

ZM21-ME has more particles in area percentile. It comprises coarse second phase particles rich in Mn and Zn Fe, Si and Ca, likely to be the Mg_xMn_y and Mg_xZn_y phases [Jiang,2017]. The presence of Fe is likely due to the Mn. Si is likely an alloying impurity or contamination from the polishing debris. Ca is a

common alloying element in Mg-Zn series alloys which usually precipitates with Mg in the form of Mg_2Ca or $Mg_5Ca_2Zn_5$ [Liu, 2016].

4.6 Summary

The microstructure of AZ31-GF, AZ31-ME and ZM21-ME is characterised. The morphology and microstructures on both longitudinal and transverse planes were checked. The composition in bulk and the features (such as the precipitates) were measured with EDX.

Both AZ31 contain coarse Al_xMn_y second phases and possible fine Mg_xZn_y particles. However, the AZ31 from different sources shows vast differences in the microstructure and impurity level and homogeneity, determined by the alloy's processing.

This chapter shows the substrates to be coated and builds up a reference for the following chapter that studies the coated samples.

1

5 $Mg(OH)_2$ film on Mg alloy substrates

5.1 Introduction

Chapter 5 described the $Mg(OH)_2$ based films applied to Mg alloy substrates with various methods, including hydrothermal, electrochemical, and additive methods. Section 5.2 shows the experimental results of the hydrothermal films on AZ31-GF substrate. The hydrothermal results are considered the benchmarks for studying the novel electrochemical and additive methods in 5.3 and 5.4.

The investigation of the EC processing is in Section 5.3. Three stages took place. Firstly, a focus on EC samples on AZ31-GF substrate at RT. A range of current densities between 42μA/cm^2 and 800μA/cm^2 were applied. Secondly, EC samples with a higher processing temperature of 60°C were studied. Finally, in the third stage, EC film on the other substrate AZ31-ME was investigated.

In Section 5.4, the additive method to apply $Mg(OH)_2$ films to Mg alloy substrates is investigated. It firstly investigated the additive process directly applied to the alloy substrate (Direct-additive). Then the combination of the additive process after the EC processing is described (EC + additive). Processing temperatures were adopted from 60 to 240°C.

Optical microscopy and SEM on the coated sample surface and sample cross-sections are shown, including the film measurements. Compositional analysis by EDX and XRD were applied to indicate features in the microstructure. The results were summarised in section 5.4.

5.2 $Mg(OH)_2$ film by hydrothermal processing

5.2.1 Characterisation of the hydrothermal film

Figure 5.2.1 shows images of the hydrothermal samples at 120ºC and 160ºC with increasing treatment time.

The colours of the samples at 160°C vary from dark grey to light grey/yellow. With short holding times in the oven, the sample surface is glossy dark grey. As treatment time increased, the gloss disappears, and surfaces appear lighter. The

samples hydrothermally treated over 4 hours have a layer detached from the alloy substrate. At 120°C, surfaces appear to keep dark grey and do not change with treatment time.

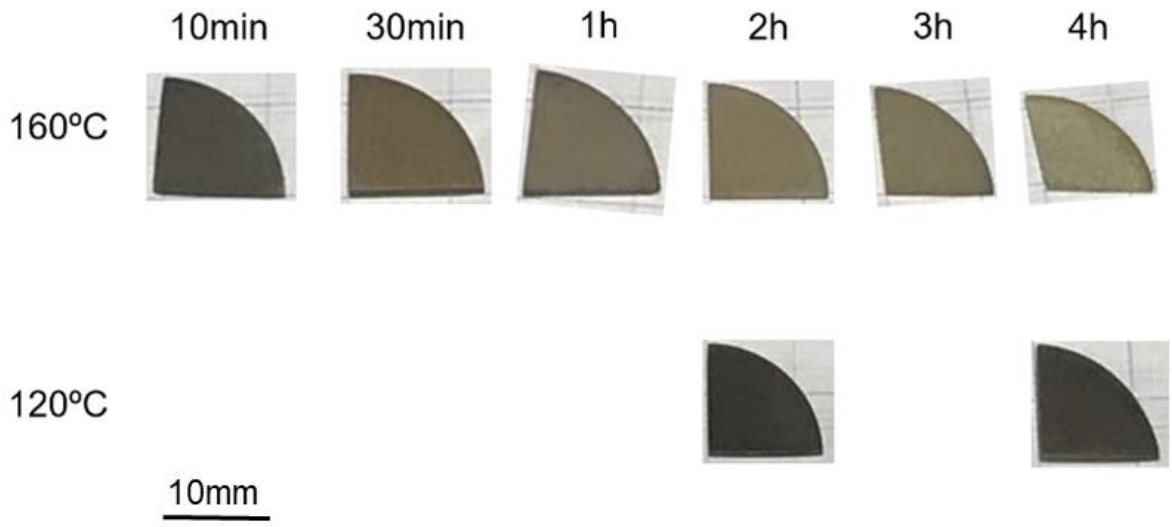

Figure 5.2.1. Photo images of the hydrothermal processed AZ31-GF sample at 160°C and 120°C for various time.

Figure 5.2.2 is an example of an SEM image of a hydrothermally grown film. It contains typical features, including precipitates, porous and scratch marks.

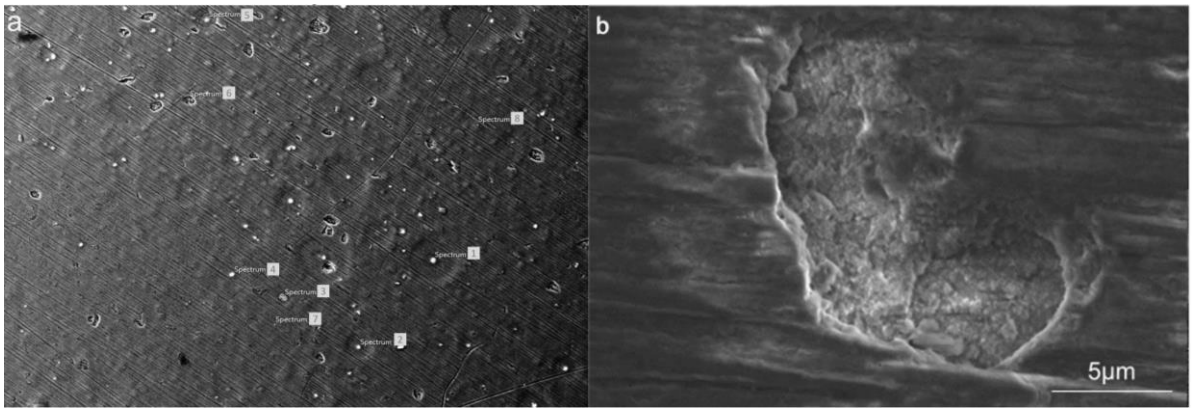

Figure 5.2.2. SEM Image of surface morphology of a hydrothermally treated film.

The precipitates and scratch marks are likely to be pre-existing scratches on the substrates during sample preparation. Figure 5.2.2a indicates two types of pores: the ‘indentation-like pores’ and the ‘open pores’. The indentation-like pores are developed around second phase particles that generated an indentation-like geometry. This type of pore is usually with a round shape, and the particles are

at the centre of the pore. These pores are shallow and coherent to the rest of the film. The ‘open porous’ are usually deep porous with irregular geometry. Inside these pores, it exhibits rough irregular morphology incoherent to the rest of the film, shown in Figure 5.2.2b with a higher magnification.

Table 5-2-1 shows the compositional information for the features corresponding to Figure 5.2.2a. For both the film surface (spectrum 7 and 8) and the ‘open porous’ (spectrum 6), the main elements are confirmed with Mg and O as $Mg(OH)_2$. A higher atomic Mg-O ratio of around 1.3 is observed, mainly by the interference of the background Mg substrate. Particles are confirmed as the Al_xMn_y intermetallics, shown in spectrums 1 to 5.

Table 5.2.1, Elemental composition of the hydrothermal film

atm% / (wt%)	O	Mg	Al	Mn	Fe	Zn
spectrum 1	8.45 (19.24)	9.14 (13.87)	10.34 (14.49)	69.79 (50.86)	1.5 (1.05)	0.79 (0.48)
spectrum 2	18 (34.87)	17.00 (21.95)	5.23 (6.23)	58.38 (36.19)	0.59 (0.35)	0.81 (0.42)
spectrum 3	10.37 (23.2)	9.15 (13.65)	8.36 (11.51)	71.80 (51.41)	0.32 (0.22)	0
spectrum 4	37.99 (51.62)	41.94 (37.99)	3.41 (2.85)	16.65 (7.24)	0	0
spectrum 5	31.63 (45.7)	35.53 (34.22)	5.24 (4.66)	27.60 (12.76)	0	0
spectrum 6	42.23 (52.07)	54.98 (45.2)	2.79 (2.12)	0	0	0
spectrum 7	41.31 (51.71)	54.76 (45.7)	1.65 (1.27)	0	0	2.28 (0.76)
spectrum 8	41.55 (51.91)	53.15 (44.27)	2.85 (2.19)	0	0	2.46 (0.82)

The hydrothermal treatment time has significant influences on the feature and morphology of the hydrothermal films. Figure 5.2.3 shows the SEM images of the AZ31-GF surface after hydrothermal treatment at 160°C for 0.5h, 1h and 2h, respectively. Figure 5.2.3 a, b, and c are backscattered images. They show precipitates and pores on the film surfaces. With a longer treatment time, the size of pores reduces. The ‘open porosity’ became shallow, closing with increasing the processing time.

Figures 5.2.3 d, 5.2.3 e and 5.2.3 f are SE images showing surface information. Variations in the surface roughness with increasing time are identified. At 30min, the surface is partially covered with rough film features. Scratch marks on the metallic surface are also revealed. At 1h, the surface has fully covered with rough homogenous features with bumps. With a longer 2h-treatment, the roughness of the surface features decreased, and the film surface homogenised.

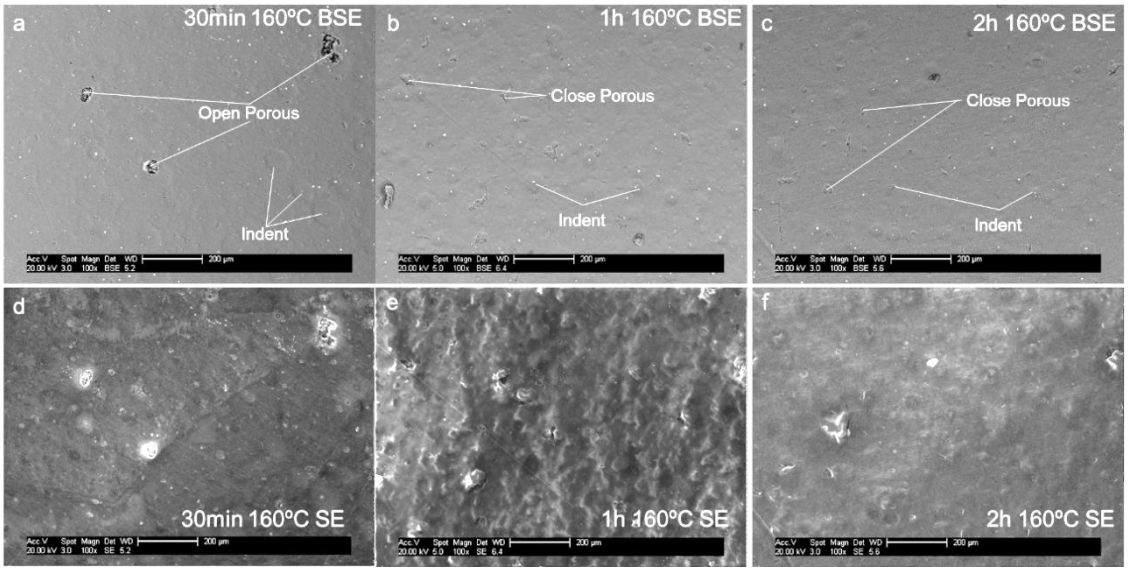

Figure 5.2.3 surface SEM images of the hydrothermal film after treatment at 160°C.

Figure 5.2.4 is an SEM image of the cross-section of the hydrothermal films. Both SE and BSE images are shown in Figure 5.2.4. A coherent film-substrate interface was observed. The film is a layered structure with cracks/ voids at 1 to 2 µm intervals through the film depth.

EDX measurements on the sample cross-section show Mg and O are the main compositional elements. The atomic Mg-O ratios are around 0.71 to 0.85, higher than the Mg-O ratio measured on the sample surface (Table 5.2.1). No difference between the top and bottom of the film was observed. The relationship between thickness and heat treatment time at 120°C and 160°C are shown in Figure 5.2.5.

There is a linear relationship between film thickness and treatment time at 160ºC (dots). There is a film growth rate of around 18µm per hour. At 120°C (circle), the coating growth rate is slower. For 2h and 4h samples, the coating thicknesses

are 1.028 μm and 1.391 μm, respectively. The growth rate is approximately 0.19μm per hour, about a tenth of the rate at 160°C.

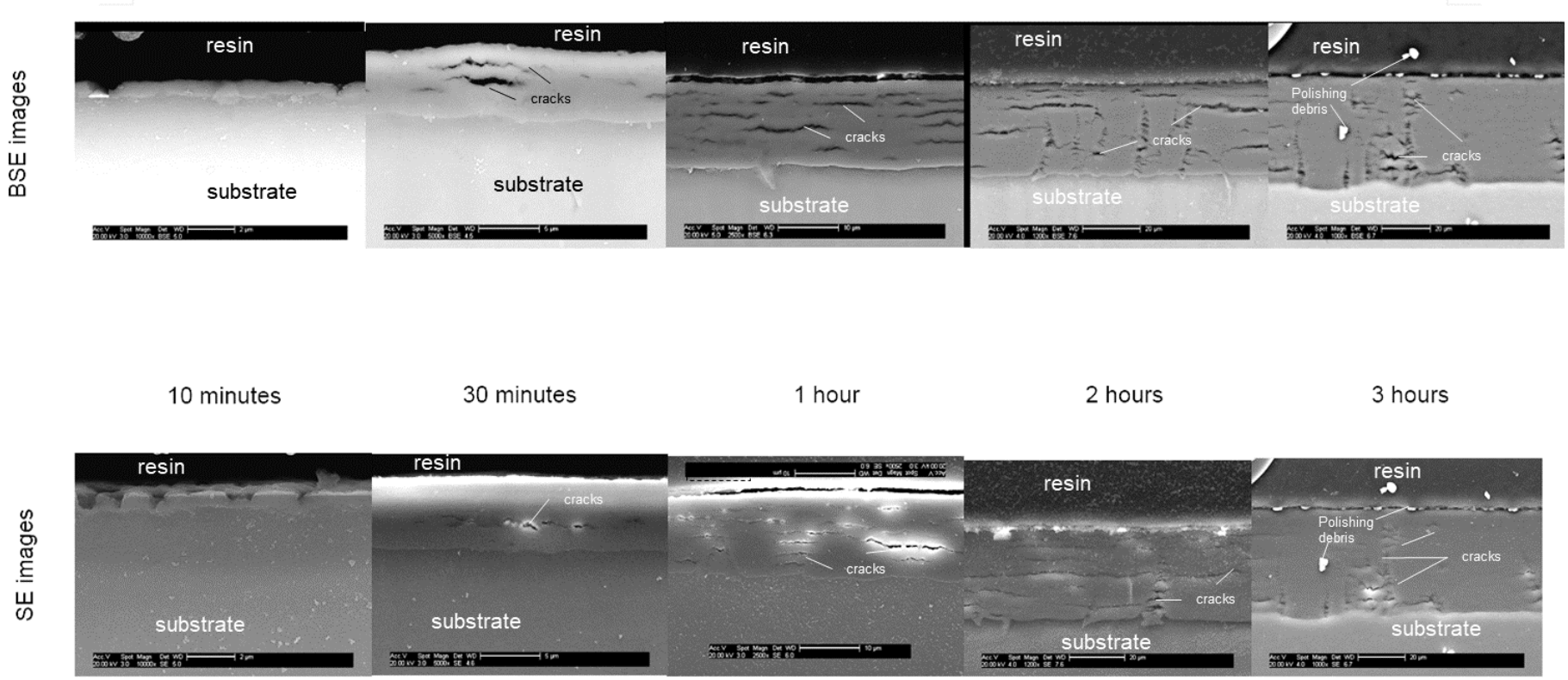

Figure 5.2.4. SEM images of the hydrothermal film Cross-section.

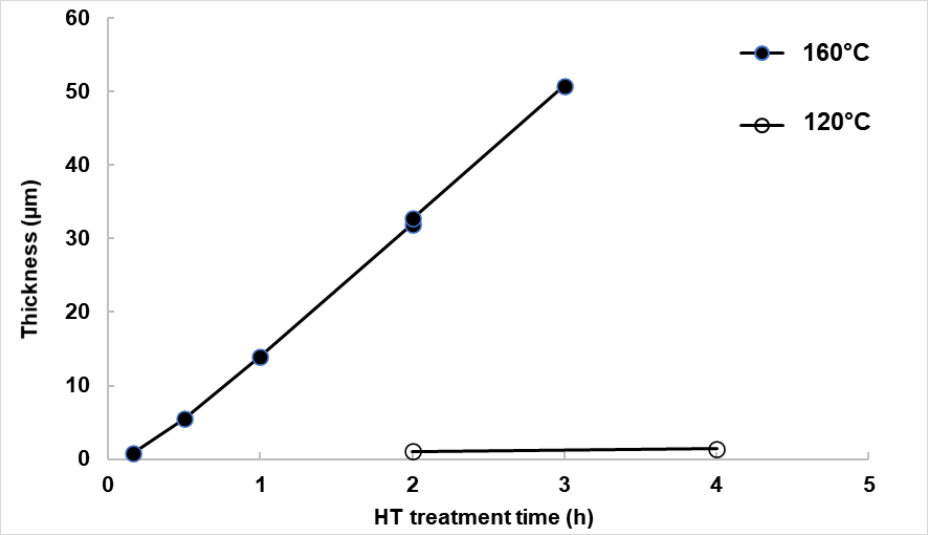

Figure 5.2.5. HT films thickness versus the treatment time at 120°C and 160°C.

5.2.2 XRD results for HT thickness prediction

Figure 5.2.6 shows the XRD pattern of extruded AZ31B substrate and its hydrothermally treated samples after 1, 2, and 3 hours respectively. The pattern matches the Mg and $Mg(OH)_2$ references, and the (h k l) of each peak is illustrated in this plot from the database [PDF, ICDD].

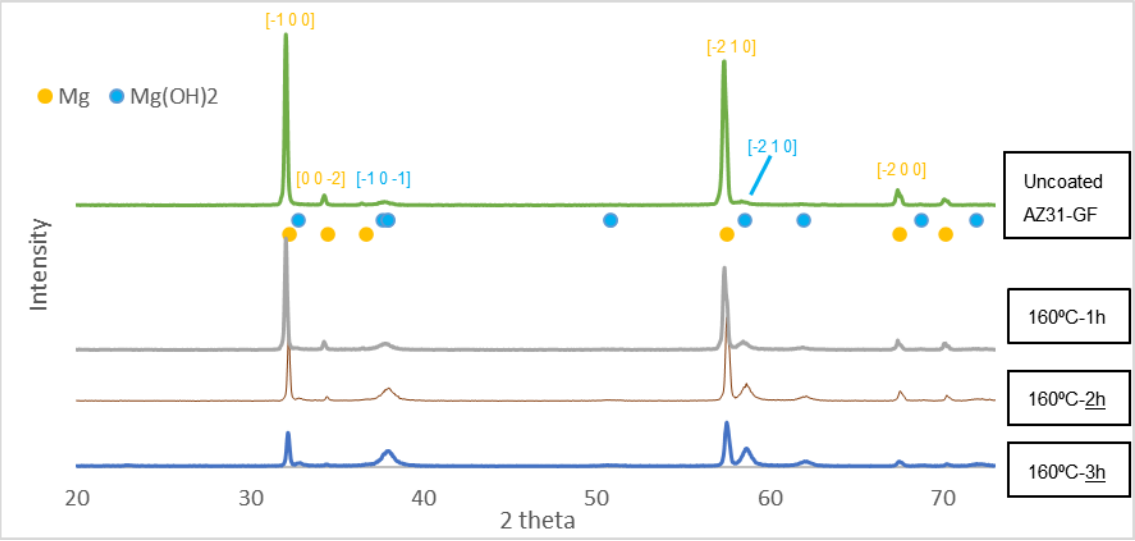

Figure 5.2.6, XRD pattern of the steamed AZ31 bar samples with 1, 2 and 3 h heat treatment.

For Mg, typical metallic phase peaks are observed at the planes of (-1 0 0), (0 0 -2), (-2 1 0) and (2 0 0) (illustrated as yellow circles). For $Mg(OH)_2$, the typical peaks at (-1 0 -1) and (-2 1 0) are illustrated as blue circles. At 160°C with an

increase in processing time, the peak intensity for $Mg(OH)_2$ increased, and the Mg peak intensity decreases. $Mg(OH)_2$ was detected only for thicker films that are processed for more than 30min at 160°C by XRD. No $Mg(OH)_2$ was detected but only the Mg peaks are detected for the samples at 120°C for both 2 and 4 hours, and the samples at 160°C for 10 min,

Figure 5.2.7 quantifies the changes of $Mg(OH)_2$ on the sample surface by showing the ratio of $Mg(OH)_2$ to Mg on their typical peak intensities. Two combinations of '$[-1\ 0\ -1]_{Mg(OH)2}$:$[-1\ 0\ 0]_{mg}$' and '$[-2\ 1\ 0]_{Mg(OH)2}$: $[-2\ 1\ 0]_{Mg}$' are shown in blue and brown. For both combinations, the intensity ratio increase with treatment time. It indicates the thickening of the $Mg(OH)_2$ films with increasing heat treatment time and the subsequent reduction in Mg on the sample surface and an indirect way of measuring the film thickness without the requirement to section the sample.

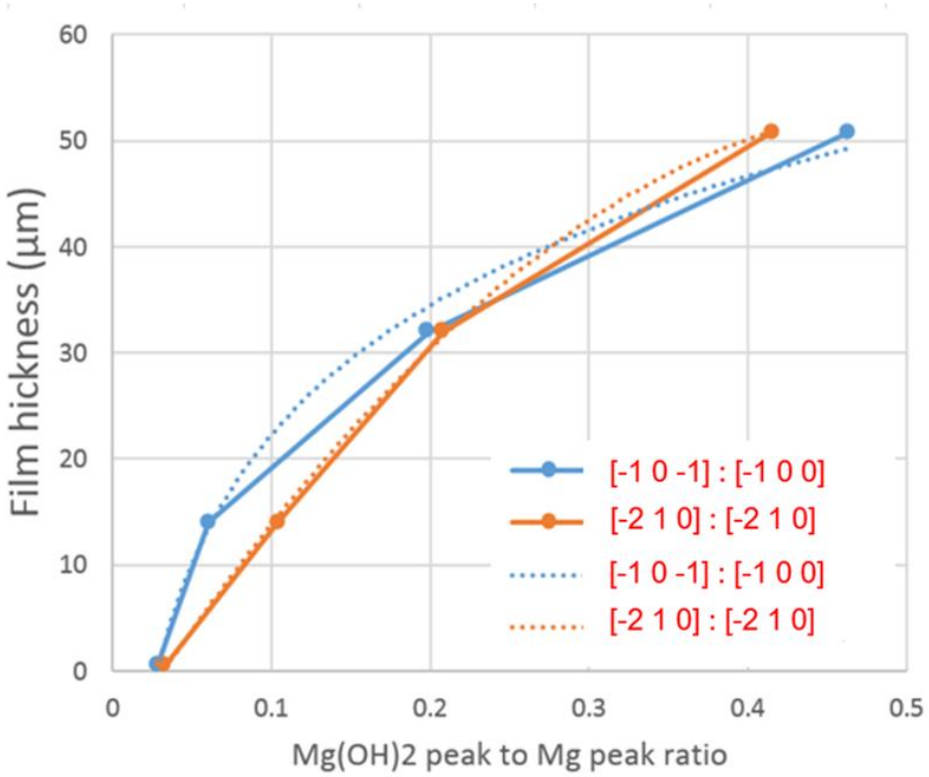

Figure 5.2.7, The relationship between the hydrothermal film thickness and the $Mg(OH)_2$ peak ratios in the XRD pattern

The thickness measured data on the cross-section were collected, and equations that express the relationship between film thickness and peak intensity ratios were fitted, (Equations 5-1 to 5-4). With this method, $Mg(OH)_2$ films above 5µm

can be evaluated. The accuracy of the estimation can be further improved by collecting more data.

$$\text{Thickness} = 17.6\ln(A) + 62.8 \quad (A) \qquad \textbf{(5-1)}$$

$$\text{Thickness}=-224.9B2+233.4xB-7.3(B) \qquad \textbf{(5-2)}$$

$$A = \text{intensity ratio of } [-10\text{-}1]Mg(OH)_2/[-100]Mg \qquad \textbf{(5-3)}$$

$$B=\text{intensity ratio of } [-210]Mg(OH)_2/[-210]Mg \qquad \textbf{(5-4)}$$

5.2.3 Comments on HT films

At 160 ºC, The hydrothermal film changes from gloss black/dark grey to light grey/yellow as treatment time increased. The colour change with time is due to the thickness increase and roughness of the film that alters the surface's light reflection. There is a much slower film growth kinetics at 120°C. It generates thin films with a gloss dark grey colour regardless of treatment time, which is only the same as the sample treated at 160ºC for 30min.

Therefore, the processing temperature is considered the primary influence factor for the $Mg(OH)_2$ film growth. The films thicken with time only at a higher processing temperature. This observation leads to the basis for developing the novel electrochemical and additive methods in the later sections.

Two types of pores-like features are observed. The first one is likely due to the presence of Al_xMn_y intermetallics. Al_xMn_y intermetallics act as cathodic sites and inhibit the reaction of Mg oxides to $Mg(OH)_2$. The other ‘open pores’ are more likely the natural gaps between films because they closed up when film further grows with time.

SEM cross-section images showed an adherent interface between the coating and substrate. The coatings have a layered structure. Cracks or voids are observed through the film at an interval of every 1 to 2µm. This feature is also observed but not reported in the literature [Ishizaki, 2013].

The most likely reason for the void is due to volume expansion. Mg and $Mg(OH)_2$ have densities of 1.738g/cm^3 and 2.39 g/cm^{3,} respectively, while the molar

masses are around 24 g/mol and 58g/mol. For every mol Mg to $Mg(OH)_2$, the volume increased from 13.8cm^2 to 24 cm^2. A 74% volume expansion on the sample surfaces when Mg transform to $Mg(OH)_2$. The film is likely bulking but under constrain stresses at interface horizontally. The schematic illustration is shown in Figure 5.2.8. Besides, the closure of the open-porous feature with processing time is also due to the bulking. Thermal expansion/contraction and hydrogen bubbles may also contribute to the lamination.

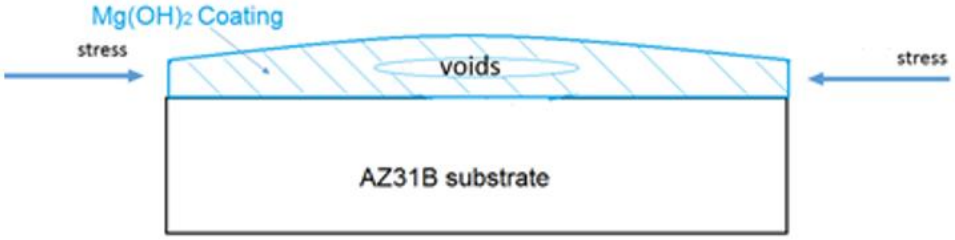

Figure 5.2.8. Schematic illustration of the formation of a void in the hydrothermal film.

The hydrothermal films in this work generally exhibit the same features compared to literature, such as the growth of films with scratch marks and bump rough features on the surface and laminate structures with cracks and voids at cross-section[Ishizaki, 2013]. The pores around Al_xMn_y intermetallics are not mentioned in the literature. They will be due to the differences between substrates. AZ31-GF substate in this work is found with less homogeneity and larger impurity contents that may aggravate local inhibition of $Mg(OH)_2$ formation.

A comparison of the film growth rates in this work with literature is shown in Figure 5.2.9. The film growth in this work is at an earlier starting point than reported in literature. It took over half of the time (1h) to reach 10 µm and a higher rate than reported by Zhu [Zhu, 2015]. For [Ishizaki,2013], has a slow growth rate 3 times slower. Between 4 to 6h, there was an increase in the rate reaching a maximum thickness near 70 µm in literature. In this work, film detachments were observed when the samples were HT treated for more than 3h (equivalent to > 50 µm). The differences in substrate and surface finishing could lead to different thickness limits. There are also possible differences in hydrothermal procedure and some

technical details such as the heat-up/cooling method which are not mentioned in the literature.

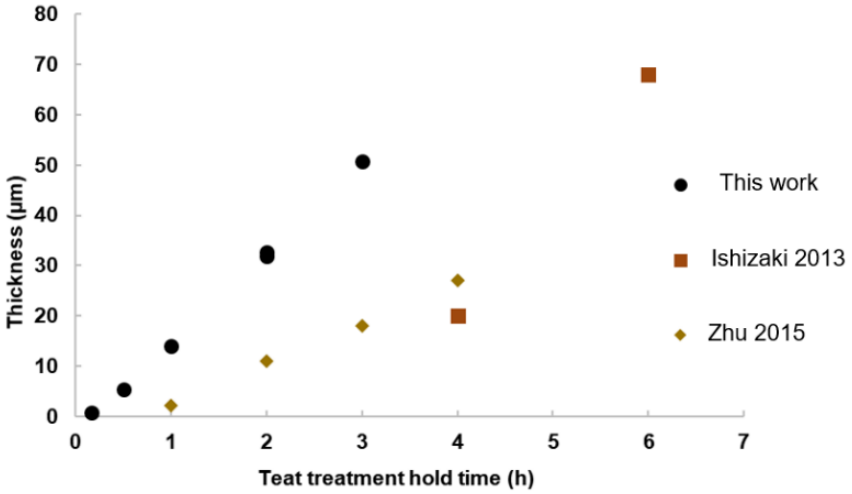

Figure 5.2.9 Comparison between literature and this work for the growth of hydrothermal films at 160 ºC

XRD was used to analyse the Hydrothermal film. The $Mg(OH)_2$ peaks can be identified when the film thickness is over 5µm. A relation between the film thickness and $Mg/Mg(OH)_2$ peak-intensity relationship is modelled. This XRD method may help predict the film thickness non-destructively if more data is received to improve its accuracy.

5.3 $Mg(OH)_2$ film by Electrochemical(EC) processing

5.3.1 Characterisation of EC film at RT

5.3.1.1 Surface View

Figure 5.3.1 shows photo images of the AZ31-GF surfaces following treatments with a range of applied currents at RT for 24h.

The sample started with a black/dark grey colour at the lowest current density, 42µA/cm^2. At 60µA/cm^2 the surface is metallic bronze. With a further increase in current density, the samples are covered with white particles, then fully covered as a film. The sample with white film contains $Mg(OH)_2$ in XRD.

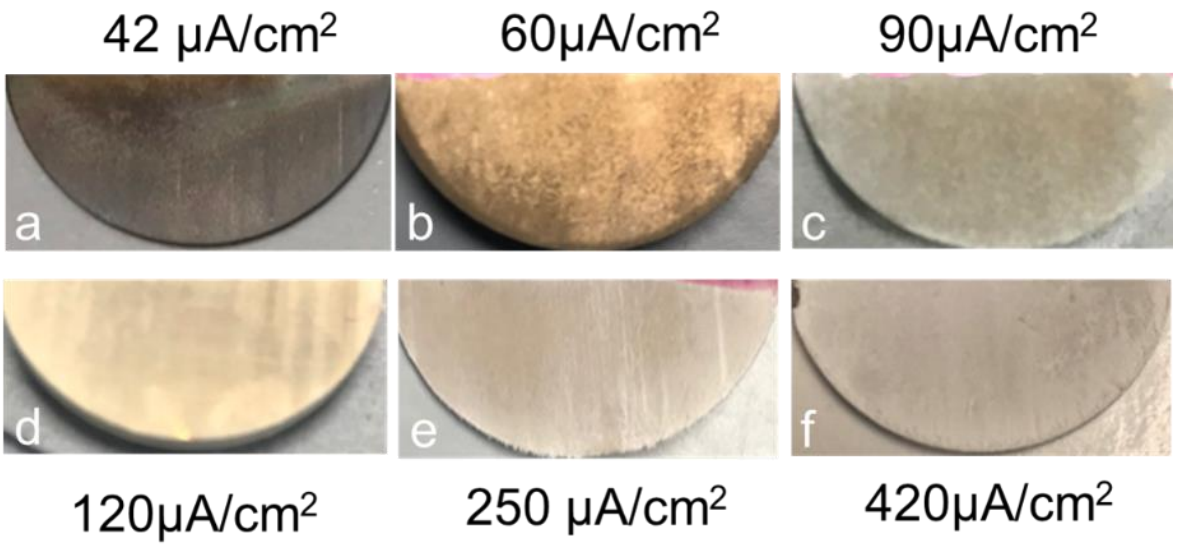

Figure 5.3.1. Photo images of the sample surface after electrochemical deposition in Mg^{2+} rich solution at RT for 24h.

Figure 5.3.2 and Figure 5.3.3 are SEM images of the EC treatment on AZ31-GF at RT. Figure 5.3.2 shows the sample after 42μA/cm^2 was applied. The surface is composed of platelet microfeatures in a perpendicular arrangement. The platelets' sizes are around 0.17μm in length and 0.035μm in thickness.

With the increase in the processing current density over 60μA/cm^2, additional flower-like clusters are observed attaching to the surface locally, shown in Figure 5.3.3. The flower-like clusters are also composed of interlocked platelets. It is similar to the feature on the base surface, but the platelet size at cluster is larger and thus a higher porosity level between platelets. A flower-like cluster has a size from 1μm to 5μm, but they can group agglomerates more than 50μm. The number and the coverage of the flower clusters increase with the applied current density, which indicates the white powder features in Figure 5.3.1 are the clusters.

XRD has confirmed the presence of $Mg(OH)_2$ for the EC samples with white powder layers at the peaks on the [-1 0 -1] and [-2 1 0] planes.

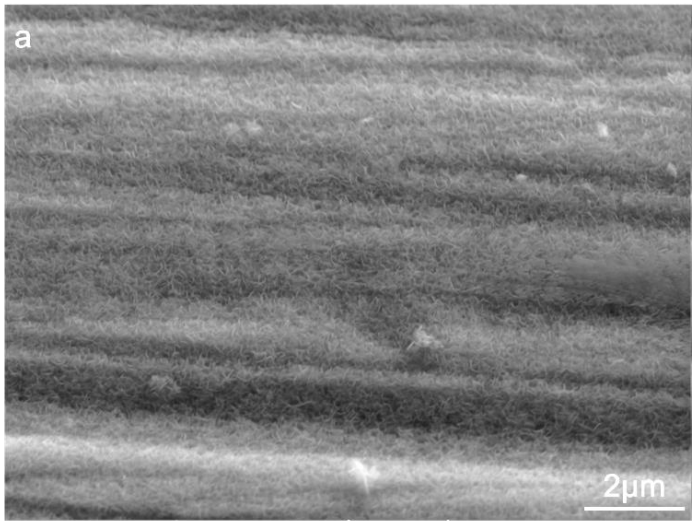

Figure 5.3.2. microstructure of the EC film with 42μA/cm^2 at RT for 24h

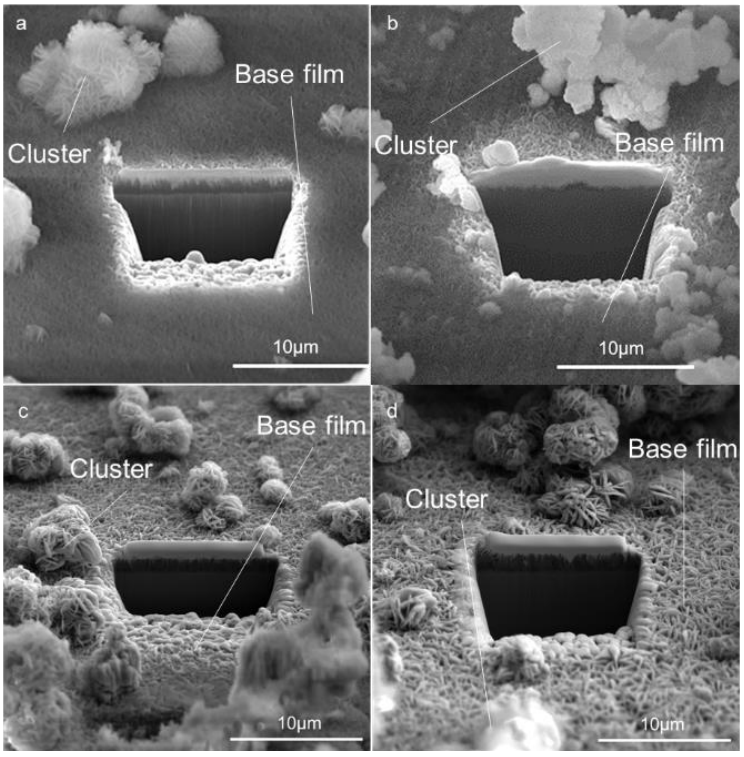

Figure 5.3.3. the SEM image of the EC film surface form at RT for 24h with a) 60μA/cm^2, b) 120μA/cm^2, c) 250 μA/cm^2 and 420 μA/cm^2.

The average sizes of the platelets at both base film and clusters are quantified and plotted against the processing current density, shown in Figure 5.3.4 and Figure 5.3.5, respectively.

The size of the platelets is influenced by the processing current density. When current density increases from 60 to 420 μA/cm^2, the length of the platelets

increases from 0.8x0.06 to 1.6x0.25 μm at cluster and 0.4x0.09 to 1.1x0.17μm at clusters. The platelets in the cluster usually have a larger size than the base film, and the thickening of the platelet at the cluster is sensitive to the increase in current density.

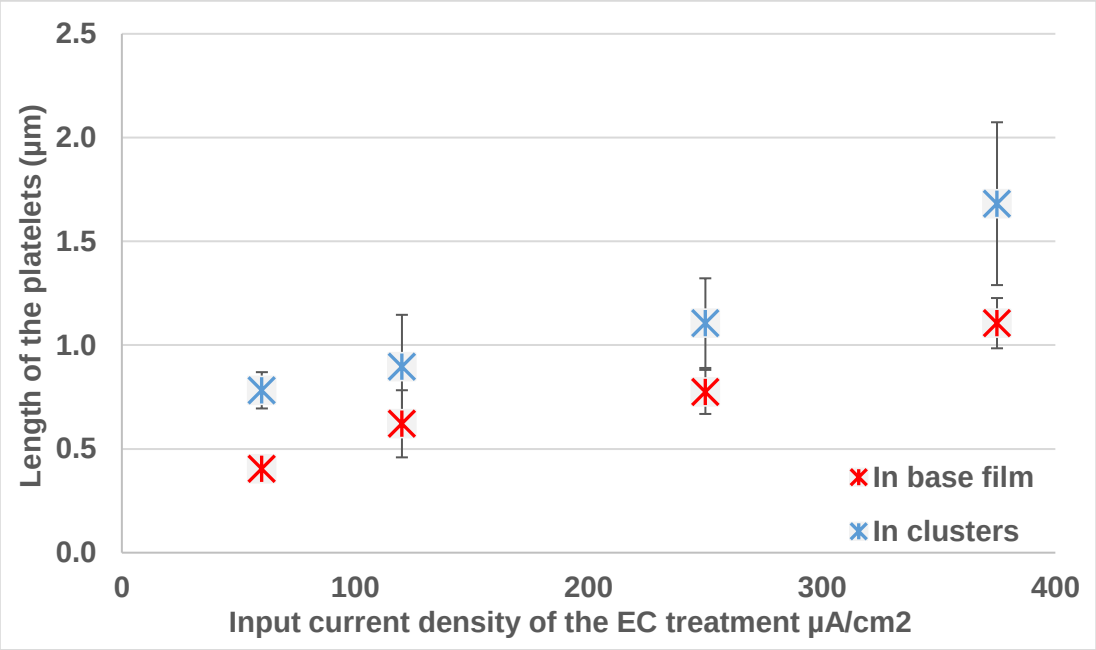

Figure 5.3.4. The average length of the platelets in the base film and cluster of the EC film at RT against the EC treatment current density.

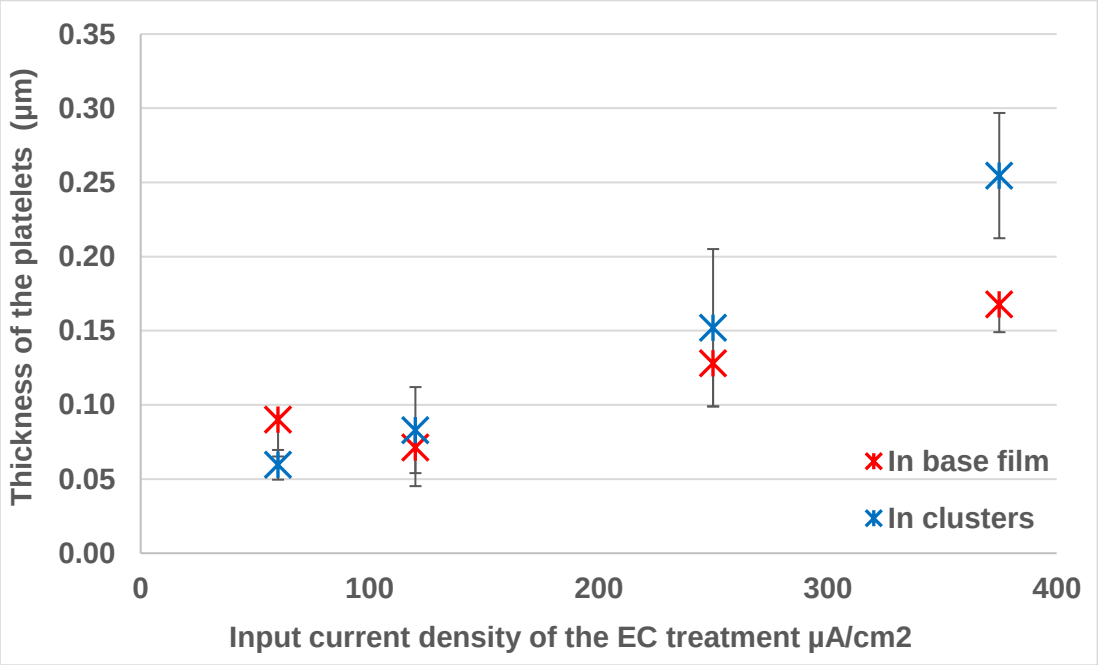

Figure 5.3.5. The average thickness of the platelets in the base film and cluster of the EC film at RT against the EC treatment current density.

5.3.1.2 Cross-sectional Characterisation

Figure 5.3.6 shows FIB cross-sections of the EC film at RT with the current density from 42 μA/cm^2 to 420μA/cm^2, Figures 5.3.6a to 5.3.6e indicate only base films corresponding to the images shown in 5.3.2 and 5.3.3., Outlined with red curves. Figure 5.3.6f shows the sample with 300 μA/cm^2. Differently, both base film and the layer of flower-like clusters are shown in Figure 5.3.6f. These two layers are separated with blue dot curves,

At 42 μA/cm^2, it produces a very thin film of 0.2μm; the film is relatively dense except for a few pores or voids on the top of the film. With an increase in the current density, the growth of crystals is observed. These crystals correspond to the cross-sections of the platelet features shown in the surface SEM (Figure 5.3.3). At 60 and 250 μA/cm^2, in Figures 5.3.6b and 5.3.6d, the film is around 1μm. Near the interface, the film is dense. Above the dense region, the crystals grow vertically and left Gaps or voids in between. The film with 420 μA/cm^2 exhibits a similar structure, except for a larger thickness around 3μm, Figure 5.3.6e. At 120 μA/cm^2, in Figure 5.3.6c, a denser near-interface region is also observed. However, the growth of the crystals is shorter and leads to a thinner film around 0.34μm. Figure 5.3.6f shows the FIB cross-section of the sample with 300μA/cm^2. A two-layer structure is observed. The boundary is indicated with a blue curve. Below the blue curve is the base film consists $Mg(OH)_2$ crystals vertically developed. The outer layer above the blue curve is the $Mg(OH)_2$ cluster layer. It is nucleated above the base film. Thus crystals grow in random orientations.

The film-substrate interface is uneven when the sample is processed with a lower current density, likely due to corrosion damage. On the other hand, the interface is more uneven and smoother with a higher treatment current density.

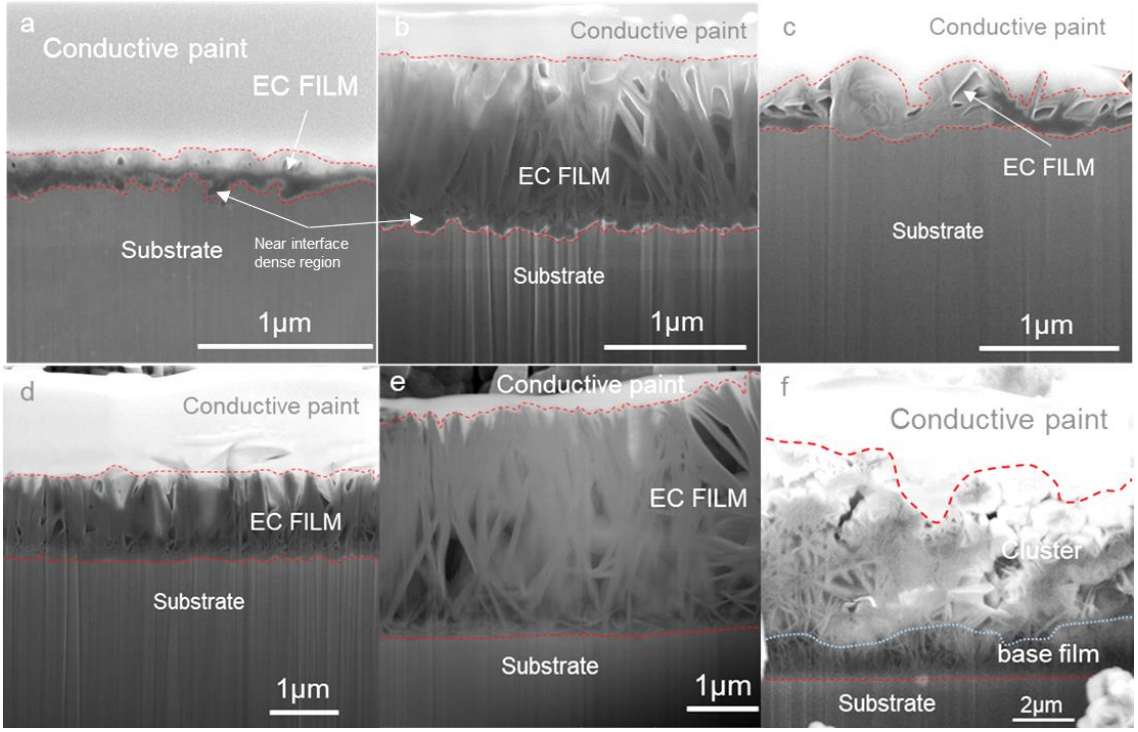

Figure 5.3.6. Electrochemical samples treated at 25°C for 24h with various current density of a) 42 μA/cm^2, b) 60 μA/cm^2, c) 120 μA/cm^2, d) 250 μA/cm^2, e) 420 μA/cm^2 and f) 300 μA/cm^2 (with cluster layer).

Based on Figure 5.3.6, the film thickness is measured and plotted against the EC current density in Figure 5.3.7. The base film thickness generally increases with an increase in the current density except for the sample with 60μA/cm^2. The sample with 300 μA/cm^2 has an additional 5 μm thickness due to the outer layer of clusters, indicated by the triangle shape in Figure 5.3.7.

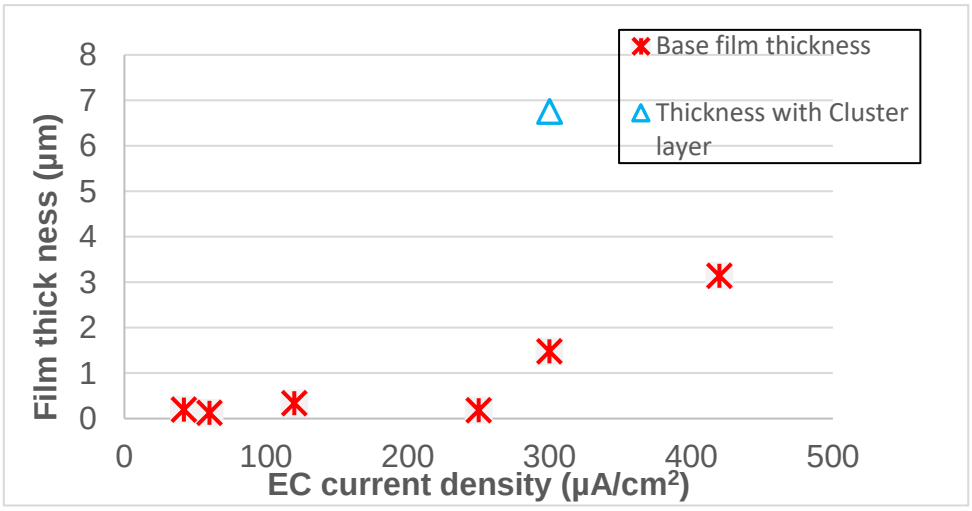

Figure 5.3.7. The EC film thickness by the FIB cross-section versus the respective applied current density at RT for 24h.

With the exponential fitting, the relationship between the base film thickness and current density is fitted exponentially and shown in Equation 5-5.

$$y = 0.2804e^{0.0059x} \quad \textbf{(5-5)}$$

5.3.2 Characterisation of EC film at 60°C

EC processing with a higher processing temperature of 60°C was applied to the AZ31-GF substrates. The photo image of the samples with 42 μA/cm^2 and 420 μA/cm^2 are shown in Figure 5.3.8. The samples at 60°C exhibit dark appearances with 42 μA/cm and are filmed with white layers with 420 μA/cm^2 which have similar trends to the sample at RT.

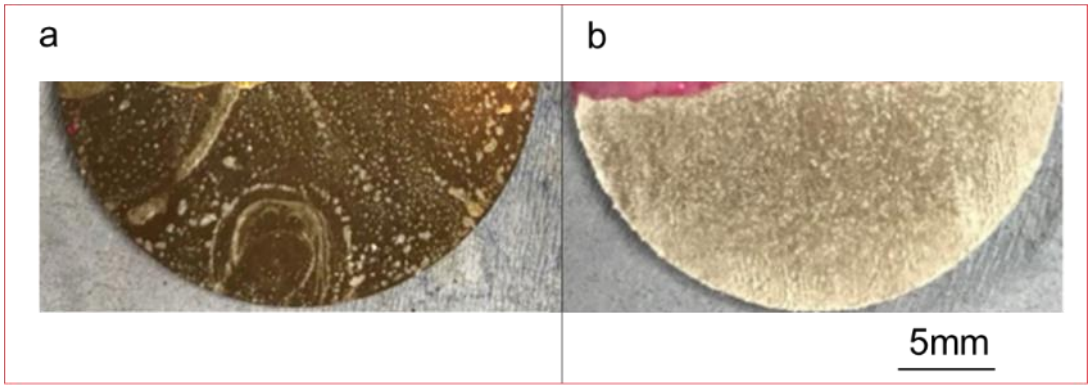

Figure 5.3.8. Photo images of the sample surface after electrochemical deposition in Mg^{2+} rich solution at RT for 24h a) 42μA/cm^2 and b) 420 μA/cm^2.

The SEM image of the EC sample surface and FIB cross-section with 42 μA/cm^2 and 420 μA/cm^2 at 60°C are shown in Figure 5.3.9 and Figure 5.3.10.

At 60°C, the sample surface is mostly covered with a base film of vertical platelets With 42 μA/cm^2, but both the base film and flower-like cluster layers are observed with 420 μA/cm^2. The size of the platelets at base with 42 μA/cm^2, is averaging 0.42x0.045μm, with 420 μA/cm^2 the platelet size is 1.9x0.29 μm at the base and 1.36x0.22 μm at clusters.

With the FIB cross-section, Figure 5.3.9b and Figure 5.3.10b, the platelets have irregular shapes. Platelets grow vertically with fine sizes in the middle but coarsened and curled at the top of the base film. The average base film thickness is around 0.79 μm and 1.5 μm for 42 μA/cm^2 and 420 μA/cm^2 respectively.

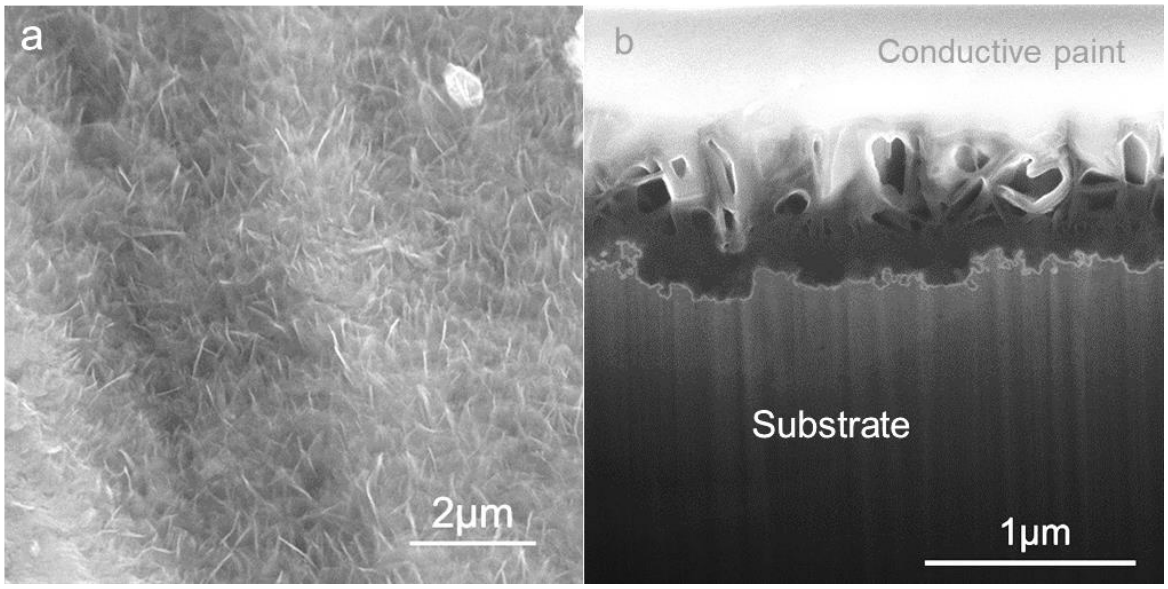

Figure 5.3.9. Microstructures of the EC film formed with 42μA/cm^2 at 60°C, a) on surface SEM and b) FIB cross-sectional image.

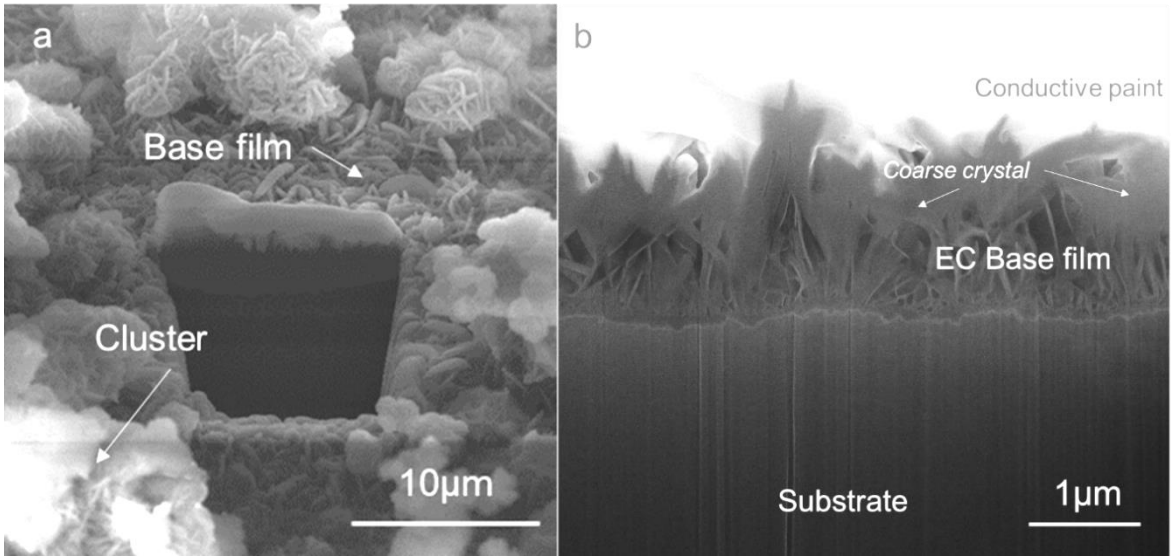

Figure 5.3.10. Microstructures of the EC film formed with 420μA/cm^2 at 60°C, a) on surface SEM and b) FIB cross-sectional image.

Compared to the crystal size at RT, An increase in temperature encourages platelets' growth, increasing the size of the platelet crystals. Furthermore, the higher processing temperature can significantly increase the amount of the surface layer. Figure 5.3.11 shows the mass gain of the sample by EC processing. It is plotted versus the current density at RT and 60°C. For both temperatures, the mass gain with processing current density at the same starting

points. However, the rate of mass gain at 60°C is around 3 times of RT. When processed with 420μA/cm^2, the mass change at 60°C is three times RT.

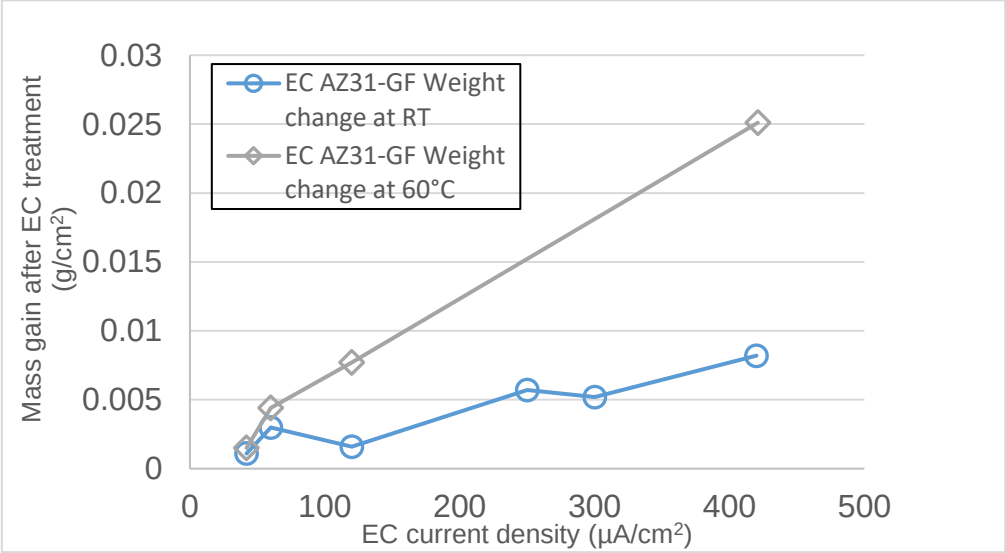

Figure 5.3.11. The mass gain of the AZ31-GF samples after EC treatment with various current densities at RT (circle) and 60°C (diamond).

5.3.3 Characterisation with polished film cross-sections.

FIB is typically used as a milling technique to cut cross-sections at the near-surface with depths upto about 5μm. In this research, most FIB images reveal the base film. When samples are processed using high current densities (e.g. 420μA/cm^2), a thick layer of the cluster formed in the order of tens of microns, alternative characterisation methods on the cross-section are required to view the coating.

Therefore, a polished cross-section was prepared and characterised with SEM.

5.3.3.1 AZ31-GF and AZ31-ME

Figure 5.3.13 shows the Mount-and-polished cross-section of the EC treated AZ31-GF at 60°C with 420μA/cm^2 with three magnifications. It exhibits a thick film composed of the agglomerates of the flower clusters with a rough surface profile. The thickness varies from 10 to 55μm. Horizontal and vertical cracks or gaps were also observed within the film, likely to be the boundaries between agglomerates.

EC treatment with another substrate, AZ31-ME were also applied. Its Mount-and-polished cross-section image, Figure 5.3.14, shows similar features as AZ31-ME.

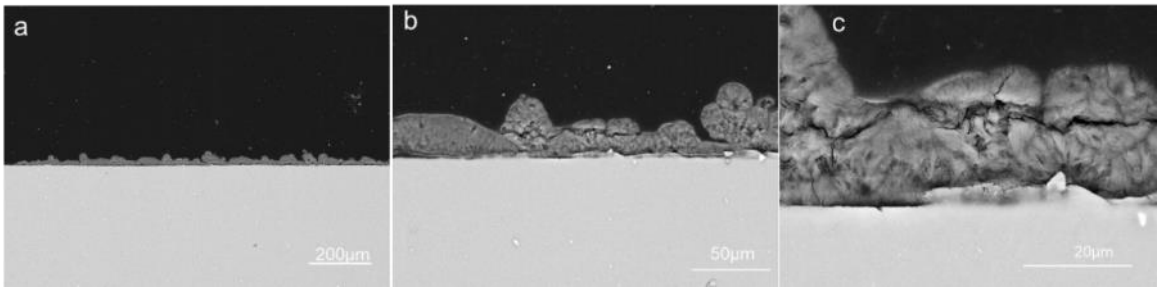

Figure 5.3.12. Mount-and-polished cross-section of the EC film formed on AZ31-GF with 420µA/cm^2 at 60°C for 24h.

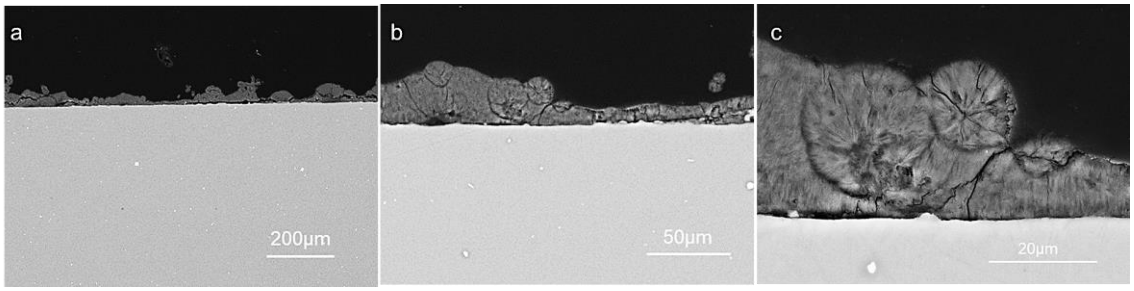

Figure 5.3.13. Mount-and-polished cross-section of the EC film formed on AZ31-ME with 420µA/cm^2 at 60°C for 24h.

When the applied current density further increases to 800µA/cm^2, discontinued films are formed, and the flower-like clusters and their agglomerates are likely to detach. It is observed on both AZ31 substrates, shown in Figure 5.3.15 and Figure 5.3.16,

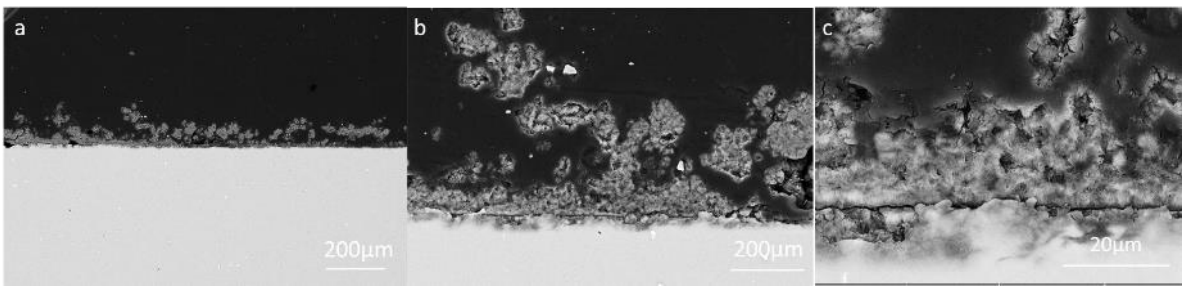

Figure 5.3.14. Mount-and-polished cross-section of the EC film formed on AZ31-GF with 800µA/cm2 at 60°C for 24h.

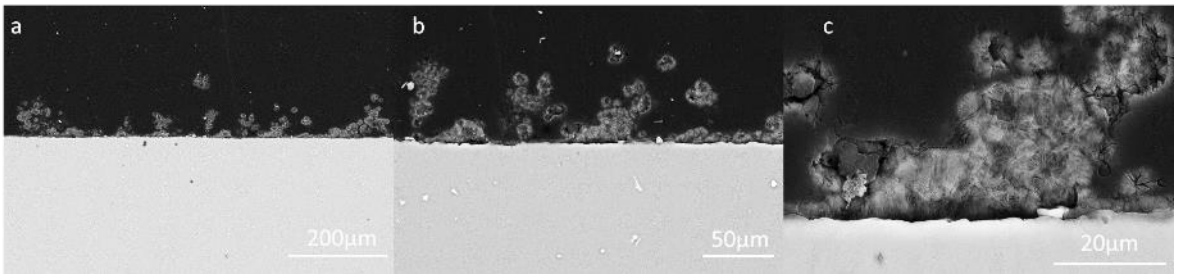

Figure 5.3.15 Mount-and-polished cross-section of the EC film formed on AZ31-ME with 800µA/cm2 at 60°C for 24h.

5.3.3.2 ZM21

EC treatments were also applied to the ZM21-ME substrate. The processing parameters are EC treatment with 420µA/cm^2 at 60°C for 24h

The SEM cross-sections for three different magnifications are shown in Figure 5.3.16. A continuous but rough film profile was also observed like the films on AZ31 substrates. The thickness varies from 10 to 60 µm due to the roughness, and the average value is around 35µm. The film contains crystals with various morphology depending on their distance to the interface. Near the interface, the crystals (platelet-like) are in an array vertically orientated. Particles were observed embedded at the interface. The crystals became randomly orientated at the top. Beach-mark features were observed across the crystals. In general, the EC+additive film has a similar morphology to the EC films on AZ31 substrates shown in Figure 5.3.12 and Figure 5.3.13 except for a larger thickness and the presence of the beach-marks features.

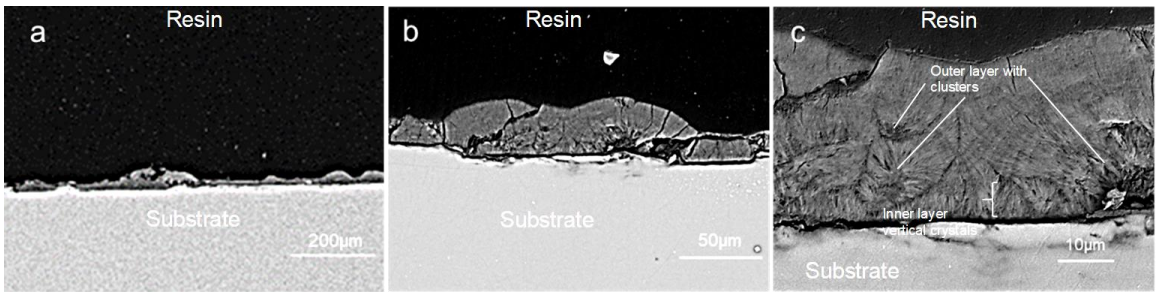

Figure 5.3.16 Cross-section of ZM21-ME sample with EC treatment only with various magnifications.

EDX analysed the composition of the EC film cross-sections on ZM21-ME. Shown in Figure 5.3.17 and Table 5.3.1 for locations with various distances to

the substrates. It has been confirmed that Mg and O are the major elements of the film. However, the Mg to O ratio is not commensurate to $Mg(OH)_2$. The proportion of O is higher near the interface. As Si is also detected, the particles embedded at the interface can be the polishing debris of colloidal silica (SiO_2) that increase O content.

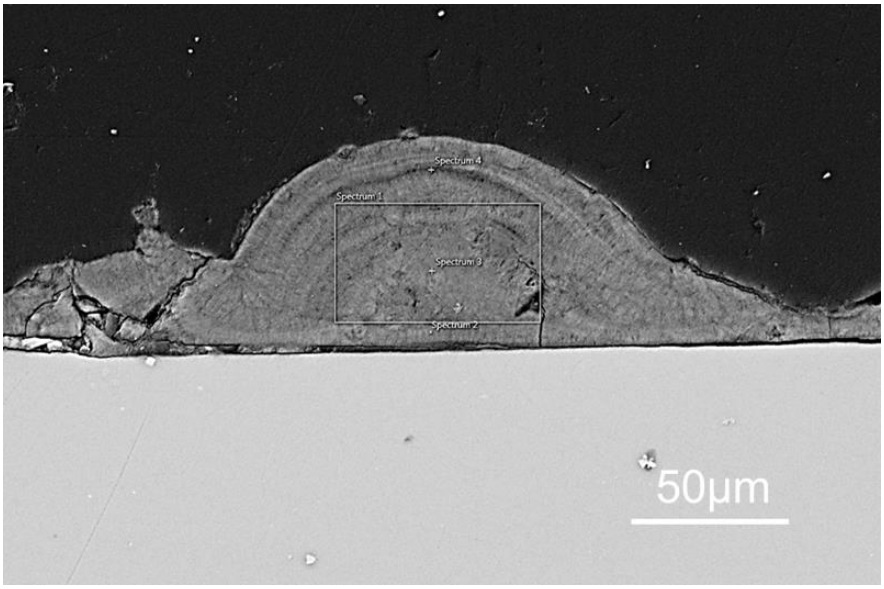

Figure 5.3.17 Cross-section of ZM21-ME sample with EC treatment only with EDX measurements.

Table 5.3.1 Compositional EDX point analysis results for the cross-section of the ZM21-ME sample with EC treatment only.

atm%/Wt%/	O	Mg	Si	Ca	Zn
Spectrum 1 (overall)	71.70 (61.76)	22.63 (29.62)	5.65 (8.53)	0	0.03 (0.09)
Spectrum 2 (near interface)	71.52 (61.46)	22.20 (28.99)	6.23 (9.40)	0	0.04 (0.16)
Spectrum 3 (middle)	68.87 (58.77)	27.09 (35.12)	3.99 (5.97)	0.07 (0.04)	0.02 (0.08)
Spectrum 4 (near surface)	41.41 (31.42)	54.07 (62.32)	4.38 (5.83)	0	0.44 (0.14)

5.3.4 Comments on EC films

The electrochemical sample contains a base film with an array of vertical platelet structures and an additional outer layer of flower-like clusters if the current density is high (>60μA/cm^2, RT). Although both layers are primarily composed of platelets crystals, their size and orientation vary due to the nucleation at different positions. For the base film, $Mg(OH)_2$ crystals nucleate at the substrate surface where the growth is constrained. Only vertical growth is preferred. On the other hand, the cluster can nucleate at a distance away from the substrate surface. It allows larger space for coarsening and a higher degree of freedom to grow with random orientations.

Previous cross-sectional images show that the base film is only one row of platelets (vertically). The base film is considered with a thickness limited by the length of a platelet. Differently, although a single cluster also has a limited size, the cluster can pile up to a thicker outer layer

At 60°C, the platelet crystal is coarsened, which increases the size of clusters, thus the overall thickness. Furthermore, coarsening of platelet crystals may also increase the density of the film. As platelets are thickened, the pores and voids between them are filled. Therefore, with a 420μA/cm^2 current density at 60°C, it produces a thick and/or denser film that is three-time mass at RT.

The EC film contains pores or other line defects so that polishing debris embeds in the films. These defects are likely due to the gaps between the base films and agglomerates, therefore, trapped debris near the interface.

EC film is mainly formed by the electrochemical deposition of the Mg ions in the electrolyte. The Mg Alloy substrate (working electrode) is negatively charged. Cathodic half-reaction occurred where water molecules are reduced to hydrogen gas and hydroxide anions (OH^-) in the electrolyte that Mg^{2+} and OH^- ions are already saturated. Over-saturation leads to $Mg(OH)_2$ compounds precipitating on the substrate surface.

Besides, corrosion product $Mg(OH)_2$ can also be produced into the EC film as the secondary mechanism.

According to the Pourbaix diagram adapt from Figure 2.3.3 [Pourbaix, 1974], shown in Figure 5.3.18. There are corrosion, passivation, and immune regions. The boundary between the corrosion region and passive region is a pH value, and the boundary between immunity and corrosion is at a certain potential. Both boundaries vary by the concentration of Mg^{2+} orders of magnitude.

In this work, the Mg^{2+} concentration of the electrolyte is equal to the solubility ($1.34x10^{-4}$ M) at RT with a pH of around 10.5. The samples are just at the boundary between the corrosion and passivation region. Figure 5.3.19 shows the average correspondent potential to the applied current density during the EC processing. Most samples are not immune except 420μA/cm^2 at RT. Therefore, corrosion reaction also happens to EC samples but is partially mitigated by the cathodic current. When the current density is low, 42μA/cm^2, a dark grey surface of the corrosion product is processed.

With an input current density of 800μm/cm^2, the substrate is likely fully immune. Its surface can be too clean for nucleation of a base film, causing a poor interface and the detachment of cluster layers.

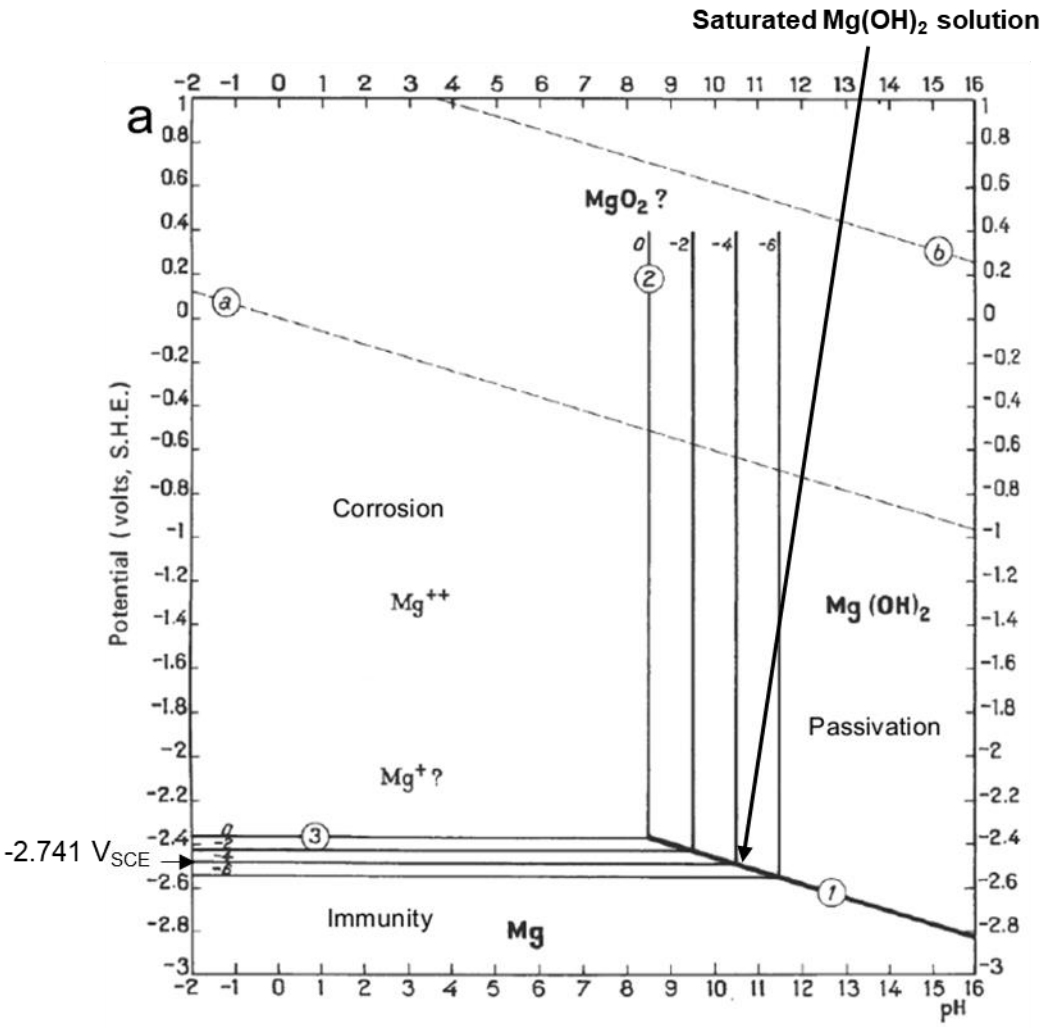

Figure 5.3.18. Adapted Pourbaix diagram [Pourbaix, 1974] that indicated the pH value and the boundary between Immunity and corrosion zones in the EC processing environment

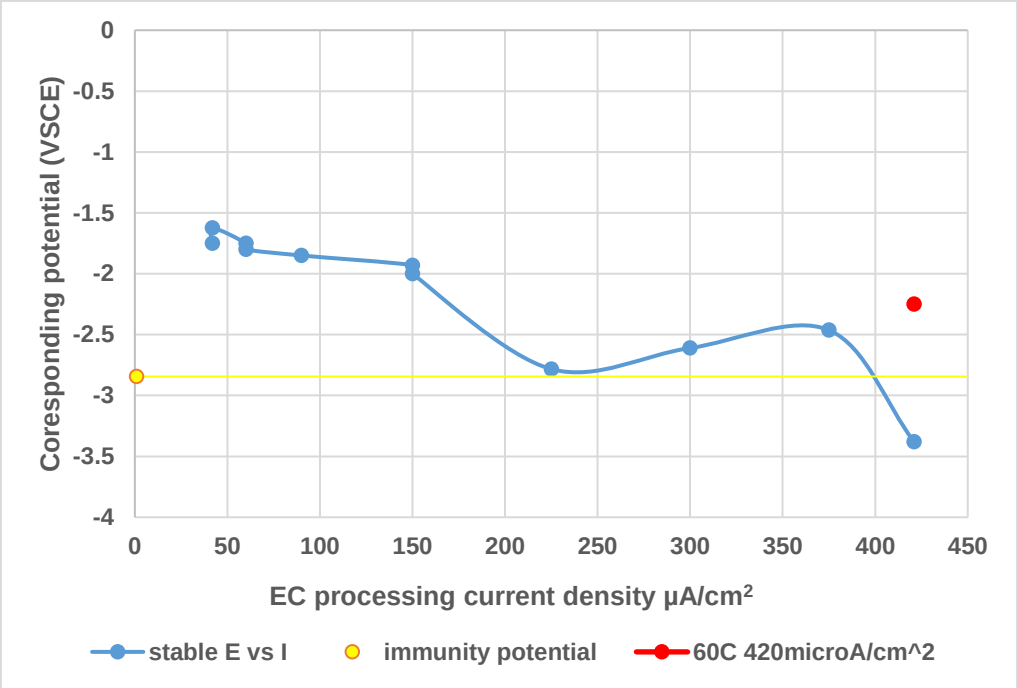

Figure 5.3.19, Voltage against current density plot. -2.7 V_{SCE} is the critical potential between Mg immune (no corrosion product film but just powdered $Mg(OH)_2$ film) and passivation (forming $Mg(OH)_2$ coating)

5.4 Additive Film of $Mg(OH)_2$

In this section, the additive method of applying $Mg(OH)_2$ films to Mg alloy substrates is investigated. It firstly investigated the additive process directly applied to the alloy substrate (Direct-additive). Then it studied the combination of the additive process after the EC processing (EC + additive). Various additive processing temperatures, from 60 to 240°C, are studied. The additive films are characterised both on surface and cross-section. The chemical composition is checked with EDX and XRD mapping.

5.4.1 Direct additive film

Figure 5.4.1 shows photo images and optical microscopy of the direct additive film formed on bare AZ31-GF substrate at 60ºC, 100ºC and 160ºC. White and light grey films are observed in the photo images. In optical microscopy, Figure 5.4.1d to f, the sample is covered with angular agglomerates (dark features) confirmed as $Mg(OH)_2$ by EDX and bright features. Bright regions are the exposed substrate surfaces without coatings.

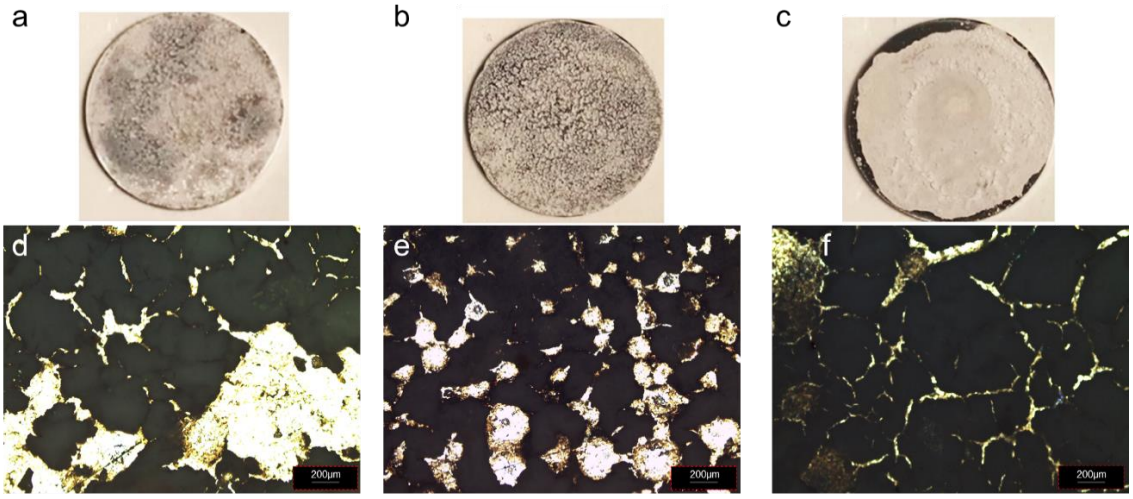

Figure 5.4.1 Images and optical microstructure of the additive layer with different processing temperatures.

At 60ºC, Figure 5.4.1d, a large area of the metal surface, around 30%, is exposed. The $Mg(OH)_2$ agglomerates have less exposed metallic surface around 15% at 100 ºC. At 160ºC, in Figure 5.4.1c, the surface film is more coherent. The metallic surface is only exposed at fine boundaries between agglomerates. Coverage is further increased to around 95%.

Figure 5.4.2 compares the SEM cross-sections of the direct additive film formed at 60 and 160 ºC. At 60ºC, Figure 5.4.2a, the film exhibits irregular morphology. Large pores are observed at the interface. Vertical cracks developed throughout the film, from the interface to the top.

Figure 5.4.2b shows the cross-section of the direct additive sample treated at 160ºC from the uncoated surface. The film has a thicker thickness which varies along the cross-section with a range between 40 to 100µm. This film is mainly the agglomerate of spherical features with a few microns in diameter. Larger angular flake features are embedded.

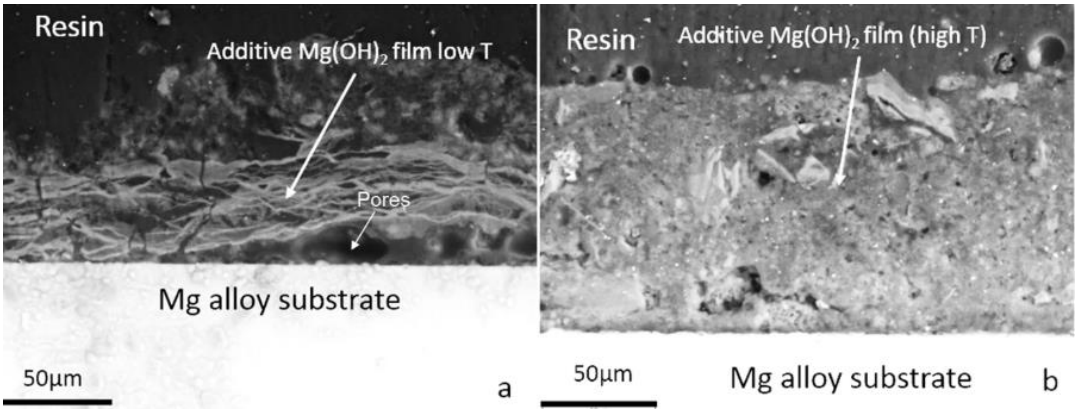

Figure 5.4.2 the SEM cross-section of the direct additive film formed at a) 60ºC and b) 160ºC.

The direct additive $Mg(OH)_2$ film has poor adherence to the substrate. Cracked films can be easily detached, especially at the lower temperature, 60 and 100 ºC.

5.4.2 EC + additive film

5.4.2.1 Surface Characterisation

Figure 5.4.3 shows the optical microscopy image of an EC + additive sample surface (EC processing with 420µA/cm^2 at 60ºC followed by additive processing at 160ºC). Instead of the angular agglomerate, the EC + additive film is composed of round clusters. An agglomerate has a size between 80 and 200µm, which is smaller than in the direct-applied additive films shown in Figure 5.4.1f. The film is confirmed as $Mg(OH)_2$ with XRD

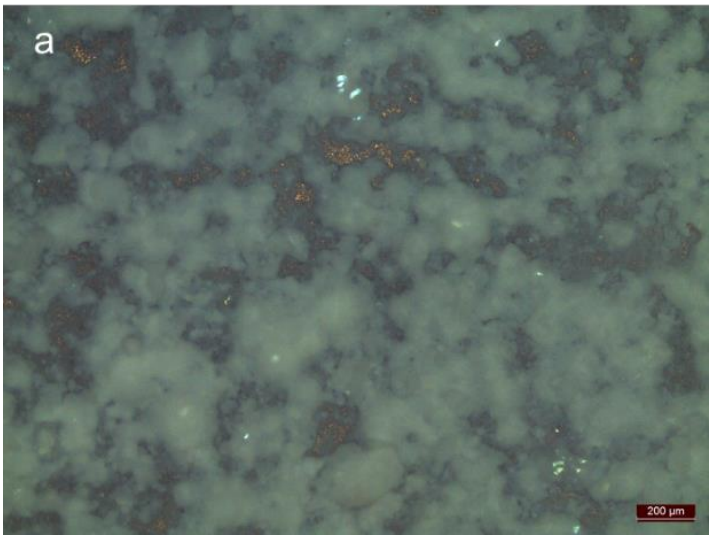

Figure 5.4.3.The optical microstructure of an EC + additive sample surface with EC pre-treatment with 420µA/cm^2 at 60°C plus additive processing at 160°C

Figure 5.4.4 shows the microstructures of the additive samples with/without the EC pre-treatment (420µA/cm^2 at 60°C) by SEM images in three magnifications.

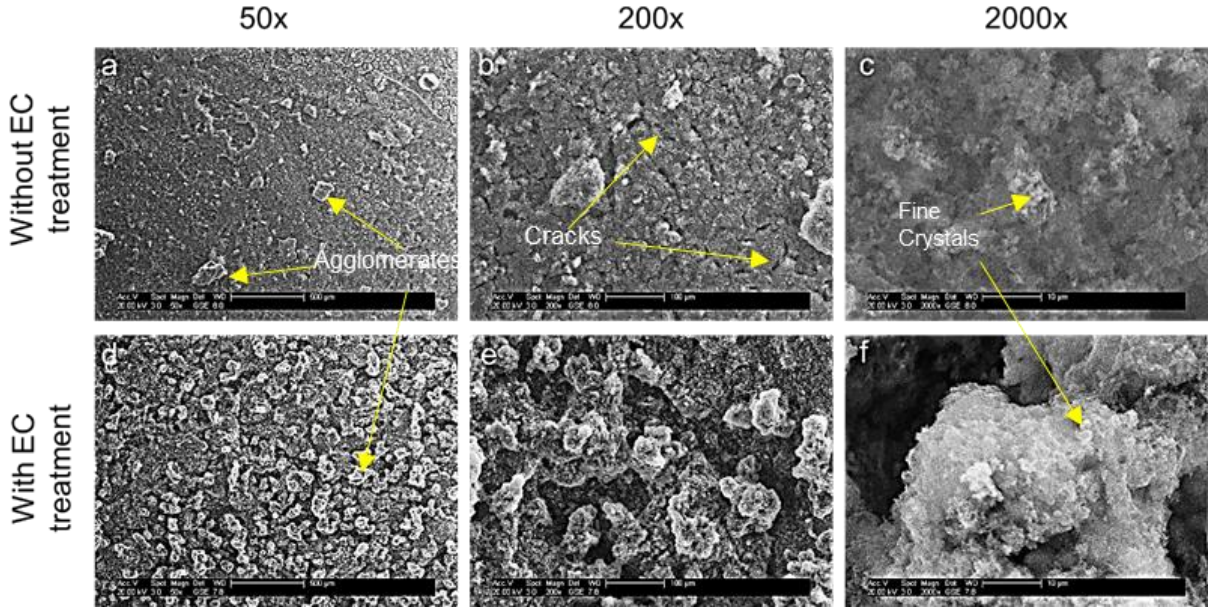

Figure 5.4.4, The surface microstructure (SEM) of, a-c), the direct additive film formed at 160°C with 50x, 200x and 2000x magnification respectively; d-f), the EC+Additive film with electrochemical treatment (420µA/cm^2 at 60°C) plus additive post-treatment at 160°C with 50x, 200x and 2000x magnification.

The sample without EC treatment has a relatively flat surface. Angular agglomerates and the gaps in between are also observed. Behind the crack is the metallic substrate, but it is not as obvious as the optical images.

For the sample with EC pre-treatment, Figure 5.4.4 d, e and f, the film is mostly covered with the round agglomerates. Rather than line-shape gaps, the EC+Additive sample is likely to have pores between agglomerates. The piles of agglomerates and the surrounding pores result in a rough profile of the film surface. With 2000x magnitude, It shows the agglomerates are composed of crystals less than 1 µm, shown in Figure 5.4.4 c and 5.4.4 f.

5.4.2.2 The EC + additive film cross-section with temperatures

Figure 5.4.5 shows the cross-section of the EC + additive sample. The average thickness is around 80µm. This film contains two layers: an inner layer with vertical crystals and a beach−mark−like outer layer.

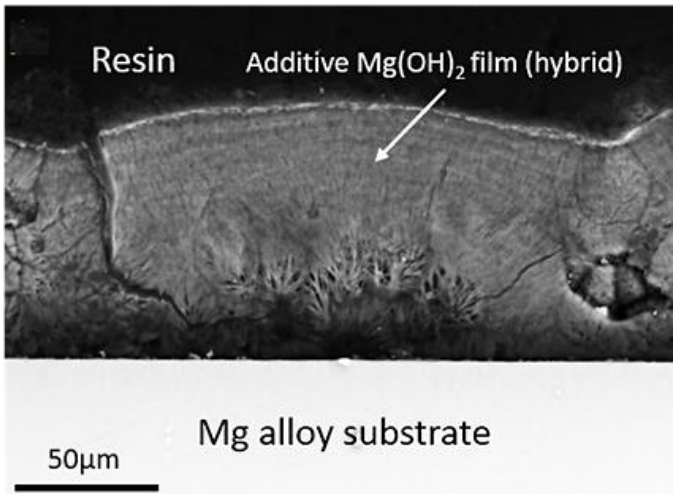

Figure 5.4.5, The SEM microstructure of an EC + additive sample cross-section with electrochemical pre-treatment with 420µA/cm^2 at 60°C plus additive processing at 160°C.

Cracks are observed through the film thickness. The cracks are likely due to the larger density and thermal expansion rate of the $Mg(OH)_2$, explained previously.

Apart from the 160°C, higher additive processing temperatures were further applied to the EC + additive samples to optimise the film property. The processing temperatures are increased up to 240°C. It is the maximum applicable processing temperature for this project and the author thinks compositional properties of the substrate are less likely to be altered below this temperature. Details about the limitation of the processing temperature are discussed in section 5.4.4.

Figure 5.4.6 shows the typical SEM cross-sections of the EC + additive sample with the additive temperatures of 160°C, 200°C and 240°C (EC pre-treated with 420µA/cm^2 at 60°C). SEM images at magnifications 200x and 1000x are shown.

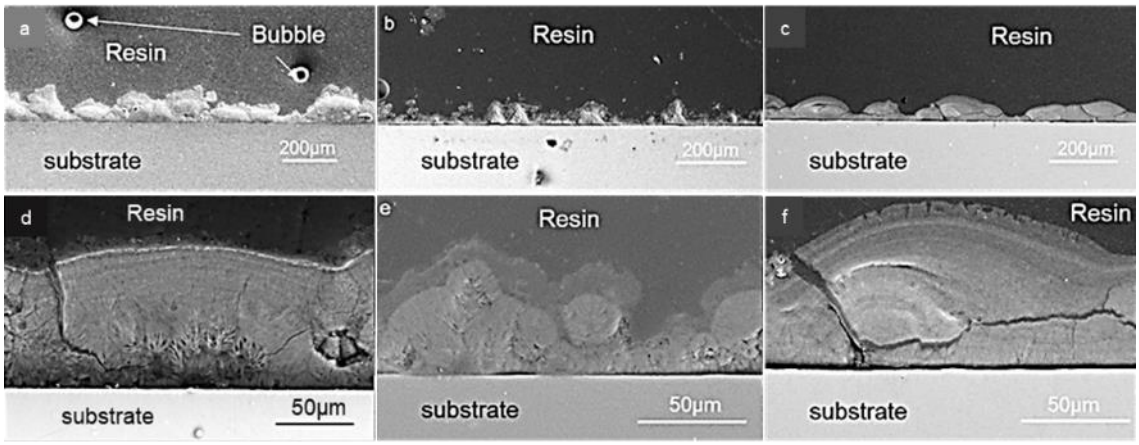

Figure 5.4.6. The cross-section of the EC + additive samples with the additive process for AZ31-GF at a) 160°C, b)200°C, and c)240°C respectively.

Generally, rough film profiles were observed on all samples. The EC + additive Films processed at 160°C is shown in Figure 5.4.6 a and 5.4.6 f. The film has a sharp and angular profile with higher film thickness. The sample processed at 200°C has a lower average thickness. The film is mainly composed of spherical agglomerates with fine porosity. Gaps are observed between agglomerates. At 240°C, the profile of the film is smoother than the sample at the other two temperatures. With higher magnifications, it shows the film is more compact and exhibits the beach-mark morphology. Long cracks are observed both along and vertical to the films.

Figure 5.4.7 shows the film thickness measurement throughout the EC + additive sample cross-sections formed at 160°C, 200 and 240°C respectively with the Image Analyser. The film thicknesses are in a cumulative probability (CP) distribution. Cumulative probability refers to the likelihood that the value of a random variable is within a given range

It shows the film thickness at 50% probability are 65, 60 and 50µm respectively.

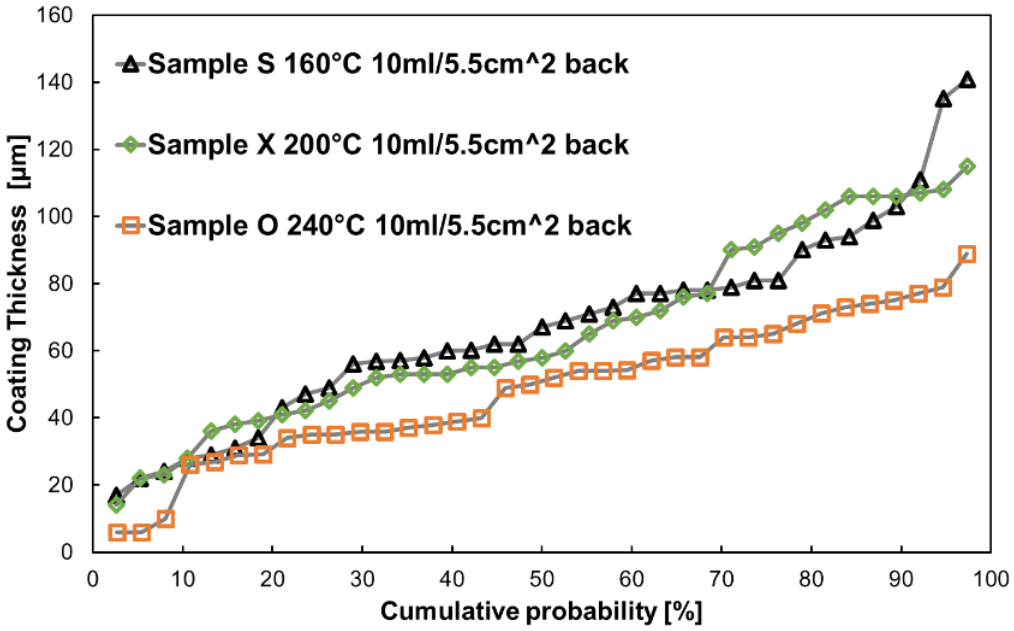

Figure 5.4.7 The cumulative probability distribution of the film thickness of the EC + additive samples formed at 240, 200 and 160°C.

5.4.3 Additive films on ZM21

EC + Additive treatments were also applied to ZM21-ME substrate. The processing parameters are EC treatment with 420µA/cm^2 at 60°C for 24h followed by the additive treatment at 240°C.

With Additive processing at 240°C after EC treatment, a thicker film is obtained with thickness from 60 to 300µm. The SEM cross-sections are shown in Figure 5.4.9 and 5.4.10 for different locations and magnifications. The film has a rough profile. Within the film, It consists of benchmark morphology horizontally. Cracks and voids are in the film, located either along or cleave through the 'benchmark. In Figure 5.4.9, round agglomerates or clusters are observed only at the top of the film surfaces. They have flower-like morphology consisting of fine platelet crystals with random orientation, similar to those observed in the films with only EC treatment in chapter 5.3.

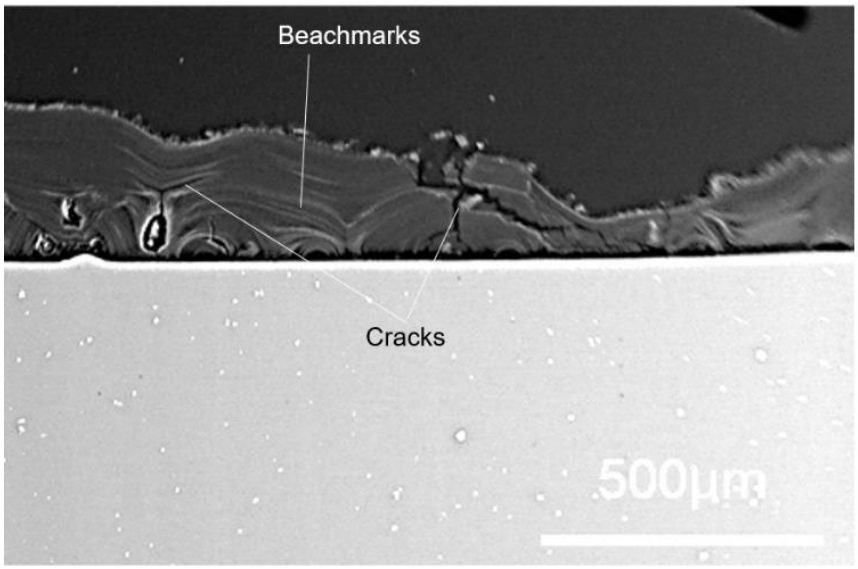

Figure 5.4.8. Cross-section of ZM21-ME sample with EC+additive treatment.

EDX analysed the composition of the EC+Additive film cross-sections on ZM21, shown in Figure 5.4.10 and Table 5.4.1, for locations with various distances to the substrates. It confirmed that Mg and O are the major elements for the film except for a small amount of Al detected near the interface, possibly contamination or alloy elements. The Mg to O ratio is around 3:1, which is even higher than in the previous film with just EC treatment. The Mg content of the film increase near the interface, which is the opposite of the sample film with just EC treatment. It indicates the branch marks morphology is denser than agglomerates of platelets. The gaps and porosity between platelets are likely to trap debris.

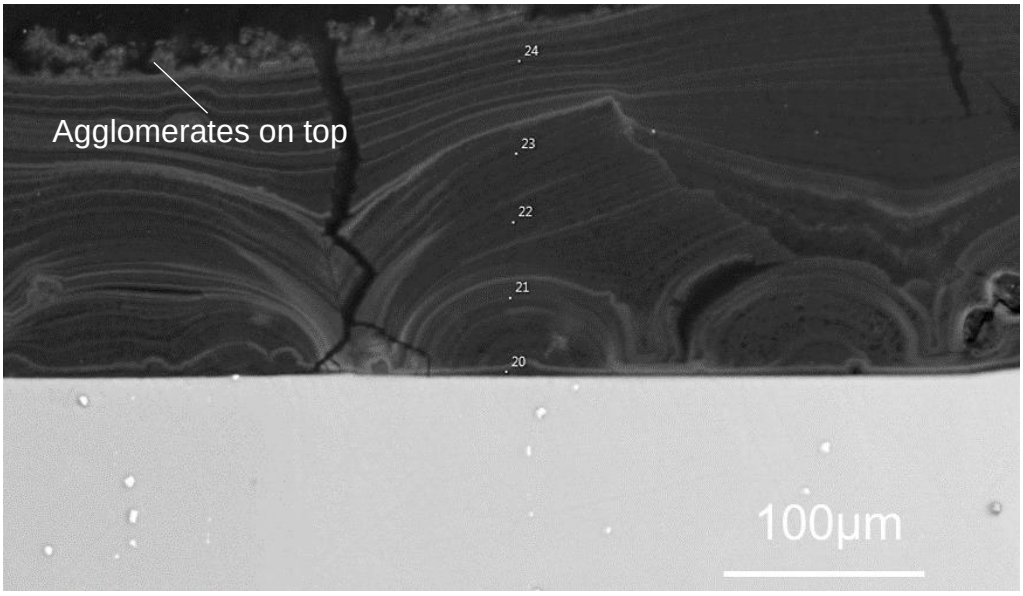

Figure 5.4.9. Cross-section of ZM21-ME sample with EC+additive treatment with EDX measurements.

Table 5.4.1 Compositional EDX point analysis results for the cross-section of ZM21-ME sample with EC +additive treatment.

Wt%(atm%)	O	Mg	Al
Spectrum 20	66.32 (74.97)	33.41 (24.85)	0.26 (0.17)
Spectrum 21	71.90 (79.54)	28.10 (20.46)	0
Spectrum 22	77.67 (84.10)	22.33 (15.90)	0
Spectrum 23	75.14 (82.11)	24.86 (17.89)	0
Spectrum 24	72.55 (80.08)	27.45(19.92)	0

Near interface

Near surface

5.4.4 Comments on $Mg(OH)_2$ Coatings

A combination of EC processing and Additive processing produced a thicker and denser film than only EC processing or Additive processing.

Figure 5.4.10 compares the contact angle of the Mg^{2+} rich solution drops on the uncoated and EC pre-treated samples. Solution drop stayed on the metallic surface with contact angles around 65°C but was spread/absorbed by EC film.

Observation of droplets on the surface shows that the presence of the EC film changes the wetting behaviour. Without the EC film, an aqueous solution with Mg ions runs off the surface. The wetting behaviour changes once the EC film has been deposited, and it is easier for the solution to remain on the surface. While no wetting study has been conducted, the hydrophilic nature of the surface is modified by the coating and presumably the surface energy.

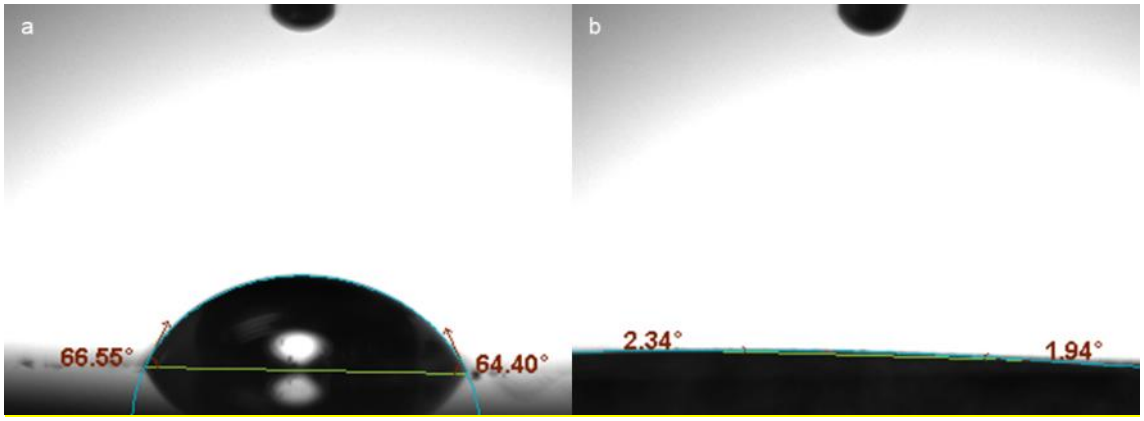

Figure 5.4.10. Contact angle measurement of the Mg^{2+} rich solution on the a) Uncoated surface and EC treated surface (420μA/cm², 60°C) of AZ31-GF substrate.

The additive process not only increases the average film thickness but also densifies the film. The additive processing is at a higher temperature, which leads to further coarsening of the $Mg(OH)_2$ crystal. Pores and voids between crystals and clusters closed up as crystals grow, thus densifying the film. The film is in the beach-mark morphology that is likely to be the coarsen crystals. It has a horizontal orientation at the top, similar to the laminar structure of a hydrothermal film.

The proportion of the benchmark features increases as the Additive temperature increase. At 160°C and 200°C, platelet crystals are still observed near the interface or at the core of a cluster, but only benchmarks are observed at 240°C.

In this study, the maximum temperatures are limited to 240°C due to the maximum working temperature of the masking tape. According to [ASTM B661-12, 2020], 260ºC is the lowest threshold of the heat treatment window for all AZ series alloys, and 300ºC is the lowest threshold of the heat treatment window for extruded AZ31 alloy [ASTM B661-12, 2020]. In other words, above these temperatures may alter the intrinsic property of the alloy substrate. Additive processing should not be over this limit.

Cracks at 240°C are observed. Unlike the pores or voids observed in EC film. The cracks for EC+Additive are more likely due to the brittleness of the film and the intrinsic volume difference between Mg and $Mg(OH)_2$, which is similar to the hydrothermal film and explained in 5.2.3.

Compare to the films on AZ31-GF, the EC+Additive Film on AZ31-ME is thinner. The inner layer near the interface is soft or porous, which can trap particles

5.5 Summary

Three approaches to applying $Mg(OH)_2$ based film on Mg alloy substrates were investigated. Hydrothermal, electrochemical, and Additive samples were characterised. The key results, including the thickness, key processing parameters, morphology, defects and interface, are listed in Table 5.4.2.

Table 5.5.1Summary of the characterisation of $Mg(OH)_2$ films

	Hydrothermal (HT)	Electrochemical(EC)	Additive (EC-pretreated)
Substrates	AZ31-GF	• AZ31-GF • AZ31-ME • ZM21	• AZ31-GF • AZ31-ME • ZM21
Film thickness	< 50µm	<35µm	<200µm
Key processing parameters	• Temperature (primary) • Time	• Current density (primary) • Temperature • Time	• Temperature (primary)
Morphology	• Lateral Laminar structure	• Array or cluster of platelet crystals	• Array or Cluster of platelets. • Beach mark crystals
Defects	Voids between layers	• Fine Pores between crystals • Voids between clusters	• Voids between layers • Brittle cracks
Interface	Coherent and strong interface	Pores or voids at interfaces	• Pores or voids at interfaces (lower T) • Coherent (High T)

6 Corrosion assessment for Mg alloy AZ31 substrate and its samples with $Mg(OH)_2$ films

6.1 Introduction

This chapter reviews the corrosion behaviour of AZ31 in a quiescent saltwater environment (3.5% NaCl) with and without Mg(OH)2 films.

Section 6.2 presents and discusses the corrosion behaviour results for two commercial sources of AZ31 alloy: AZ31-GF and AZ31-ME. Corrosion tests were applied in 3.5^{wt}% NaCl solution for both 48h and 96h. OCP and EIS measurements were applied at intervals during immersion to record the corrosion behaviour with immersion time.

Section 6.3 shows the experimental results regarding the corrosion behaviour in 3.5^{wt}% NaCl solution. AZ31-GF and AZ31-ME with $Mg(OH)_2$ based films with various treatments, including hydrothermal (HT), electrochemical (EC) and additive treatments. Electrochemical corrosion tests, including the EIS and OCP measurements, were applied to the samples at intervals during the immersion tests.

The corrosion rates results based on section 6.2 and 6.3 are summarised and quantified and discussed in Chapter 8.

6.2 Corrosion assessment of uncoated substrate

6.2.1 Electrochemical corrosion tests

6.2.1.1 AZ31-GF

Figure 6.2.1 shows the OCP vs time of immersion for AZ31-GF. Black dots are the first test up to 48h. The grey dots represent a repeating test for a longer extent upto 96h.

In test 1 (black dots) up to 48h, the first OCP measurement took place when the sample had been immersed in NaCl solution for 30min. The E_{OCP} is around -1.552 V_{SCE}. The E_{OCP} then sharply decreases to around -1.637 V_{SCE} after 3 hours of immersion and then back to around -1.61 to -1.62 V_{SCE} after 6 hours. In test 2 (grey dot), 96h, the OCP keeps stable around -1.533 ± 0.009 V_{SCE} throughout. There is a variation of OCP around 100mV potential difference between the two tests. It is likely due to the substrate. Details are shown in the later discussion section 6.2.3.

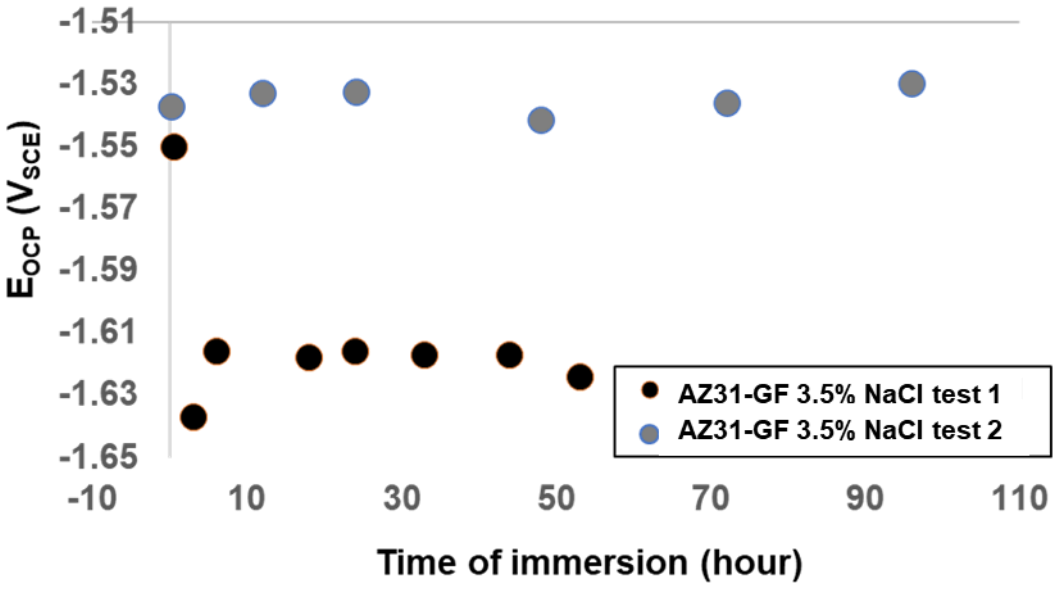

Figure 6.2.1. Open circuit potential of uncoated AZ31-GF versus the time of immersion in 3.5^{wt}% NaCl solutions for 48h (black) and 96h (grey).

Figure 6.2.2 shows the Nyquist plots for EIS measurements taken during immersion tests 1 and 2 of AZ31-GF. It also summarises their charge transfer resistances (R_{ct}) versus the time of immersion.

In test 1, all measurements have the same starting point near the origin, where the average R_0 of the measurements is 1.64±0.3 Ω.cm^2. Most Nyquist plots in test 1 exhibit a semi-circle loop except for the reduction of Z' observed at the mid-low frequency range, the right corner of the semicircle. When frequency further decreases, It shows possible negative loops at the low-frequency region after the semicircle intersects with the x-axis, which indicates a possible inductive behaviour of the sample/solution interface.

In test 2, Figure 6.2.2 b, the R_0 is averaging 1.2±0.1 Ω.cm^2, similar to test 1. The semicircle loops in test 2 are less regular, indicating the surface or sample/solution interface is less stable. Inductive loops are also observed.

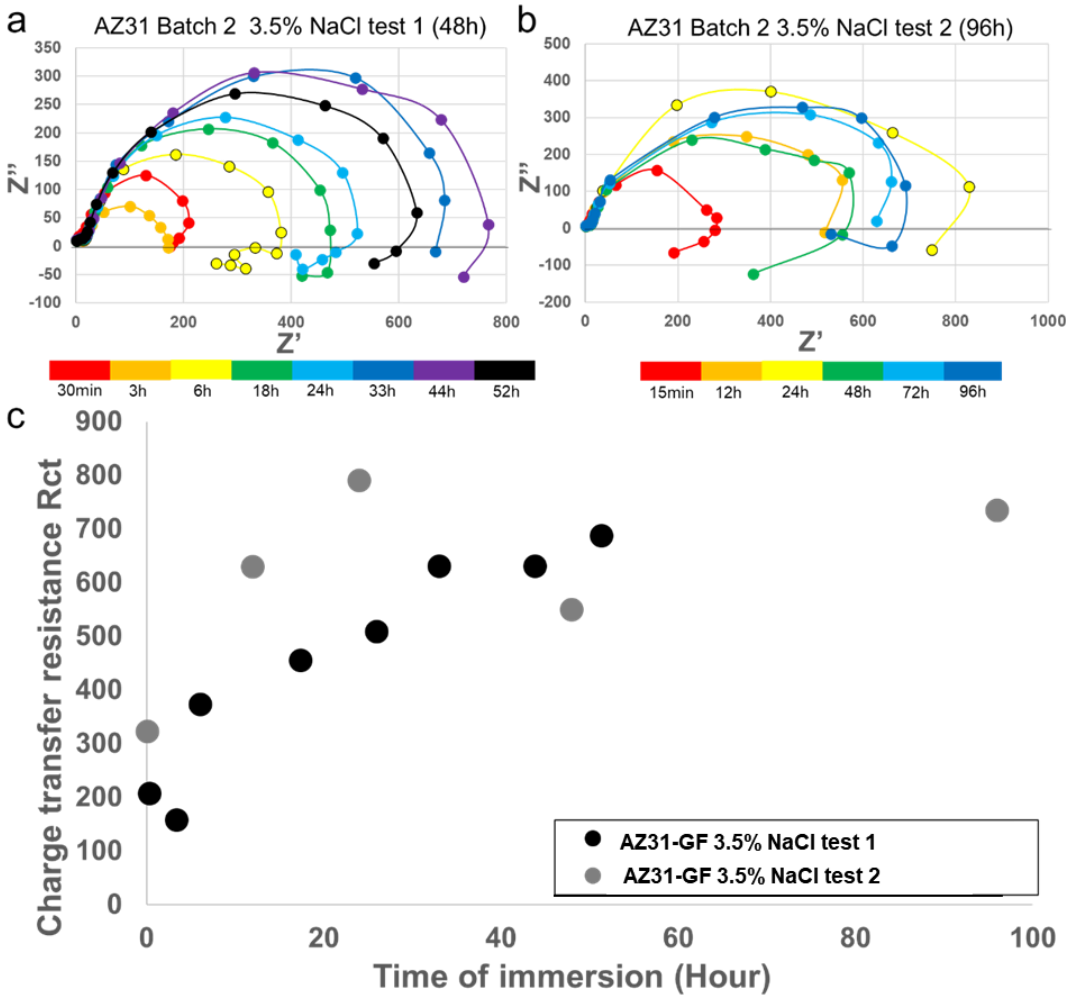

Figure 6.2.2. EIS Nyquist plots for the tests that uncoated AZ31-GF immersed in 3.5% NaCl solution for a) 48h and b) 96h and c) the summary of the charge transfer resistance versus the immersion tests of 48h (black) and 96h (grey).

Figure 6.2.2c summarises the Rct in test 1 and test 2 and plots them against immersion time. In test 1 upto 48h (black), R_{ct} started with around 200Ω.cm^2 at 30min and then dropped at 3h. The Rct increases to around 400 Ω at 6h and increases with the immersion time almost linearly. In test 2, R_{ct} started at around 300 Ω.cm^2 at 30min and then sharply increased to around 800 Ω.cm^2 at 24h. Then, it dropped to 550 Ω.cm^2 at 48h and bounced back to 740 Ω.cm^2 at the end of the test of 96h. The general trends of R_{ct} with time are similar in both tests. However, the data in test 2 is more scattered than in test 1, especially when immersion time is short (<24h).

6.2.1.2 AZ31-ME

Figure 6.2.3 shows the OCP vs time of immersion for AZ31-ME. Black boxes are the test 1' up to 48h of immersion, and the grey boxes represent the test 2' up to 96h of immersion.

In test 1' the starting OCP began at around -1.590 V_{SCE} and increased to -1.57 V_{SCE} at 2.5h. Then, the OCP fluctuated and reached the peak value of -1.54 V_{SCE} at 29h. Finally, OCP dropped to -1.56 V_{SCE} at 48h with another fluctuation. In test 2' the OCP has the same starting point as test 1' but is followed with a stronger inclination to the peak value of -1.55 V_{SCE} at 3h. Then, the OCP dropped to around -1.57 $V_{SCE,}$ followed by another incline to the second peak value of -1.56 V_{SCE}. The OCP declined until the end of the test at 96h, where the OCP is -1.57 V_{SCE}.

Generally, both tests have similar OCP behaviour. After an inclination from the starting value around 3h, the OCP for both tests ranges between -1.55 and -1.57 V_{SCE}. Test 1' has smaller time gaps between each measurement and more fluctuations observed.

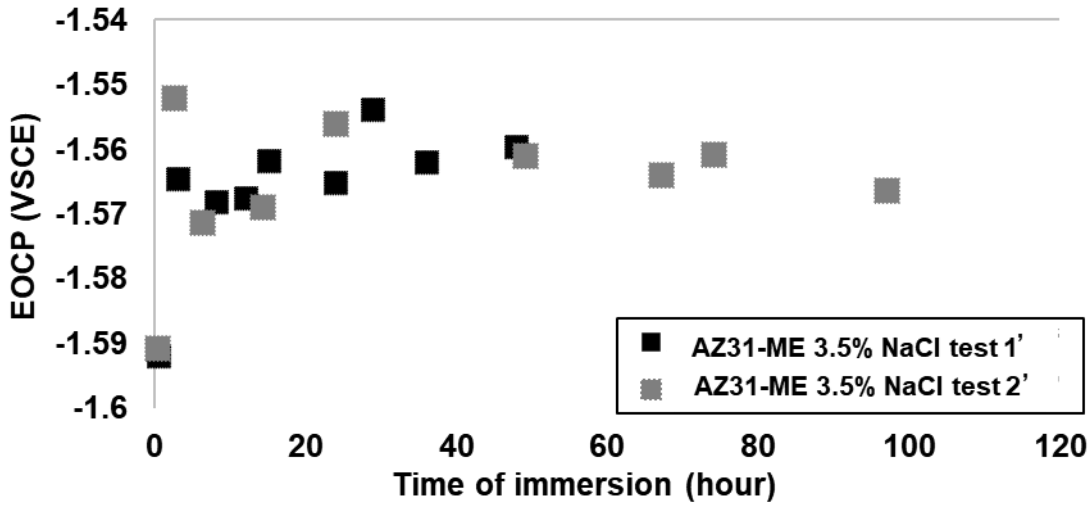

Figure 6.2.3. Open circuit potential of uncoated AZ31-ME versus the time of immersion in 3.5^{wt}% NaCl solutions for 48h (black) and 96h (grey).

Figure 6.2.4 shows the Nyquist plots of the EIS measurements in the immersion test 1' (48h) and test 2' (96h) of AZ31-ME. It also summarised their charge transfer resistances Rct versus the time of immersion.

The average R_0 for test 1' and test 2' are 13.25±1.5Ω.cm^2 and 17.50±1.5Ω.cm^2 respectively. For both test 1' and 2', Figure 6.2.4a and 6.2.4b, regular semi-circle loops are observed in the Nyquist plots. Reduction of Z' observed at mid-low frequency range tendencies for induction loop is observed. It gives a shrunk or collapsed right corner of the semicircle. As the frequency further decreases, the negative inductive loops were observed on most measurements for both tests.

Figure 6.2.4c summarised the Rct from each Nyquist plot for both tests and plotted against the respective time length of immersion. For both test 1' and 2', the Rct started at around 200 to 270 Ω.cm^2 and incline with immersion time with a linear behaviour except a small negative scattered point at 24h and a large positive scattered point at 29h in test 1'. After 48h immersion, the samples in both tests increased to around 1100 ± 60 Ω.cm^2. After 96 h immersion, the sample in test 2' reached an Rct around 1350 Ω.cm^2.

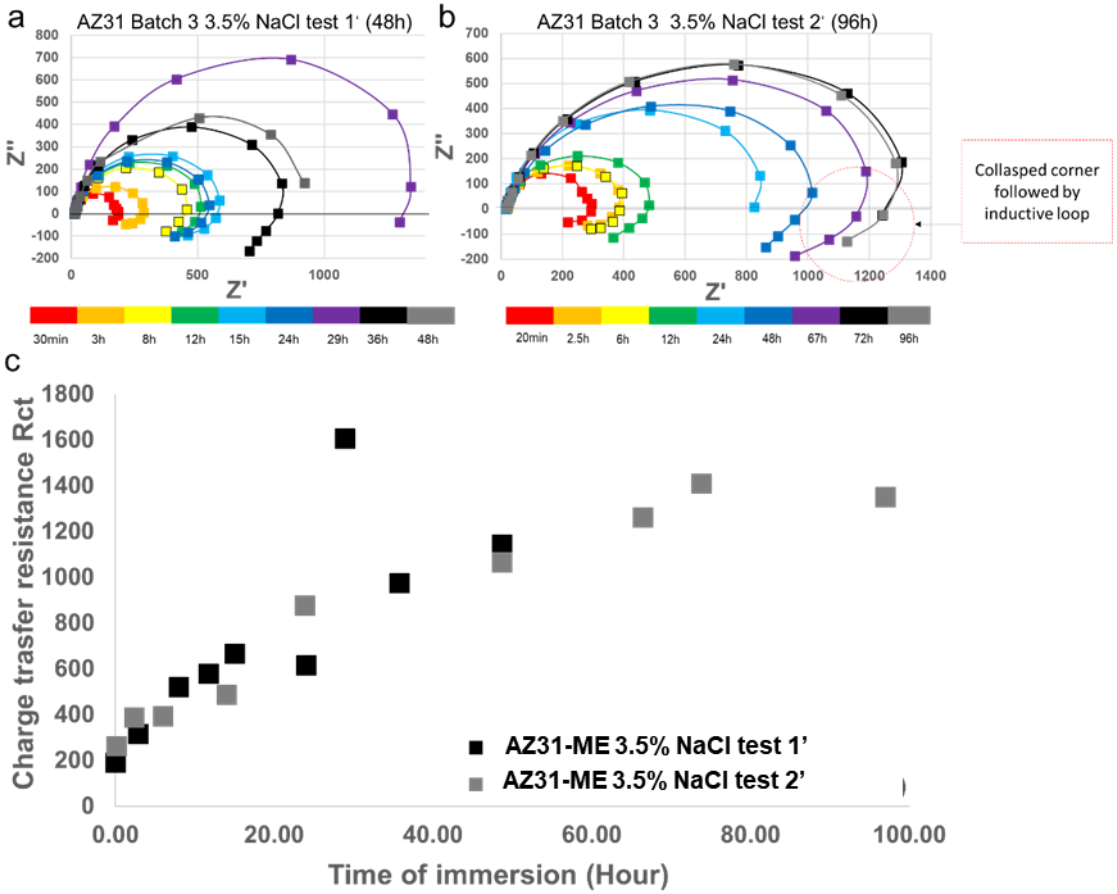

Figure 6.2.4. EIS Nyquist plots for the tests that uncoated AZ31-ME immersed in 3.5% NaCl solution for a) 48h and b) 96h and c) the summary of the charge transfer resistance versus the immersion tests of 48h (black) and 96h (grey).

6.2.1.3 Potentiodynamic polarisation and Tafel extrapolation

Figure 6.2.5 shows the potentiodynamic polarisation curve of the uncoated AZ31-GF. The fresh abraded sample was used in 3.5 ^{wt}% NaCl. It shows the E_{OCP} is -1.57±0.001 V_{SCE}. When the sample is anodically polarised to 900 mV, there is a disconnection to the curve, which is the starting point where pitting begins. Pits were observed on the sample surface after anodic polarisation.

With Tafel extrapolation, it gives B_A equal to 40.46 and B_c 145. The B value is 13.75mV

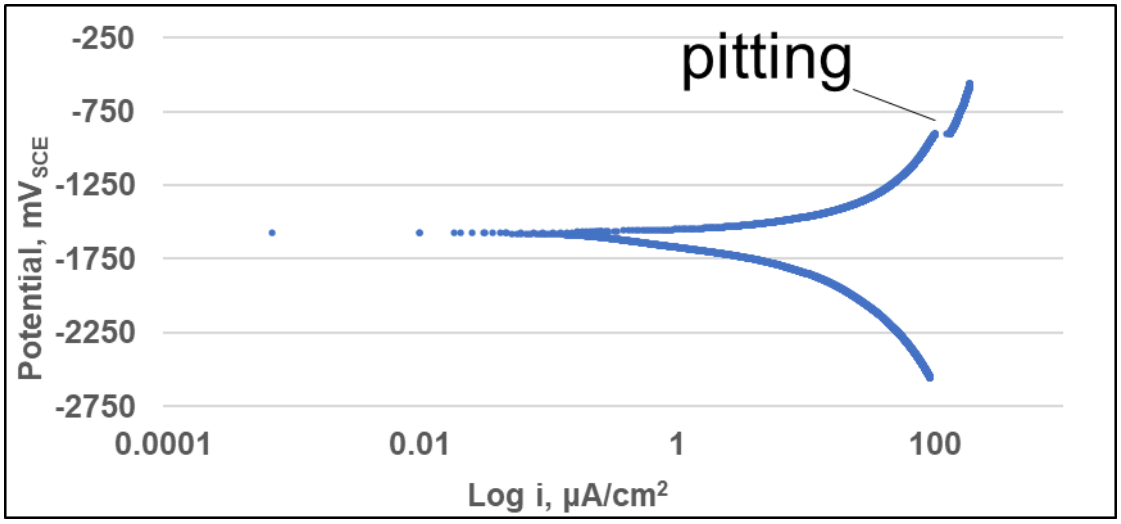

Figure 6.2.5 Potentiodynamic polarisation curves of the Mg alloy AZ31-GF at ±500mV overpotential with a rate of 10 mV/min.

6.2.2 Longer-term Corrosion test by Mass loss and Post corrosion measurement

In this section, a longer period of immersion tests of uncoated AZ31-GF and AZ31-ME were carried out in 3.5^{wt}% NaCl solution. The immersion test is up to 18 days for AZ31-GF and 21 days for AZ31-ME. The surface of the samples are characterised, and the weight of the samples is measured at intervals of the immersion tests. The post-corrosion characterisation of the cross-section was undertaken after the immersion tests. Corrosion rates are estimated by the mass change measurement during the test or the dimensional change prior/post-tests.

6.2.2.1 Surface post corrosion characterisation shows the progress of the corrosion.

AZ31-GF

An 18-day immersion test of an uncoated AZ31-GF sample is undertaken. Figure 6.2.6 shows the photo images of the sample has immersed in NaCl solution for 3, 7 and 15 days.

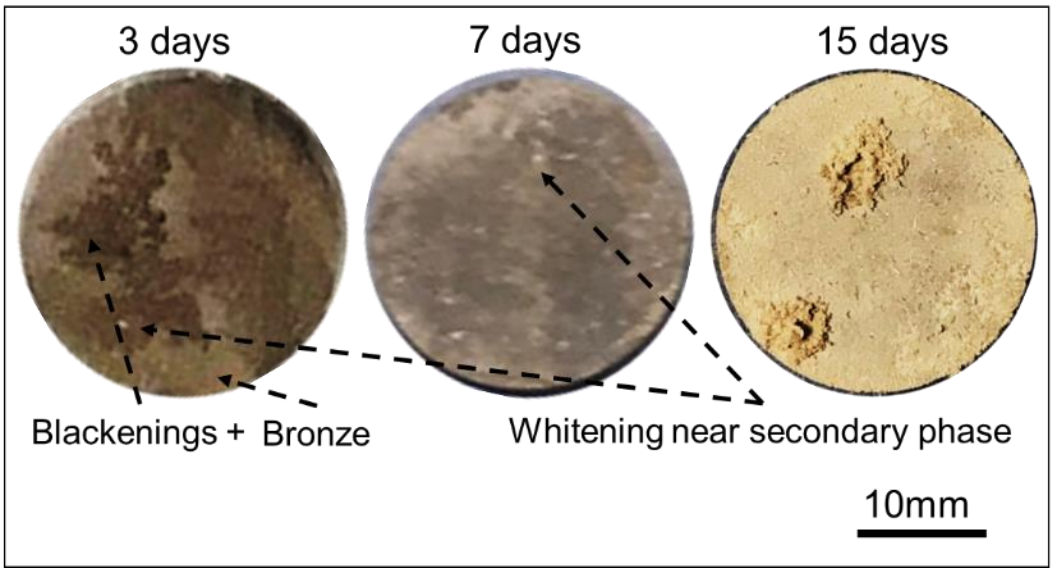

Figure 6.2.6. The uncoated AZ31-GF substrate after immersion into and 3.5^{wt}% NaCl solution for a) 7 and b) 15 days respectively.

Between day 1 and day 3 of immersion, the shiny silver metallic surface of AZ31-GF substrate became a dull metallic surface with bronze. Meanwhile, black or dark grey corrosion products are formed locally and continue to grow with immersion. Between day 3 and day 7, The blackening became light grey, covering most of the surface, and the rest of the bronze metallic surface became yellow corrosion products. Meanwhile, small white spots are observed on day 3, and their number grows with immersion time. Since day 15, yellow corrosion products have mostly covered the sample surface, and some white spots developed into large pores with volcano morphologies. These pores are caused by local galvanic corrosion as the number of impurities detected in AZ31-GF is larger than the standard value. The backside of the sample exhibits similar morphology as the top side.

AZ31-ME

The 21-day immersion test of the uncoated AZ31-ME sample is undertaken. Figure 6.2.7 shows the appearance of the uncoated AZ31-ME sample in 3.5^{wt}% NaCl solution for upto 21 days. Photos were taken every 3 days of immersion.

Between day 1 and day 3, the glossy silver metallic surface became dull metallic bronze. Meanwhile, black filaments also started to form. From day 3 to day 6, black filaments grow darker, but the area was reduced. Meanwhile, the bronze

areas transformed into yellow corrosion products and changed fully by day 9. Pits are also observed as black spots on day 9. The size and number of pits grew with immersion time. Besides, the blackening was also kept reduced and then fully transferred to the yellow corrosion product on day 18.

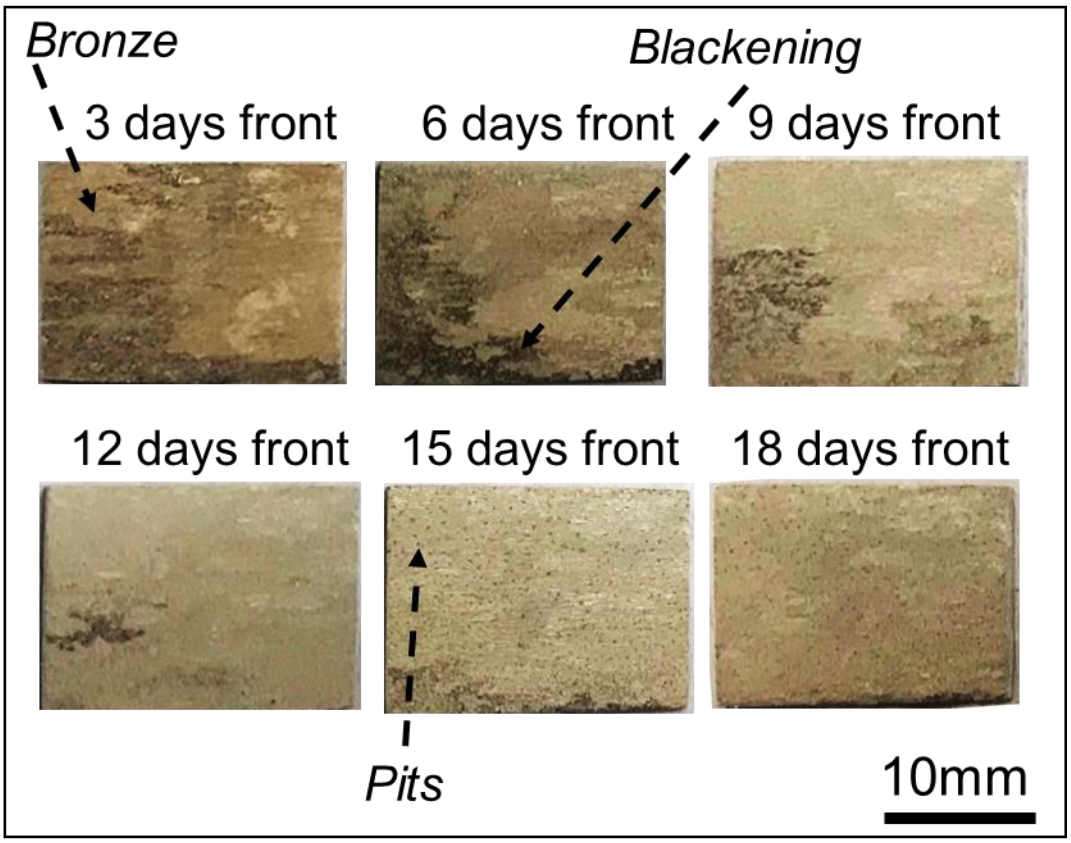

Figure 6.2.7. The uncoated AZ31-ME sample after immersion into and 3.5^{wt}% NaCl solution for a) from 3 to 18 days (top side).

The backside of the sample exhibits a different way of surface development. The photo images on the backside are shown in Figure 6.2.8. On day 3, the silver gloss surface mostly turned dull bronze with small areas of blackening. The blackening filament corrosion products were then reduced after 6 days. There is a much slower process of bronze transferring to corrosion products on the backside. At the end of the test, small areas stay with metallic bronze surrounded by very fine black filament corrosion products. After 12-day immersion, some white corrosion product is formed and increased, covering most of the back surface at the end of the test.

The progress of corrosion development on the backside of the sample surface is lagging behind. A slow disappearance of bronze that transforms into a yellow area is observed at the backside.

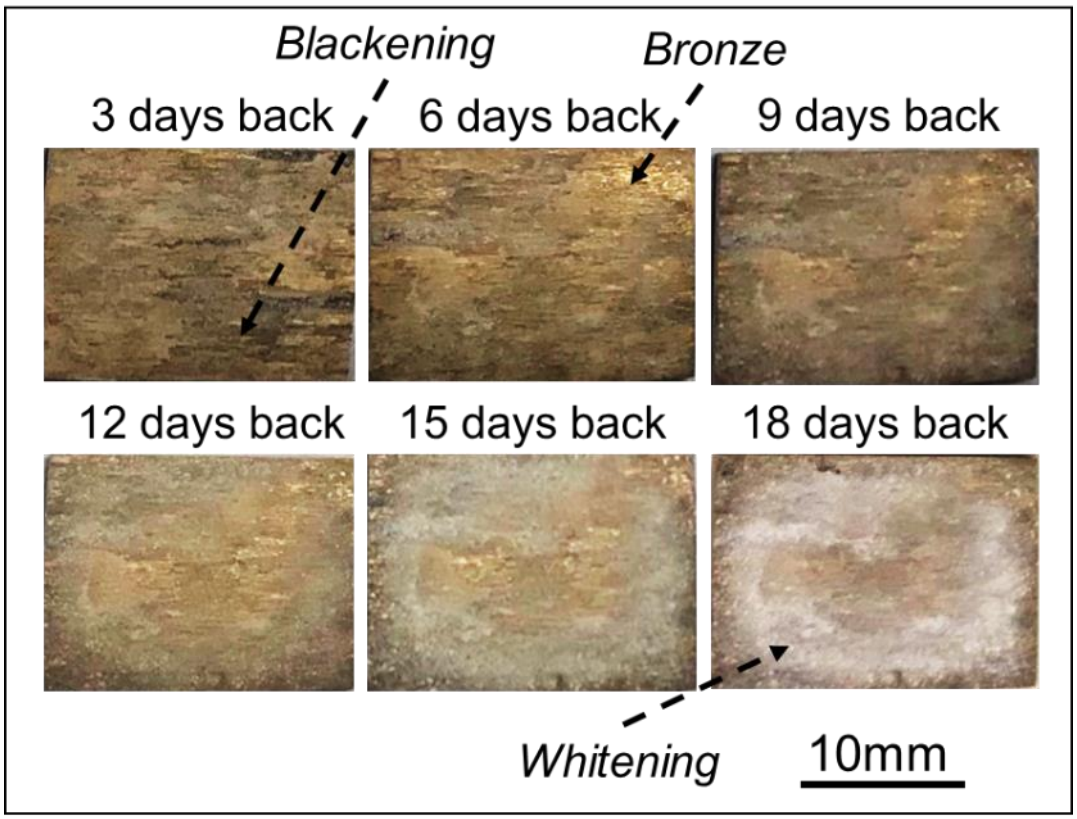

Figure 6.2.8. The uncoated AZ31-ME sample after immersion into and 3.5^{wt}% NaCl solution for a) from 3 to 18 days (backside).

6.2.2.2 Cross-sectional post corrosion characterisation.

AZ31-GF

The AZ31-GF sample cross-section after 18-day corrosion tests in 3.5^{wt}% NaCl solution is characterised. Stitched Optical microscopies image at the cross-section. The optical image is shown in Figure 6.2.9a. Both top and bottom of the sample under similar self-corrosion. A rough surface profile is formed after the corrosion test.

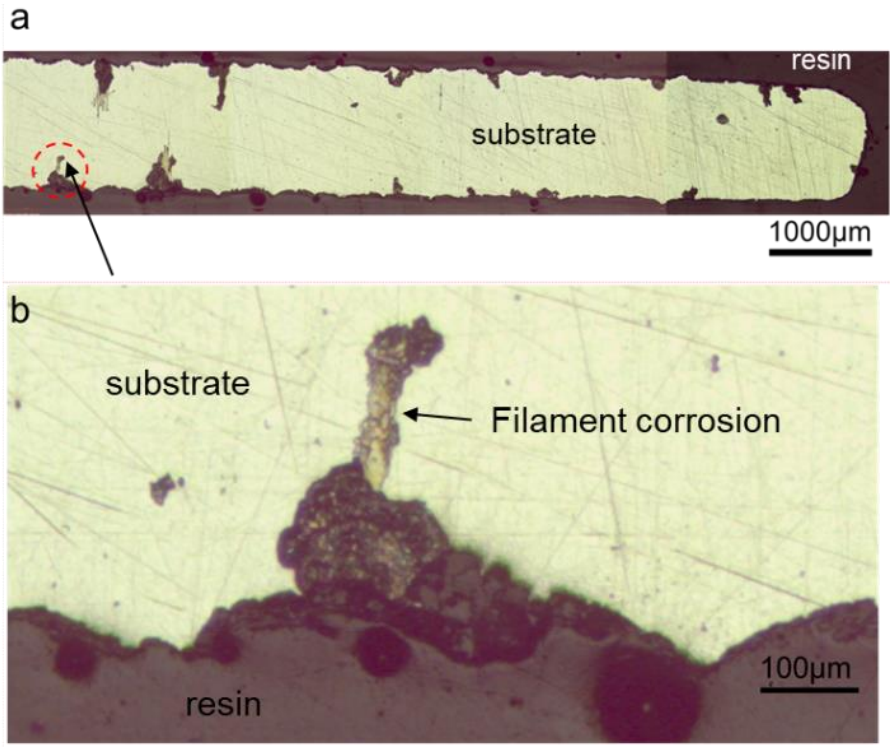

Figure 6.2.9. The cross-section uncoated AZ31-ME sample after immersion into and 3.5^{wt}% NaCl solution for 21 days.

The edge of the sample cross-section is covered with a corrosion product layer which is around 40μm thick. Apart from the sample surface, corrosion also occurred in the substrate, shown in Figure 6.2.9b. The corrosion products are in the form of black filament that develops along the grain boundaries. The formation of the filament corrosion products is likely due to the residual NaCl salts kept in the nearby resin bubbles or the surface corrosion product. Residual NaCl with air moisture allows the corrosion to happen after the sample is mounted.

AZ31-ME

The cross-section of AZ31-ME after 21-day corrosion tests in 3.5^{wt}% NaCl solution is shown in Figure 6.2.10. Figure 6.2.11a shows the stitched optical images of the AZ31-ME. Rough surface profiles on both sides are also observed for the post corrosion than the smooth surface before corrosion. Near the sample edges, corrosion attack is more severe.

The corrosion product layers of the top side and the bottom side have different average thicknesses. The thickness of the top side is around 77.7μm, and the bottom side is 54.3μm. It shows different corrosion rates between the top and

bottom, thus explaining the difference in post corrosion appearances shown in Figure 6.2.7 and Figure 6.2.8.

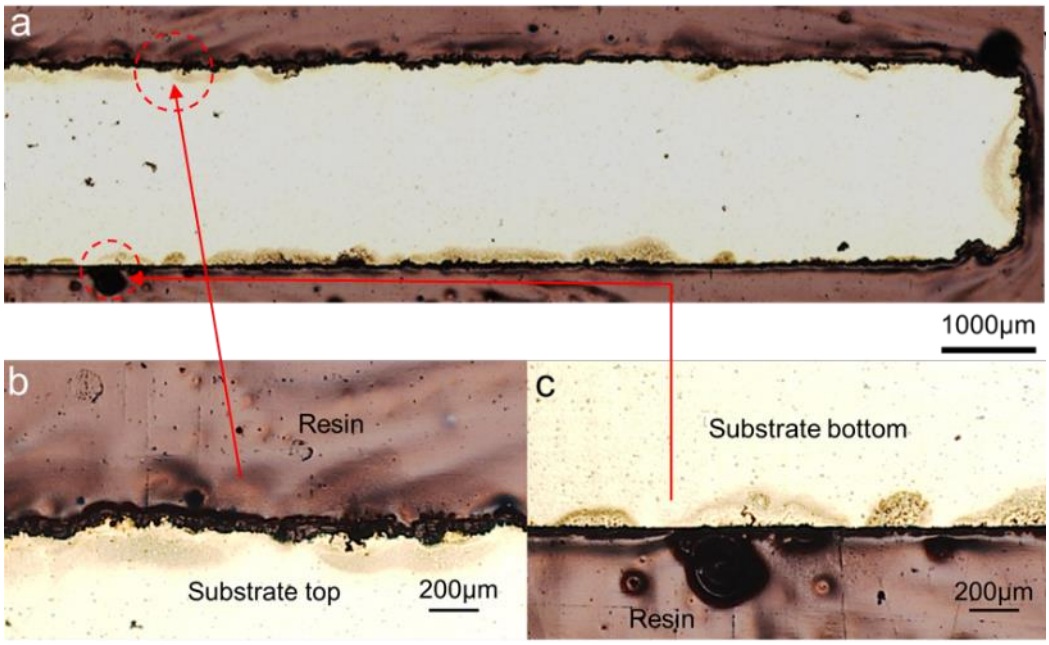

Figure 6.2.10. ~~6~~The cross-section uncoated AZ31-ME sample after immersion into and 3.5^{wt}% NaCl solution for 21 days.

Shadows are observed at substrates near the interface on both sides of the samples. Black corrosion filaments are likely developed from these shadows, which are also due to the residual NaCl salts. The bottom side has more shadows corrosion than the top side.

Figure 6.2.11 shows the SEM backscattered images of the topside and bottom side of the AZ31-ME samples after the 21day test in 3.5^{wt}%NaCl. SEM images show more details of the corrosion product layer. Cracks and voids are observed in the corrosion product for both sides. At the top side, corrosion products developed into the substrate, which leads to an uneven profile. Pittings may develop due to the unevenness of the corrosion product layer. Corrosion product filament after mounting and polishing is also observed. On the backside, cluster like morphology of the corrosion product is observed on the surface. Although not the same, this morphology has some similarities to the EC film. This morphology may result in a white appearance on both samples. There is a continuous crack along with the interface. The corrosion products are likely to detach. Some

granular features on the substrate surface were observed. It is likely to be the corrosion which are the shadow features observed in the optical images shown in Figure 6.2.11.

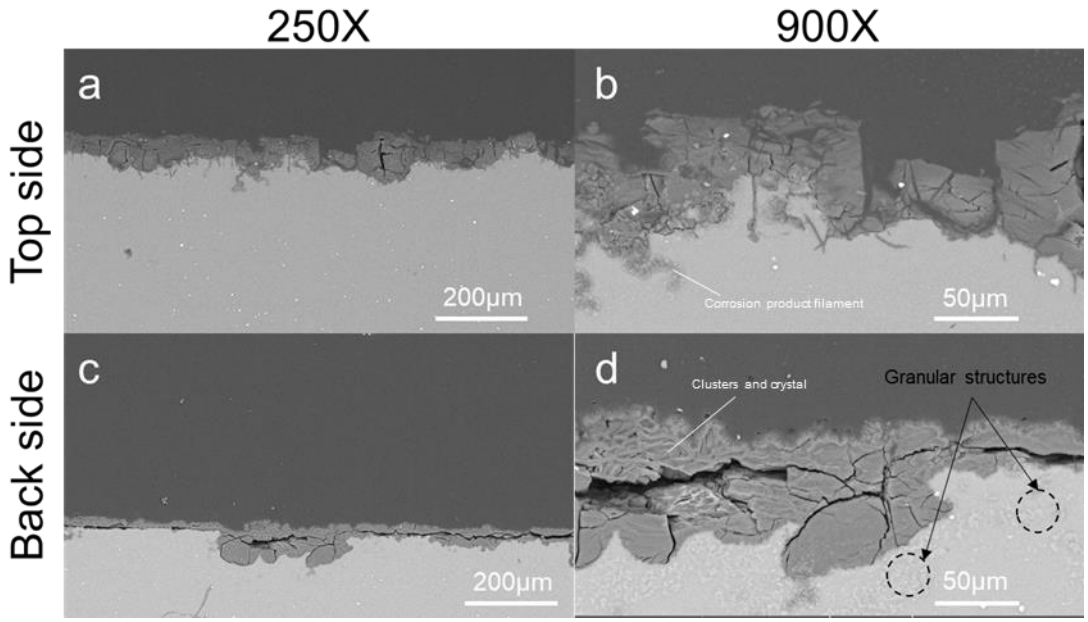

Figure 6.2.11. The SEM cross-sectional images of the AZ31-ME substrate after 21-day corrosion test in 3.5^{wt}% NaCl solution. a) and b) the top side of the sample with 250x and 900x magnitude respectively; c) and d) the bottom side of the sample with 250x and 900x magnitude respectively.

Measurements to the corrosion product layer based on the SEM images are made on both the top and bottom sides of the sample. The average thickness from the measurements are 54µm on the top and 40µm at the bottom. The thickness measurement on SEM is more accurate than it measured in optical images as it has a higher resolution. Thick and uneven corrosion product layer on the top side also indicates its corrosion is more vigorous than on the bottom side.

6.2.2.3 Mass change vs immersion time

Figure 6.2.12 shows the mass change per unit area versus immersion time for both AZ31 substrates AZ31-GF (dots) and AZ31-ME (boxes).

At the initial 3 days, AZ31-GF and AZ31-ME have similar behaviour with a slight increase in the mass. After 3 days, there are opposite mass-change behaviours between AZ31-GF and AZ31-ME substrates. The AZ31-GF substrate kept

gaining mass after a slight mass loss between day 3 and day 5. The rate of mass gain was at its Ω between day 9 and day 15. Meanwhile, the AZ31-ME substrate kept losing mass after day 3 until the end of the tests on day 21. For AZ31-GF substrate, it gained 0.004g/cm^2 at the end of the test for 18 days. The AZ31-ME substate lost 0.0027g/cm^2 at the end of the test for 21 days.

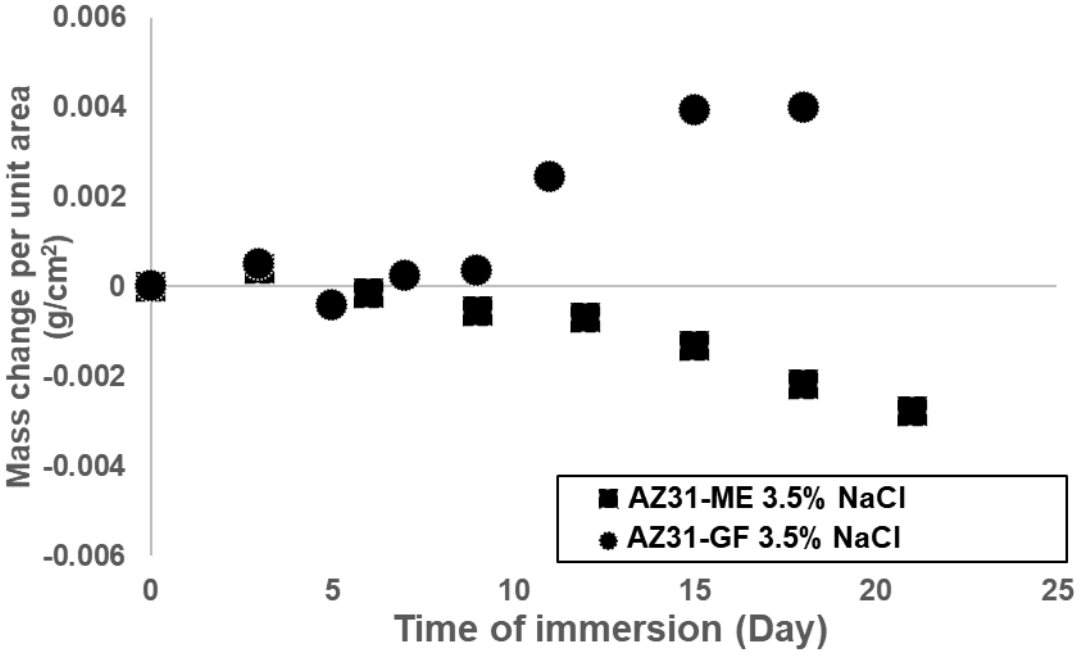

Figure 6.2.12. Weight (mass) change per unit area of the uncoated alloy AZ31-GF and AZ31-ME diagram against the time of immersion in 3.5^{wt}% NaCl.

6.2.3 Comments on 6.3

The corrosion assessments for AZ31-GF and AZ31-ME substrates are carried out in 3.5NaCl ^{wt}% solution. The assessment includes two sets of immersion tests. The first immersion test is based on electrochemical techniques up to 96 hours of immersion. EIS and Tafel extrapolation were applied to estimate the corrosion rate (mm/year) of the samples at a snap of time during immersion.

For the OCP tests, E_{OCP} usually fluctuates at the very beginning of 2 hours of immersion before stabilising. AZ31-GF samples differ in OCP in the parallel tests either ~ -1.53 V_{SCE} or ~-1.6 V_{SCE}. AZ31-ME samples show greater reparability in the OCP test, and both are stabilised around -1.56 V_{SCE}.

The variation of E_{OCP} for AZ31-GF is likely due to its poor homogeneity in the alloying elements and second phase particles. According to the mixed-potential theory [Scully, 1990], If a pure Mg is coupled with a heavier metal, the overall potential shifts up. For Mg alloys AZ31, the Mg matrix is also coupled with its alloying elements in solid solution or second phase particles. Their mixed potential is, therefore, the E_{ocp}. Once the alloy bar with inhomogeneous distribution of alloying elements is sliced into sample plates, each slice may vary in composition. Some sample slices can contain larger alloying elements such as Al, Fe and Mn than the standard, and some may have less. Therefore, the E_{OCP} of the over-alloyed sample slice is further increased, and the E_{OCP} of the under-alloyed samples slice is low.

Pidcock [Pidcock, 2014] has reviewed the E_{OCP} of AZ31 in 3.5^{wt}% from various research. In this work, the E_{OCP} of AZ31 lies between -1.47 V_{SCE} to -1.59 V_{SCE}. Such variation between the E_{OCP} in literature may also be due to the segregation of elements with an alloy.

Different R_0 are obtained in the EIS between AZ31-GF and AZ31-ME. It is likely due to the different distances between the sample and another testing electrode by error. Nevertheless, the value of R_0 is small and its influence on the EIS results can be neglected.

In some of the EIS measurements, the Nyquist plots tend to have conductive loops at lower frequency regions. If further lower the frequency, the loop will extend and intersect the X-axis again. Polarised resistance R_p is equal to the distance between R_0 and the new intersection. The real resistance of the sample is closer to R_p which is smaller than R_{ct}. However, It takes a long time for hours in the EIS measurements at the low-frequency region to complete the induction loop, which may significantly alter the sample surface. Therefore, in this work, R_{ct} by semicircle fitting is more prefered

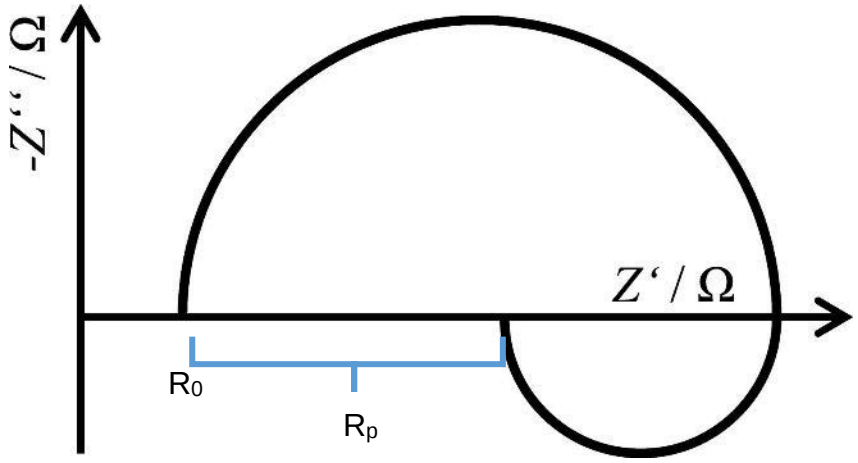

Figure 6.2.13. An example of the Nyquist plot with a conductive loop adapted from literature [Klotz, 2018]

For the longer term immersion tests upto 21 days, gradual change of the colour on the sample appearances with immersion time is relevant to the formation corrosion product layer, including the morphology and thickness.

As described earlier, The self-corrosion of Mg and its alloy involves both anodic and cathodic partial reactions at local anodic and cathodic sites. The local anodic reaction usually takes place near the second phase particle or defects such as grain boundaries. The locally black or dark corrosion products and filaments are likely to initiate at these local anodic sites. Other areas with more cathodic reactions underwent slower corrosion rates hence keeping a thinner corrosion product layer at the initial stage. Therefore, the metallic gloss appearance is kept at the local cathodic sites.

With longer immersion, the corrosion product layers on both anodic and cathodic are thickened. The roughness of the surface profile is also increased thus altering light refraction and exhibiting colours such as yellow, and light grey. It has the same pattern for developing HT films that exhibit black thin film but yellow or light grey when the film is thick.

The difference between the front side and back side is because the sample sits at the petri-dish bottom. The backside of the sample has a limited diffusion and exchange of the ions, therefore, with a slower corrosion process than the topside.

6.3 Corrosion assessment for the AZ31 Alloys with $Mg(OH)_2$ films.

6.3.1 Electrochemical corrosion tests results (OCP and EIS)

6.3.1.1 Hydrothermal film

In this section, a series of immersion tests in 3.5^{wt}% NaCl are applied to the AZ31-GF samples with Hydrothermal (HT) processing. OCP and EIS measurements are applied at intervals of immersion. The HT samples treatment at 160°C for 30min, 1h and 3h corresponding 5 µm, 15 µm and 50µm film thickness， are studied. For the 5 µm and 50 µm samples, the immersion tests took about 2 days (44h and 48h respectively). For the 15 µm sample, the immersion is around 1 day (26h).

The E_{OCP} of the test is shown in Figure 6.3.1. For the 5µm sample, the initial E_{OCP} is around -1.56 V_{SCE}. After that, it is slightly increased to around -1.54 V_{SCE} to -1.55 V_{SCE} and then back to -1.56 V_{SCE} at the end of the 2-day immersion.

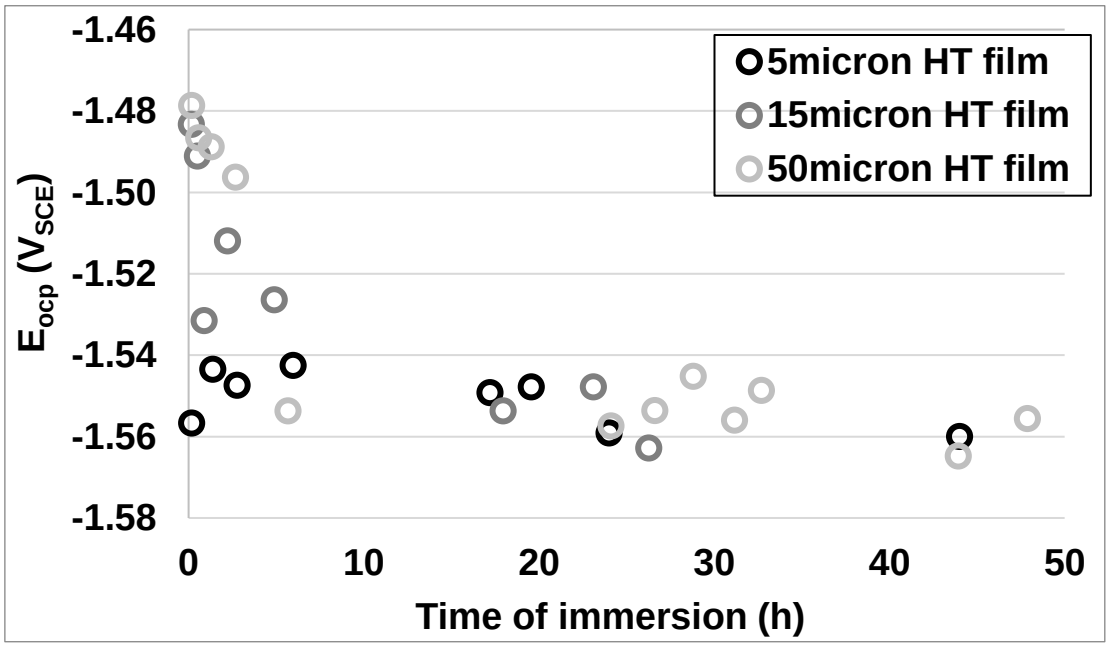

Figure 6.3.1 the E_{OCP} vs time of the AZ31-GF samples with HT films treated at 160°C for 30min,1h and 2h respectively (with 5, 15 and 50 µm thickness.

For the sample with 15 µm film (dark grey), the initial E_{OCP} is between -1.48 V_{SCE} and -1.49 V_{SCE} at the first hour of immersion. Then it dropped to between -1.51

V_{SCE} and -1.53 V_{SCE} from 1h to 5h. At 18h, the E_{OCP} dropped to around -1.55 V_{SCE} and -1.56 V_{SCE} until the end of the test for 26h.

The sample with 50µm HT film (light grey) exhibits a high E_{OCP} around -1.48 V_{SCE} at the beginning of immersion. It drops to around -1.50 V_{SCE} at around 3h immersion. The E_{OCP} further dropped to around 1.55 V_{SCE} at around 6h and kept steady until the end of the test at 2 days.

The sample with 15 and 50 µm films has higher initial E_{OCP} than the sample with 5 µm film. Nevertheless, the OCP finally converges to around -1.55 or -1.56 V_{SCE}.

Figure 6.3.2a and b show the Nyquist plots of the HT sample with 5µm film, measured at the intervals of the immersion test for 44h in 3.5^{wt}% NaCl solution. The size of the Nyquist plot generally decreases with the immersion time. Some of these plots are not regular semi-circles shapes. They usually have a smaller aspect ratio than a perfect semi-circle (0.5). The plots measured at 6h (green), 17h (sky blue), and 44h (black) have a significantly lower aspect ratio lower than 0.40). The plot at 3h (yellow) is an exception with a large aspect ratio of 0.59.

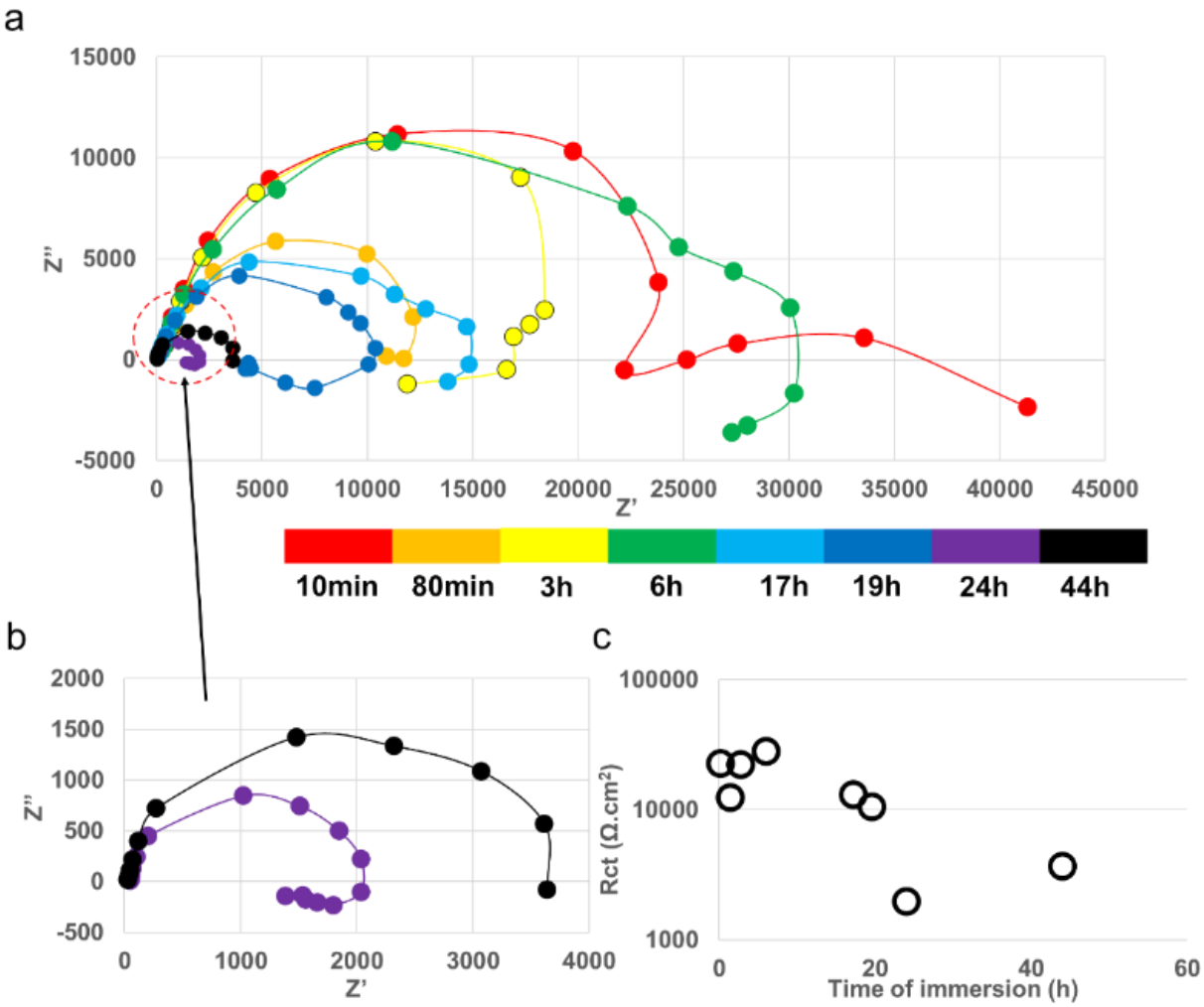

Figure 6.3.2 a) and b): EIS Nyquist plots f the immersion tests that hydrothermal treated AZ31-GF sample at 160°C for 30min in 3.5% NaCl solution for 44h; c) the summary of the charge transfer resistance versus the immersion time.

Figure 6.3.3 summarises the EIS results of the sample with 15µm HT film in 3.5^{wt}% NaCl solution. Figure 6.3.3 a and b show the Nyquist plots measured at the intervals of the immersion test for 26h. The plots at the beginning 2 hours have much larger sizes (red, orange, yellow and green). These plots also have a low aspect ratio from 0.24 to 0.30. Therefore, the plots are more likely semi-elliptical shapes. Diffusion loop is observed in the low-frequency region indicated with blue circles. From 5h immersion to the end of the test, the size of the plot greatly drops. The shape of the plots back to a semicircle-like shape. The trends

of the inductive loop at the mid-low frequency region of these plots are observed and indicated with red circles.

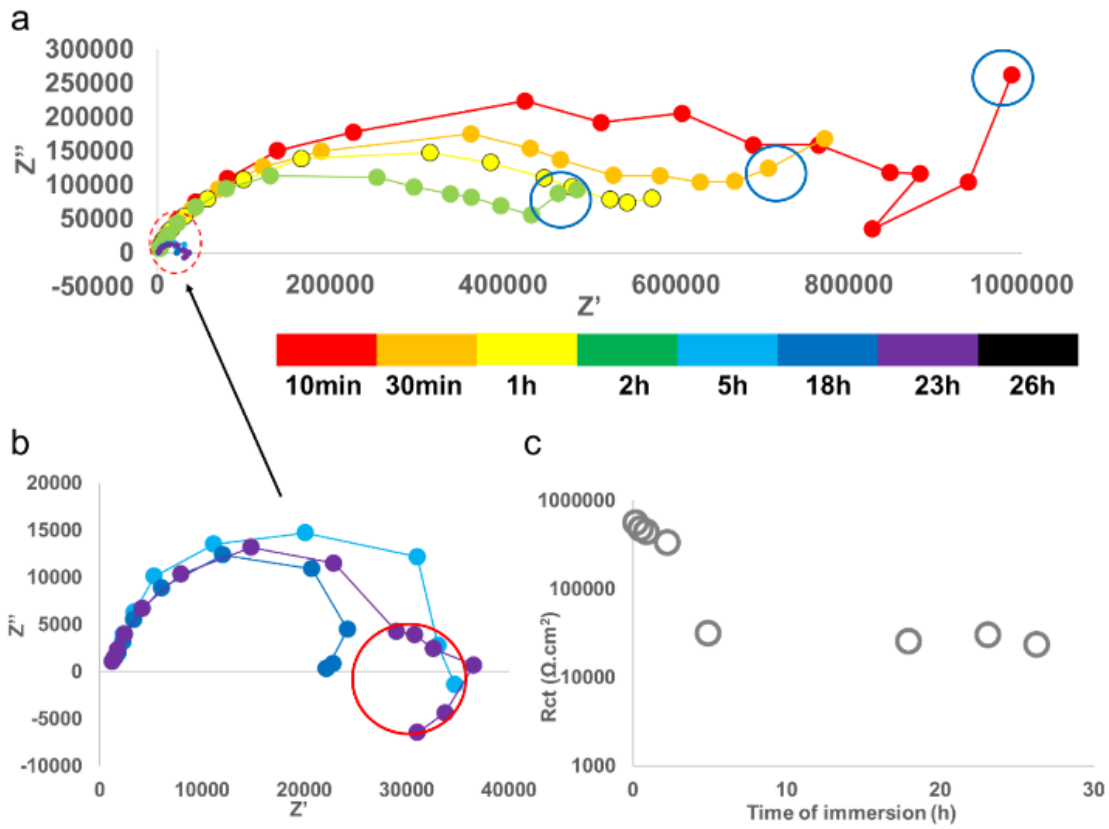

Figure 6.3.3. a) and b): EIS Nyquist plots for the immersion tests that hydrothermal treated AZ31-GF sample at 160°C for 1h in 3.5% NaCl solution for 26h; c) the summary of the charge transfer resistance versus the immersion time.

The R_{ct} is evaluated summarised in Figure 6.3.3c with the logarithmic scale against immersion time. The R_{ct} are 5 orders of magnitude in the beginning. At the first 2 hours it decreases from 550kΩ.cm^2 to 340kΩ.cm^2. Between 2h and 5h, R_{ct} had drastically dropped ten times to 31kΩ.cm^2. After that, the R_{ct} stabilised at this level until the end of the test.

The Nyquist plots in the HT sample with 50 µm film also show similar behaviour to the HT sample with 15 µm film. The R_{ct} is 5 orders of magnitude at the initial few hours of immersion, followed by a drop of R_{ct} to 4 orders of magnitude. The plots are also semi-elliptical at the initial hours of immersion.

The R_{ct} versus immersion time of the HT samples with 5µm, 15µm, and 50µm films are summarised in Figure 6.3.4 and with the reference for uncoated AZ31-GF substrates.

Generally, HT films significantly increase the R_{ct} of the samples compared to the uncoated samples. At the beginning of immersion, the R_{ct} of HT samples can be 50 to 500 folds to the uncoated sample. There is a drop of Rct for the HT sample with a longer immersion time. The difference is about 6 to 12 folds after 2 days of immersion.

The sample with 5 µm HT film (black) has the lowest R_{ct} among the three HT samples. It is more than a 20-time to the other HT samples for 1 day. At around 2 days, the difference between the 5 µm samples and the other two has reduced to around 2 times. The 50 µm samples have a similar initial R_{ct} to the 15 µm sample for 24h immersion except for scattered data at 1.5h immersion.

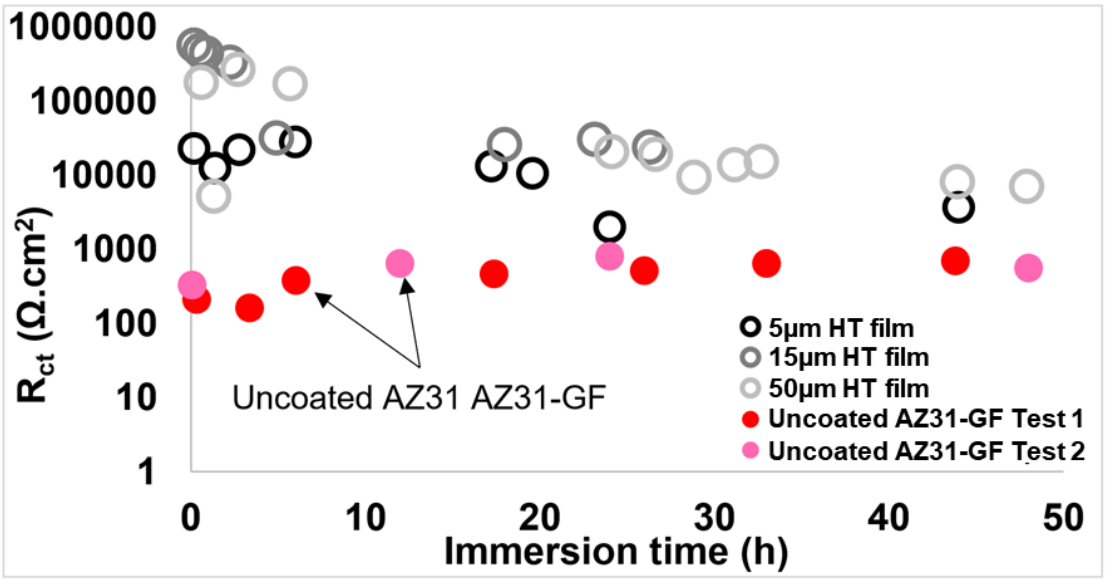

Figure 6.3.4 Summary of the Rct against immersion time for the HT samples at 160°C for 30min,1h and 2h respectively (with 5, 15 and 50 µm thickness respectively).

6.3.1.2 Electrochemical (EC) films

The corrosion immersion test in 3.5^{wt}% NaCl solution was carried out for EC films upto 1 to 4 days. Samples (AZ31-GF as substrate) underwent OCP and EIS measurements at intervals of immersion. It compares the corrosion behaviour of

the EC samples with a different processing temperature (RT and 60°C) and different applied current densities (42µA/cm^2 and 420µA/cm^2).

OCP results of the test are shown in Figure 6.3.5. The white and light grey stars with black backgrounds are the EC sample processed at RT with 42 µA/cm^2 and 420 µA/cm^2 respectively. With 42µA/cm^2, RT, the sample has the E_{OCP} between -1.52V_{SCE} and -1.55V_{SCE} during the immersion of 96h. With 420µA/cm^2, RT, the sample has an initial E_{OCP} of -1.68 V_{SCE} and then increased and stabilised at around -1.64 V_{SCE}.

Black and dark grey stars are processed at 60°C with 42 µA/cm^2 and 420µA/cm^2 respectively. With 42µA/cm^2, 60°C, the E_{OCP} started with -1.53 V_{SCE} but quickly dropped to between -1.55 V_{SCE} and -1.56 V_{SCE} and then stabilised. With 420µA/cm^2, 60°C, the E_{COP} of the sample kept around -1.60 V_{SCE} throughout, except for a scattered data point around -1.55V_{SCE} at 24h.

Each EC sample has a stable E_{OCP} versus immersion time where the variations are less than 0.05 V_{SCE}. However, the E_{OCP} differences between samples are large, which is between -1.52 V_{SCE} and -1.67 V_{SCE}.

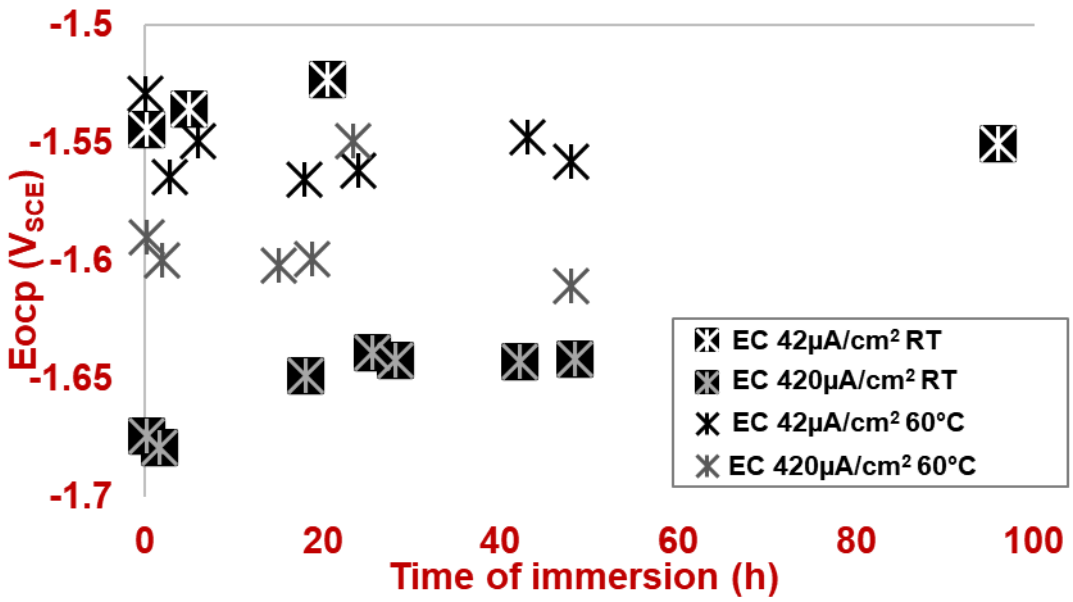

Figure 6.3.5 The E_{OCP} vs time of the AZ31-GF samples with EC treatment with two different processing current densities (42µA/cm^2 and 420µA/cm^2) at two different temperatures (RT and 60°C) respectively.

The large differences are likely due to the composition varies between specimens as AZ31-GF is not chemically homogeneous. It has been explained in section 6.2.3.

Figure 6.3.6a shows the EIS results of the EC sample treated with 42μA/cm^2 at RT. The Nyquist plots have semi-circles shapes with a smaller aspect ratio of around 0.38-0.43. It trends to have inductive loops if the lower frequency further decreased.

R_{ct} of the plots versus immersion time is plotted in Figure 6.3.6b. There is a trend of increasing in R_{ct} with immersion time. After 96h, the R_{ct} of this sample increased from 400 Ω.cm^2 to around 700 Ω.cm^2.

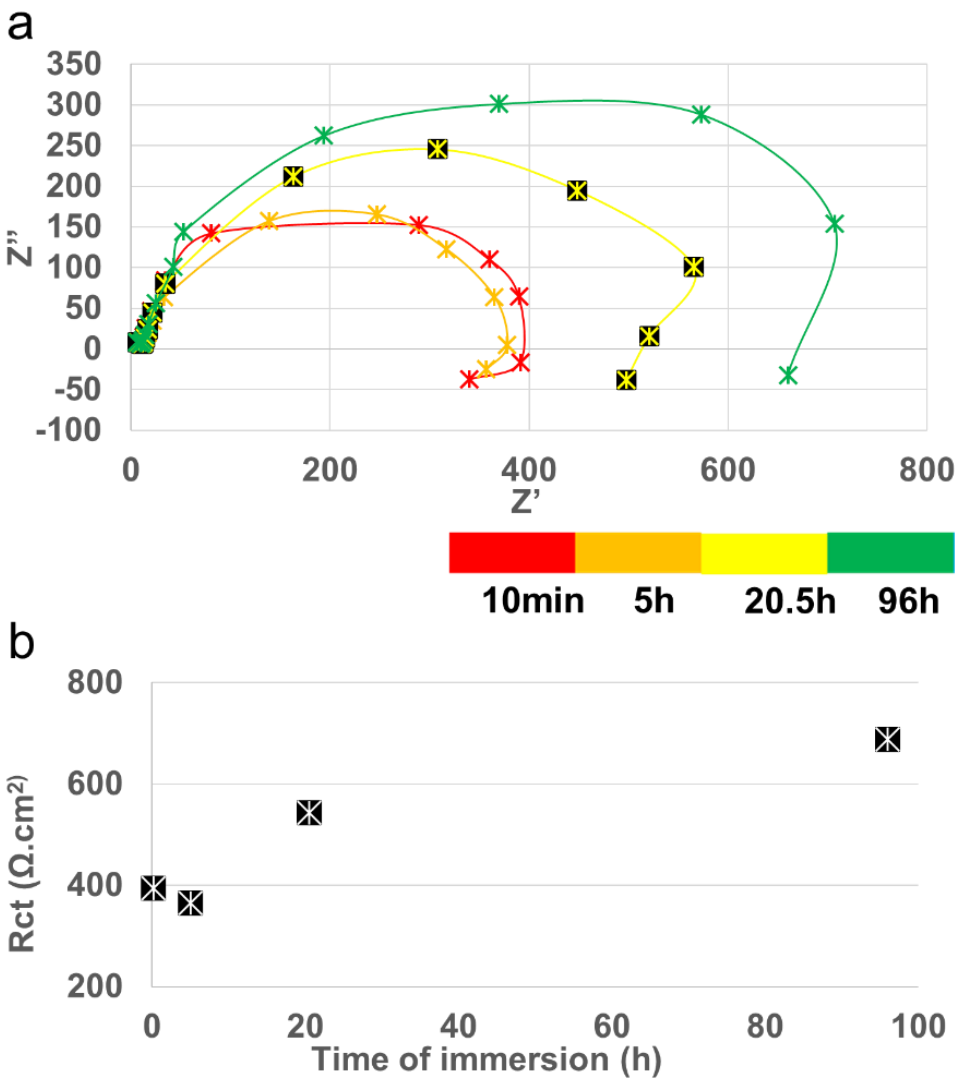

Figure 6.3.6. The EIS results of EC-treated AZ31-GF samples (42µA/cm^2, RT and 24h) under 96h immersion test in 3.5^{wt}% NaCl solution. a) the Nyquist plots of the EIS measurements during immersion, b) R_{ct} vs time of immersion.

The EIS measurements were also undergone for the AZ31-GF EC sample with a higher processing current (420µA/cm^2) at RT and with a lower current density (42µA/cm^2) at a higher processing temperature (60°C). Both samples show similar EIS results to Figure 6.3.6.

EIS results of the AZ31-GF EC sample with both higher current density and temperature (420µA/cm^2 and 60°C) are shown in Figure 6.3.7. Figure 6.3.7a shows the Nyquist plots. There is a scattered data point at 10min (red) at the mid-low frequency region as device error (indicated with the green arrows). The Nyquist plots have a more semicircle shape after 15h immersion.

The R_{ct} of the EIS measurements is shown in Figure 6.3.7b. The R_{ct} kept a higher value around 1600 Ω.cm^2 at the first 15h. between 15 and 19h, the R_{ct} sharply dropped to around 800 Ω.cm^2 and kept at this level until the end of the experiment at 48h.

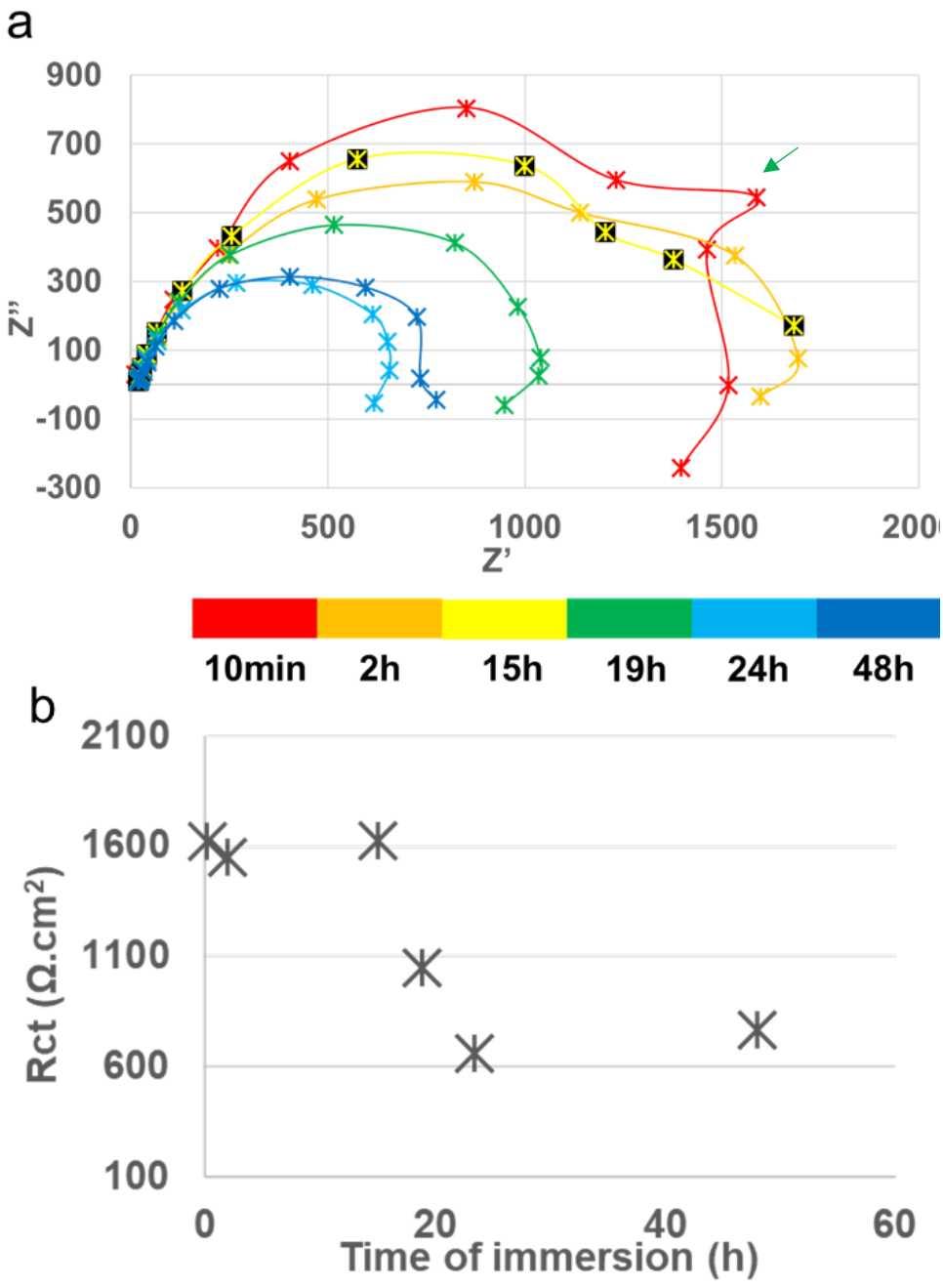

Figure 6.3.7. The EIS results of EC-treated AZ31-GF samples (420μA/ cm^2, 60°C and 24h) under a 2-day immersion test in 3.5^{wt}%. a) the Nyquist plots of the EIS measurements during immersion, b) R_{ct} vs time of immersion

Figure 6.3.8 summarised the R_{ct} versus immersion time for the EC samples with AZ31-GF. The R_{ct} against the time of the uncoated AZ31-GF samples (red dot) is also shown in this figure as the benchmark.

It shows that the EC samples processed at RT have the same level of R_{ct} as the uncoated sample since the beginning of immersion. At a higher processing temperature of 60°C, the samples kept a larger R_{ct} at the beginning of the test. However, the R_{ct} still dropped to a similar level to the uncoated samples with time. With 420μA/cm^2 at 60°C, the R_{ct} kept a higher level (around 1600 Ω.cm^2) for 15h. After 15h, the R_{ct} dropped to the same level as the uncoated samples until the end of the 2-day immersion test.

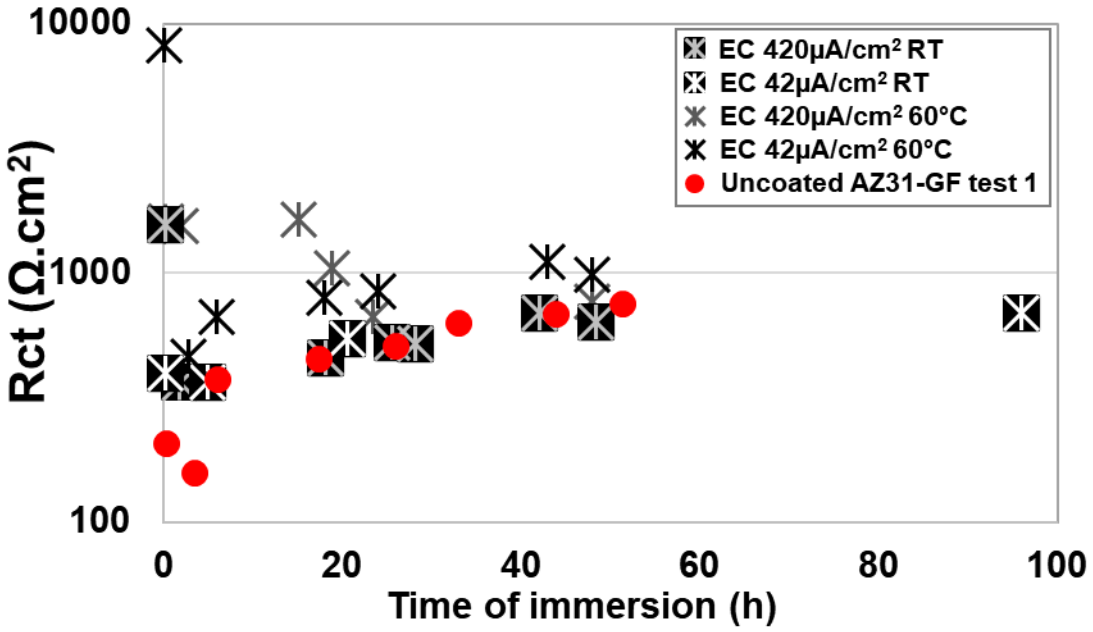

Figure 6.3.8 Summary of the R_{ct} against immersion time for the EC samples at 42μA/cm^2 and 420μA/cm^2 at RT and 60°C, compared with uncoated AZ31-GF as reference.

6.3.1.3 Additive films

6.3.1.4 EC+Additive vs direct additive samples

The R_{ct} versus immersion time for samples with additive treatments at 160°C is shown in Figure 6.3.9. The data indicated with blue circles correspond to the direct-additive sample process at 160°C. The data with green circles correspond to an EC+Additive sample with a thin EC primer coat (made with 42μA/cm^2, 60°C). The red dotted circle corresponds to the EC+Additive sample with a thicker

EC primer coat (made with 420μA/cm^2, 60°C). The grey and black dots show the results of uncoated Mg alloy (grey) and a 5μm thick hydrothermal film (black) as references.

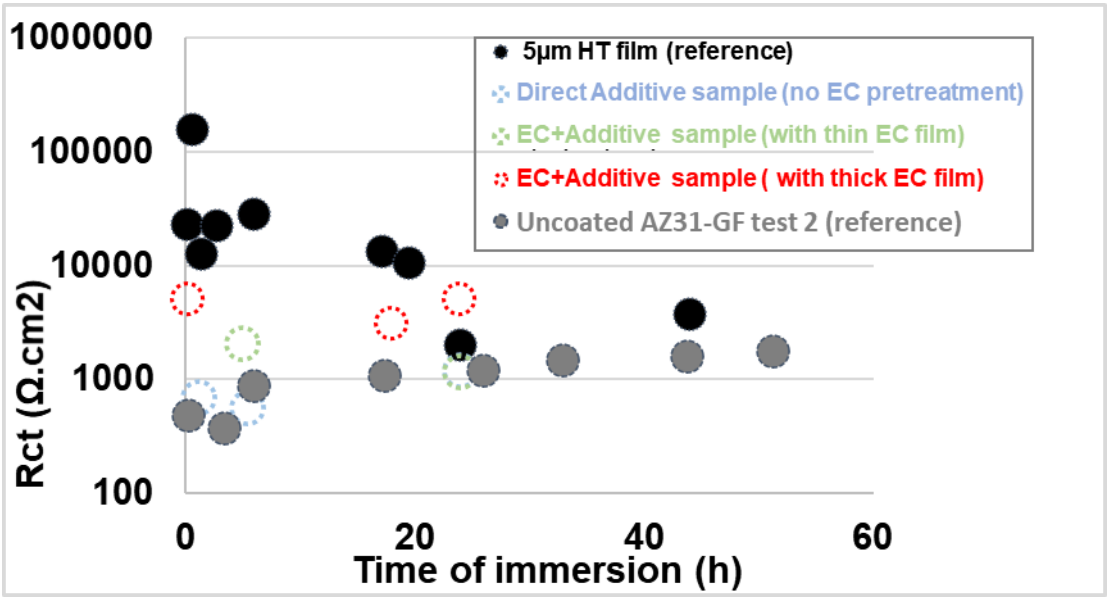

Figure 6.3.9. Summary of the R_{ct} against immersion time for the additive samples (AZ31-GF as the substrate) at 160°C for with an EC pre-treatment with 42μA/cm^2 60°C (green), an EC pre-treatment with 420μA/cm^2 60°C, and without EC pre-treatment. The data for the uncoated substrate and HT sample is also shown as a reference.

The direct-additive sample without EC pre-treatment (blue) shows a similar behaviour of R_{ct} to the uncoated samples, which is around 1kΩ.cm^2 after 24h immersion. The EC+Additive sample 1 with a thin EC primer film (green) has a higher initial R_{ct} (~2kΩ.cm^2). However, at around 24h, it reduced to the same level as the uncoated sample. The EC+Additive sample with a thick EC primer film (red) has the highest R_{ct} among these three samples, near 5kΩ.cm^2 at both the beginning and end of the immersion test.

EC+Additive sample with a thicker prime coating (red) has the best corrosion resistance, more than 10-fold the uncoated sample. Its R_{ct} also converges to the 5μm hydrothermal (black dots) and meets at 24h.

The effect of additive processing temperature

This section shows the OCP and EIS results of the EC+Additive samples with various additive temperatures of 160 ºC, 200 ºC and 240 ºC during 2-day

immersion tests in 3.5^{wt}% NaCl. All three samples had EC pre-treatment with 420µA/cm^2 at 60 ºC. The OCP results are shown in Figure 6.3.10 shows the E_{OCP}

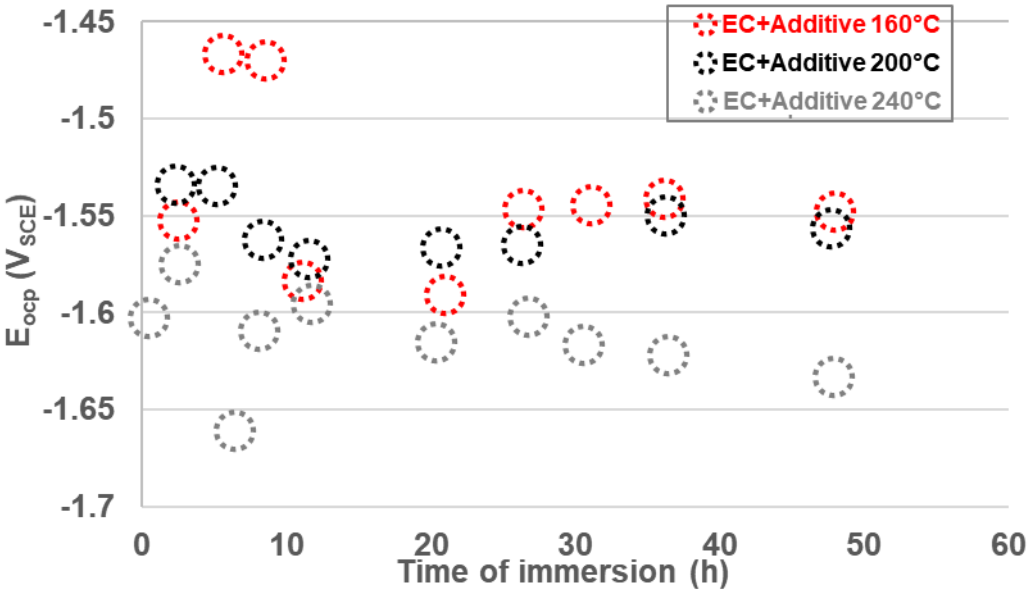

Figure 6.3.10. The E_{OCP} vs time of the AZ31-GF samples with EC treatment (420µA/cm^2, 60°C) and additive processing at various temperatures of 160°C, 200°C and 240°C.

The sample with the additive treatment of 160°C (red) has the highest average E_{OCP}. It has a large variation at the beginning 20h of immersion which varies between -1.47 V_{SCE} to -1.59V_{SCE}. Then its E_{OCP} stabilised at around -1.54 V_{SCE}.

The sample at 200°C (black) has a lower average E_{OCP} than the sample at 160°C. Its E_{OCP} varies between -1.53 V_{SCE} and -1.57 V_{SCE}. With a longer immersion of more than 20h, the E_{OCP} is at around -1.56±0.01 V_{SCE}.

The sample at 240°C (grey) has the lowest E_{OCP} between -1.58 and -1.66 V_{SCE}. The behaviour of E_{OCP} against immersion time is stable but slightly decrease from -1.58 V_{SCE} to -1.63 V_{SCE}. A scatter point is observed at 6h immersion with the lowest E_{OCP} of -1.66 V_{SCE}.

Figure 6.3.11 shows the EIS measurements of an EC+Additive sample at 160°C in 3.5% NaCl solution for 2 days. The Nyquist plots from the EIS measurements are shown in Figure 6.3.11 a and 6.3.11b, and the R_{ct} of the EIS measurements versus time are shown in Figure 6.3.11c.

For the first 11h of immersion, the sample has large Nyquist plots from the EIS measurements where the R_{ct} exceeds four orders of magnitudes. The Nyquist plots are not regular semicircles as some data points at the mid-low frequency region (0.1-0.4Hz) vary, and shrink along the x-axis. These data points are indicated with red arrows. After 20h to 40h immersion, the Nyquist plots reduced where the R_{ct} is around 3kΩ.cm^2. At this stage, the Nyquist plots are smoother but with smaller aspect ratios from 0.37 to 0.41. At the end of immersion, 48h, the R_{ct} was further reduced to 1300Ω.cm^2.

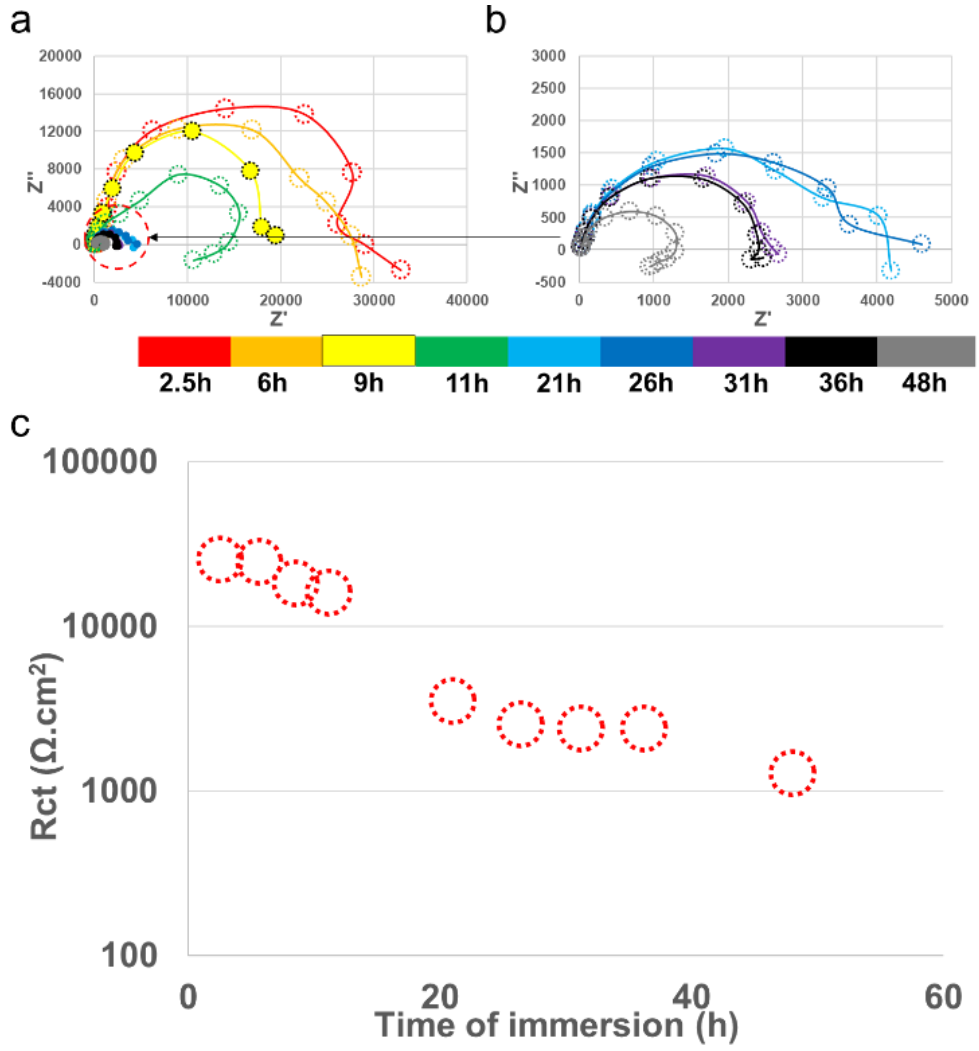

Figure 6.3.11 a) and b): EIS Nyquist plots for the immersion tests of AZ31-GF with EC pre-treatment (420μA/cm^2, 60°C) followed with the additive processing (160°C) under 3.5% NaCl solution; c) the summary of the charge transfer resistance versus the immersion time.

Figure 6.3.12 shows the EIS measurement of an EC+Additive sample at 200°C in 3.5% NaCl solution for 2 days. The Nyquist plots of the EIS measurements are

shown in Figure 6.3.12 a and 6.3.12 b. The R_{ct} versus immersion time is shown in Figure 6.3.12c.

This sample has higher resistances at the beginning 5 hours of immersion where the R_{ct} exceeds 4 orders of magnitude. The shape of the Nyquist plots at the first 5h is not a regular semi-circle shape that the data points shrink along the x-axis at mid-low frequency range, indicated with red arrows. Then there is a sudden drop in the resistance, which exhibits smaller but more regular Nyquist plots. R_{ct} of the sample steeped down to around 2kΩ.cm^2 and gradually dropped to 1300 Ω.cm^2 at the end of the immersion test.

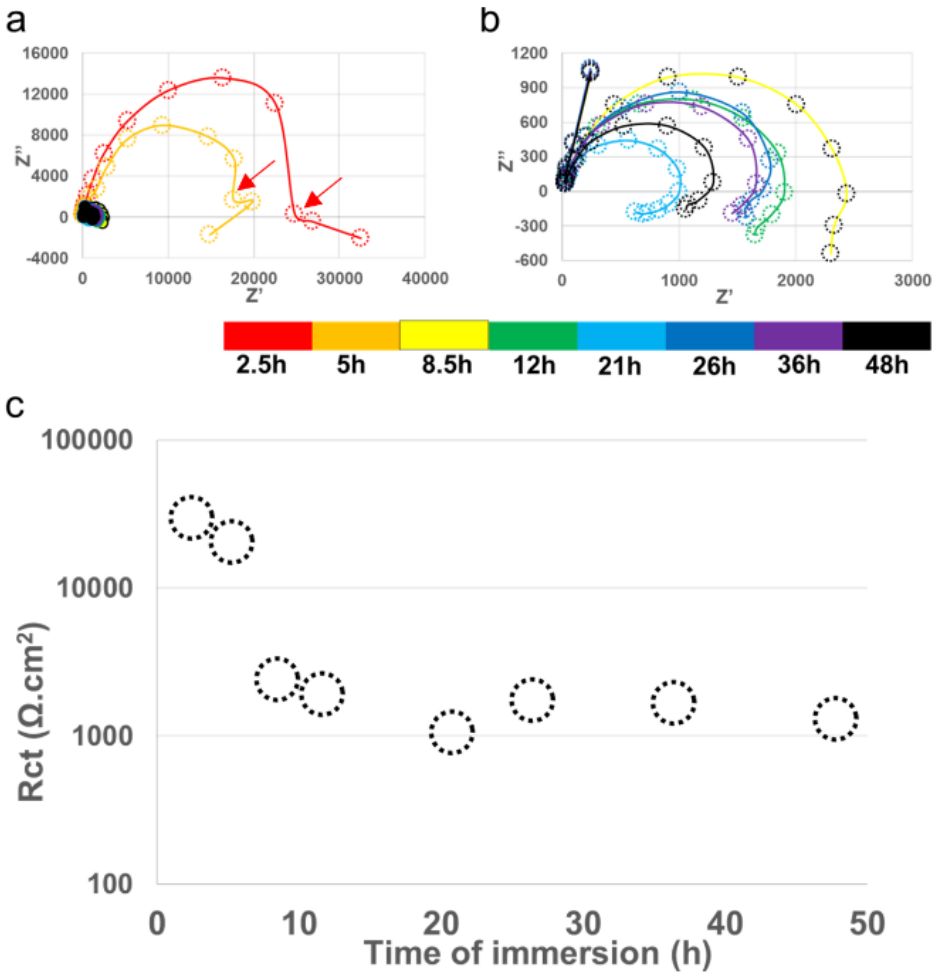

Figure 6.3.12. a) and b): EIS Nyquist plots for the immersion tests of AZ31-GF with EC pre-treatment (420μA/cm^2, 60°C) followed with the additive processing (200°C) under 3.5% NaCl solution; c) the summary of the charge transfer resistance versus the immersion time.

Figure 6.3.13 shows the EIS measurement of an EC+Additive sample at 240°C in 3.5% NaCl solution for 2 days. The Nyquist plots from the EIS measurements are shown in Figure 6.3.13 a and 6.3.13 b, and the R_{ct} of the EIS measurements versus time are shown in Figure 6.3.13 c. The resistances are higher at the first 8h of immersion, where the R_{ct} is over four orders of magnitude. At this stage, the Nyquist plots are not in regular shape. At 3h (orange) and 8h (green), the Nyquist plots of measurements are irregular and squeezed on the x-axis, leading to higher aspect ratios around 0.56. For the measurement at 8h, the data points at the high-frequency region also collapsed. After 10h, the R_{ct} quickly dropped to 9kΩ.cm^2 and then stabilised at around 6kΩ.cm^2. The Nyquist plots at this stage are in a regular semicircle shape.

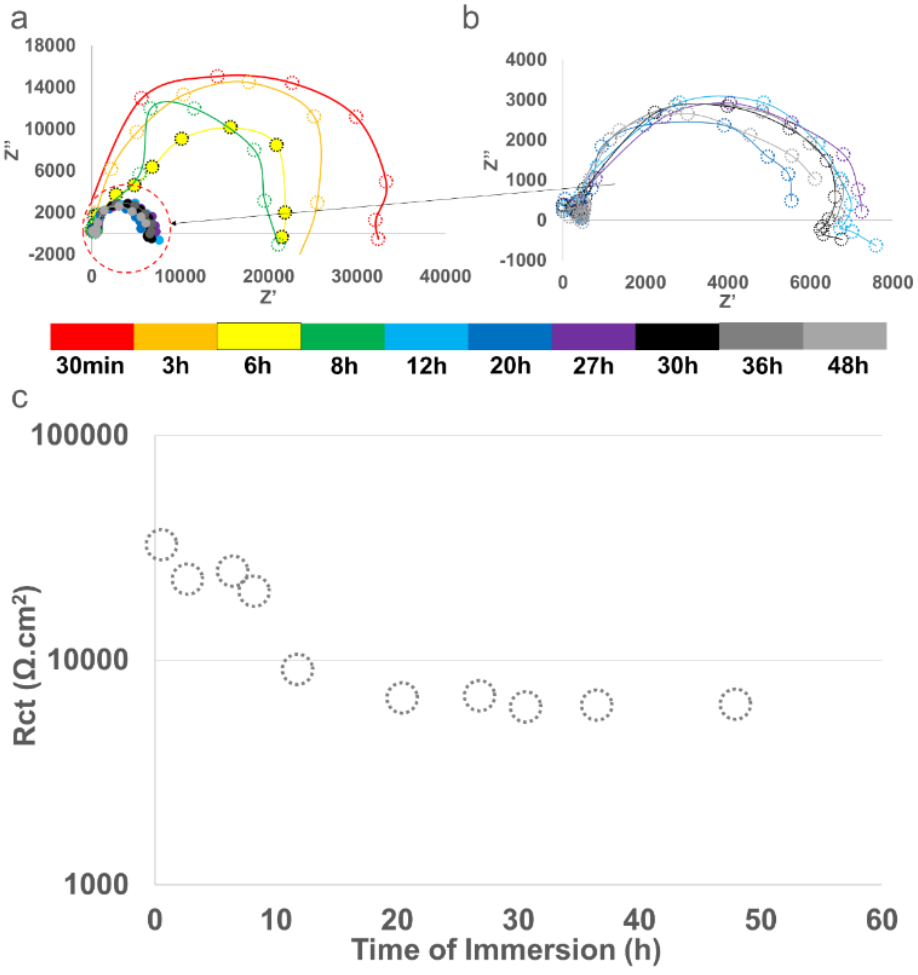

Figure 6.3.13 a) and b): EIS Nyquist plots for the immersion tests of AZ31-GF with EC pre-treatment (420μA/cm^2, 60°C) followed with the additive processing (240°C) under 3.5% NaCl solution; c) the summary of the charge transfer resistance versus the immersion time.

Figure 6.3.14 summarises the R_{ct} vs time of the EC+Additive samples (AZ31-GF) with additive treatment at 160 ºC (red circle), 200 ºC (black circle) and 240 ºC (grey circle), which are just shown in Figure 6.3.11 to Figure 6.3.13.

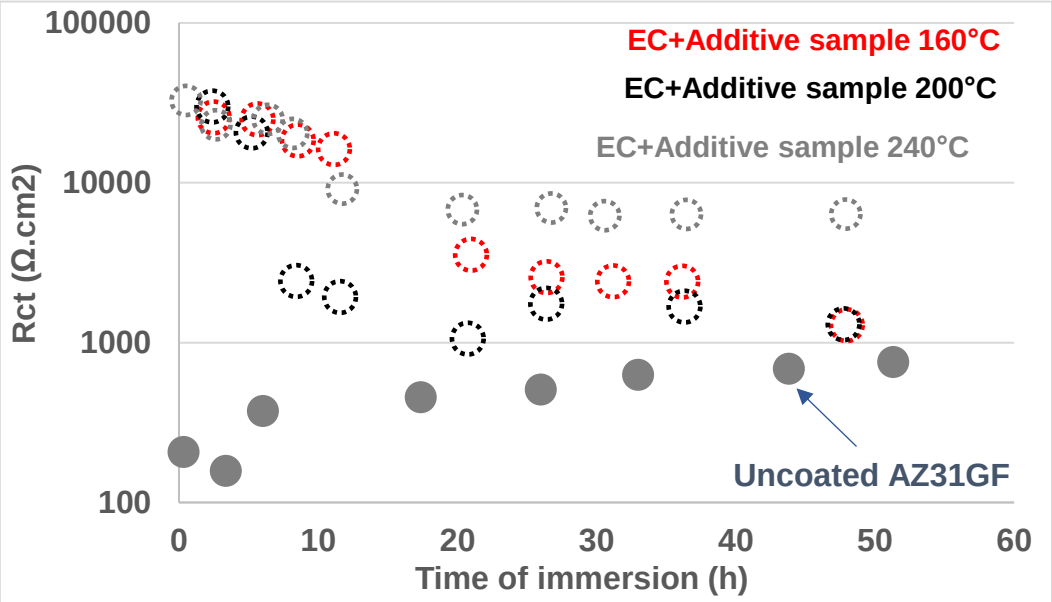

Figure 6.3.14 Summary of the R_{ct} against immersion time (up to 2 days) for the additive samples (AZ31-GF as the substrate) with the EC pre-treatment with 420μA/cm^2 at 60°. The additive processing temperatures are 160°C (red), 200°C (black) and 240°C (grey) respectively. The data for the uncoated substrate is also shown as a reference.

For all three EC+Additive samples, there is a significant increase in the R_{ct} compared to the uncoated substrate, especially at the beginning of immersion.

All three samples have a similar R_{ct} between 4 and 5 orders of magnitude at the beginning of 5 to 10 hours of immersion. Then, the R_{ct} of all three samples decreased and stabilised after around 1 day of immersion. After the steep decrease of R_{ct} during immersion, the R_{ct} was still above the uncoated sample.

Samples at 160ºC and 200ºC show similar R_{ct} after stable. Both samples end up with the same R_{ct}, around 1300 Ω.cm^2, after 2-day immersion.

The sample at 240ºC kept the highest stable R_{ct} amongst the three, around five times the samples at 160ºC and 200ºC.

A parallel set of tests was conducted for the AZ31-GF samples with the same additive treatment at 160 ºC, 200 ºC and 240 ºC in 3.5^{wt}% NaCl solution for up to 1 day. It has similar behaviour to the tests for 48h, especially the sample with the additive treatment at 240 ºC. It indicates reasonable repeatability of the samples and the corrosion test.

Figure 6.3.15 summarises the EIS results versus immersion time for the EC+Additive samples formed at 240°C in several repeating tests, including the tests shown in Figure 6.3.14. The data points with error bars mean the lower and upper bound of the R_{ct} obtained at that time. The data points without error bars mean there is only one measurement applied at that specific point of time. Between the dotted curves is the region that R_{ct} of the EC+Additive sample (240°C) is likely to be versus immersion time. It shows that the EC additive samples can achieve a stable R_{ct} of at least 5kΩ.cm^2

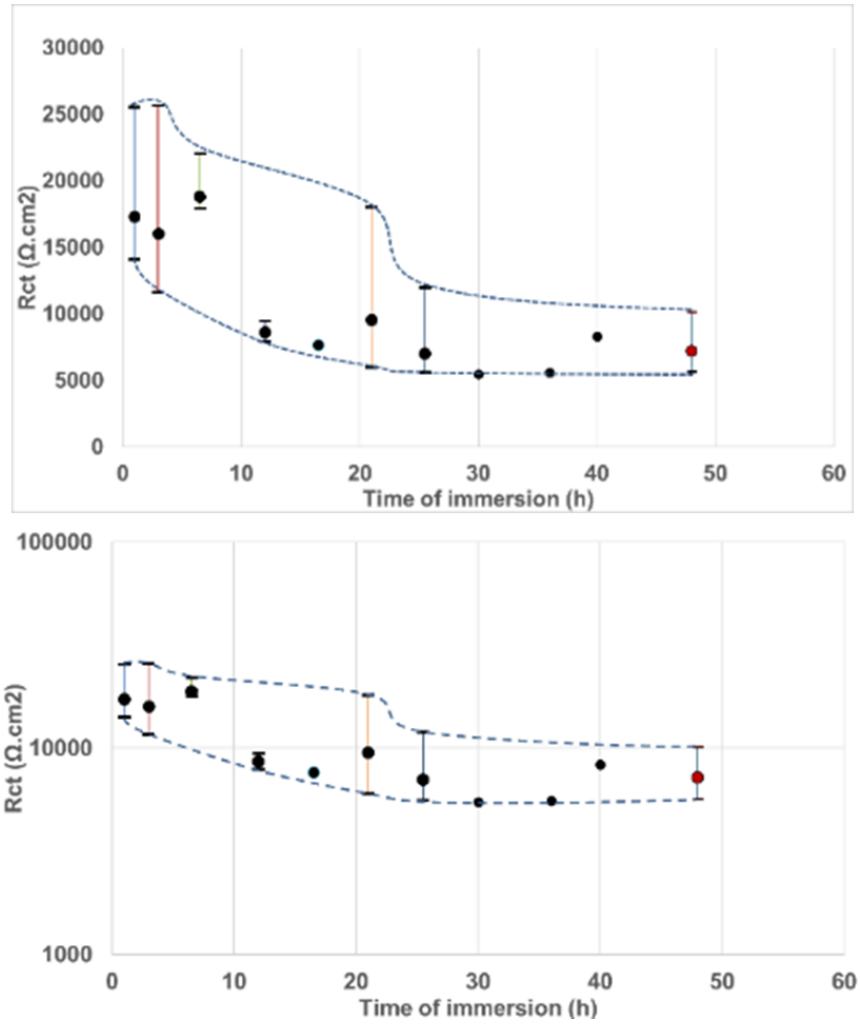

Figure 6.3.15 Collection of the old and new EIS vs immersion data of the additive sample (EC+Additive) formed at 240 °C (transfer to R_{ct} vs time).

6.3.1.5 $Mg(OH)_2$ films on AZ31 ME substrates

EC treatment and Additive processing are also applied to the AZ31-ME substrates. Immersion tests in 3.5^{wt}% NaCl solution and EIS measurements are also undertaken in the coated samples. This section shows the OCP and EIS results for the EC sample and EC+Additive sample of AZ31-ME substrates.

AZ31 ME with EC film

Figure 6.3.16 shows the EIS and OCP results of the AZ31-ME sample with EC treatment in 3.5^{wt}% NaCl solution for upto 45h. The sample is treated with 420µA/cm^2 current density at 60°C.

The Nyquist plot from the EIS measurements is shown in Figure 6.3.16 a. The plots of this sample have a smoother profile than the EC samples with the AZ31-

GF substrates. The Nyquist plots of this sample are also semi-elliptical shapes squeezed at the y-axis with an aspect ratio of 0.32 at the first 5 minutes of immersion. The plots are more regular semi-circle shaped with longer immersion that the aspect ratio increased to 0.42 at the end of the test.

The size of the plot decreases with immersion time which indicates a decrease in R_{ct}. Figure 6.3.16 b shows the R_{ct} versus the time of immersion. The initial R_{ct} at 5 min reaches 15800 Ω.cm^2. It quickly dropped to around 7700 Ω.cm^2 at 2h and followed by 5200 Ω.cm^2 at 8h. Then, the drop of R_{ct} slows down. The R_{ct} after 1 day keeps around 3kΩ.cm^2. After 2 days, the R_{ct} dropped to around 2300 Ω.cm^2. The E_{OCP}, Figure 6.3.16, stables at around -1.55V_{SCE} similar to the uncoated AZ31-ME substrate.

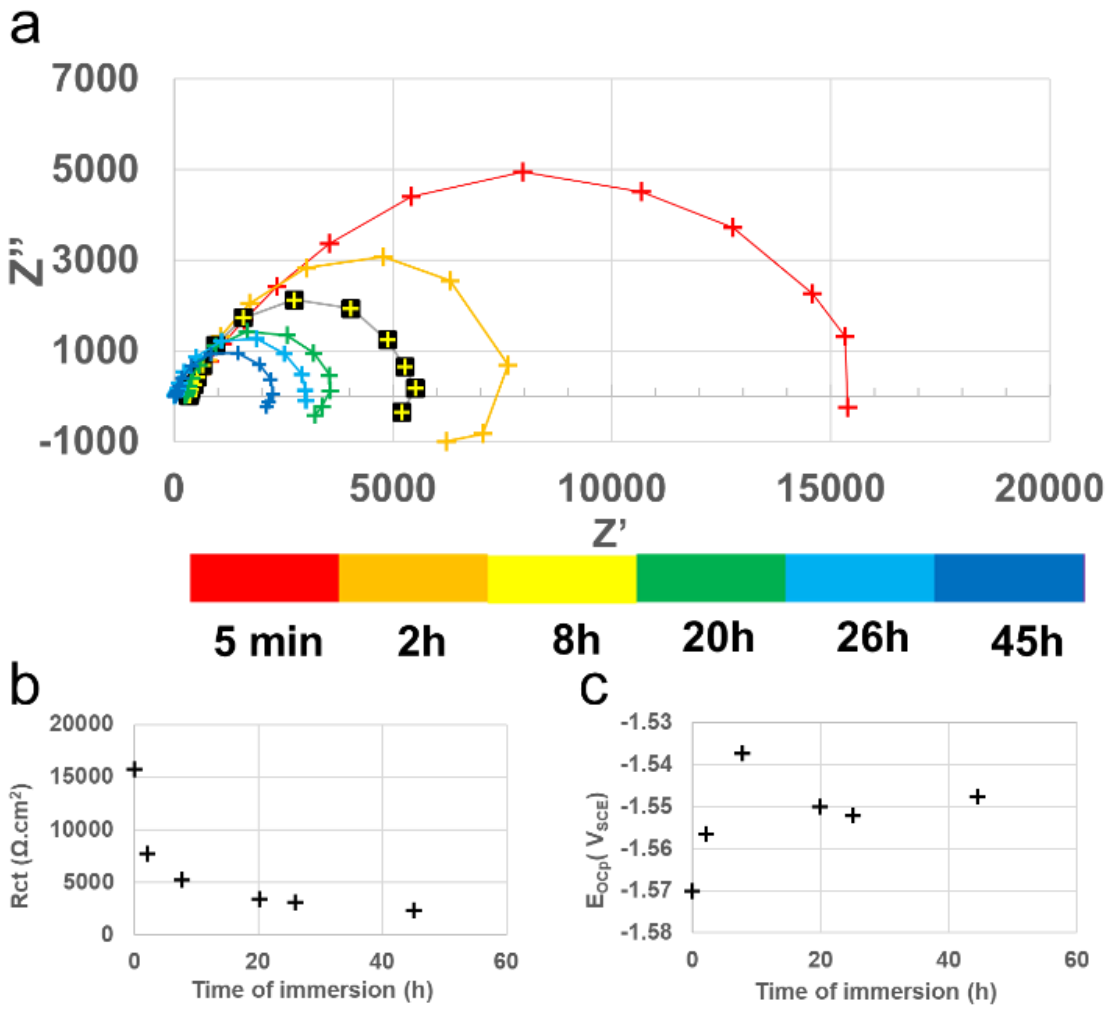

Figure 6.3.16. The EIS and OCP results of the EC-treated AZ31-ME sample (420μA/cm^2, 60°C and 24h) under 45h immersion test in 3.5^{wt}%. a) the Nyquist

plots of the EIS measurements during immersion, b) R_{ct} vs time of immersion and c) E_{OCP} vs time of immersion.

Figure 6.3.16 c shows the E_{OCP} of the measurement versus the time of immersion. The initial E_{OCP} at 5min is around -1.57 V_{SCE}. During the first 8 hours of immersion, the E_{OCP} increased to around -1.54 V_{SCE}. Then it slightly dropped to around -1.55 V_{SCE} at 20h and stabilised at this level until the end of the test of 45h. E_{OCP} of this EC sample shows a similar E_{OCP} range measured from the uncoated AZ31-ME substrate, Figure 6.2.3.

Figure 6.3.17 compares the R_{ct} vs time of the EC-treated (420µA/ cm^2, 60°C) samples with uncoated AZ31-ME substrates. Besides, the R_{ct} vs time of the uncoated AZ31-ME sample is in the figure as a reference

The R_{ct} of the EC AZ31-ME samples (cross) is four orders of magnitude at the beginning of immersion, around 50 folds of the uncoated sample. Then R_{ct} dropped to around 2kΩ.cm^2. Compare to the EC+Additve film on AZ31-GF. The EC+Additve sample exhibits a higher overall corrosion resistance.

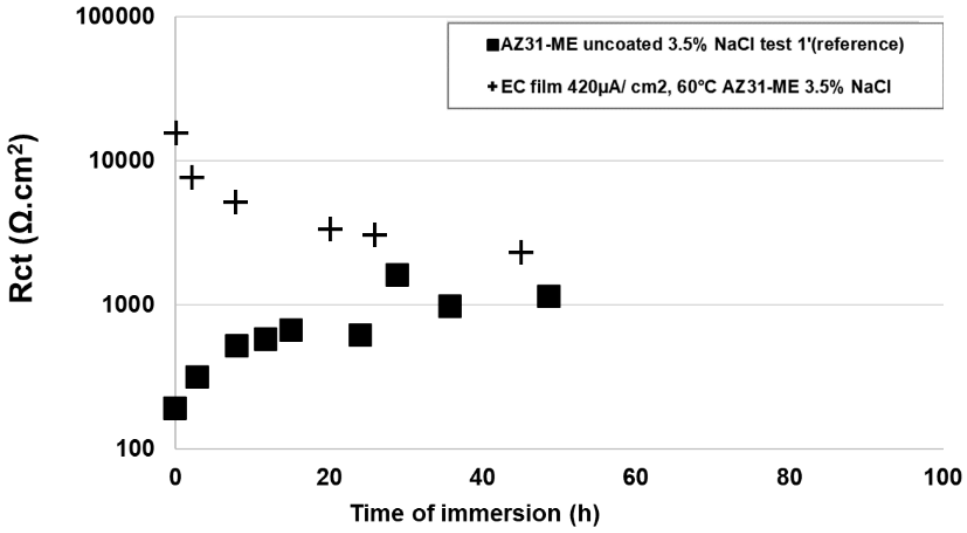

Figure 6.3.17 Summary of the R_{ct} vs time of EC treated samples (AZ31-ME as substrate) (cross) (420µA/cm^2, 60°C and 24h) compared with the results of uncoated substrate.

AZ31-ME with EC+Additive film

Figure 6.3.18 shows the EIS measurement of an EC+Additive sample with AZ31-ME substrates in 3.5% NaCl solution for upto 2 days.

The Nyquist plots from the EIS measurements are shown in Figure 6.3.18a and 6.3.18b. The R_{ct} of the EIS measurements versus time is summarised in 6.3.19c. All the Nyquist plots of this sample are smoother than the sample of AZ31-GF with the same treatment. At the initial 10min of immersion, it has a large semicircle at the initial 10 min of immersion, leading to a R_{ct} of about 15kΩ.cm^2. Then the later EIS measurement gave smaller plots, and the R_{ct} dropped around 4kΩ.cm^2. The OCP measurement fitted from the Nyquist plots against immersion time is shown in Figure 6.3.18 d. The OCP of this sample are between -1.54 and -1.55 V_{SCE} during immersion which is also similar to the uncoated AZ31-ME.

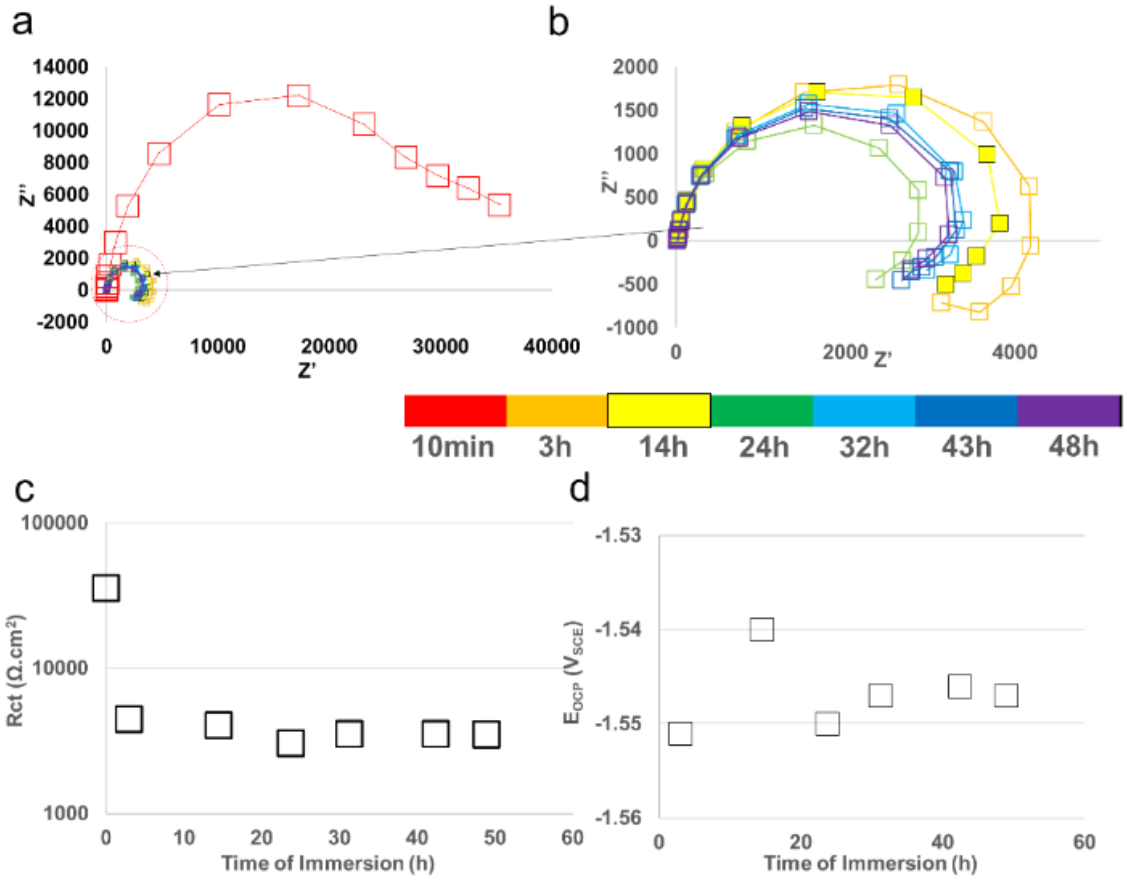

Figure 6.3.18. The EIS results of the EC+Additive sample on AZ31-ME substrates (with EC treatment with 420μA/cm^2, at 60°C for 24h, and additive treatment at 240°C) under 2 days immersion test in 3.5^{wt}%. a) and b): the Nyquist plots of the EIS measurements during immersion, and c) E_{OCP} vs time of immersion.

Figure 6.3.19 compares the R_{ct} vs immersion time of the EC+Additive sample in AZ31-ME (EC treatment 420µA/cm^2 60°C plus additive treatment at 240°C), and the results for the uncoated AZ31-ME samples are also shown as a reference.

The EC+Additive sample on AZ31-ME substrate has around three times the R_{ct} of the uncoated samples. However, the R_{ct} is halved compared to the EC+Additive sample on the AZ31-GF substrate (Figure 6.3.14). It is attributed to the film thickness difference that the film thickness of the EC+Additive sample in AZ31-GF is double of the EC+Additive sample in AZ31-ME substrate.

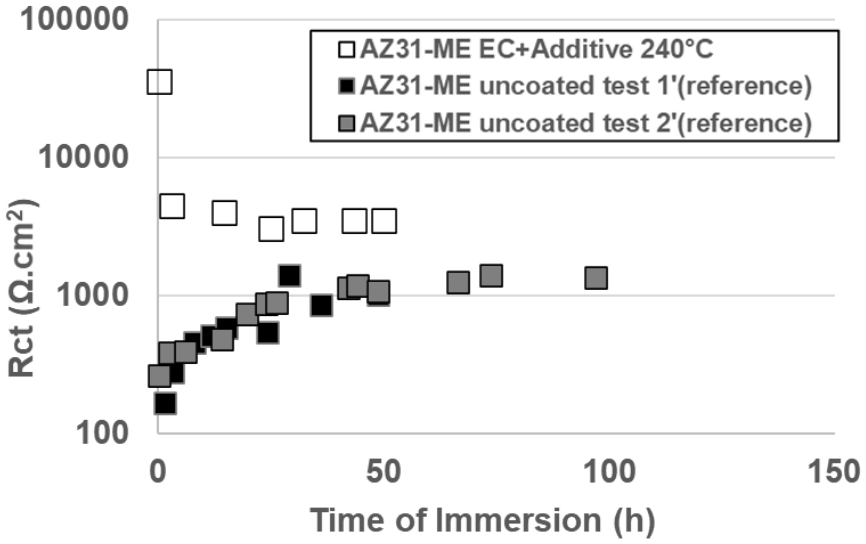

Figure 6.3.19 Summary of the R_{ct} vs time of additive sample (AZ31-ME as the substrate) at 240°C with the EC pre-treated (420µA/cm^2, 60°C and 24h).

Compare the EC+Additive sample in AZ31-ME with the just EC treated sample in AZ31-ME (Figure 6.3.17). There is a small increase to the R_{ct} around 1kΩ.cm^2.

6.3.2 Post corrosion characterisation

6.3.2.1 AZ31 GF

HT film after immersion tests (with EIS)

The SEM cross-sections of the HT sample at 160°C for 30min and 1h after immersion test in 3.5^{wt}%NaCl solution for 1 day is shown in Figure 6.3.23 a and 6.3.6b respectively. The films are indicated between yellow marks.

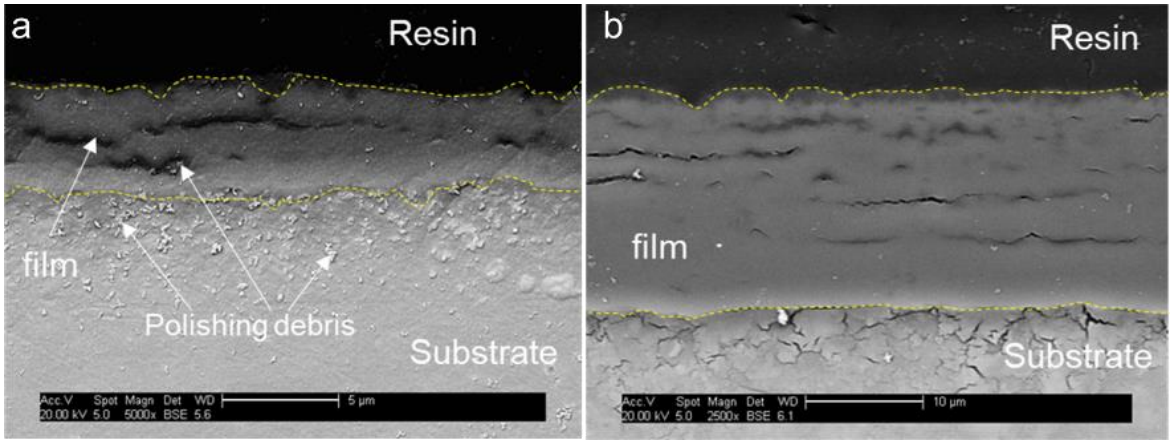

Figure 6.3.20 the post-corrosion the cross-sectional SEM image of the HT sample at 160°C for a) 30min and b) 1h.

The average thicknesses measured from this figure are 4.5 µm and 18.2 µm respectively. It indicates no significant change in the film thickness after 1-day immersion in 3.5% NaCl. The HT films kept the laminar structures with lateral gaps and voids as the cross-section before corrosion previously shown in chapter 5.1. Defects at the interfaces after corrosion tests. Crevices are observed in Figure 6.3.21b. it may be due to corrosion damage; otherwise, it is just due to residual NaCl that corrodes substrate with air moisture post mount. For the HT sample with 30min processing, Figure 6.3.21a, polishing debris near interface was observed. It is due to the crevices that trap polishing debris.

EC+Additive film

Figure 6.3.22 shows the typical cross-section microscopy of the EC+Additive films formed at 160°C, 200°C and 240°C immersion in 3.5^{wt}% NaCl solution for 1 day and 2 days. These samples are the same samples tested with EIS measurement and are shown in Figure 6.3.14.

There is no significant change in the EC+Additive samples at 160°C, after one-day of immersion. But after 2 days, a large number of pores of voids are observed near interface. Formation of the voids is likely due to the loss of the crystals feature of the film shown in 5.4.5. At 200°C and 240°C, there is no significant change for the EC+Additive films except small gaps or pores in the film were expanded after 2 days, shown in 6.3.22e and 6.3.22f. Corrosion filaments are also observed in some of the samples to the corrosion post mount.

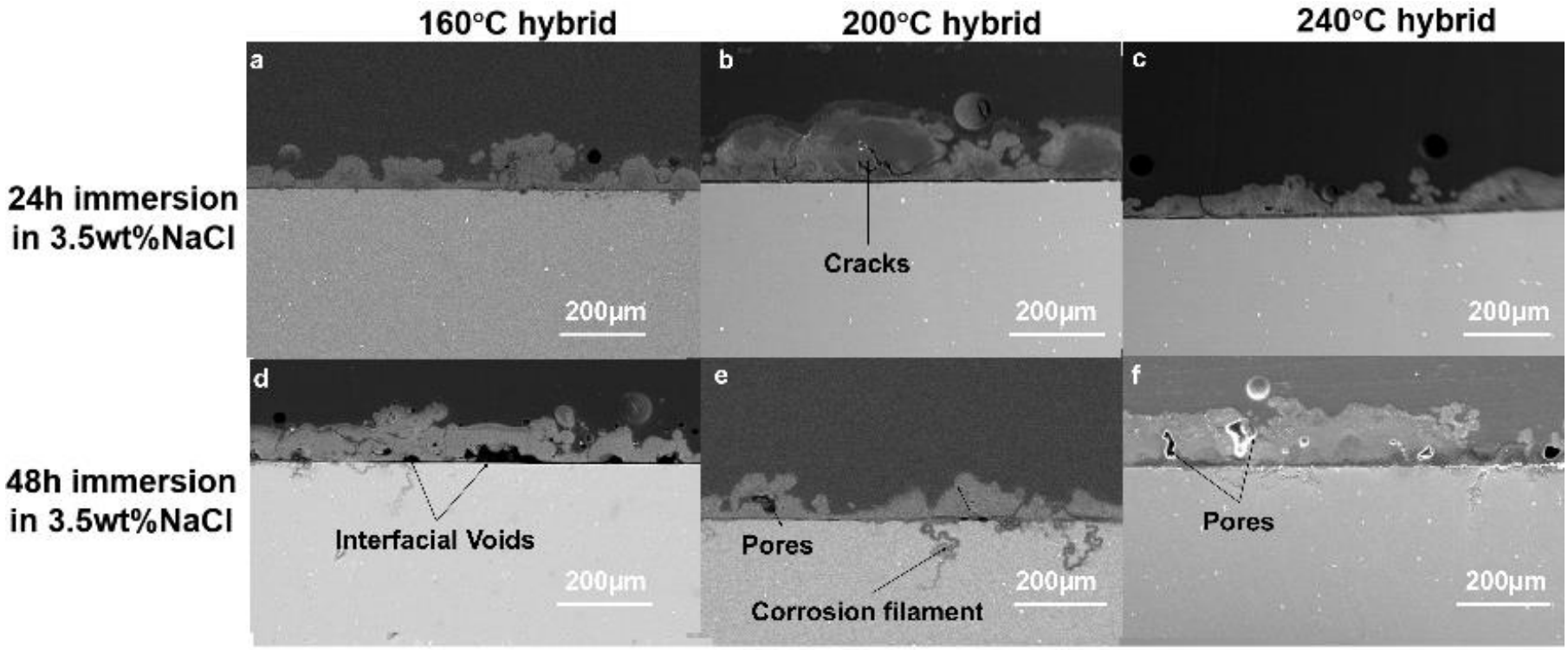

Figure 6.3.21. The cross-section of the EC+Additive films on AZ31-GE after immersion for 1 and 2 days.

6.3.2.2 AZ31 ME

Figure 6.3.22 shows the post corrosion characterisation of the EC+Additive film on AZ31-ME at 240°C, corresponding to Figure 6.3.16 and 6.3.17. There is no significant damage to the film. However, the film-substrate interface is undermined because particles are likely embedded at the interface.

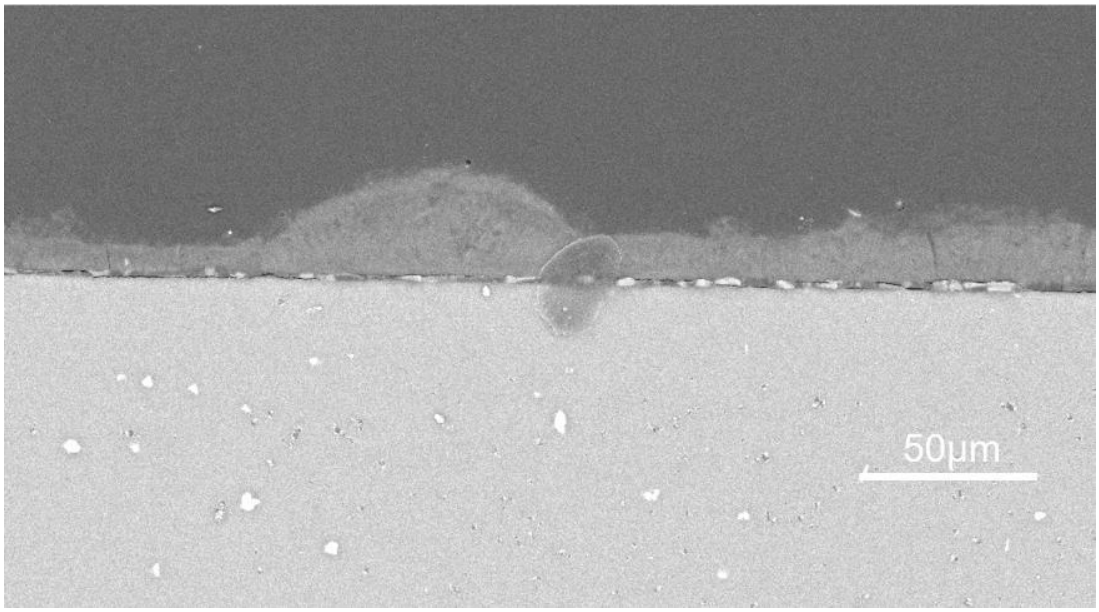

Figure 6.3.22 The cross-section of the EC+Additive film (at 240°C) on AZ31-ME after immersion for days.

6.3.3 Comments on 6.3

When the sample is coated with HT films, the charge transfer resistance, $R_{ct,}$ greatly increased compared with the uncoated substrates. The R_{ct} sharply reduced by 2 to 3 orders of magnitude with an unstable E_{OCP} at the first few hours of immersion. Post corrosion characterisation shows no significant damage to the integrity of the coatings and interface., Considering the laminar structure with lateral cracks observed on the HT films, At the initial exposure, the pathway between the solution and the substrates may be opening up through the layers, therefore, leading to the sharp decrease in R_{ct}. the coating of the sample with just EC processing exhibiting platelets morphology with higher porosity level seems much easier to open up the pathway for solution to reach substrate therefore with a much lower R_{ct} than the HT and EC+Additive films.

The combination of EC and additive processing can produce $Mg(OH)_2$ based films that improve the corrosion resistance of substrate for a period if optimal processing parameters are adopted. The cross-section image of the additive films in Chapter 5.4 also shows the EC+Additive sample has dense film structures compared to the additive sample without EC treatment. It also narrows down the processing parameters for the following investigation of the additive film. The following experiments only focus on the EC+Additive samples with the EC pre-treatment with 420μA/cm^2 at 60 ºC.

6.4 Summary

Mg alloy AZ31 samples with various $Mg(OH)_2$ coating methods are tested for corrosion resistance by OCP and EIS measurements in the tranquil 3.5% NaCl solution close to the seawater.

The charge transfer resistance R_{ct} of uncoated AZ31 samples started around 200 to 400 Ωcm^2 just exposed to the solution and then increased to around 700 Ωcm^2 after 48h immersion. The increase in R_{ct} is due to the formation of the corrosion product layers.

At the initial exposure to the solution, the coated samples with hydrothermal treatment have R_{ct} up to five orders of magnitude (550kΩcm^2), more than uncoated substrates, showing corrosion resistance is offered to the alloy. However, R_{ct} sharply decreased since the beginning of immersion, possibly due to the wetting and degradation of the films, and then stabilises to four orders of magnitude at around 12h immersion.

With the EC processing at RT, the AZ31 samples exhibit similar resistance to the uncoated sample. When processed at 60°C, the R_{ct} at the initial exposure slightly increases to between 1 to 2k Ωcm^2 but then decreased to a similar level to the uncoated sample after 48h. The low resistance of EC film is due to the limited thickness and the porous structure of the $Mg(OH)_2$ platelet structures.

The additive coating with an EC seeding layer can reach a R_{ct} upto 30k Ωcm^2 when initially exposed to the solution, and the R_{ct} dropped to 3-10kΩcm^2. Specific results are summarised and listed in Table 6.4.1

The corrosion test in the 3.5^{wt}% NaCl solution is considered aggressive to the Mg(OH)2 coating, leading to severe degradation regardless of the processing methods. The next chapter shows the corrosion tests in less aggressive solutions with the ZM21 substrate that is more biocompatible.

Table 6.4.1. Summary of the corrosion test results for this chapter (coated and uncoated AZ31 substrates in 3.5^{wt}% NaCl solution).

Substrate	AZ31-GF			AZ31-ME		
	Initial Exposure (Ωcm^2)	2-4days immersion (Ωcm^2)	Longer term mass loss ($mg/cm^2/day$)	Initial Exposure	2-4days immersion	Longer term mass loss ($mg/cm^2/day$)
Uncoated	200-400	~700	0.22	200-400	1-1.4k	0.11
Hydrothermal	<1M	<30k	n/a	n/a	n/a	n/a
Electrochemical (EC only)	<8k	~1k	n/a	15k	2.3k	n/a
EC+Additive	<20k	<6k	Shown in next Chapter 7	15k	4k	Shown in next Chapter 7

7 Biomedical application investigation

7.1 Introduction

In this chapter, further studies are carried out, considering the application and corrosion of Mg alloys with $Mg(OH)_2$ film for less aggressive biomedical environments. An extruded Mg alloy ZM21 (2^{wt}% Zn and 1^{wt}% Mn) from Magnesium Elektron (ZM21-ME) is used in this study. Although it is also a commercial grade alloy, ZM21-ME is considered more suitable for biomedical-related experiments than the AZ31 substrates as the Al element is neurotoxic [El-Rahman, 2003].

Section 7.2 firstly shows the characterisation and element composition of ZM21-ME. Then, Corrosion tests with Hanks solution are carried out for the Mg alloy samples uncoated and with EC+Additive films. The results are shown in section 7.2 and 7.3 respectively. The corrosion tests firstly include the 1-2 day immersion tests based on EIS and OCP measurements. Besides, longer-term immersion tests based on mass change measurements were also applied to simulate the degradation of Mg alloy. The results for the equivalent tests in other solutions (saline solution and 3.5^{wt}% NaCl solutions) and the previous substrate (AZ31-ME) are also shown as a comparison and reference.

7.2 Corrosion assessment

In this section, corrosion assessment for the Mg alloy ZM21-ME substrate and its sample after EC+additive treatment in the Hanks solution are shown. The assessment includes shorter-term (2-days) immersion tests with Electrochemical measurement (OCP and EIS) and longer-term (9 and 21 days) immersion tests with sample mass change measurements. Apart from Hanks solution, the test results in normal saline (0.9^{wt}% NaCl) and 3.5^{wt}% NaCl solution are also shown as a reference. The saline solution has a similar concentration of Cl^- irons to the Hanks solution but without other elements. 3.5^{wt}% solutions are used for the corrosion tests shown in the previous chapter 5.4 and 6.4 for ease of comparison. Besides, the results for AZ31 substrates are also shown for comparison.

7.2.1 Mg alloy substrate

7.2.1.1 Short term immersion test with OCP and EIS measurements

Figure 7.2.1 shows the OCP results for uncoated ZM21-ME substrates during immersion. Orange, blue and black triangles represent the OCP measurement in Hanks, saline and 3.5^{wt}% solutions respectively. Samples in all three solutions have initial lower E_{OCP} followed increase with immersion time. It can be explained by the initial altering of the sample surface that metals react with solutions to form a corrosion product layer of $Mg(OH)_2$. For a longer immersion, the E_{OCP} stabilised, which indicates the full coverage of the surface layer. E_{OCP} in Hanks solution spends a longer time (~25h) to stable than in the saline solution (~11h) and 3.5^{wt}% NaCl solution (~15h). After stabilising, the E_{OCP} is around -1.50V in Hanks and saline solution and -1.55V in 3.5^{wt}% NaCl solution. The lower E_{OCP} in 3.5^{wt}% NaCl solution is attributed to its higher Ion concentrations, thus a higher solution conductivity.

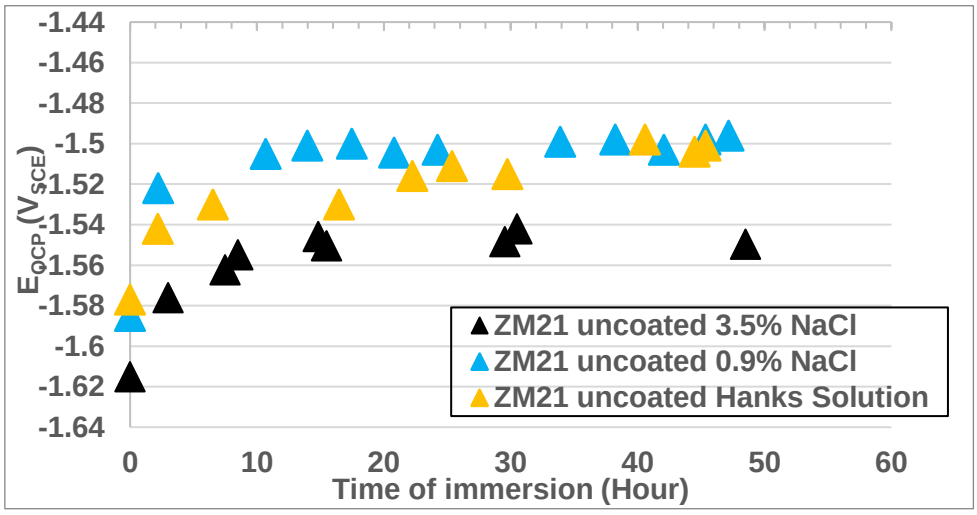

Figure 7.2.1. open circuit potentials vs immersion time of the uncoated ZM21-ME substrate in Hanks, saline and 3.5^{wt}% NaCl solutions for a 2-day immersion test.

Figure 7.2.2 shows the Nyquist plots from the EIS measurement just after OCP measurements. The EIS measurements at different immersion times are represented with different colours. It produces uniform semi-circles shape plots except for a small variation in the low-frequency region. The diameters of the semi-circle plots are between 8kΩcm^2 to 11kΩcm^2. EIS measurements are also

carried out for ZM21-ME substrates in 0.9 and 3.5^{wt}% NaCl. Both show semi-circle shapes except with smaller diameters.

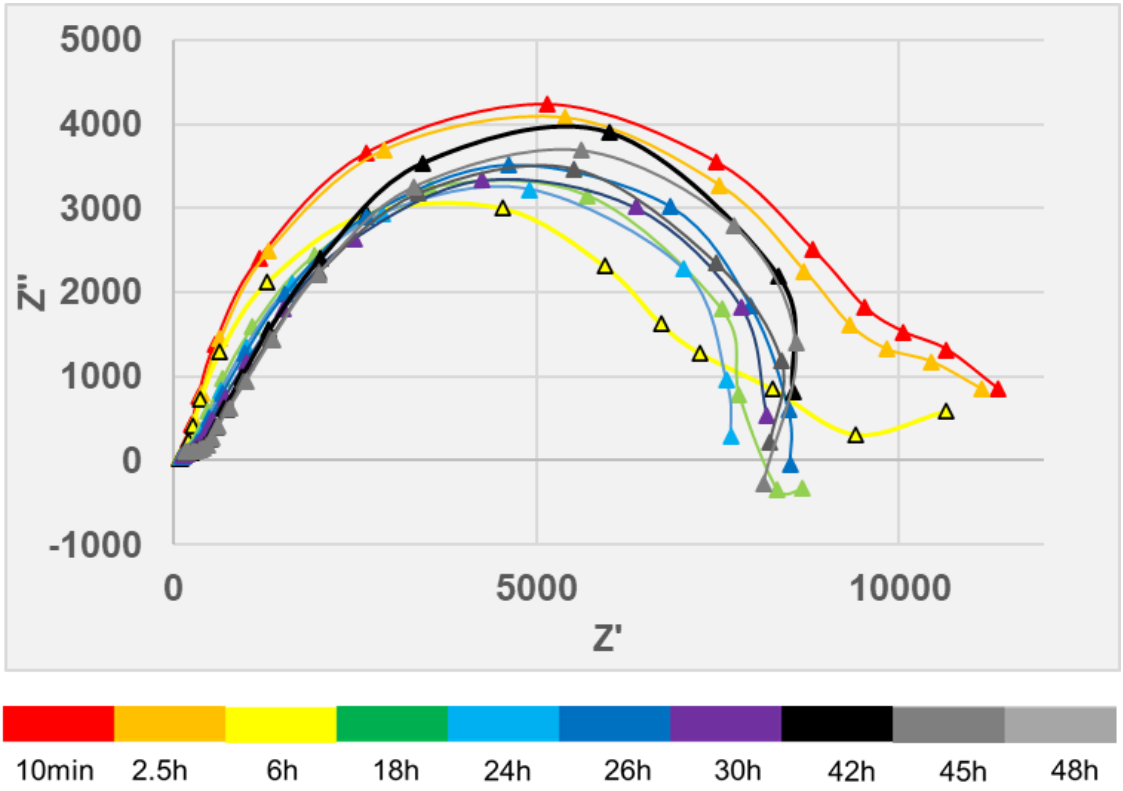

Figure 7.2.2. EIS Nyquist plots for the immersion tests that ZM21-ME sample Hanks solution for 48h.

Then the charge transfer resistances R_{ct} are evaluated with the semicircle fitting to the Nyquist plots. The R_{ct} are summarised in Figure 7.2.3 against the time of immersion. | In Hanks solution, the ZM21 substrate has an initial R_{ct} around 9k Ωcm^2 and slightly drops to around 7kΩcm^2 at 7h. Then, the Rct gradually increases and reached a maximum of 17kΩcm^2 then followed by a drop and ended at around 10k. For saline and 3.5^{wt}% NaCl solution, the Rct keep at a lower level around 2k and 1k respectively. They also rise and drop in R_{ct} in the beginning few hours of immersion and then increase gradually with further immersion. In Hanks solution, the R_{ct} keeps stables at around 10kΩcm^2, around ten folds to the R_{ct} in 3.5^{wt}% NaCl solution and 5 times to the saline solution. It indicates that both the concentration of NaCl and other elements can significantly influence the aggressiveness of the test solutions. The rise-and-drop of the Rct in the beginning few hours just corresponds to the period of increase in E_{OCP}. It

is likely due to a sequence of oxides decomposition, metallic surface exposes and then corrosion product layer buildup.

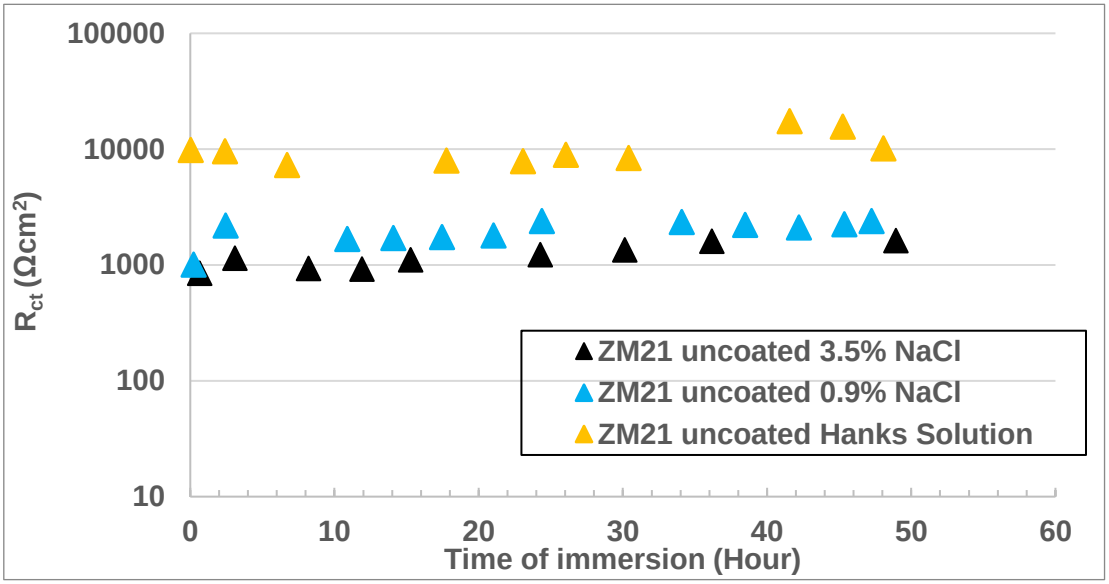

Figure 7.2.3 Summary of the charge transfer resistance versus the immersion time for uncoated ZM21-ME substrate in Hanks, saline and 3.5^{wt}% NaCl solution during 48h immersion tests.

OCP and EIS results versus immersion time for AZ31-ME are summarised in Figure 7.2.4 as a reference to ZM21. Generally, both E_{OCP} and R_{ct} for AZ31-ME have similar trends for ZM21-ME where Hanks solution > saline solution > 3.5% NaCl solution. The R_{ct} and E_{OCP} data points of AZ31-ME are slightly more scattered. The OCP measured in saline solution is also lower than in Hanks solution. Besides, at the end of immersion in Hanks solution for 41 and 48h, the R_{ct} of AZ31-ME in Hanks solution further increased rather than decreased in ZM21.

a)

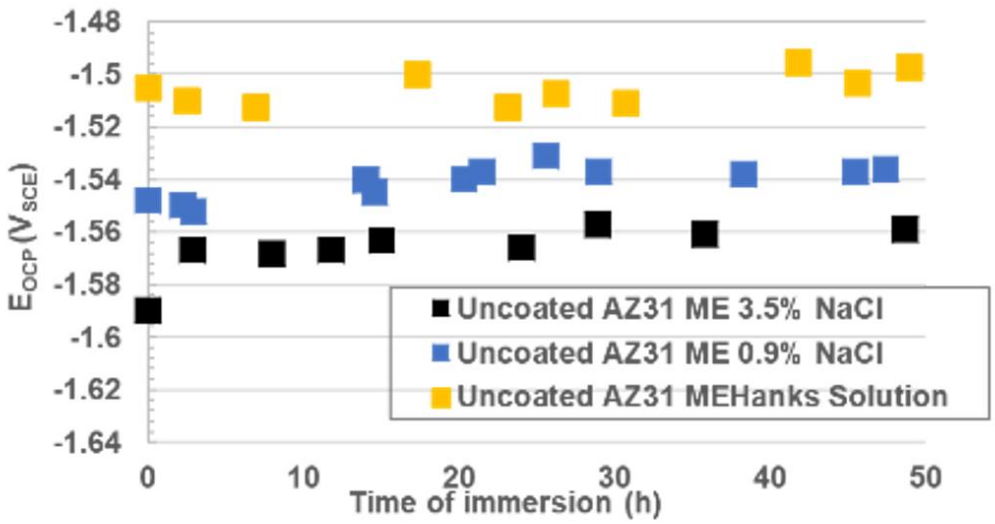

b)

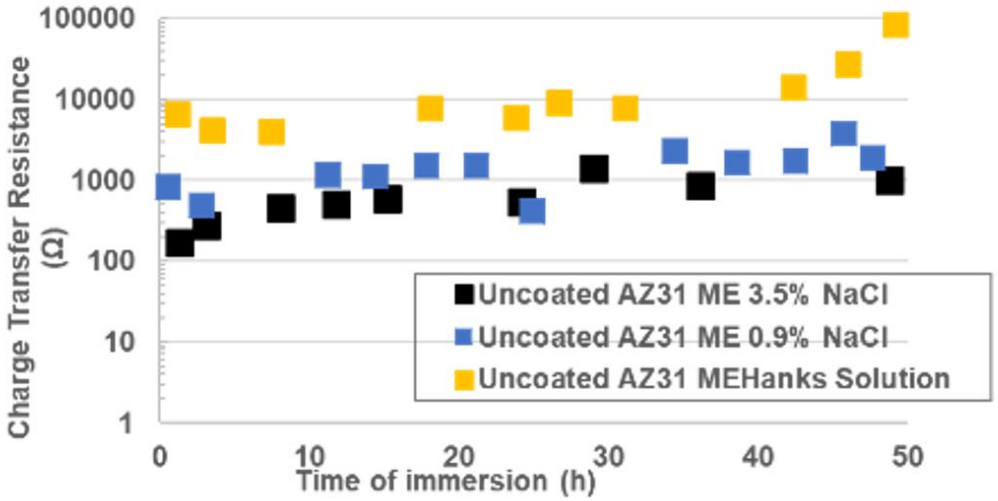

Figure 7.2.4. Summary of the a) E_{OCP} and b) charge transfer resistance versus the immersion time for uncoated AZ31-ME substrate in Hanks, saline and 3.5^{wt}% NaCl solution during 48h immersion tests.

7.2.1.2 Long term immersion tests with mass change measurement

The mass changes of ZM21-ME substrates during 21-day immersion tests in Hanks solution are shown in Figure 7.2.5, with the tests in saline and 3.5^{wt}% NaCl solutions as reference. It shows the sample mass at the first 3 days of immersion increases or stays the same and then followed by a continuous decrease. The mass increase is because $Mg(OH)_2$ corrosion product surface layer has a higher

molar mass than metallic Mg. With longer immersion, the corrosion product layer dissolves into the solution and leads to mass loss. The average mass reduction rate for ZM21 in Hanks solution is at a low rate of 0.00005g/cm^2/ day^{-1}.

The total mass loss of ZM21 in Hanks solution after 21-day immersion is about 30% of 3.5^{wt}% NaCl and 40% of saline solution after 21 days. At the end of immersion, the mass-loss rates trend to increase for NaCl solutions while the mass in Hanks solution tends to be stable and unchanged. It indicates a trend that mass loss differences between Hanks solution and NaCl solutions are likely to become larger with longer immersion.

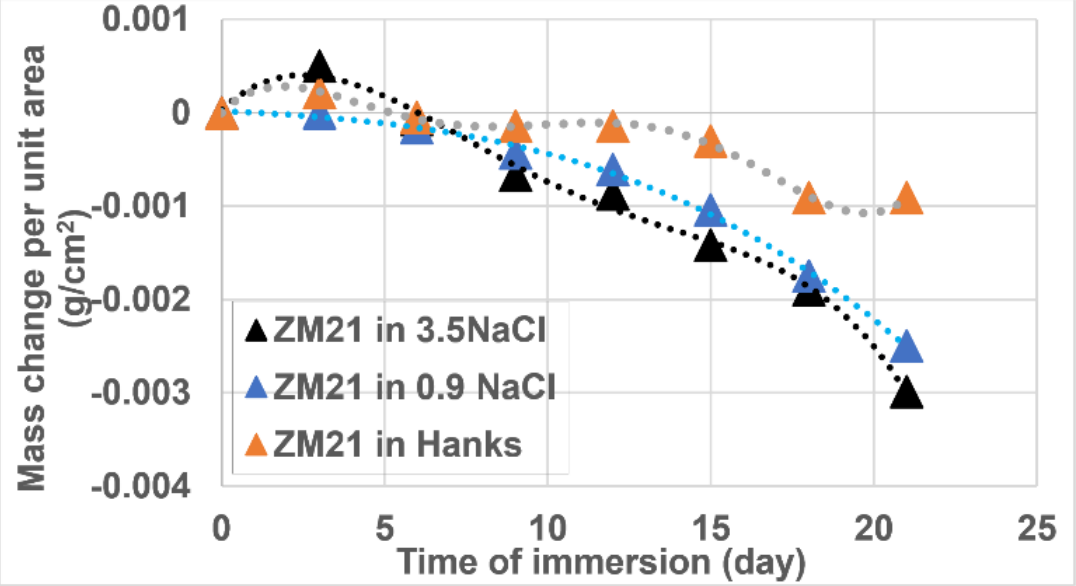

Figure 7.2.5. Mass change per unit area versus immersion time of uncoated ZM21-ME substrates in Hanks, saline and 3.5^{wt}% NaCl solution for 21 days of immersion tests.

For AZ31-ME substrate in the same condition is applied and shown in Figure 7.2.6. At Hanks solution, AZ31-ME substrate started to increase mass instead of losing mass between day 3 and day 5. Then the mass stabilised with around 0.00035g/cm^2 mass gain. The test in 3.5^{wt}% NaCl solution for AZ31-ME shows the same behaviour as the ZM21-ME samples that an initially increased mass on day 3 and then dropped to around -0.003g/cm^2 on day-21.

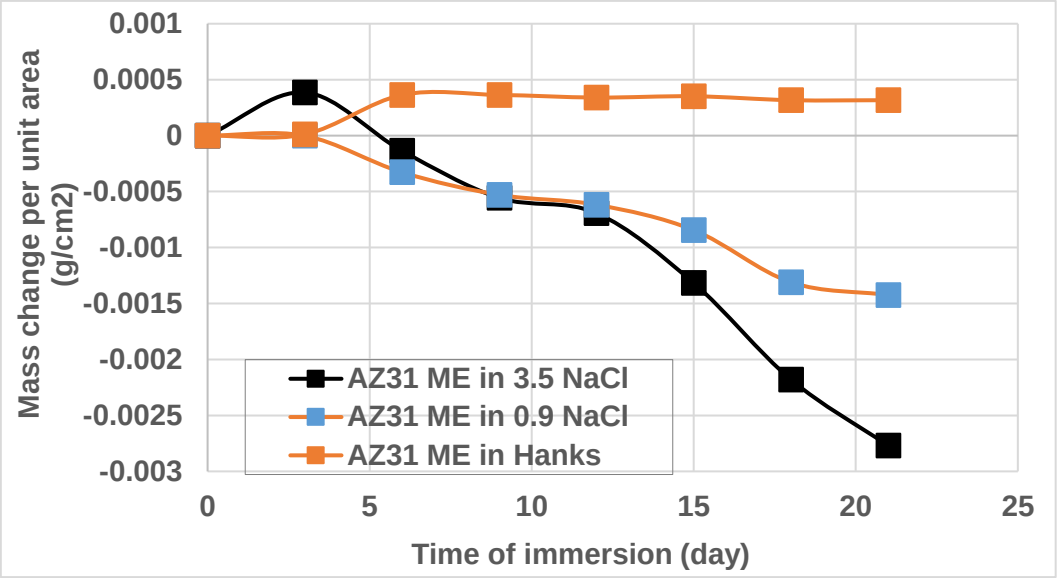

Figure 7.2.6 Mass change per unit area versus immersion time of uncoated AZ31-ME substrates in Hanks, saline and 3.5 wt% NaCl solution for 21 days of immersion tests.

7.2.1.3 Post corrosion characterisation

The top surface of the samples during long term immersion tests with Hanks solution, saline solution and 3.5 wt% NaCl solutions are shown in Figure 7.2.7. The ZM21 surface in Hanks solution, Figure 7.2.7 row 1, was first transferred from silver metallic surface(just abraded) to Bronze Metallic surface. Then part of the metallic surface became dull. Pits and a small portion of black corrosion product layers were observed at the centre and edges of the sample respectively (day 3). With longer immersion, the dull surface area increases and darkens into black or dark grey corrosion product layers. The area of the black corrosion product layer further increases with immersion time. At the end of the test of 21 days, the black corrosion product layer dominates the surface area, leaving a small portion of the area with the bronze metallic surface area. Meanwhile, at a corner of the sample, some newly formed yellow or light grey areas are observed with higher roughness.

In saline solution, Figure 7.2.7 Row 2, it shows the same steps of surface altering but with faster progress. On day 3, the sample is dominated by the dull surface with a small portion of the bronze metallic surface. The dull surface further develops and darkened during immersion. At the end of immersion, the black

corrosion product layer covered most of the sample surface, and yellow/grey corrosion products also developed, having more area than the sample in Hanks solution.

With 3.5 ^{wt}% NaCl, Figure 7.2.7 Row 3, solution much faster progress of surface altering is observed. On day 3, the metallic surface had already fully transformed into a dull surface with black corrosion product filament developed. On day 9, the surface was already covered most with black corrosion products area. Yellow/grey corrosion products were also observed on day 9 in 3.5w^{wt}% NaCl solution, which was only observed at the end of the test in Hanks and saline solution. With further immersion, the proportion of yellow/grey corrosion product further increases. At the end of the immersion, the yellow/grey corrosion product became dominant, leaving a rough surface.

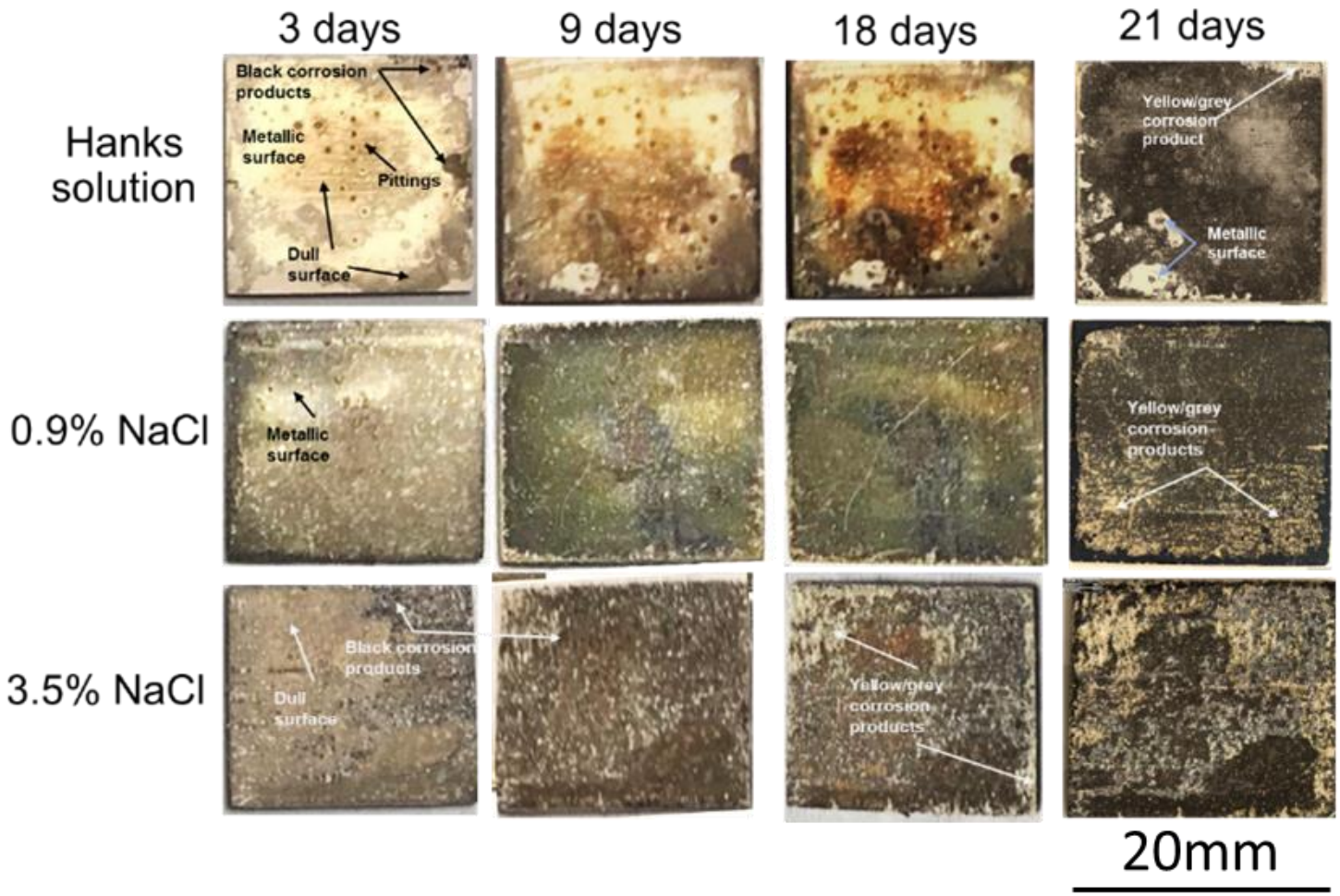

Figure 7.2.7. The characterisation of the top side of ZM21-ME samples shows the surface change during the immersion tests with Hanks solution, saline solution and 3.5 ^{wt}% NaCl solution for up to 21 days.

The back of the samples has slower progress than the top of the surface. Take an example of ZM21-ME in hanks solution for 21 days, Figure 7.2.8, it still contains a considerable area of the metallic surface (bronze). The black corrosion products are more likely developed as the filaments form, indicating a slower development. The yellow/grey corrosion product is not observed at the back of the sample. This difference is because the sample sits at the petri-dish during immersion, and the backside of the sample adjacent to the bottom of the petri-dish has less contact with the test solution. As the immersion is static, the diffusion and ion exchange at the backside of the sample is limited.

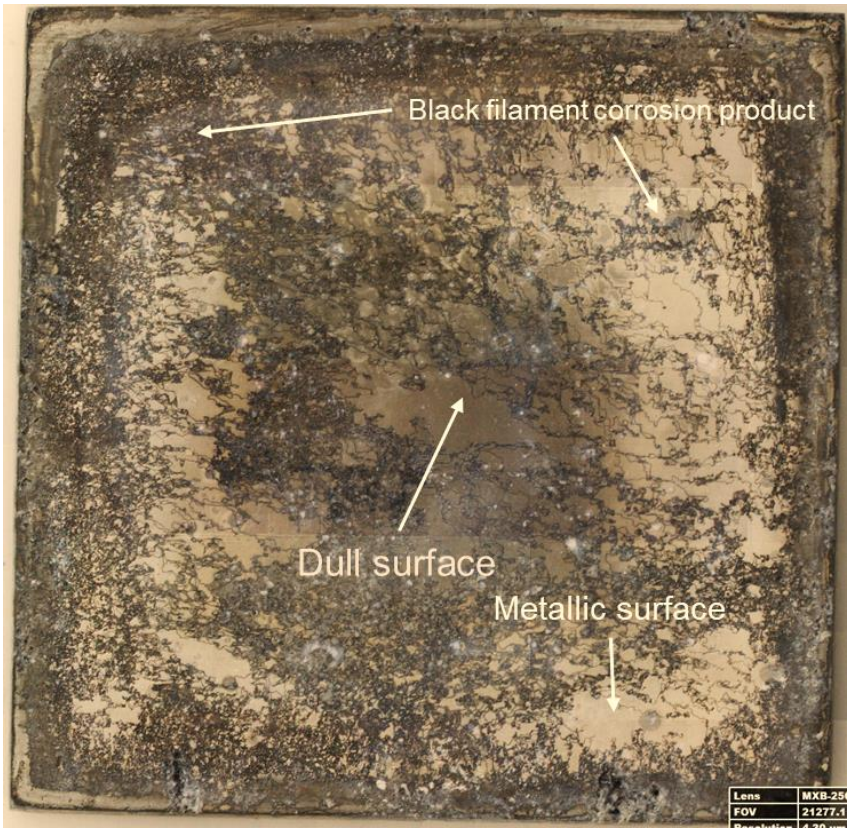

Figure 7.2.8 The characterisation of the backside of ZM21-ME samples immersed in Hanks solution for 21 days.

The AZ31-ME immersed in various solutions for 21 days are also shown in Figure 7.2.9 as a comparison. It has a different way of colour change and corrosion product development than the ZM21-ME substrates. After the metallic surface became dull, black corrosion products only developed in a small area with a filament form at the beginning of immersion and further reduced with immersion.

Other dull surface transforms into yellow/grey corrosion products directly. Corrosion products develop as both black and yellow/grey corrosion product likely to form along with the extrusion texture firstly. Defects usually have higher chemical activity and are more prone to corrode. With the development of corrosion products, it left fragmentary metallic surface areas (for ZM21-ME, the metallic surface area is more continuous. Large pits are not observed in the Hanks solution, but there are more small pits in 3.5 wt% NaCl solution for AZ31-ME compared to ZM21-ME. It is likely because the pits are from the local galvanic corrosion by the second phase particles such as Al-Mn intermetallics.

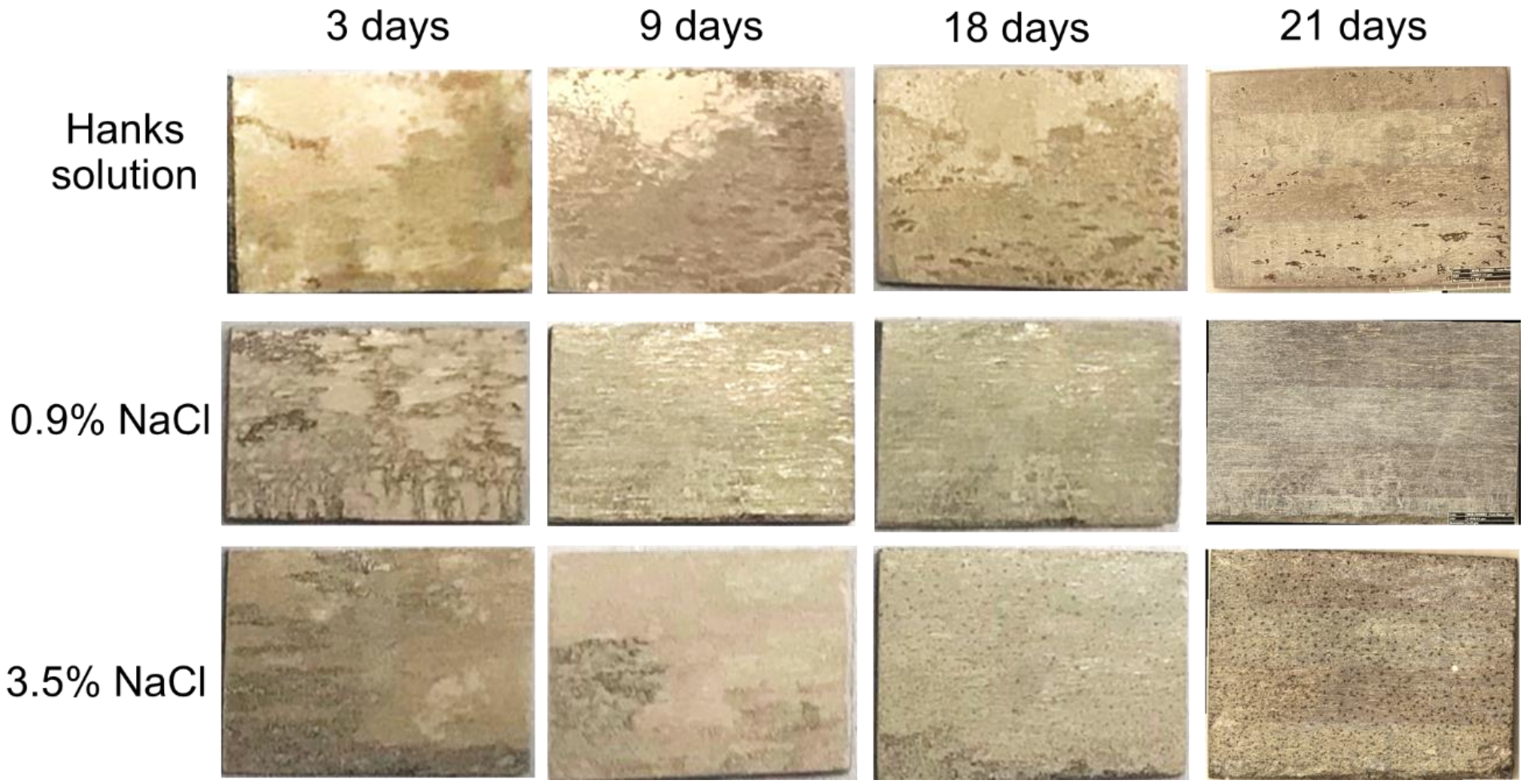

Figure 7.2.9. The characterisation of the top side of the uncoated AZ31-ME substrate shows the surface change during the immersion tests with Hanks solution, saline solution and 3.5 ^{wt}% NaCl solution for up to 21 days.

Figure 7.2.10 compares the post corrosion cross-section of the ZM21-ME substrate in Hanks and 3.5^{wt}% NaCl solutions respectively for 21 days. It produced a deeper loss of substrate in 3.5^{wt}% NaCl solutions which is up to around 100µm and left a rough surface. In the Hanks solution, the depth of corrosion is around 40 µm, and the corrosion products layer is well attached. Besides, an additional layer is deposited on the top that is rich in Ca detected by EDX.

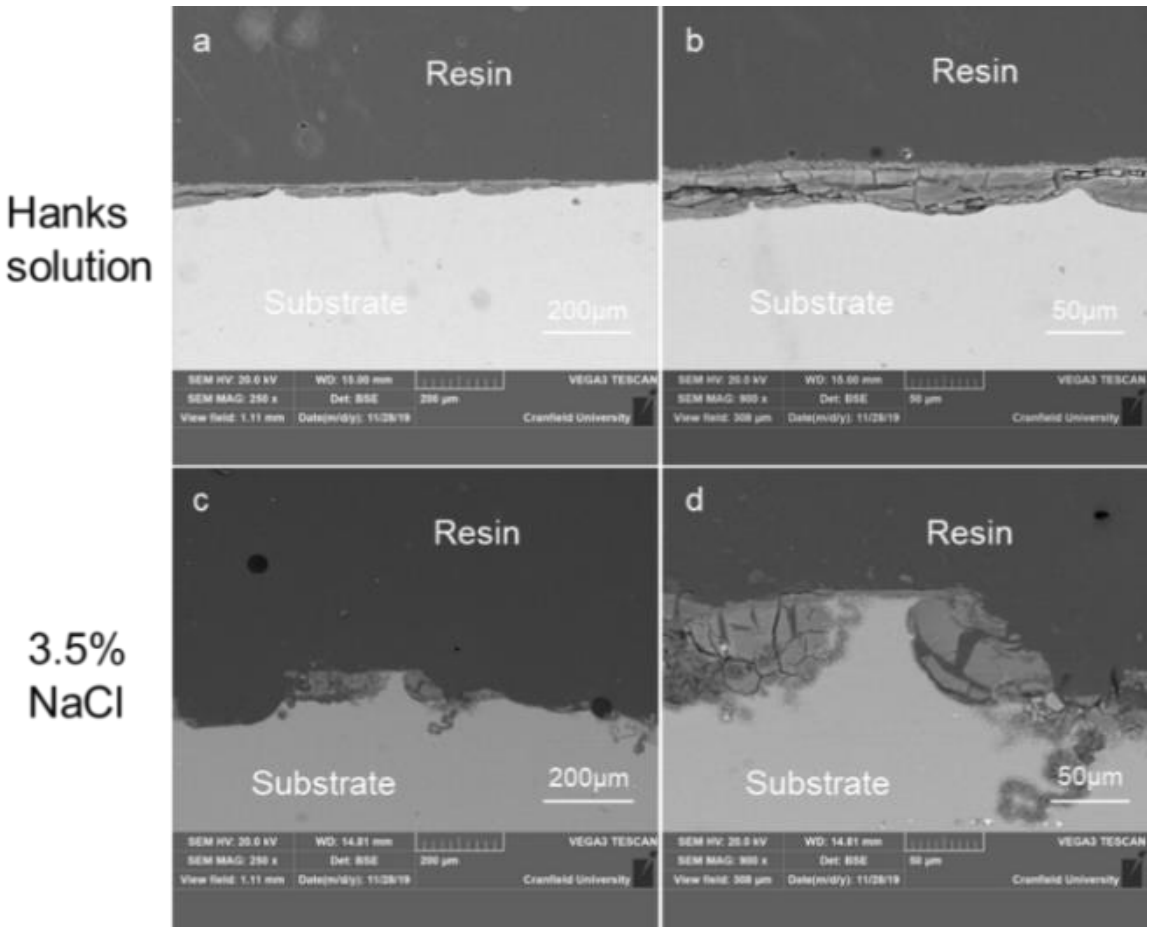

Figure 7.2.10 The cross-sectional SEM images of the ZM21-ME substrate immersed in a and b), Hanks solution and c), d), 3.5^{wt}% NaCl solution for 21 days. (corrosion product depth 24.7µm and 98.7 µm.

7.2.2 Coated Alloy with EC+Additive treatment

7.2.2.1 Short term immersion test with OCP and EIS measurements

Figure 7.2.11 and 7.2.12 summarise the OCP and EIS results of the coated ZM21-ME (with EC+Additive processing) in Hanks solution, saline solution and 3.5^{wt}% NaCl solution versus the time of immersion. It shows similar trends of the E_{OCP} results to the Uncoated samples except for a shorter time for E_{OCP} to stabilise (5-8h) for coated samples than for uncoated substrates (11h-25h). It is attributed to the existed $Mg(OH)_2$ film for the uncoated samples. Besides, the E_{OCP} for the Hanks solution and the saline solution is around 200mV higher than the uncoated ZM21-ME.

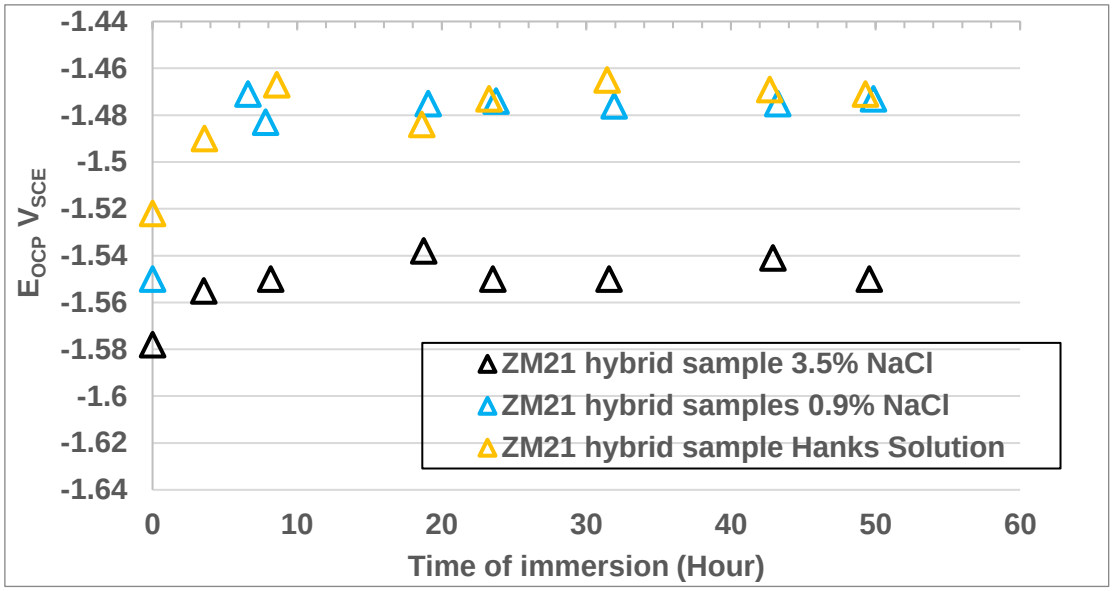

Figure 7.2.11 Summary of the E_{OCP} versus the immersion time for coated ZM21-ME samples in Hanks, saline and 3.5^{wt}% NaCl solution during 48h immersion tests.

For the EIS results, the coated samples in Hanks solution and saline solution kept stable R_{ct} throughout the immersion, which is around 35kΩ.cm^2 and 15k Ω.cm^2 respectively. In 3.5%^{wt}% NaCl solution, there is a decrease of R_{ct} around 15k - 3kΩ.cm^2 then stabilised. Compare to the uncoated substrates, coated sample has a 3 times, 4.5 times and 2 times improvement in the stabilised Rct for the coated sample in Hanks solution, saline solution and 3.5%^{wt}% NaCl solutions respectively.

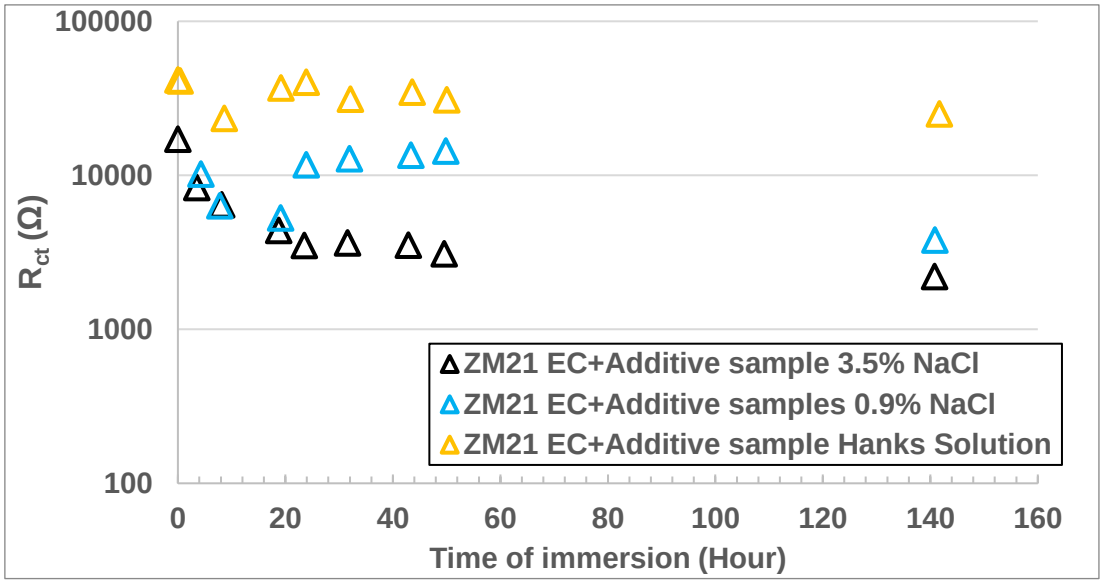

Figure 7.2.12 Summary of the charge transfer resistance versus the immersion time for coated ZM21-ME samples in Hanks, saline and 3.5^{wt}% NaCl solution up to 144h immersion tests.

7.2.2.2 Long term mass change measurement

Longer-term immersion tests were carried out for coated ZM21 samples with mass change measurements. The tests are up to 9 days in Hanks and 3.5^{wt}% NaCl solutions. The same tests were also carried out for AZ31-ME as a comparison.

The mass change results versus the time of immersion for coated ZM21-ME are summarised in Figure 7.2.13 a with the results of coated AZ31-ME as a comparison in Figure 7.2.13 b. The results for uncoated samples previously shown in Figure 7.2.5 and 7.2.6 are also put together as benchmarks in solid triangles and boxes.

Comparing all coated samples to the uncoated substrates generally, larger mass losses are observed for coated samples. It is possibly due to the dissolving or detachment of the films.

For the coated ZM21 samples, there is a loss mass of around 0.0012 g/cm^2 after in Hanks solution and 0.0026 g/cm^2 in 3.5^{wt}% NaCl solution after 9-day immersion. The AZ31-ME coated samples have a larger mass change loss. AZ31-ME samples in both Hanks solution and 3.5^{wt}% NaCl solution reduced

around 0.003g after 9-day immersion. AZ31-ME in Hanks solution exhibit a large variation in mass change with an initial increase then with a great reduced rate.

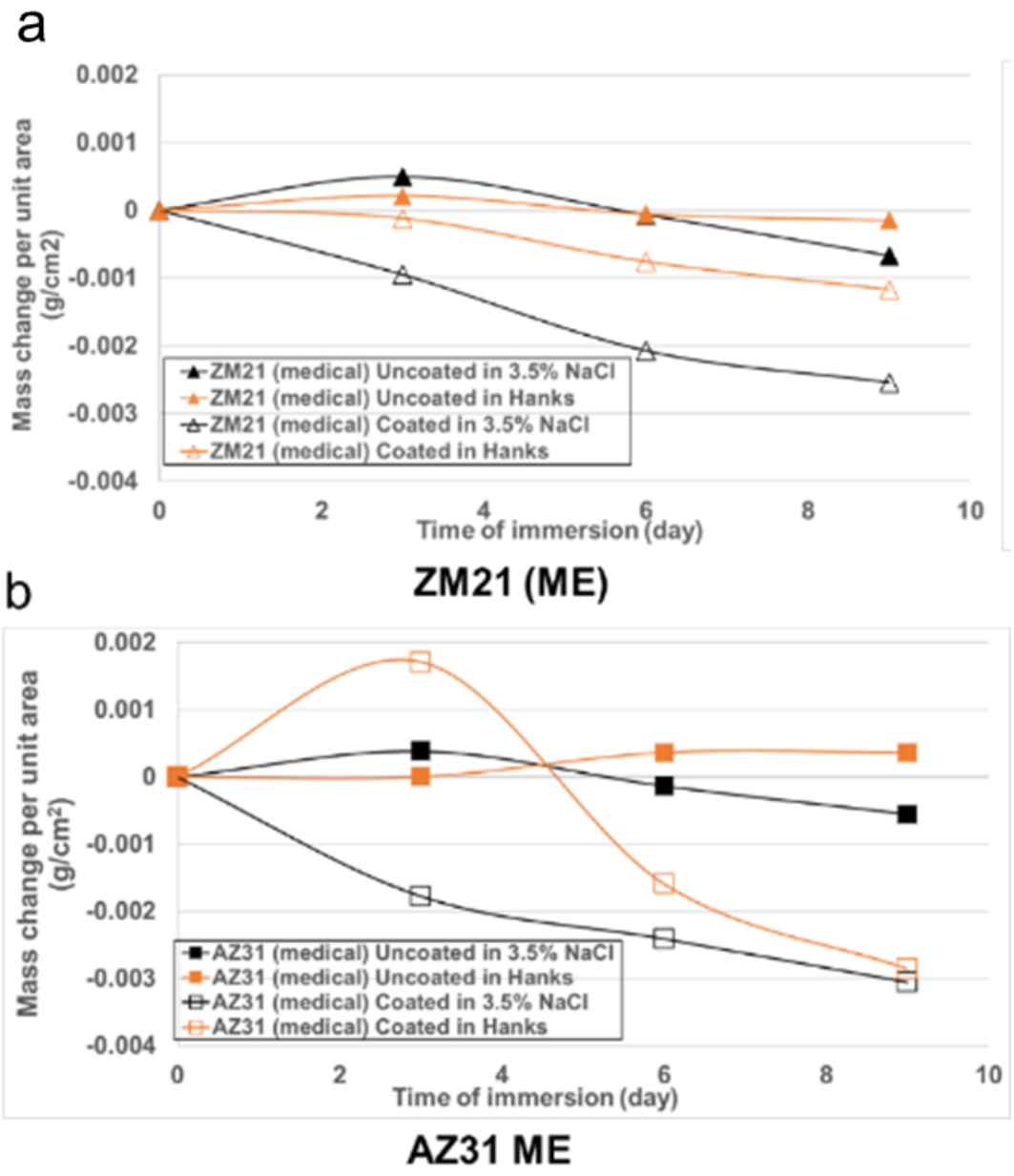

Figure 7.2.13 Mass change per unit area versus immersion time of a) ZM21-ME and b) AZ31-ME samples with EC+Additive film in Hanks solution and 3.5^{wt}% NaCl solution for 9 days of immersion tests.

7.2.2.3 Post corrosion characterisation

Figure 7.2.14 shows the post-corrosion characterisation of the coated ZM21-ME and AZ31-ME samples after 3 and 9-day immersion in various solutions. The

white features are the EC + Additive film produced, and the grey feature is the corrosion product layer from the corrosion of alloy substrates.

For both alloys in the Hanks solution, the sample surfaces did not change significantly with immersion time. For the test 3.5^{wt}% NaCl solution, the ZM21 have relatively large coating coverage at 3 days. However, the EC+ additive film disappeared after 9-day and the sample surface was exposed. The AZ31-ME sample in 3.5^{wt}% NaCl has already lost most EC + Additive film at 3 days. It indicates a fast film decomposition that is matching the mass change results shown in Figure 7.2.13.

Figure 7.2.15 shows the cross-sections of EC+ additive-processed ZM21-ME samples after 21-day immersion in Hanks solution and 3.5^{wt}% NaCl solution. After 21-day in Hanks solution, Figure 7.2.15a, the dense film degraded to porous agglomerates with honeycomb-like structures. Cracks are further developed by immersion. The substrates near the interface are attacked and left with a corrosion product layer around 8 µm. Nevertheless, the EC+Additive film kept coherent, and it still has a similar thickness profile/topography to the film just fabricated. The Ca from the hanks solution is observed in EDX at the coating after immersion. The presence of Ca may result in the morphology of the film cross-section post-immersion, which is discussed in the next chapter 8.

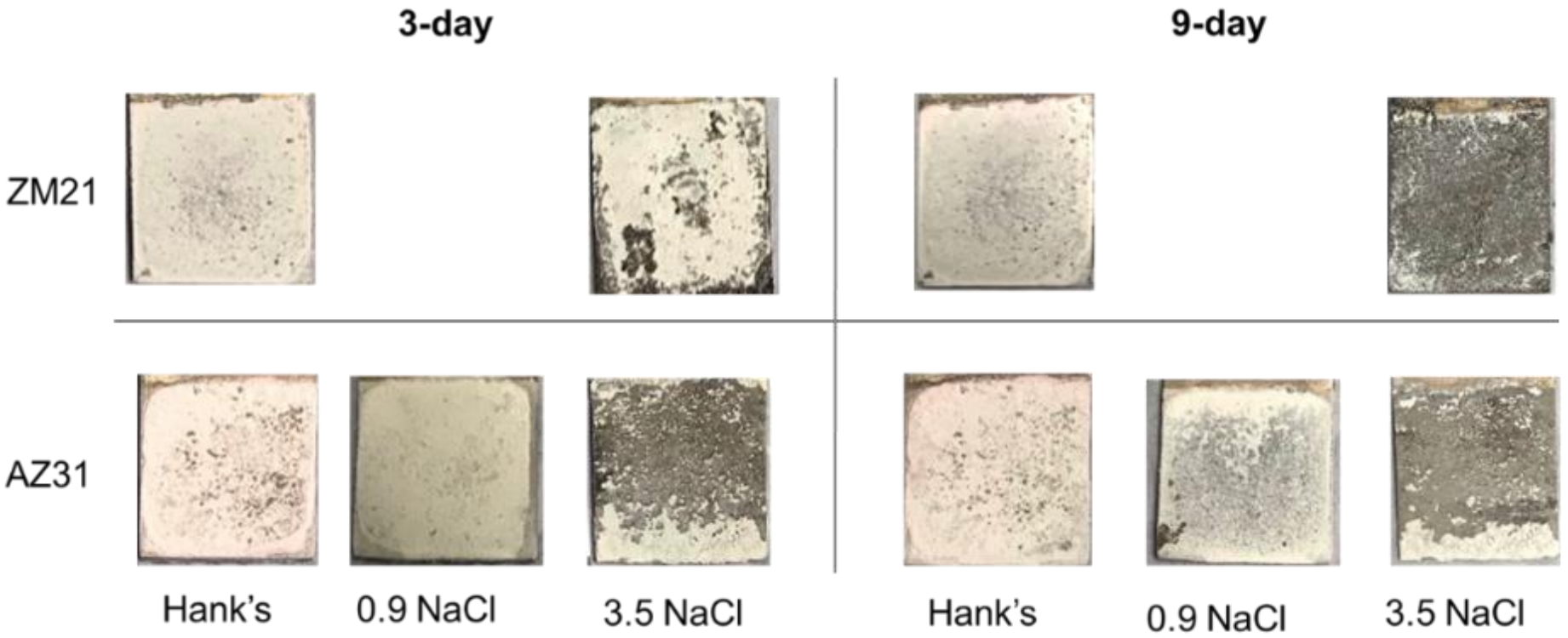

Figure 7.2.14. The characterisation of the AZ31-ME samples with EC+ Additive treatment shows the surface change during the immersion tests with Hanks solution, saline solution and 3.5^{wt}% NaCl solution for up to 9 days.

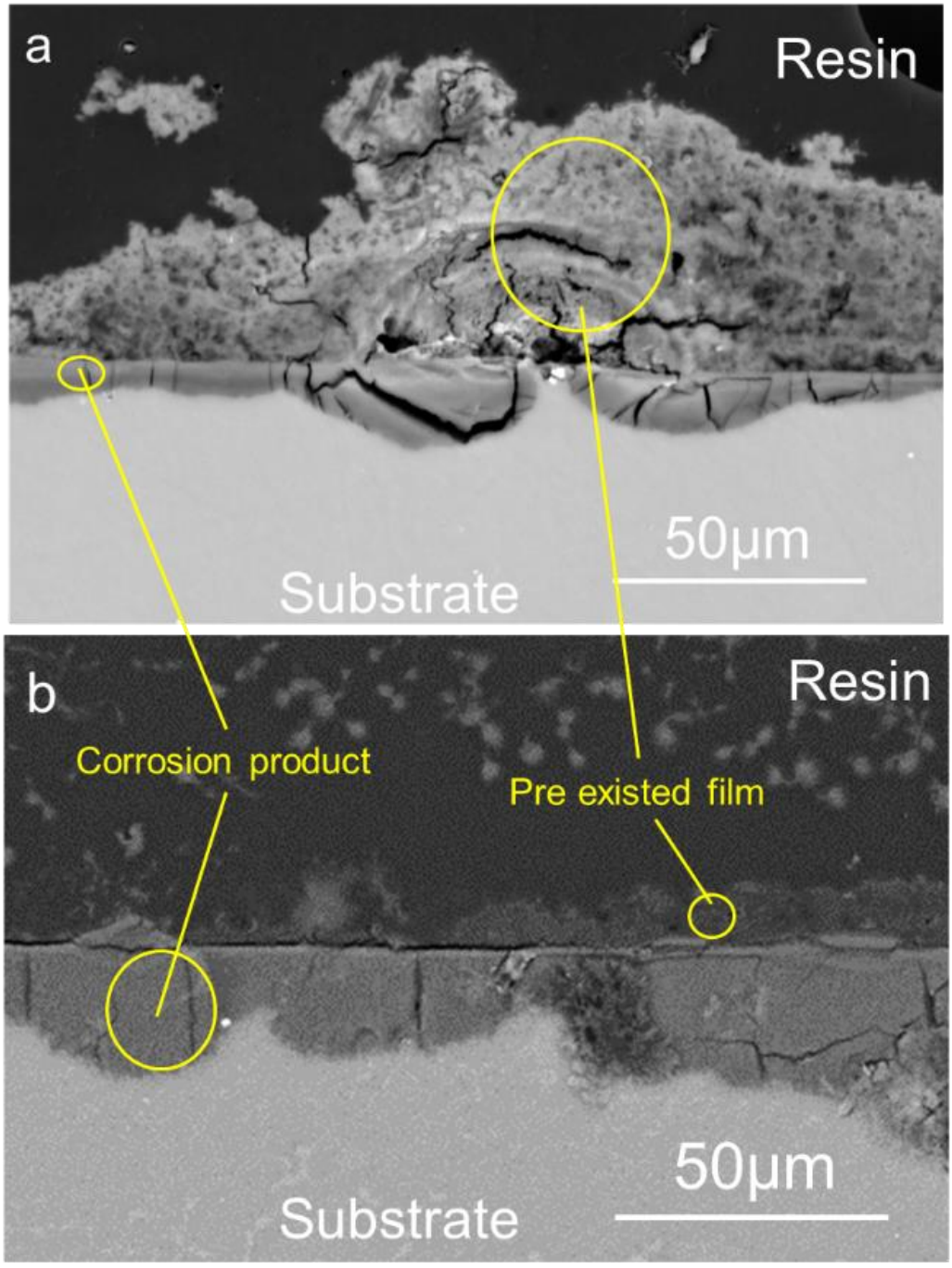

Figure 7.2.15 The cross-sectional SEM image of the ZM21-ME with EC+Additive treatment immersed in a) Hanks solution, b) 3.5^{wt}% NaCl solution for 21 days.

In 3.5% NaCl solution, the ZM21-ME sample with EC+Additive film underwent greater degradation. Less than 10μm film thickness remains at the sample surface. A thicker corrosion product layer, around 21μm, is built up at the substrate near interfaces.

7.3 Summary

The EIS tests in less aggressive test solutions such as saline and Hank's solution undertaken to the EC+Additive films showed a shift in the E_{OCP} and R_{ct} regardless of the type of substrates and the coating types. Hanks solution shifts the R_{ct} at least ten times to the 3.5^{wt}%NaCl solution.

Another Mg alloy ZM21, which is considered more bio-compatible, was also subjected to corrosion tests coated or uncoated, Which shows similar results to the AZ31 samples.

With the longer-term immersion tests for 9 days, EC+additive samples in Hanks solution, close to human body fluid, has degradation in the film but kept coherent to the substrates, but the EC+additive film in 3.5%NaCl solution is mostly broken down. The results are summarised in Table 7.3.1

The results in this chapter 7, including chapter 6, are to be further discussed in the general discussion (section 8.2) regarding the corrosion behaviour and the protectiveness of $Mg(OH)_2$ coatings to the substrate.

Table 7.3.1. Summary of the corrosion test results for Chapter 7.

Sample\solution	Saline solution			Hanks Solution		
	Initial Exposure (Ωcm^2)	2-4days immersion (Ωcm^2)	Longer term mass loss ($mg/cm^2/day$)	Initial Exposure (Ωcm^2)	2-4days immersion (Ωcm^2)	Longer term mass loss ($mg/cm^2/day$)
ZM21 (uncoated)	~1K	~2K	~0.12	~10K	~10K	~0.04
AZ31-ME (uncoated)	~1K	~3k	~0.07	~9k	~80k	~0.015(mass gain)
ZM21 (EC+ Additive)	~10K	~4K	n/a	~40K	~25K	~0.13
AZ31-ME (EC+ Additive)	n/a	n/a	~0.52	n/a	n/a	~0.32

8 General discussion

8.1 Introduction

Previous Chapter 4 to Chapter 7 has illustrated the research work regarding research objectives 1 to 4. It is to develop and optimise the $Mg(OH)_2$ films on Mg alloy substrates using various techniques, to investigate its self-corrosion behaviour, and to quantify the corrosion resistance. This chapter discussed the following objectives 5 and 6 regarding the corrosion resistance performance of $Mg(OH)_2$ based film and its potential application for biomedical implantation to control the degradation.

To examine the corrosion performance, the data provided in Chapter 6 as charge transfer resistance R_{ct}, is converted to corrosion rates by applying the Stern Geary equation. The selection of the Stern Geary constant B is discussed in Section 8.2.1.

Section 8.2.2 discusses the corrosion behaviour regarding the observations. Choosing an aggressive solution, equivalent to a marine environment, 3.5% NaCl solution, the effectiveness of the range of deposited coatings in minimising corrosion (if at all) compared with unprotected alloys will be explored with the magnesium alloys used in this study AZ31 and ZM21.

The behaviour of the coated alloys in a range of less aggressive environments is then considered. The corrosion rates and coating performance are finally compared with the literature. The comment is also provided on predictions with exposure times longer than undertaken in this work.

Based on the review of the coating corrosion protection from Section 8.2, Section 8.3 discusses applications for the $Mg(OH)_2$ coatings in this work. Recommendations for suitable applications are addressed in this section. Potential future work for manufacturing is also discussed.

8.2 Corrosion performance of $Mg(OH)_2$ film on Mg alloy substrates

8.2.1 Comment on Stern-Geary constant, B used in this work

Charge transfer resistance R_{ct} is measured in the EIS based corrosion tests, shown in previous chapters 6 and 7. According to the Stern-Geary equation with Equation (2-28) and Equation (2-29), R_{ct} can be interpreted to equivalent corrosion current density I_{corr} ($\mu A/cm^2$) then the corrosion penetration rate 'P' (mm/year).

In an experimental measurement using Tafel extrapolation of the potentiodynamic polarisation tests, the B value is calculated at 13.75mV, reported in section 6.2.1.3. This was measured on uncoated AZ31 in 3.5% NaCl solution. The equivalent corrosion rate interpreted from the EIS tests is very dependent on the value used. To examine this a range of B values from literature are presented in Table 8.2.1.

Table 8.2.1 Summary of Stern-Geary values varies in this work and literature.

LITERATURE	SUBSTRATE	METHOD	B_A	B_C	B (mV)
THIS RESEARCH	AZ31B	Tafel	40.46	145	13.75
[SINGH 2015]	AZ31	Tafel	61	117	17
[FEILIU 2011]	AZ31	gravimetric	N/a	N/a	65
[GARCIA-GALVAN 2021]	AZ31B	Tafel			23
[PARDO 2008]	Pure Mg	Reviewed from previous literature	N/a	N/a	26
[SCULLY, 2014]	Pure Mg	Tafel	90-150	315	30-44

Table 8.2.1 shows a spectrum of B values of Mg alloy from the literature between 12.5 and 65mV. The Stern-Geary constant (determined by the Tafel constants) is the only variable that is normally not measured but commonly assumed to be a value of 20 to 30 MV [Covino, 2004]. The B value measured in this work (Section 6.2.1.3) is 13.75mV which is low compared to other values in Table 8.2.1.

The value of the Stern-Geary constant, *B*, for AZ31 in different electrolytes was studied by [García-Galvan, 2021] They report “numerous researchers have determined corrosion rates from weight loss measurements up to 15 times higher than those obtained by electrochemical techniques”. The authors propose reasons for the significant differences:

(a) An increase in the hydrogen evolution rate observed during anodic polarization (the negative difference effect or NDE);
(b) The partial disintegration of specimens into fine metallic particles;
(c) Participation of reaction intermediates during anodic dis-solution; and
(d) A significant difference in the instantaneous corrosion rate determined by the electrochemical techniques compared with the average corrosion rate provided by weight loss.

Analysis of the results shows that if B values are used instead of B′ for i_{corr} determination using R_p in the Stern–Geary equation, the real corrosion rate (as determined by weight loss) is underestimated by between one and two orders of magnitude. The authors suggest that the B constant used in the Stern–Geary equation cannot be obtained by the direct determination of the Tafel slopes.

In view of the variation in B (and B’) between researchers, techniques and time and conditions at which the measurements are taken, all data is reported as R_{ct} in previous chapters, so corrosion rate values can be adjusted. Indeed this author, Y Wang, suggests that the temperature and subsequent concentration of Mg ions in the local environment are all an influence on the degree of passivation, oxide development and state of the surface and may influence the determination of B value in a dynamic way and B is not a constant.

However, an arbitrary Stern-Geary constant of 25.5mV was adopted for all conversions since this is more aligned to that of expected literature than the measured value. Further, in this current research work, comparison of corrosion rates from EIS measurements using this value of B constant (25.5 mV) and comparison of the equivalent corrosion rates obtained from mass change

experiments (see Figure 8.2.4) are of the same magnitude. The results can be seen stitched together with the corrosion rate from the EIS measurements at initial exposure at the left of Figure 8.2.4.

When interpreting I_{corr} to penetration rate 'P', a ratio between penetration rate 'P' and 'I_{corr}' should be calculated by Faraday's equation with a norm I_{corr}, Equation (2-30) and (2-31).

The ratio reported by Pidcock for Mg that 1 μA/cm^2 = 0.023 mm/y for Mg, is adopted for convenience in this work [Pidcock, 2014]. The real ratio for Mg alloys samples can be slightly different to the ratio for pure Mg as their density "ρ" and 'I_{corr}' varies between pure Mg and alloys. Nevertheless, the errors are considered acceptable as AZ31 and ZM21 mainly comprise Mg with a small amount of alloying elements.

8.2.2 Exposure of coated and uncoated AZ31 in 3.5% NaCl solution

To examine the effectiveness of the $Mg(OH)_2$ coatings, this section discusses the corrosion performance of AZ31 coating (using a range of methods) with that of uncoated AZ31 Figure 8.2.1 allows a comparison of the corrosion resistance between various $Mg(OH)_2$ coatings in this work.

Figure 8.2.1 summarises the equivalent corrosion rates with immersion time in 3.5^{wt}% NaCl using EIS corrosion test results in chapter 6. The Upper and lower bounds of the corrosion rates for the uncoated AZ31 substrates are shown in red, the hydrothermal samples shown in black, electrochemically treated (EC) AZ31 in green and EC + Additive Mg solution additions in blue.

For the uncoated AZ31 substrates, in the beginning, there is an equivalent corrosion rate of between 0.8 and 3 mm/year. After 2-day immersion, this decreases to between 0.6 and 0.9 mm/year and around 0.7 mm/year at the end of 4-day immersion (96h).

For the EC treated samples (in green), corrosion rates decrease with immersion time and show similar behaviour in the upper range to that of an uncoated sample. However, the lower bounds (equivalent to thick EC films) have lower

corrosion rates for the first few hours of the test which increase with immersion time.

The EC+Additive samples (sky blue) and hydrothermal samples (black) have similar corrosion behaviour in 3.5^{wt}% NaCl solution to each other. The hydrothermal samples initially achieve a low corrosion rate of 0.001mm/year which is a 1000 fold reduction compared to the uncoated samples and a tenfold reduction with the EC+Additive samples (0.01mm/year). After 2-day immersion, both hydrothermal and EC+Additive samples have similar corrosion rates of around 0.8mm/year, around 10 times less than the uncoated samples. The lower bound of EC+Additive is about 0.03 mm/year which is slightly lower than the lower bound hydrothermal sample.

The reduction in the initial corrosion rate of the immersed uncoated AZ31 sample is attributed to a corrosion product build-up. With the uncoated sample is immersed in the test solution, the magnesium ions move into the solution and form a corrosion product of $Mg(OH)_2$, which increases the electrical resistance and results in the reduction in corrosion rate.

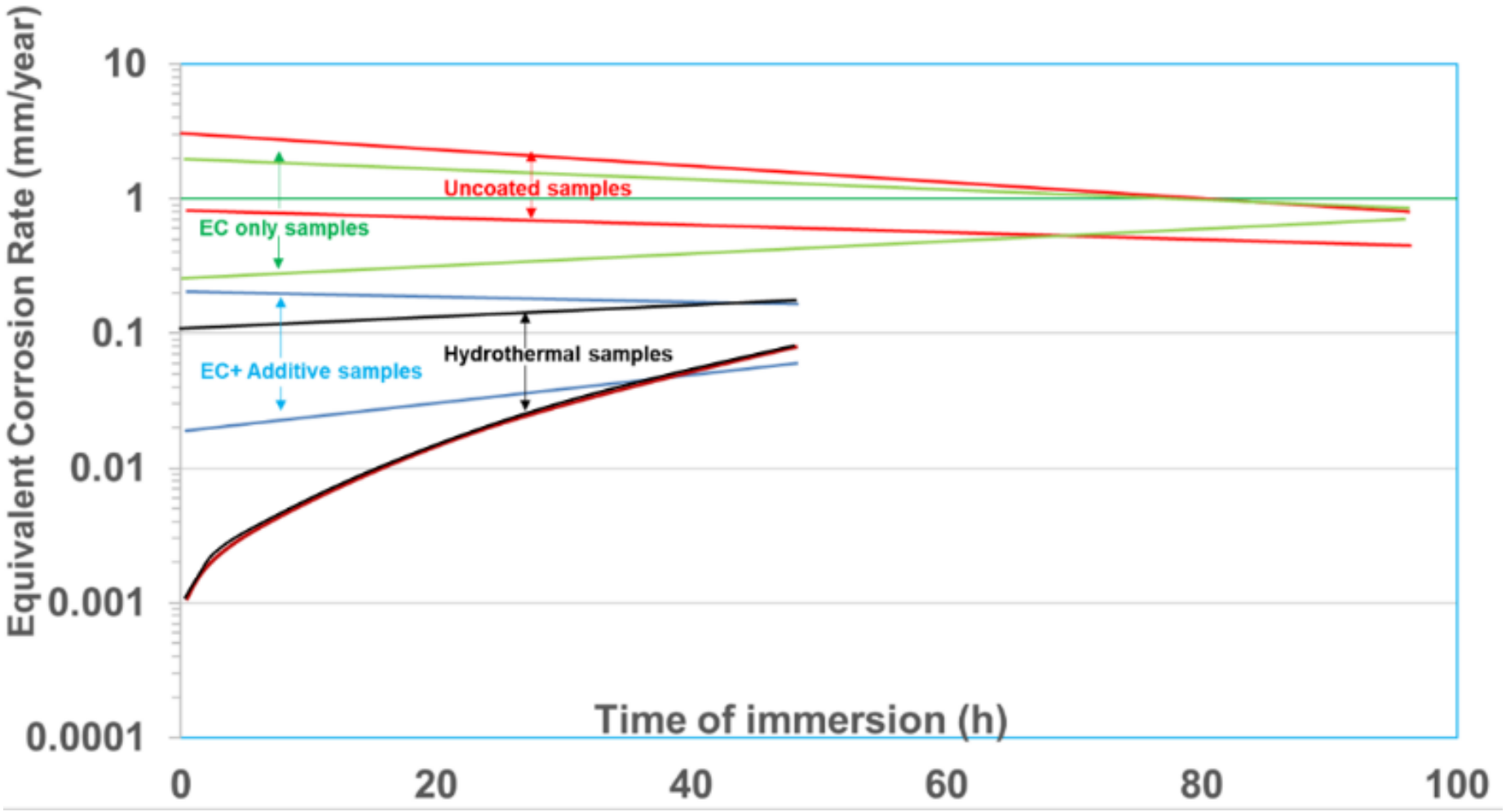

Figure 8.2.1 Summary of the equivalent corrosion rates versus immersion time for coated and uncoated AZ31 samples in the EIS tests in 3.5^{wt}% NaCl solution.

Considering the overall behaviour of corrosion rates for coated samples. In comparison with the unprotected AZ31, both the hydrothermal and EC+Additive samples provide early protection. There is an extensive range of reduction in corrosion rates at the lower bound, around 0.001 mm/year attributed, in this case, to samples with thicker hydrothermal films.

In general, Figure 8.2.1 shows the equivalent corrosion rates while reduced compared to the uncoated AZ31 samples, increase steadily with the time of immersion indicating all coatings become less protective. Extrapolating beyond the 100 h shown, there is a likely steady-state where the corrosion rates of coated samples are equal to that of uncoated samples. Thus the coated samples provide reasonably short term protection over 100h in an aggressive environment such as seawater immersion. The implications and possible applications are discussed further in section 8.3 and 8.4. The next part of the discussion looks at the effectiveness of the various coating methods in more detail.

8.2.2.1 Coated AZ31 immersed in 3.5% NaCl solution

EC coated samples provide a small amount of corrosion resistance initially and are the least protective coatings of the other manufacturing methods. The corrosion rates of the uncoated samples and coated samples become equivalent to around 70h in 3.5% NaCl solution.

The hydrothermal and EC+Additive coated alloys show reduced corrosion rates compared with uncoated AZ31 approximately 2 orders of magnitude at initial exposure and 1 order of magnitude after 2-days immersion. It is estimated that any coating protection is lost with longer times of immersion; the hydrothermal samples around 100 hours and the EC+Additive samples remain protective for longer, around 150h in 3.5% NaCl.

The $Mg(OH)_2$ coating cross-sectional images and thickness measurement in sections 5.2.4, and 5.4.2, show hydrothermal samples typically have a more uniform morphology than the EC+Additive films. Distinguishing features of the hydrothermal films are the lateral cracks parallel to the sample surface, while the

EC+Additive films, typically thicker coatings than the hydrothermal films, develop cracks with random orientation.

With initial exposure to 3.5% NaCl for hydrothermal and EC+Additive coated samples, the coating acts as a barrier protecting the Mg alloy surface from releasing ions into solution. From this low level of corrosion the subsequent increase of corrosion rates with immersion time is likely due to the electrolyte penetrating through the coating via cracks and porous defects reaching the metallic substrate at the coating-alloy interface permitting dissolution of Mg ions to $Mg(OH)_2$. Direct access to the interface by the electrolyte through the cracks with the EC+Additive films at the beginning of the immersion, and lack of uniformity, therefore, may result in a faster initial corrosion rate for these films, particularly for thinner films. Once the hydrothermal and EC+ additive films are fully wetted, both types of samples exhibit similar behaviour. The lower corrosion rate of the thicker EC+Additive samples at the lower bound after 2-day immersion, indicate these to be slightly more protective than hydrothermal samples.

Additionally, the coating also decomposes or degrades during immersion as the Cl^- ions induce a reaction from $Mg(OH)_2$ to a more soluble $MgCl_2$, shown in Equation 8-1 [Song, 2003; Poinern 2012].

$$Mg(OH)_2(\text{less dissolvable}) + 2Cl^- \rightarrow MgCl_2(\text{more dissolvable}) + 2OH^- \quad \textbf{(8-1)}$$

Returning to Figure 8.2.1, in terms of general coating performance, EC coated AZ31 samples offer some corrosion protection to AZ31 for around 70 and 80h. Hydrothermal and EC+Additive coated samples show reduced corrosion rates compared with uncoated AZ31 around an order of magnitude for 2-day immersion. If immersed for a longer time, it is estimated that the protection gained from thicker hydrothermal coated samples and EC+Additive coatings (lower bounds) is lost after 100h and 150 h respectively. After this point, the corrosion rates of 0.2 mm/year or 0.15mm/year are equivalent to that of an uncoated alloy immersed in tranquil (non-flowing) seawater with a corrosion product on the surface developed from the open conditions.

Comparison of coated AZ31 and ZM21 in 3.5^{wt}% NaCl solution

Given that these coatings were deposited onto AZ31, the question was posed would corrosion protection be offered to other Mg alloys by these coating at a similar level.

ZM21 alloy has been one of the most suitable candidate materials for implant owing to its bio-compatibility properties. Rapid corrosion of ZM21 alloy has raised the question regarding its adaptability in bio-implant application [Srirama, 2019]

Figure 8.2.2 shows the corrosion rates for uncoated ZM21 alloy (solid triangles) are initially around 0.8mm/year and reduce to around 0.4mm/year after 48h immersion in tranquil 3.5^{wt}% NaCl solution. The corrosion rates are for a single data set and are compared with a range of results for uncoated and EC+Additive coated AZ31 alloy in red and blue respectively for upper and lower bounds.

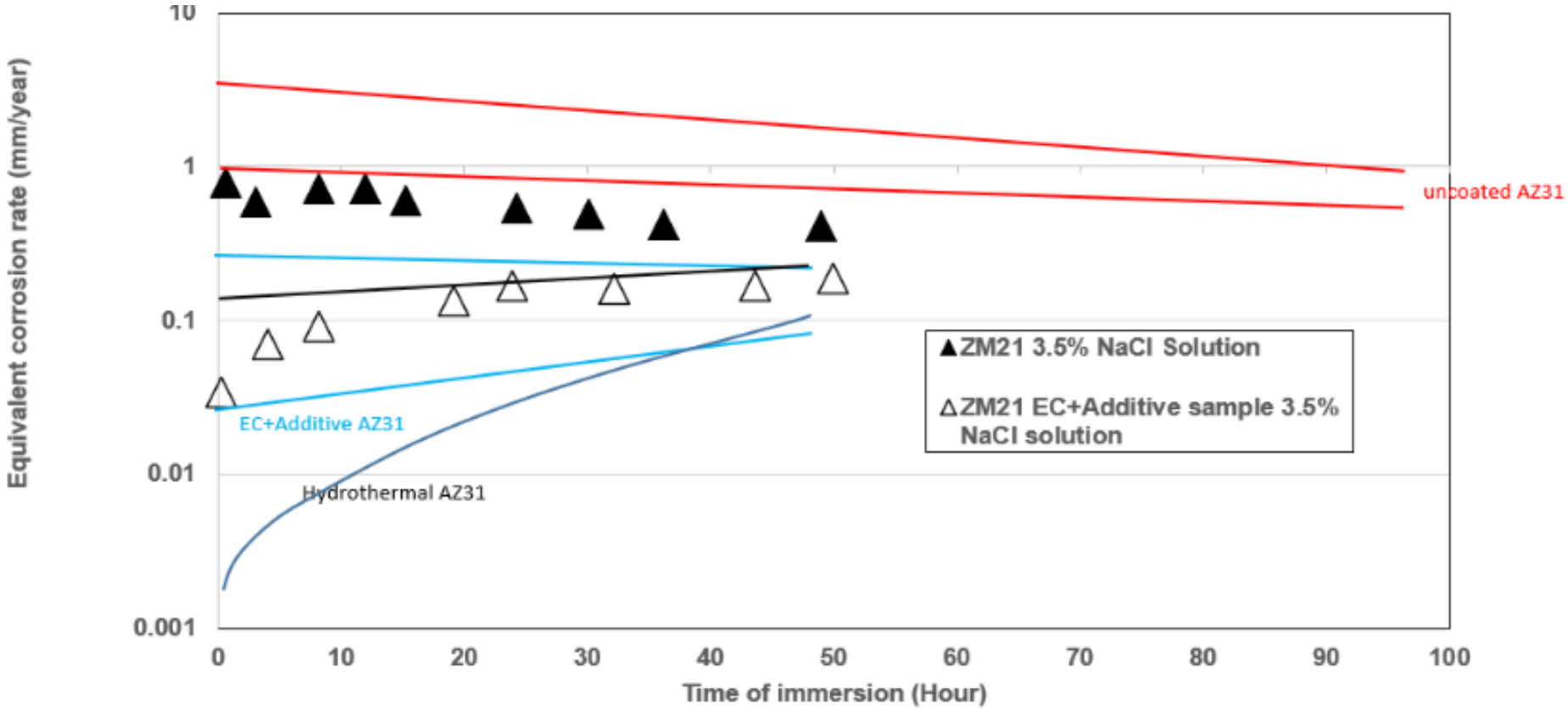

Figure 8.2.2 Equivalent corrosion rates with immersion time for EC+Additive coated and uncoated ZM21 compared with AZ31 from EIS tests in 3.5^{wt}% NaCl solution.

In comparison with AZ31, corrosion rates of uncoated ZM21 are reduced. If this single data set is typical, this may reflect the different composition and microstructure of ZM21. Chapter 5 shows that ZM21 is aluminium free, has a large grain size and a greater portion of precipitates (likely to be Mn-rich second phase).

For EC+Additive coated ZM21 sample (hollowed triangles), the corrosion rate is initially 0.03mm/year, quickly increased to 0.2mm/year, then stabilised at around 0.2mm/year with a minimal trend of rising. The corrosion rates of ZM21 sit within the bands of AZ31 samples (blue). It indicates both AZ31 and ZM21 exhibit similar corrosion behaviour EC+Additive coatings.

EC+Additive coating on ZM21 alloy offers some corrosion protection to uncoated alloy estimated at 90h of immersion after which the degradation proceeds at 0.25mm/year equivalent to that of an uncoated alloy immersed in tranquil (non-flowing) seawater with a corrosion product on the surface developed from the open conditions. Thus, the coating shows the initial rapid corrosion of ZM21 considered a cause for concern with implant applications is limited.

The next sections consider corrosion behaviour in environments more appropriate to those representing salts in the body.

8.2.3 Exposure of ZM21 in normal saline and Hanks solution

There are a few typical simulated body fluids such as normal saline (NS), phosphate-buffered saline (PBS), Hanks' balanced salt solution (HBSS) and simulated body fluid (SBF). Of these, normal saline has the maximum chloride content of 0.9^{wt}%. PBS contains a large amount of phosphate as a buffer system to maintain physiological pH. Hanks solution contains phosphate, sulphate and carbonate which could react with Mg and yield stable compounds along with magnesium chloride and organic glucose. In this work, normal saline and Hanks solution were used.

Figure 8.2.3 shows and compares the equivalent corrosion rates of the ZM21 sample from EIS tests in saline solution (blue) and Hanks solution (orange), compared with the results in 3.5$^{wt\%}$ NaCl solution (black). In Hanks solution, both uncoated (solid triangles) and coated samples (hollow triangles), show corrosion rates are an order of magnitude less than in 3.5$^{wt\%}$ NaCl solution, respectively. A steady-state corrosion rate after 6 days (around 0.02 mm/year) in Hanks solution is measured, a tenfold reduction to uncoated ZM21.

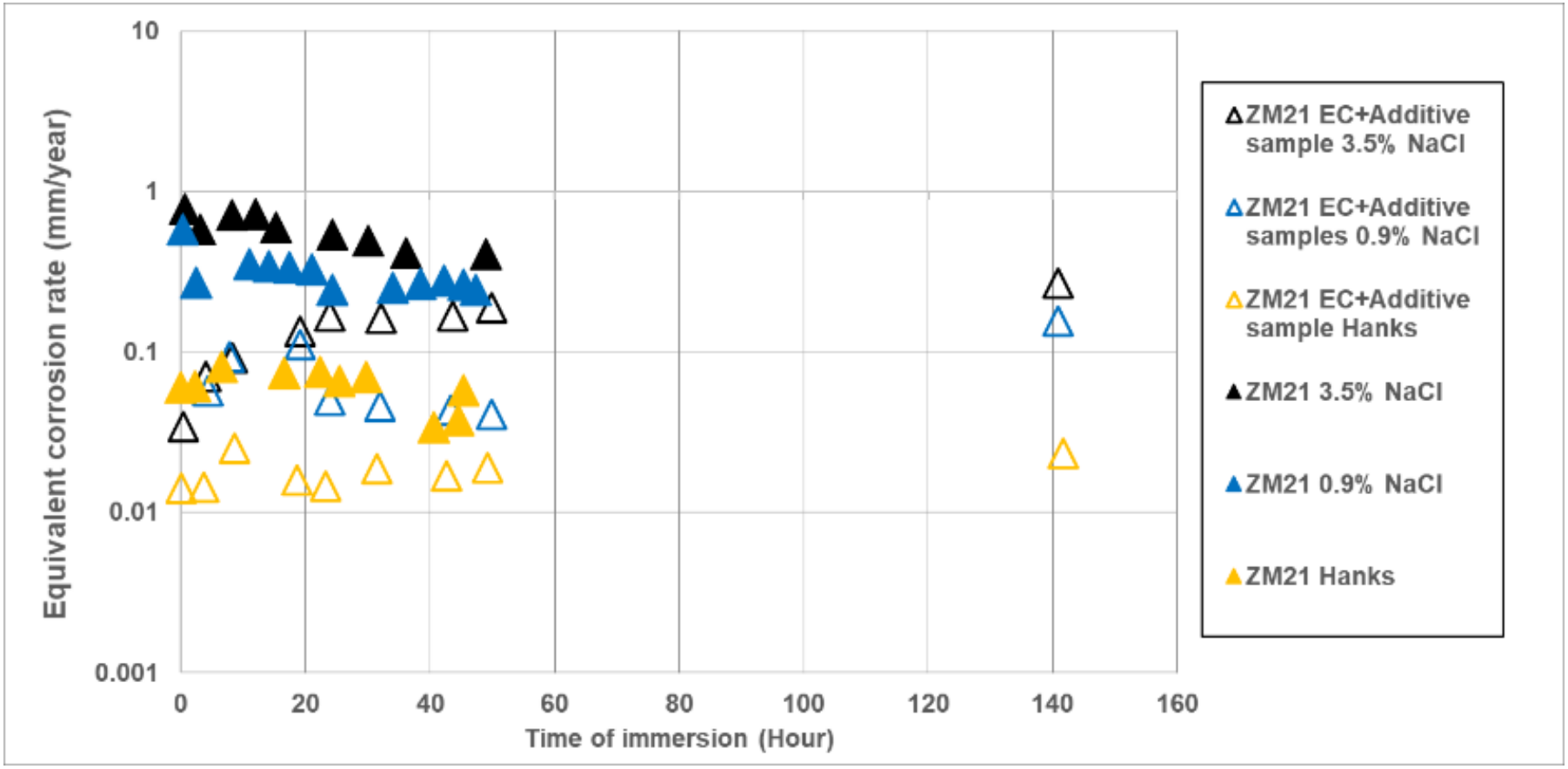

Figure 8.2.3 Comparison between the Equivalent corrosion rates of Coated and EC+Additive samples in 3.5^{wt}%, saline solutions and Hanks solutions.

An increased concentration of Cl^- is the key influential factor with Cl^- as a catalyst for the corrosion reaction of Mg dissolution to Mg^{2+}. It is well documented in a range of literature that increased Cl^- concentration positively correlates to increased corrosion rates. Cl^- also tends to exchange the hydroxide groups in the $Mg(OH)_2$ and form $MgCl_2$ with much higher solubility [Song, 2003]. Thus the deposited $Mg(OH)_2$ coatings break down faster when the surrounding aqueous environment has a higher concentration of chloride.

In Figure 8.2.3, blue data points representing tests with saline solution, show a greater corrosion rate than that in Hanks solution, with a similar chloride concentration. Hanks solution contains phosphate, sulphate and carbonate which could react with Mg and yield stable compounds. In addition to containing MgCl2·6H2O and organic glucose elements such as Ca^{2+} and Mg^{2+} that may stabilise the sample surface. Therefore, lower corrosion rates are shown in Hanks solution than in pure saline solution. Chapter 7, Figure 7.2.15, confirms an additional Ca-rich layer forms on the sample surface in Hanks solution which may increase the resistance of the sample. It is not clear if the additional ions provide any benefit to the deposited $Mg(OH)_2$ coatings such that there is slower degradation in Hanks solution than with the 0.9% or 3.5% NaCl solution.

Overall Figure 8.2.3 shows both uncoated alloys (AZ31 and ZM21) have decreasing corrosion rate with time, as a natural $Mg(OH)_2$ film develops on the surface. Conversely, in the coated samples, the corrosion rate increased as the deposited $Mg(OH)_2$ film becomes less protective. At some point, it is thought the corrosion rate of both uncoated and coated alloy will be equivalent and longer duration than 6 days for tests may prove valuable to clarify this situation. Some further discussion is given in the following sections.

8.2.4 corrosion rates for longer-term corrosion tests

The duration of EIS immersions tests is between 2 or 4 days (96h with a small number of tests undertaken for 6 days (144h). Over 4 days, a practical issue with

connections to the alloy sample results in some interference with galvanic corrosion and the Nyquist plots become unstable. Although ways to mitigate this was explored, it was found that the electrochemical approach was challenging for long term corrosion rate studies generally. Thus, another measurement technique using mass loss was undertaken for 21 days.

8.2.4.1 Estimated corrosion rates from mass loss

In Chapters 6 and 7, the mass change results of various samples are given as g/cm^2. Eq 2-23 in the previous chapter has shown to present mass change results in equivalent corrosion rate, mm/y. Eq 2-23 can also be shown as the following expression (eq 8-2):

$$\boldsymbol{P = k\frac{\Delta m_{loss}}{\rho \times A \times t}} \qquad \textbf{(8-2)}$$

'K' is a constant which is 87.6, '$\Delta \boldsymbol{m_{loss}}$ ' is the total weight loss of the metal (mg), 't' is the time taken for the loss of metal (h). 'A' is the surface area of the exposed metal (cm^2). 'ρ' is the metal density (g/cm^3).

This expression applies to the mass change results in this research work (Y Wang 2021), except where samples gain mass (due to the formation of corrosion product $Mg(OH)_2$) rather than lose mass during the corrosion test. The total sample mass will increase if the corrosion product sticks or stays on the sample surface.

In this mass gaining situation, a modified approach way is applied. It is to transfer the mass gain to the equivalent mass loss from the corrosion reaction. It assumes:

1. Only Mg took part in the corrosion reaction, and $Mg(OH)_2$ is the only corrosion product.
2. When the sample gains mass with immersion, the corrosion product layer is well attached to the sample and the dissolving of corrosion product is negligible.

3. The metallic mass of Mg that oxidised to $Mg(OH)_2$ corrosion product layer (Δm_{Mg}) can be considered as the equivalent mass loss(Δm_{loss}).

Therefore, the increased mass during corrosion test M_{cp} is the difference between $Mg(OH)_2$ and Mg:

$$m_{cp} = \Delta m_{Mg(OH)_2} - \Delta m_{Mg} \quad \textbf{(8-3)}$$

the amount of Mg and $Mg(OH)_2$ in mol during the corrosion test are equal:

$$\Delta n_{Mg} = \Delta n_{Mg(OH)_2} \quad \textbf{(8-4)}$$

The amount of substance in mol is equal to the mass over its molar mass

$$n = \frac{m}{M} \quad \textbf{(8-5)}$$

Therefore:

$$\frac{\Delta m_{Mg}}{M_{Mg}} = \frac{\Delta m_{Mg(OH)_2}}{M_{Mg(OH)_2}} \quad \textbf{(8-6)}$$

And

$$\Delta m_{Mg(OH)_2} = \frac{\Delta m_{Mg} \times M_{Mg(OH)_2}}{M_{Mg}} = 2.4\Delta m_{Mg} \quad \textbf{(8-7)}$$

$$m_{cp} = 2.4\Delta m_{Mg} - \Delta m_{Mg} = 1.4\Delta m_{Mg} \quad \textbf{(8-8)}$$

Therefore The equivalent mass loss of Mg Δm_{Mg} equals to:

$$\Delta m_{Mg} = \Delta m_{loss} = \frac{m_{cp}}{1.4} \quad \textbf{(8-9)}$$

8.2.4.2 Mass change results

Mass change measurements are not ideal to monitor the detail of initial immersion. Thus EIS measurements at initial exposure are used. Figure 8.2.4 shows EIS measurements as small marks on the left of the figure, stitched together with the equivalent corrosion rate interpreted from mass change measurements of the uncoated AZ31-ME and ZM21-ME.

The combined corrosion rates, plotted on a log scale, of EIS measurements followed by mass change measurement, are without significant mismatch. In this way Figure, 8.2.4 shows that the corrosion rate (measured by EIS) initially decreases as a corrosion product layer forms. It reaches a turning point after 3-day to 6-day immersion where the corrosion rates (measured by mass change) start to increase. Beyond this point, the corrosion of AZ31-ME and ZM21-ME substrates in 3.5^{wt}% and saline further increase while fluctuations in the corrosion rates in Hanks solution are observed.

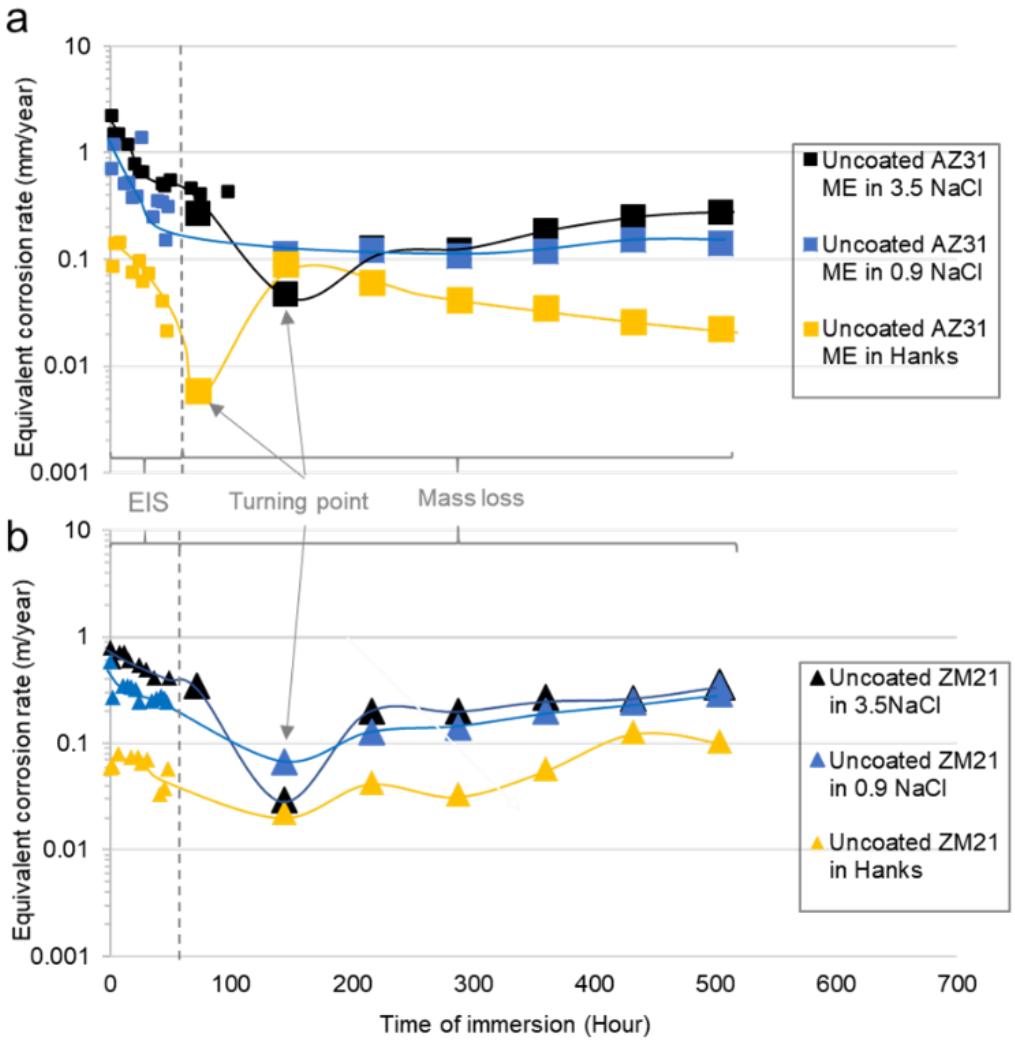

Figure 8.2.4 Combined corrosion rates taken from EIS exposure tests and the longer-term mass change, for a) AZ31-ME and b) ZM21-ME substrates in various tests solutions.

With a pre-existed coating, the equivalent corrosion rates by mass change always have a greater value leading to a significant mismatch between the initial

exposure (by EIS test) and longer-term mass change results. The greater mass change value for the coated sample is due to the pre-exited coating detachment/dissolve of from the sample in the test solution and this mass change does not attribute to the mass loss due to corrosion reaction. Therefore, Quantifying mass change measurement is considered valid for uncoated samples but not applicable to samples with pre-existed coating.

In support of longer-term corrosion performance, post-corrosion characterisation of the coated samples is conducted.

8.2.4.3 Post characterization

Figure 8.2.5 compares the typical cross-sectional SEM images for the uncoated and EC+Additive ZM21 samples in 3.5^{wt}% NaCl solution and Hanks solution for 21 days, respectively.

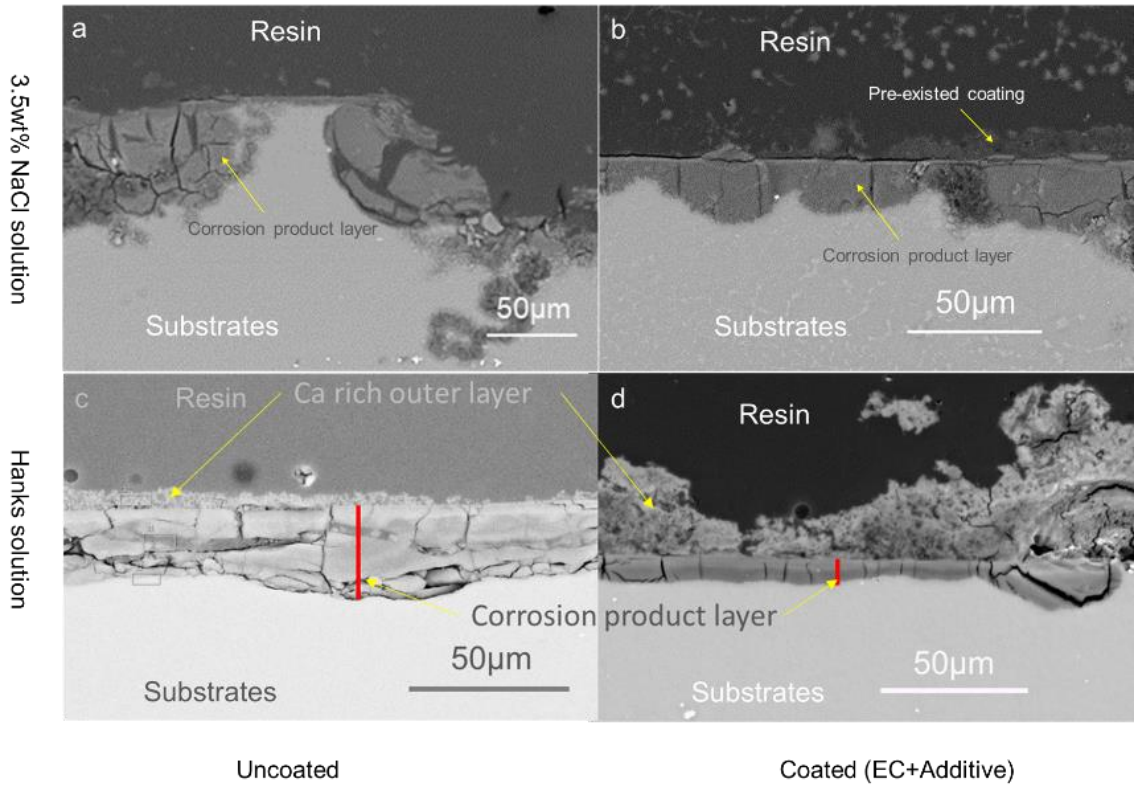

Figure 8.2.5 Post-corrosion SEM cross-sections of ZM21 in 3.5^{wt}% NaCl of a) uncoated b) EC+Additive c) uncoated substrate in Hanks solution, and d) EC+Additive in Hanks solution for 21days.

Generally, the uncoated samples show more corrosion damage to the substrate than coated samples. Severe corrosion damage (90μm deep pits) is observed on

the uncoated ZM21 surface in 3.5^{wt}% NaCl solution for 21 days, as in Figure 8.2.5a. Corrosion products are detached from the sample surface exposing metallic substrate to solution. The interlocked cracks in the corrosion products may lead to detachment.

When the sample is coated with EC+Additive and immersed in 3.5^{wt}% NaCl for 21 days, a continuous thin corrosion product layer is generated (25±10µm), about a third of the uncoated samples. The coating slows the slower corrosion rate compared to uncoated samples.

In Hanks solution, the corrosion product layer for the uncoated sample is around 35±5 µm. With EC+Additive coating, a 10 µm corrosion product layer is formed, thinner than 3.5^{wt}% NaCl solution.

This shows that an EC+Additive coating can significantly reduce the depth of penetration of corrosion by two thirds for ZM21 Mg alloy samples in both aggressive and mild solutions. In mild Hanks solution, the uncoated and coated samples in the aggressive NaCl solution show similar damage, additionally Ca is detected on the surface of both corrosion products and deposited in the EC+Additive coatings.

A Pourbaix-diagram, Figure 2.3.2, shows high pH and Mg^{2+} concentration negatively influence corrosion kinetics and even passivate the sample surface. An increase in local pH and Mg^{2+} concentration adjacent to the substrate can readily occur in limited volumes of static solution. A larger volume of solution and some agitation would enable the local ion concentration to disperse faster changing the local environment. A coating of $Mg(OH)_2$ protecting a substrate has a slower development Mg^{2+} concentration and high pH. The pre-existing $Mg(OH)_2$ coating may also cover some local anodic/cathodic sites or second phase particles at the metallic surface mitigating local galvanic couples that would otherwise forms. The pre-existed coating also physically constrains the corrosion product layer to the surface reducing detachment, leaving a new metallic area exposed.

This observation shows that the pre-existed EC+Additive coating can significantly reduce the corrosion depth to a third for the Mg alloy samples in both aggressive and mild solutions. Besides, the coated sample in the aggressive NaCl solution has similar damage to the uncoated sample in mild Hanks solution. Ca is detected in the pre-existed coatings for the EC+Additive sample, or, as the top layer for the uncoated sample

Several possible mechanisms can explain the influence of the pre-existed EC+Additive film. Firstly, the main composition of the EC+Additive film is $Mg(OH)_2$. It can increase the local pH and Mg^{2+} concentration adjacent to the substrate. According to the Poubaix diagram, Figure 2.3.3, higher pH and Mg^{2+} concentration negatively influence corrosion kinetics and even passivate the sample surface.

This improvement can be prominent when the corrosion is in a static solution with a limited solution amount. However, in a sufficient amount of solution with fluctuated/agitated state, the local Mg^{2+} ion concentration is to be significantly reduced hence increasing the corrosion rate.

Secondly, the pre-existed film may also cover some local anodic/cathodic sites at the metallic surface that may mitigate local galvanic couples.

The pre-existed coating physically constrains the corrosion product layer to the samples without detachment or leaving the new metallic area exposed.

8.2.5 Summary

In summary to describe the general corrosion behaviour of coatings with Mg alloys:

- Initially, uncoated AZ31 and ZM21 have a rapid corrosion rate in a limited volume of static salt solution. HT or EC+Additive $Mg(OH)_2$ coatings reduce the corrosion by 1000 fold reduction compared to the uncoated samples. After 2-day immersion, both hydrothermal and EC+Additive samples have similar corrosion rates of around 0.8mm/year, around 10 times less than uncoated alloys.

- The uncoated alloy forms a $Mg(OH)_2$ corrosion product layer which reduces the rate of further corrosion. The coated sample increases its corrosion rate as the deposited coating degrades.
- Deposited $Mg(OH)_2$ coatings provide reasonable short term protection to about 100h in 3.5% NaCl solution. Thereafter the effect of coating appears reduced as uncoated and coated alloys are equivalent in terms of further corrosion. $Mg(OH)_2$ protects the Mg alloy either in short periods of hours or longer-term in weeks.
- EC coated samples provide a small amount of corrosion resistance initially and are the least protective coatings of the other manufacturing methods. The corrosion rates of the uncoated samples and coated samples become equivalent to around 70h in 3.5% NaCl solution.
- The hydrothermal and EC+Additive coated alloys show reduced corrosion rates compared with uncoated AZ31 approximately 2 orders of magnitude at initial exposure and 1 order of magnitude after 2-days immersion. It is estimated that any coating protection is lost with longer times of immersion; the hydrothermal samples around 100 hours and the EC+Additive samples remain protective for longer, around 150h in 3.5% NaCl.
- Post-corrosion SEM images of 21-days exposure show corrosion rate of an unprotected Mg alloy increases after 150h of immersion, possible due to the detachment of the protective corrosion product layer.
- Hanks solution provides a less aggressive environment that leads to a ten-fold reduction in corrosion rate than in the equivalent 0.9% NaCl solution. The $Mg(OH)_2$ film formed in Hanks solution is more stable and degrades more slowly than in 0.9% NaCl solution. This is attributed to Ca^{2+} ions in the Hanks solution
- Similar corrosion behaviour is observed for coatings irrespective of the Mg alloy substrate, indicating the coating methods in this work are applicable for many Mg alloys.

8.2.6 Literature comparison

Figure 8.2.6 summarises the equivalent corrosion rates in 3.5^{wt}% NaCl solution reported in literature with Mg alloys and $Mg(OH)_2$ based films (hydrothermal coatings). The data previously shown in this reported research in Figure 8.2.1 (Y. Wang) is used in Figure 8.2.6 as a comparison.

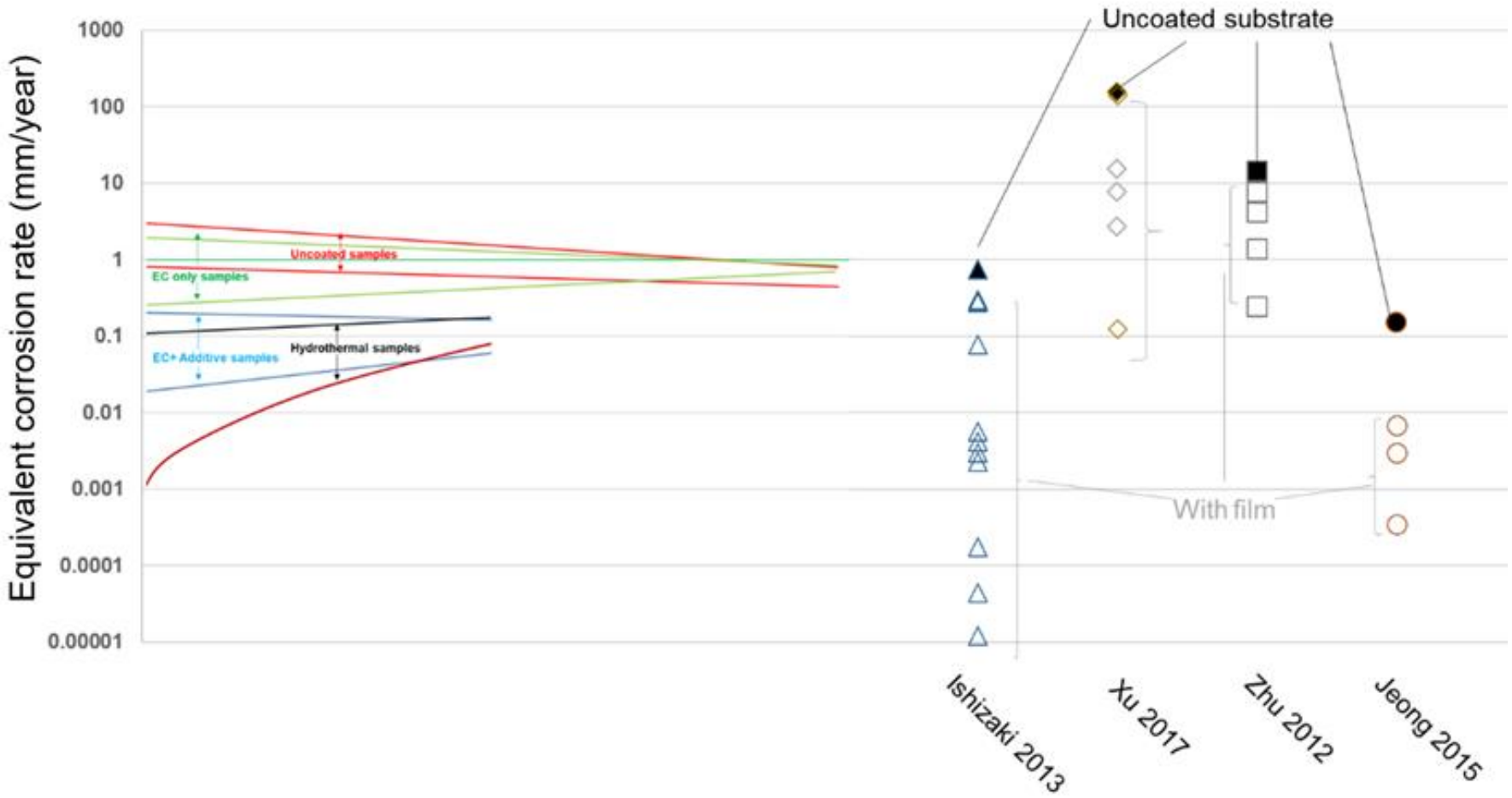

Figure 8.2.6 Summary of the equivalent corrosion rates for coated and uncoated AZ31 samples in the EIS tests in 3.5^{wt}% NaCl solution compared with literature, using EIS in 3.5^{wt}% NaCl solution compared with literature.

On the RHS the data points with solid shapes represent the equivalent corrosion rates for uncoated samples, and the hollow data points represent coated samples with various processing parameters. The literature shows various levels of reduction in the equivalent corrosion rates once the sample is coated.

However, there is considerable variation observed when comparing literature started on the uncoated alloy. In this current research (Y Wang) differences in the alloy composition and manufacturing history, corrosion test methods, and test conditions have been noted to give variation. Some further detail and discussion is given below:

Substrates

The different properties of alloys can lead to some variation, particularly when uncoated. For the AZ31 samples from three sources in this work, its microstructure and impurity level can be affected by the processing and heat treatments, hence its corrosion behaviour. Even though the specification of the AZ31 is the same, the AZ31-ME which is aerospace-grade, has a different thermal history, and composition than the other sources of commercial AZ31 (such as AZ31-GF) behaves differently in corrosion with time of immersion in 3.5^{wt}% NaCl solution as reported in Figure 8.2.6 The differences with lower corrosion rates in AZ31-ME are attributed to the lack of impurities in this alloy and homogeneity of second phase particles containing heavy elements (Section 6.2).

Further different materials ZM21 and AZ31 showed similar trends but different values compared to the AZ31 used in this work and other literature. ZM21 does not contain Al. The change in composition is attributed to changes in corrosion rate although the trends and tendencies are similar.

Test methods and test time

Different tests methods can be responsible for variation in corrosion results between literature. Potentiodynamic polarisation tests are used for corrosion tests with the reported rates given in Figure 8.2.6. It is a destructive method requiring the sample to be anodically polarised so will modify the surface such as

developing pits due to the accelerated corrosion and its result is usually a snapshot in a time.

In this work, EIS tests and mass change results are reported. Absolute values do vary between these. Further different techniques report different measurements of the Stern Geary constant B [Wang 2018] which will give different corrosion rates.

The Mg alloy surface rapidly build-up a corrosion product layer during immersion. Measuring a just-immersed sample with a fresh-polished metallic surface can lead to a much higher corrosion rate than a sample already immersed for a time with the corrosion product surface layer. Samples stored for long period in the atmosphere may lead to thin surface oxides, which may affect the results when compared to freshly prepared or pre-immersed, pre-corroded samples.

Electrolyte condition

The test or electrolyte conditions can vary between literature reports. The volume, flow rate and concentration of the NaCl solution can certainly significantly influence the test. In this current research changing the electrolyte from 3.5% NaCl solution, to the saline solution or Hanks solution results in very different corrosion rates. This is also reported in literature [Wang 2018] among many other authors.

Ishizaki et al. [Ishizaki 2013] report using 5% NaCl solution in tests rather than $3.5^{wt\%}$ NaCl solution. The corrosion rates reported by Ishizaki's work would be lower if it was reported using 3.5^{wt}% NaCl solution.

Generally, it is challenging to compare the corrosion rates in this work with the literature as the immersion time, and exact test conditions are not always given in literature.

Processing temperature

Processing temperature influences the morphology of $Mg(OH)_2$ films. However, in this research the processing temperatures are limited.

Increases to the processing temperature above 400°C, transform $Mg(OH)_2$ to MgO by calcination, shown in equations 8-10 [cited by Balducci, 2017]. The absence of a hydroxide group in the oxide may make MgO more hydrophobic than $Mg(OH)_2$. MgO is already considered as corrosion resistant. MgO coatings in an aqueous environment will undergo a hydration process to $Mg(OH)_2$ and extends the life of the coating before dissolution or degradation.

$$Mg(OH)_2 \rightarrow MgO + H_2O \quad \Delta H^o\ (298K)\ 98.4KJ/mol\ H_2O \qquad \textbf{(8-10)}$$

There are some considerations for the calcination of $Mg(OH)_2$ to MgO coatings. Firstly calcination requires temperatures of at least 400°C, higher than the 300°C tolerated by Mg alloy substrates before these thermally modify.

Different varieties of magnesium oxide are formed from a magnesium hydroxide precursor, depending on the conditions of the thermal decomposition, such as caustic, burnt and mixed magnesia. Magnesia calcined at lower temperatures (400–600 °C) exhibits significantly greater activity and is likely to rehydrate than the including MgO tends to become less stable than when calcinated between 400°C-600°C than an inactive (“burnt”) form of magnesium oxide formed at higher temperatures [cited by Pilarska 2017]. The increase in temperature causes a fall in the reactivity of the material and susceptibility to hydration. It is reported that MgO coatings can quickly be rehydrated to $Mg(OH)_2$ within 20h in simulated body fluid [Wang, 2018].

Wang [Wang, 2018], reports that R_{ct} of MgO coated Mg alloys AZ31 formed by plasma enhanced oxidation, in the EIS measurement is similar to the R_{ct} value of the $Mg(OH)_2$ coated AZ31 reported in this research [Y. Wang]. If the MgO had micro-porosity, or large pores with open pathways for the solution to reach the substrate, and it is easily rehydrated, It may have a similar effect to $Mg(OH)_2$.

8.3 Potential Application for $Mg(OH)_2$ Coatings on Mg Alloys; Bio-Medical Implants

Mg alloys are widely used for engineering applications but also most recently as with biomedical engineering applications as they have great potential as biodegradable implantation applications. A stable coating that is easy to

consistently apply to medical devices is key to unlocking this technology. This section will discuss in more detail possible applications suitable for using this coating system and its benefits. Then it will review challenges and future work for problem solving and optimisation. Application of $Mg(OH)_2$ based film/coating for corrosion protection.

The main drawback of the use of magnesium in orthopaedic implants is its high corrosion rate in the electrolytic physiological environment. According to Ghali et al. [Ghali, 2004], two different corrosion modes are possible, uniform and localized. Mg alloys with a slow and constant degradation rate (lower than 0.5 mm/year [Chen 2015] are required to provide sufficient time to heal bone). This rate helps to and extend the service life, reduce the change of hydrogen evolving, thus reducing the risks of implant failure and health problems. Thus a biodegradable coating such as Mg(OH) 2 could (a) slow the rate of Mg alloy degradation making a range of alloys fit for the purpose of using $Mg(OH)_2$ coatings to tailor the implant degradation to the requirement and (b) extend the life span. Mg alloys used in implants are mainly divided into orthopaedic and vascular implants. For orthopaedic applications, 6 to 12 months are required and vascular applications require a 3 to 6-month life span [Yang 2020].

Although some alloy substrates will achieve the threshold corrosion rates, as in this work, there can be an acceleration of corrosion rates in the long term. Application of $Mg(OH)_2$ coatings can reduce corrosion rates by 1/3 to 1/4 compared with the uncoated substrate for up to 21 days. It should be noted that this coating is sacrificial coating and long term protection is not provided indefinitely. However, the coating slows the rate of degradation, which is spike free, slow and predictable.

Some things to consider, firstly the corrosion assessment in this work is at room temperature in static conditions. corrosion rates can increase at body temperature and/or with a more frequent exchange of body fluid. Further study of the corrosion behaviour in vivo and in vitro is necessary.

8.3.1 Mechanical Property Challenges

The mechanical behaviour of the $Mg(OH)_2$ films is an area that is not widely reported or discussed. Although not tested in this work it was observed that the $Mg(OH)_2$ films, susceptible to cracks when cross-sectioned, may indicate a brittleness such that they could be mechanically damaged. This would bring challenges for orthopaedic implants. It could be that the appearance of cracks in cross-section results from the removal of the test piece from the solution. Rapid changes in volume may result in cracks in the coating as this is well adhered to the substrate and constrained.

HT coatings may be able to sustain higher integrity but are likely to have higher residual stress. With an applied force, a large area may detach due to the lateral cracks. Some delamination was observed in cross-section so the coating peels from the surface. Although cracks were mainly perpendicular in the EC+Additive coatings, lateral cracks linking these were also observed.

It is thought that the cracks support slow degradation and are beneficial. For an implant, these may support the application such that when an implant is stressed. In oxide-based coatings typically do not have the elasticity of the underlining metal. Thus, when the implant is stressed, this might crack open the coating. In this case, cracks (horizontal and perpendicular) exist in the coatings before stressing. The coating is sacrificial and not reliant on being crack free. As cracks relieve stress, this cracking is helpful. It is thought a stressed implant may see accelerated coating removal however it may also tolerate stressing well since cracks already exist in the coatings. Although a delaminated/cracked coating might not cause a problem from a materials point of view, in extreme cases of delamination, a physical effect on body fluid or body tissues may result.

It would also be of interest to consider how the coating copes when abraded by bone i.e. when screwing into a pre-drilled bone. There were no tests undertaken to examine if the coating would peel off when scratched by bone. Also in application high abrasion might be required. As indicated, the $Mg(OH)_2$ would have little elastic properties however some of these challenges could be explored by adding a binder to the film or forming composites with other compounds [Ng,

2010]. It would be interesting to examine using calcium phosphate and binder. Further study with $Mg(OH)_2$ using a binder or an additional top coating is recommended.

A uniform degradation mode is important since localized corrosion could lead to the early failure of an implant. However, corrosion is not only corrosion mode. Mg alloys suffer localized corrosion such as pitting. Findings from the localized corrosion are linked to the presence of second phases, precipitates or impurities on the surface of the Mg alloys. Common impurities such as Fe, Ni and Cu are widely present in Mg alloys. They reduce corrosion resistance due to their negative corrosion potential and are cathodic with respect to the Mg matrix, resulting in a fast corrosion rate resulting in more susceptibility to pitting that quickly damages the $Mg(OH)_2$ protective film. Once this film is removed, the surrounding electrolyte has contact with the Mg, causing further corrosion. If the inhomogeneities are not uniformly distributed or above a critical limit the material will corrode in a localized manner. This was demonstrated with the AZ31-ME an aerospace alloy with a few well distributed second phase particles and the AZ31-GF, and It is thought that the presence of the coating might support the reduction in early galvanic corrosion from second phase particles, compared to the uncoated alloy.

Control of the corrosion rate in Mg alloys with the $Mg(OH)_2$ coatings might reduce the susceptibility to hydrogen embrittlement.

8.3.2 Product manufacturing of complex shapes and large components.

One key factor in manufacturing is to control processing temperature, which influences the film properties to provide the preferred microstructure; dense grains are preferred. In Chapter 5, HT samples prepared at 160°C show greater film growth than at 120°C.

EC+Additive samples at a higher temperature have better coverage to the sample surfaces particularly at over 160°C. With further increases in the additive processing temperature, an inner film near the interface densifies rather than tiny

crystallites. Control of the thickness is also important to determine the long-term protection of the alloy.

For mass production, HT is not so flexible since the requirement for an autoclave might limit the production. EC+ additive films can be modified to permit EC treatment + dip coating. It may be a way to achieve the required film properties.

The coating method using a solution-based approach is flexible provided consistent and even temperatures can be maintained. It may be necessary to adjust the viscosity to enable a smooth application. The EC film as a precursor before applying the additive film was required to adjust the wettability. If the coating method is used for engineering components and large complex shapes, spray or brush coatings can be used for repair and maintenance. Using local application the coating can be tailored to engineer the coating thickness to the properties required.

This chapter considered the development and optimisation of $Mg(OH)_2$ films on Mg alloy substrates. The range of corrosion resistance that the coatings offer was discussed and the benefits of slow degradation were considered. Consideration is also given to applications of these coatings to biomedical implants.

9 Conclusion

This research demonstrates Mg-based film can provide protection to the Mg alloys AZ31 and ZM21 and corrosion resistance qualified and controlled by $Mg(HO)_2$ based film.

A hydrothermal film was developed on AZ31-GF substrate as a benchmark. A film upto 50µm in thick with a uniform structure but lateral cracks was developed. When immersed 3.5^{wt}% NaCl solution in a tranquil small volume of fluid, corrosion rates around 0.1mm/year are achieved up to 48h.

With the combination of EC and Additive processing, a two-layered $Mg(OH)_2$ film of more than 100µm is developed. The application of $Mg(OH)_2$ coatings with these methods are applicable for a range of different Mg alloy substrates.

The films with all methods in this work deliver a reduction in corrosion resistance with immersion time until such a time generally over 100h when this becomes equivalent to the natural degradation of $Mg(OH)_2$. By optimising the processing parameters, especially the temperature, the protected alloys undergo slower degradation.

Compared to uncoated samples, the sample with the HT films and EC+Additive coatings demonstrates a 10 fold reduction of corrosion rate after two-day immersion and a 3 fold reduction sustained after 21-day immersion. The benefit of the coating remains after 100h in a seawater environment There is a ten-fold reduction in corrosion rates when samples are immersed in less aggressive Hanks solution than the 3.5^{wt}% NaCl solutions The films in Hanks solution tend to be more stable.

Because this work a lot more aware of the time dependency of the degradation

Both HT and EC+Additive films have the potential to increase the service life of components for at least 3 weeks. Their corrosion rates are reduced to below the threshold rate of 0.5 mm/year required for biodegradable implants. The EC+Additive method has greater flexibility in manufacturing and repairing than the HT process. EC+Additive methods also show greater opportunities for further

enhancement that are less accessible for HT treatment, such as adding calcium phosphate or binders.

Further work

Multiple manufacturing procedures are necessary that require precise control to achieve the required coating properties. Further work that could be investigated are:

- Corrosion behaviour in flowing conditions and at body temperature.
- Approaches to mitigate brittleness and to optimise the mechanical properties of the coatings using post-treatments such as binder.
- Manufacturing approaches using solutions, such as dipping for the additive method or spraying
- Local application to enable repair and control of thickness at different parts of components as required

List of references

- ASTM 661-12, (2020), Standard Practice for Heat Treatment of Magnesium Alloys ASTM International.
- A. Atrens, W. Dietzel, (2007), The negative difference effect and unipositive Mg, Advanced Engineering Materials, 9, 292–7
- A. D. King, N. Birbilis, J. R. Scully, (2014), Accurate electrochemical measurement of magnesium corrosion rates; a combined impedance, mass-loss and hydrogen collection study, Electrochimica Acta, 121, 394.
- A. A. Nayeb-Hashemi, J. B. Clark, (1988), A.S.M. International: Phase diagrams of binary magnesium alloys, ASM International, Metals Park, Ohio.
- A. A. Pilarska, L. Klapiszewski, T. Jesionowski (2017), Recent development in the synthesis, modification and application of Mg(OH)2 and MgO: A review Mg(OH)2 and MgO. Powder Technology, 319, 373-407.
- A. J. Floor (2006), The chemical composition of seawater, seafriends. org. nz.
- A. Pardo, M.C. Merino, A.E. Coy , R. Arrabal, F. Viejo, E. Matykina (2008), Corrosion behaviour of magnesium/aluminium alloys in 3.5 wt.% NaCl, Corrosion Science, 50, 823–834.
- A. Pardoa, M.C. Merino, A.E. Coy, F. Viejo, R. Arrabal, S. Feliu Jr. (2008), Influence of microstructure and composition on the corrosion behaviour of Mg/Al alloys in chloride media, Electrochimica Acta journal, 53, 7890-7902.
- A. Pidcock. (2014), Control of magnesium alloy corrosion through the use of engineered intermetallics. PhD Thesis, Cranfield University.
- A. Prasad, P.J. Uggowitzer, Z. Shi, A. Atrens, (2012), Production of high purity magnesium alloys by melt purification with Zr, Advanced. Engineering. Materials, 14, 477–490
- A. Samaniego, B. L. Hurley, G.S. Frankel, (2015), On the evidence for univalent Mg, Journal of Electroanalytical Chemistry, 737, 123–8.
- A. Witecka, A. Bogucka, A. Yamamoto, K. Máthis, J. Jaroszewicz, S. Wojciech, (2016) Influence of biodegradable polymer coatings on corrosion,

cytocompatibility and cell functionality of Mg-2.0Zn-0.98Mn magnesium alloy, Colloids and Surfaces B: Biointerfaces, 144, 284–292

- A. Witecka, A. Bogucka, A. Yamamoto, K. Mathis,, Ś. Wojciech, J. Jaroszewicz, S. Wojciech, (2016), In vitro degradation of ZM21 magnesium alloy in simulated body fluids, Materials Science and Engineering C, 65, 59–69.
- A.J. Bard, L.R. Faulkner, (2001)Electrochemical Methods: Fundamentals and Applications, Wiley, New York
- Ash, Russell (2005). The Top 10 of Everything 2006: The Ultimate Book of Lists. Dk Pub. ISBN 978-0-7566-1321-1. Archived from the original on 5 October 2006.
- B. Denkena, A. Lucas, (2007), Biocompatible Magnesium Alloys as Absorbable Implant Materials – Adjusted Surface and Subsurface Properties by Machining Processes, CIRP Annals, 56, 1, 113-116.
- B. S., Covino.Jr, S. J, Bullard, S. D. Cramer, G. R. Holcomb, M. Ziomek-Moroz,; Cayard, M. S.Cayard, D.A. Eden, (2004). . Electrochemical corrosion rate probes for high temperature energy applications. United States. Office of Fossil Energy. USDOE - Office of Fossil Energy (FE), Twenty-First Annual International Coal Conference, Osaka, Japan, Sept. 13-17, 2004 publ. Pittsburgh Coal Conference (PCC), PA, 15261, USA.
- B951-10, (2010), Standard practice for codification of unalloyed magnesium and magnesium-alloys, cast and wrought, ASTM International.
- C Henrist, J Mathieu, C Vogels, A. Rulmont, R. Cloots, (2003), Morphological study of magnesium hydroxide nanoparticles precipitated in dilute aqueous solution, Journal of Crystal Growth, 249, 321–330
- C. Blawert, N. Hort, K.U.Kainer, (2004). Automotive Applications of Magnesium and its Alloys, Transactions of the Indian Institute of Metals, 57(4), 397-408.
- C. E. Housecroft, A. G. Sharpe, (2008). Inorganic Chemistry (3rd ed.). Prentice Hall. pp. 305–06. ISBN 978-0-13-175553-6.

- C. Iglesias, O. G. Bodelón, R. Montoya, C. Clemente,; M.C. Garcia-Alonso, J. C. Rubio, M.L. Escudero, (2015), Fracture bone healing and biodegradation of AZ31 implant in rats, Biomedical Materials, 10, 025008.
- C. Wang, L. Wu, F. Xue, R. Ma, I.-I.N. Etim, X. Hao, J. Dong, W. Ke, Electrochemical noise analysis on the pit corrosion susceptibility of biodegradable AZ31 magnesium alloy in four types of simulated body solutions. J, Journal of Materials Science & Technology. 2018, 34, 876–1884.
- C. D. Fernández-Solis, A. Vimalanandan, A. Altin, J. S. Mondragón-Ochoa, K. Kreth, P.Keil and A. Erbe, (2016), Fundamentals of Electrochemistry, Corrosion and Corrosion Protection, Springer International Publishing Switzerland.
- D. Hoche, C. Blawert, S. V. Lamaka, N. Scharnagl, C. Mendis, M. L. Zheludkevich, (2016), The effect of iron re-deposition on the corrosion of impurity-containing, Physical Chemistry Chemical Physics, 18, 1279--1291
- D. Klotz, (2018), Negative capacitance or inductive loop – A general assessment of a common low frequency impedance feature, Electrochemistry Communications, 98, 58-62.
- D. Lysne, S. Thomas, M. F. Hurley, N. Birbilis, (2015) On the Fe enrichment during anodic polarization of magnesium and its impact on hydrogen evolution, Journal of The Electrochemical Society, 162, C396–402.
- D. Song, C. Li, L. W. Zhang, X. L. Ma, G. H. Guo, F. Zhang, J. H. Jiang 1, A. B. Ma, (2017), Decreasing Bio-Degradation Rate of the Hydrothermal-Synthesizing Coated Mg Alloy via Pre-Solid-Solution Treatment, Materials 10, 858
- D. Y. Jiang, Y.L. Dai, Y. Zhang, Y. Yan, J.J Ma, D. Li, and K. Yu, (2017), Effects of Heat Treatment on Microstructure, Mechanical Properties, Corrosion Resistance and Cytotoxicity of ZM21 Magnesium Alloy as Biomaterials, Journal of Materials Engineering and Performance, 28, 33-43.
- E. Ghali, W. Dietzel, K. Kainer, (2004), General and localized corrosion of magnesium alloys: A critical review. Journal of Materials Engineering and Performance Volume 23 13(1), 7–23.

- E. Ghali, W. Dietzel , K. Kainer , (2004), Testing of general and locolized corrosion of magnesium alloys; A critical review, Journal of Materials Engineering and performance, 13, 517-529.
- E112–12, (2010) Standard Test Methods for Determining Average Grain Size, ASTM International.
- F.R. García-Galvan, S. Fajardo, V. Barranco, S. Feliu, Jr. (2021), Experimental Apparent Stern–Geary Coefficients for AZ31B Mg Alloy in Physiological Body Fluids for Accurate Corrosion Rate Determination. Metals 2021, 11, 391.
- F.X. Wu, J. Liang, W.X. Li (2015), Electrochemical deposition of $Mg(OH)_2$ /GO composite films for corrosion protection of magnesium alloys, Journal of Magnesium and Alloys, 3,231–236.
- F. Y. Cao, Z. M. ShI, J. Hofstetter, P. J. Uggowitzer, G. L. Song, M. Liu, A. Atrens,(2013), Corrosion of ultra-high-purity Mg in 3.5% NaCl solution saturated with $Mg(OH)_2$. Corrosion Science journal, 75, 78-99.
- F. Y. Cao, G. L. Song, A. Atrens, (2016), Corrosion and passivation of magnesium alloys, Corrosion Science, 111, 835-845.
- G. Balducci, L. B. Diaza and D. H. Gregor (2017) Recent progress in the synthesis of nanostructured magnesium hydroxide: Cryst Eng Comm, 19, 6067-6084.
- G. S. Frankel, (2014), Electrochemical techniques in corrosion: status, limitations, and needs. Journal of Testing and Evaluation, 42, 517–40.
- G. S. Frankel, A. Samaniego, N. Birbilis, Evolution of hydrogen at dissolving magnesium surfaces, Corrosion Science. 70 (2013) 104–111.
- G. S. Frankel, S. Fajardo, B. M. Lynch, (2015), Introductory lecture on corrosion chemistry: a focus on anodic hydrogen evolution on Al and Mg, Faraday Discuss, 180, 11–33.
- G. L. Song, (2007), Control of biodegradation of biocompatable magnesium alloys, Corrosion Science, 49, 4, 1696–1701.
- G. L. Song, A. Atrens, (2003), Understanding Magnesium corrosion: A Framework for Improved Alloy Performance, Advanced Engineering Materials, 5, 12, 837-858.

- G. L. Song, (2011), Corrosion of Magnesium alloys, Woodhead Publishing
- G. L. Song, (2012), The effect of texture on the corrosion behavior of AZ31 Mg alloy, The Journal of The Minerals, Metals & Materials Society, 64, 671–679.
- G. L. Song, A. Atrens, D. A. St John, (2001), hydrogen evolution method for the estimation of the corrosion rate of magnesium alloys, Magnesium technology, John Wiley & Sons, Inc, 254–62.
- G. L. Song, Z. Xu, (2010), The surface, microstructure and corrosion of magnesium alloy AZ31 sheet. Electrochim. Acta, 55, 4148–4161.
- Gamry instrument, (acquired on 2019) , Basics of Electrochemical Impedance,Spectroscopy,https://www.gamry.com/application-notes/EIS/basics-of-electrochemical-impedance-spectroscopy/
- G. Williams, Birbilis N, H. N. McMurray, (2013),The source of hydrogen evolved from a magnesium anode, Electrochemistry Communications, 36, 1–5.
- G. Williams, H. N. McMurray, (2008), Localized corrosion of magnesium in chloride-containing electrolyte studied by a scanning vibrating electrode technique. Journal of The Electrochemical Society, 155, C340-C9.
- H. E. Friedrich, B.L. Mordike, (2006) Magnesium technology: Metallurgy, design data, applications, Springer-Verlag Berlin Heidelberg.
- H. Jeong, Y. Yoo, Synthesis and characterization of thin films on magnesium alloy using a hydrothermal method, Surface. Coatings Technology, 284 (2015) 26–30.
- H. S. Kim, G. H. Kim, H. Kim, W. J. Kim, (2013), Enhanced corrosion resistance of high strength Mg–3Al–1Zn alloy sheets with ultrafine grains in a phosphate-buffered saline solution, Corrosion Science 74 139–148.
- H. M. Krebs, The microstructure and corrosion performance of AZ31B-H24 magnesium alloy sheet, PhD Thesis, University of Manchester.
- H. Liu, (2011), The effects of surface and biomolecules on magnesium degradation and mesenchymal stem cell adhesion. J. Biomed. Mater. Res. Part A, 99, 249–260.

- I. J. Polmear, (2006), Light Alloys: From Traditional Alloys to Nanocrystals, 4th ed., Butterworth-Heinemann,
- J. Bockris, A. Reddy, (2000), Modern electrochemistry. New York: Kluwer Academic/Plenum Publishing.
- J. A. Boyer, (1928), The corrosion of magnesium and of the magnesium aluminum alloys containing manganese Report 248. American Magnesium Corporation.
- J. E. Gray, B. Luan, Protective coatings on magnesium and its alloys - A critical review, Journal of Alloys Compdounds, 336 (2002) 88–113.
- J. K. Gjaldbaek, Solubility of $Mg(OH)_2$ (l) existence of different modifications of $MgOH)_2$ (ll) solubility product and the dissociation constant of $Mg(OH)_2$, Z. Anorg. Allgem. Chem., 144 (1925) 269.
- J. D. Hanawalt, C. E. Nelson, J. A. Peloubet, (1942), Corrosion studies of magnesium and its alloys, Trans. Am. Inst. Min. Metall. Eng. 147, 273–299.
- J. A. Liu, Y.S. Xie, Z.X. Ma（2016，Concise magnesium alloy material Handbook，Chinese Metallurgical Industry Press. ISBN 9787502472238.
- J. Liao, M. Hotta, (2016), Corrosion products of field-exposed Mg-Al series magnesium alloys, Corrosion Science, 112, 276–88
- J. S. Liao, M. Hotta, N. Yamamoto, (2012) Corrosion behavior of fine-grained AZ31b, Corrosion Science, 61, 208-214.
- J. C Scully, (1990). The Fundamentals of Corrosion (3rd ed.). Oxford: Pergamon Press.
- J. Vormann, (2003), Magnesium: Nutrition and metabolism, Molecular Aspects of Medicine, 24, 1-3, 27-37.
- J. L. Wang, J. Tang, P. Zhang, Y.D. Li, J. Wang, Y.X Lai, L. Qin,(2012) Surface modification of magnesium alloys developed for bioabsorbable orthopedic implants: a general review. J. Biomed. Mater. Res. B 100, 1691–1701.
- J. C. Yu, A. Xu, L.Z. Zhang, R.Q. Song, and L. Wu, (2004), Synthesis and Characterization of Porous Magnesium Hydroxide and Oxide Nanoplates, The Journal of Physical Chemistry B, 108, 64-70.

- K. Chen, J. Dai, X. Zhang, (2015), Improvement of corrosion resistance of magnesium alloys for biomedical applications. Corrosion Review, 33, 101–117
- K. Gusieva, C. H. J Davies, J. R. Scully, N. Birbilis, (2015), Corrosion of magnesium alloys: the role of alloying, International Materials Reviews, 60, 169–94.
- K. U. Kainer (2003), Magnesium: Alloys and Technologies, Weinheim.
- K. N. Reichek, K. J. Clark, J. E. Hillis, (1985), Controlling the salt water corrosion performance of magnesium AZ91 alloy, SAE Transactions. 94 318–329.
- K.S. Williams, J. P. Labukas, V. Rodriguez-Santiago, J. W. Andzelm, (2015), First principles modeling of water dissociation on Mg(0001) and development of a magnesium surface pourbaix diagram. Corrosion, 71, 209–23
- L. Pompa, Z. U. Rahman, E. Munoz, W. Haider, (2015), Surface characterization and cytotoxicity response of biodegradable magnesium alloys Material Science and Engineering C, 49, 761–768.
- L. Nan, Y.F. Zheng (2013), Novel Magnesium Alloys Developed for Biomedical Application: A Review, Journal of Material. Science and Technology, 29(6), 489-502.
- L. Wang, T. Shinohara B-P Zhang. (2010). XPS Study of the Surface Chemistry on AZ31 and AZ91 Magnesium Alloys in Dilute NaCl Solution. Applied Surface Science, 256, 5807-5812.
- M. Avedesian (1999), ASM Specialty Handbook: Magnesium and Magnesium Alloys, ASM international.
- M. Curioni, (2014), The behaviour of magnesium during free corrosion and potentiodynamic polarization investigated by real-time hydrogen measurement and optical imaging, Electrochimica Acta, 120, 284–92
- M. Erinc, W. H. Sillekens, R. Mannens, R. J. Werkhoven, (2009), Applicability of existing magnesium alloys as biomedical implant materials. In: Nyberg EA, Agnew SR, Neelameggham NR, Pekguleryuz MQ, editors. Magnesium Technology. San Francisco. Warrendale, PA: Minerals, Metals and Materials Scociety; 2009. p. 209–14.

- M. G. Fontana, (1987). Corrosion Engineering (3rd ed.). McGraw-Hill International Editions.
- M. K. Kulekci, (2008). Magnesium and its Alloys Applications in Automotive Industry. The International Journal of Advanced Manufacturing Technology, 39, 851–865.
- M. Mhaede, F. Pastorek, B. Hadzima, (2014), Influence of shot peening on corrosion properties of biocompatible magnesium alloy AZ31 coated by dicalcium phosphate dihydrate (DCPD). Material Science and Engineering. C, 39, 330–335.
- M. M. Gawlik, (2018), The Effect of Surface Treatments on the Degradation of Biomedical Mg Alloys—A Review, Materials, 11, 2561, doi:10.3390/ma11122561.
- M. Pourbaix,(1974), Atlas of Electrochemical Equilibria in Aqueous Solutions, 2nd Ed, National Association of Corrosion Engineers.
- M. S. Song, R.C Zeng, Y. F. Ding , R. W. Li, M. Easton, I. Cole, N. Birbilis, Nick. X. B. Chen (2019), Recent advances in biodegradation controls over Mg alloys for bone fracture management: A review, Journal of Materials Science and Technology, 35, 4, 535-544
- M. Taheri, R. C. Phillips, J. R. Kish, G. A. Botton, (2012), Analysis of the surface film formed on Mg by exposure to water using a FIB cross-section and STEM – EDS, Corrosion Science, 59, 222-228
- M. Taheri, M. Danaie, J. R. Kish, (2014), TEM Examination of the Film Formed on Corroding Mg Prior to Breakdown, Journal of the Electrochemical Society, 161, 3, 89-94
- M. Thirumurugan, G. M. Thirugnasambandam, S. Kumaran, T. S. Rao, (2011), Microstructural refinement and mechanical properties of direct extruded ZM21 magnesium alloys, Trans. Nonferrous Met. Soc.China, 21, 2154-2159.
- N. N. Aung, W. Zhou, (2010) Effect of grain size and twins on corrosion behaviour of AZ31B magnesium alloy, Corrosion Science, 52, 2, 589-594

- N. Birbilis, A. D. King, S Thomas, G. S. Frankel, J. R. Scully, (2014) Evidence for enhanced catalytic activity of magnesium arising from anodic dissolution, Electrochimica Acta, 132, 277–83.
- N. Sriraman, S Kumaran, (2019), Improved bio-acceptability of thermomechanically processed ZM21 magnesium alloy, 6, 5.
- N. Stanford, D. Atwell, (2013), The effect of Mn-rich precipitates on the strength of AZ31 extrudates, Metallurgical and Materials Transactions A: Physical Metallurgy and Materials Science, 44, 4830-4843.
- N. Stanford, D. Atwell, (2013), The effect of Mn-rich precipitates on the strength of AZ31 extrudates, Metallurgical and Materials Transactions A: Physical Metallurgy and Materials Science, 44 4830-484.
- N. Winzer, A. Atrens, G. L. Song, E. Ghali, W. Dietzel, K. U. Kainer, (2005), A critical review of the stress corrosion cracking (SCC) of magnesium alloys. Advanced Engineering Materials, 7, 659–93.
- N. Zhao, D. Zhu, (2014), Collagen Self-Assembly on Orthopedic Magnesium Biomaterials Surface and Subsequent Bone Cell Attachment. PLoS ONE, 9, e110420.
- O. Lunder, T. K. Aune, K. Nisancioglu, (1987), Effect of Mn additions on the corrosion behavior of mould-cast magnesium ASTM AZ91, Corrosion. 43 291–295.
- P. Liang, T. Tarfa, J. A. Robinson, S. Wagner, P. Ochin, M. G. Harmelin, H. J. Seifert, H. L. Lukas, F. Aldinger, (2017), Experimental investigation and thermodynamic calculation of the Al-Mg-Zn system, Thermochemistry Acta, 314 (1998) 87-110.
- P. Marshall (2015). Retrieved 07 22, 2015, from Philipcmarshall.net: http://philipmarshall.net/Teaching/rwuhp382/metals/galvanic_corrosion.htm
- Powder Diffraction File (PDF). International Centre for Diffraction Data (ICDD).
- S. Das, A. Dey, A. K. Mandal, N. Dey, A. K Mukhopadhyay, (2013), Synthesis of $Mg(OH)_2$ micro/nano flowers at room temperature, Journal of Advanced Ceramics 2013, 2(2): 173–179.

- Q. Zhao, W. Mahmood, Y. Zhu, (2016), Synthesis of dittmarite/$Mg(OH)_2$ composite coating on AZ31 using hydrothermal treatment, Applied Surface Science 367, 249–258.
- Q. Zhao, W. Mahmood, Y.Y. Zhu, (2016), Synthesis of dittmarite/$Mg(OH)_2$ composite coating on AZ31 using hydrothermal treatment, Applied Surface Science, 367, 249-258.
- Q.H.Yuan, Z.W. Lu, P.X Zhang, X.B. Luo, X.Z Ren, Teresa D. Golden 2014.
- R. Ambat, N. N. Aung, W. Zhou, (2000) valuation of microstructural effects on corrosion behaviour of AZ91D magnesium alloy, Corrosion Science, 42, 8, 1433-1455.
- R. Q. Hou, N. Scharnagl, F. Feyerabend, R. W. Römer, (2018), Exploring the effects of organic molecules on the degradation of magnesium under cell culture conditions, corrosion science, 132, 35-45.
- R. Xu, Y. Shen, J. Zheng, Q. Wen, Z. Li, X. Yang, P.K. Chu, Effects of one-step hydrothermal treatment on the surface morphology and corrosion resistance of ZK60 magnesium alloy, Surface. Coatings Technology, 309 (2017) 490–496.
- S. Abela, (2011).Protective Coatings for Magnesium Alloys, Magnes. Alloy. - Corrosion and Surface Treatments, Janeza Trdine 9, 51000 Rijeka, Croatia, InTech.
- S. Fajardo, G. S. Frankel, (2015), Gravimetric method for hydrogen evolution measurements on dissolving magnesium. Journal of The Electrochemical Society, 162, C693–701.
- S. Fajardo, G. S. Frankel, (2015), Effect of impurities on the enhanced catalytic activity for hydrogen evolution in high purity magnesium. Electrochimica Acta, 165, 255–67.
- S. Fajardo, C. F. Glover, G. Williams, G. S. Frankel, (2016), The source of anodic hydrogen evolution on ultra high purity Mg. Electrochimica Acta, 212, 510–21.
- S. Feliu, A Samaniego, A. A. El-Hadad, & I. Llorente (2013). The Effect of NaHCO3 Treatment Time on the Corrosion Resistance of Commercial

Magnesium Alloys AZ31 and AZ61 in 0.6M NaCl Solution. Corrosion Science, 67, 204-216.

- S. Fajardo, C. F. Glover, G. Williams, G. S. Frankel, (2017), The evolution of anodic hydrogen on high purity magnesium in acidic buffer solution. Corrosion, 73, 482–93.
- S. Feliu, I. Llorente, (2015). Corrosion Product Layers on Magnesium Alloys AZ31 and AZ61: Surface Chemistry and Protective Ability, Applied Surface Science, 347, 736-746.
- S.S.A. El-Rahman, (2003) Neuropathology of aluminum toxicity in rats (glutamate and GABA impairment), Pharmacology Research, 47 189-194.
- S. V. Lamaka, D. Höche, R. P. Petrauskas, C. Blawert, M. L. Zheludkevich, (2016), A new concept for corrosion inhibition of magnesium: suppression of iron re-deposition, Electrochemistry Communications, 62, 5–8.
- S.M. Wang, L.X. Fu, Z.G. Nai, J. Liang, B.C. Cao, (2018), Comparison of Corrosion Resistance and Cytocompatibility of MgO and ZrO2 Coatings on AZ31 Magnesium Alloy Formed via Plasma Electrolytic Oxidation, Coatings, 2018, 8, 441;
- T. Cain, S. B. Madden, N. Birbilis, J. R. Scully, (2015), Evidence of the enrichment of transition metal elements on corroding magnesium surfaces using rutherford backscattering spectrometry, Journal of The Electrochemical Society , 162, C228–37
- T. Ishizaki, N. Kamiyama, K. Watanabe, A. Serizawa, Corrosion resistance of $Mg(OH)_2$/Mg-Al layered double hydroxide composite film formed directly on combustion-resistant magnesium alloy AMCa602 by steam coating, Corrosion Science, 92 (2015) 76–84.
- T. Ishizaki, S. Chiba, K. Watanabe, H. Suzuki, Corrosion resistance of Mg–Al layered double hydroxide container-containing magnesium hydroxide films formed directly on magnesium alloy by chemical-free steam coating, Journal of Materials Chemistry A, 1 (2013) 8968.
- T. L. Zhang, Z. H. Ji, S. Y. Wu, (2011), Effect of extrusion ratio on mechanical and corrosion properties of AZ31B alloys prepared by a solid recycling process, Materials and Design, 32, 2742–2748.

- W F Ng, & M Wong, F Cheng. (2010). Stearic acid coating on magnesium for enhancing corrosion resistance in Hanks' solution. Surface & Coatings Technology, 204. 1823-1830.
- Witte, F. The history of biodegradable magnesium implants: a review. Acta Biomaterialia. 6, 1680–1692 (2010)
- X. Z. Deng, Y.W. Wang, J.P. Peng, . Zhong. (2015), Current efficiency of synthesis magnesium hydroxide nanoparticles via electrodeposition, 3rd International Conference on Material, Mechanical and Manufacturing Engineering.
- X. Li, X. M. Liu, S. l. Wua, K. W. K. Yeung, Y. F. Zheng, P. K. Chu, (2016), Design of magnesium alloys with controllable degradation for biomedical implants: From bulk to surface, Acta Biomaterialia, 45, 2-30.
- Y. Feng, X. Chen, T. Liu, L. Liu, Y. Zou, Y. Wang, Z. Ren, Y. Fan, Lv, M. Zhang, In-situ hydrothermal crystallization $Mg(OH)_2$ films on magnesium alloy AZ91 and their corrosion resistance properties, Materials Chemistry and Physics, 143 (2013) 322–329. Y, Wang (2015)
- Y. D. Wang, (2015), Study of the Corrosion behaviour of the Mg-Al-Zn Alloys with Corrosion products. MSc Thesis, Cranfield University.
- Y. P. Wang, Y. H. He, Z. J. Zhu, Y. Jiang, J. Zhang, J. L. Niu, L. Mao, G. Y. Yuan (2012), In vitro degradation and biocompatibility of Mg-Nd-Zn-Zr alloy, Chinese Science Bulletin, 57, 2163–2170.
- Y. Zhu, G. Wu, Y.H. Zhang, Q. Zhao, Growth and characterization of $Mg(OH)_2$ film on magnesium alloy AZ31, Applied Surface Science, 257 (2011) 6129–6137.
- Y. Zhu, Q. Zhao, Y. H. Zhang, G. Wu, Hydrothermal synthesis of protective coating on magnesium alloy using de-ionized water, Surface & Coatings Technology, 206 (2012) 2961–2966.
- Y. D. Li, M. Sui, Y. Ding, G.H. Zhang, J. Zhuang, C. Wang, (2000), Preparation of $Mg(OH)_2$ nanorods, Advanced Materials, 12, 11, 818-821
- Y. W. Yang, C.X. He, D.Y. E, W.J Yang, F.W. Qi, De.Q. Xie, L.D. Shen, S.P. Peng, C.J Shuai, (2020), Mg bone implant: Features, developments and perspectives,Materials & Design,185, ISSN 0264-1275,

- Z. P.Cano, M.Danaie, J. R. Kish, J. R. McDermid, G. A. Botton, G. Williams, (2015), Physical characterization of cathodically-activated corrosion filaments on magnesium alloy AZ31B, Corrosion, 71, 2, 146-159.
- Z. S. Seyedraoufi, (2018), The Development and Investigation of Biocompatibility Properties of Biodegradable Magnesium–Zinc Scaffold Electrodeposited with Hydroxyapatite, Surface Engineering and Applied Electrochemistry, 54, 6, 607–613.
- Z. M. Shi, A. Atrens (2011), An innovative specimen configuration for the study of Mg corrosion, Corrosion Science, 53, 226–246.
- Z. M. Shi, Liu. Ming, A. Atrens, (2010) Measurement of the corrosion rate of magnesium alloys using Tafel extrapolation, Corrosion Science, 52, 2, 579-588